Engineered Nanomaterials for Selective Detection of Toxic Gases and Volatile Organic Compounds

Thesis Submitted by

Saptarshi Ghosh

Doctor of Philosophy (Engineering)

Department of Instrumentation & Electronics Engineering
Faculty Council of Engineering & Technology
Jadavpur University
Kolkata 700032,
India

April, 2016

JADAVPUR UNIVERSITY
KOLKATA – 700 032, INDIA

Index No. : 05/14/E

Title of the Thesis	**Engineered Nanomaterials for Selective Detection of Toxic Gases and Volatile Organic Compounds**
Name, Designation & Institution of the Supervisors	**Prof. Rajib Bandyopadhyay** Department of Instrumentation and Electronics Engineering, Jadavpur University Salt Lake Campus Kolkata –700 098 West Bengal, India
	Dr. Amarnath Sen Retd. Chief Scientist, Sensor & Actuator Division CSIR-Central Glass and Ceramic Research Institute 196 Raja S.C. Mullick Road, Kolkata –700032 West Bengal, India
	Dr. Somenath Roy Senior Scientist, Sensor & Actuator Division CSIR-Central Glass and Ceramic Research Institute 196 Raja S.C. Mullick Road, Kolkata –700032 West Bengal, India

List of Publications

Papers Published in International Journals

[1] Saptarshi Ghosh, Mousumi Narjinary, Amarnath Sen, Rajib Bandyopadhyay, Somenath Roy, "Fast detection of low concentration carbon monoxide using calcium-loaded tin oxide sensors", Sensors and Actuators B: Chemical 203 (2014) 490-496.

[2] Saptarshi Ghosh, Deblina Majumder, Amarnath Sen, Somenath Roy, "Facile sonochemical synthesis of zinc oxide nanoflakes at room temperature", Materials Letters 130 (2014) 215-217.

[3] Saptarshi Ghosh, Somenath Roy, "Effect of ageing on $Sn_6O_4(OH)_4$ in aqueous medium—simultaneous production of SnO and SnO_2 nanoparticles at room temperature", Journal of Sol-Gel Science & Technology (Accepted, in press).

[4] Saptarshi Ghosh, Ujjal Chowdhury, Somenath Roy, Rajib Bandyopadhyay, "Detection of low ppm carbon monoxide with charge ordered $LuFe_2O_4$ gas sensor–A novel sensing mechanism", Ceramics International 42 (2016) 14944-14948.

[5] Debasis Dutta, Saptarshi Ghosh, Mousumi Narjinary, Nabarun Bhattacharya, Rajib Bandyopadhyay, "Tin oxide based gas sensor array in electronic nose to monitor aroma of black tea", Sensor Letters 14 (2016) 396-401

Articles in International Conference Proceedings/Archives

[1] Saptarshi Ghosh, Deblina Majumder, Amarnath Sen, Somenath Roy, "Sensors comprising ZnO nanoflakes for detection of principal VOCs in tea aroma", International Conference on Sensors, Materials and Manufacturing (ICSMM - 2015), Vissai Saigon Hotel, Ho Chi Minh City, Vietnam, 6th – 7th February, 2015.

[2] Saptarshi Ghosh, Bipan Tudu, Nabarun Bhattacharyya, Rajib Bandyopadhyay, "Electronic nose for on-line quality evaluation of black tea using incremental SOM techniques", Proceedings of the 2015 2nd International Symposium on

Physics and Technology of Sensors, IEEE Xplore (2015) 272-277 (doi: 10.1109/ISPTS.2015.7220128).

[3] Saptarshi Ghosh, Mousumi Narjinary, Amarnath Sen, Somenath Roy, "Ca, Ba and Sr – incorporated SnO_2 sensors for detection of sub-10 ppm carbon monoxide", International Conference on MEMS and Sensors (ICMEMSS - 2014), IIT Madras, Chennai, India, 18th – 20th December, 2014.

[4] Nabarun Bhattacharyya, Debashis Dutta, Saptarshi Ghosh, Saikat Mandal, Mousumi Narjinary, Amarnath Sen, "SnO_2 based tea aroma sensors for electronic nose", 14th International Meeting on Chemical Sensors (ICMS - 2014), Nuremberg, Germany, 20th – 23rd May, 2012.

List of Patents

[1] "Sensor compositions for detection of linalool, geraniol, methyl salicylate and trans-2-hexenal with an intention to classify black tea aroma"
by Amarnath Sen, Mousumi Narjinary, Saikat Mandal, and Saptarshi Ghosh
(Application Number: 537/DEL/2015)
Filing date: 25/02/2015; Publication Date: 26/08/2016

List of Presentations in National / International Conferences

[1] International Conference on Sensors, Materials and Manufacturing (ICSMM - 2015), Vissai Saigon Hotel, Ho Chi Minh City, Vietnam, 6th – 7th February, 2015.

[2] International Conference on MEMS and Sensors (ICMEMSS - 2014), IIT Madras, Chennai, India, 18th – 20th December, 2014.

[3] 2nd International Symposium on Physics and Technology of Sensors (ISPTS - 2), Yashwantrao Chavan Academy of Development Administration (YASHADA), Pune, India, 8th – 10th March, 2015.

Certificate from the Supervisors

Date: April, 2016

This is to certify that the thesis titled **"Engineered nanomaterials for selective detection of toxic gases and volatile organic compounds"**, *submitted by* ***Mr. Saptarshi Ghosh****, who got his name registered on 14th May, 2014 for the award of Ph.D. (Engineering) degree of Jadavpur University, is absolutely based upon his own work under the joint supervision of the undersigned; and that neither his thesis nor any part of it has been submitted for degree / diploma or any other academic award anywhere before.*

--------------------	----------------------	-----------------------
Prof. Rajib Bandyopadhyay Dept. of Instrumentation & Electronics Engineering, Jadavpur University Salt Lake Campus, Kolkata – 700098, West Bengal, India	Dr. Amarnath Sen Retd. Chief Scientist, Sensor & Actuator Division CSIR-Central Glass and Ceramic Research Institute (CGCRI), 196 Raja S.C. Mullick Road, Jadavpur, Kolkata – 700098 West Bengal, India	Dr. Somenath Roy Senior Scientist, Sensor & Actuator Division CSIR-Central Glass and Ceramic Research Institute (CGCRI), 196 Raja S.C. Mullick Road, Jadavpur, Kolkata – 700098 West Bengal, India

Dedicated to My Parents

Mr. Suniti Kr. Ghosh

And

Mrs. Sarmila Ghosh

They have been my Inspiration

Acknowledgement

It is my privilege to express profound sense of gratitude and indebtedness to Prof. Rajib Bandyopadhyay, Department of Instrumentation & Electronics Engineering, Jadavpur University, Kolkata, to Dr. Amarnath Sen, Retd. Chief Scientist, Sensor & Actuator Division, CSIR - Central Glass and Ceramic Research Institute, Kolkata and to Dr. Somenath Roy, Senior Scientist, Sensor & Actuator Division, CSIR - Central Glass and Ceramic Research Institute, Kolkata for providing me a very cooperative and precious guidance at every stage of the thesis program. Completion of this thesis would not have been possible without their persistent guidance.

I sincerely acknowledge the opportunity provided by the Director, CSIR-CGCRI to carry out my research in this institute. I would like to take this opportunity to express my gratitude towards all the staff members of Sensor & Actuator Division, CSIR-CGCRI for their cooperation and assistance towards completion of this work. I specially thank Ms. Mousumi Narjinary, Technical Officer for her constant support and help during the experiments. I record my heart-felt thanks for Mr. Sagnik Das, Technical Officer and Md. Jalaluddin Mondal, Senior Technical Assistant for their help with the hardware setups. I also thank Mr. Ashim Kr. Halder, Sk. Md. Mursalin, Mr. Raju Manna, technical staffs and Mr. Tarak Hazra, project assistant for their kind cooperation and necessary support. I sincerely acknowledge the inspirations received from Dr. Debdulal Saha, Dr. Shrabanee Sen, Dr. Sushmita Kundu, Dr. Anshuman Seal during different phases of my research. I would express my sincere gratitude to the Materials Characterization Department, CSIR-CGCRI for their constant support. I would like to take this opportunity to express heartiest regards and gratitude towards Dr. Saikat Mandal and Dr. Dinesh Topwal, Former Fellow Scientists, CSIR - CGCRI for their constant guidance and inspiration in the initial phase of my graduation years. In addition, I would like to thank Dr. K. Dana, Senior Scientist, Refractories and Traditional Ceramics Dicision, CSIR-CGCRI for providing me the opportunity to work with layered double hydroxide.

I must express profound gratitude to Prof. BipanTudu, Department of Instrumentation & Electronics Engineering, Jadavpur University for his immense support and valuable suggestions at every step of this research program. I am also thankful to Dr. Nabarun Bhattacharya, Associate Director, Centre for Development of Advanced Computing (C-DAC), Kolkata, for his valued inputs towards the research program.

I must thank the DST-CSIR Sensor Hub program for their financial support. I am further indebted to Dr. Amarnath Sen, Administrative-coordinator of DST-CSIR Sensor Hub program to provide me with an opportunity to work as a senior research fellow in the project and for bestowing the necessary supports including the valuable training sessions. I duly acknowledge the support received from International Travel Scheme (ITS), Department of Science and Technology (DST), Government of India, for providing me with financial assistance for presenting a research article in an international conference in Vietnam. Funding from Council of Scientific & Industrial Research (CSIR), Government of India, is also acknowledged.

I am thankful to all my co-workers of Sensor Hub, especially to Dr. Arunangshu Ghosh, who was extremely helpful. I express earnest thanks to all the co-authors of my publications. I record my heart-felt thanks for Ms. Deblina Majumder, Mr.Preetam Guha Ray, Mr. Dipankar Panda, Ms. Madhurima Das, PhD Research Scholars of Sensor & Actuator Division, for their help during the experiments.

Finally, I would like to take this opportunity to dedicate this thesis work to my parents who inspired me to take up this program. I would like to express immense and earnest gratitude for both my Father and Mother who blessed me with unstinted and unconditional support, love, encouragement and motivation during this research work that demanded long hours at laboratory, study and travels. I owe my uncle Prof. Siddhartha Sankar Ghosh, Professor, IIT Guwahati and aunt Dr. Paramita Ghosh, for all their love and encouragement during demanding situations. I thank my brothers and sisters, Srijeeta, Pushkar, Debajit, Souvik and Suranjana for their unconditional love and support. I thank my friends Tanay, Ranjan, Samik, Debraj, Kaushik, Nandini and Sujata, for their confidence in me and constant encouragement. I specially thank Ms. Priyanka Das for being a constant motivator and for her help in all and every possible way throughout this enlightening journey.

April, 2016

Saptarshi Ghosh
Department of Instrumentation &Electronics Engineering
Jadavpur University

Contents

Chapter 4: Creation of exotic morphologies of ZnO and their carbon monoxide sensing 115-158

Chapter 5: Detection of principal VOCs in black tea aroma – role of different additives on sensing behaviour of SnO_2 and ZnO 159-184

Chapter 6: Conclusion and future scope 185-192

List of Tables

List of Figures

Chapter 1: Introduction and Scope of the Thesis 1-46

Chapter 2: Optimization of synthesis for tin oxide nanoparticles 47-82

Chapter 3: Grain growth inhibition of SnO_2 by Group II elements for fast detection of carbon monoxide 83-114

Chapter 4: Creation of exotic morphologies of ZnO and their carbon monoxide sensing 115-158

List of Abbreviations

ACGIH	American Conference of Governmental Industrial Hygienists
AEDA	Aroma Extract Dilution Analysis
AIHA	American Industrial Hygiene Association
ALD	Atomic Layer Deposition
ANN	Artificial Neural Network
AQI	Air Quality Index
BET	Brunauer–Emmett–Teller
BF	Bright Field
CB	Conduction Band
CBM	Conduction Band Minimum
CNT	Carbon Nano Tube
CO	Carbon Monoxide
CTAB	Cetyltrimethylammonium Bromide
CTC	Crush-Tear-Curl
CTL	Cataluminiscence
CVD	Chemical Vapour Deposition
DI	Deionized
DLE	Deep Level Emission
DSC	Differential Scanning Calorimetry
EPA	Environmental Protection Agency
ESM	Egg Shell Membrane
FD	Flavour Dilution
FESEM	Field Emission Scanning Electron Microscopy
FFT	Fast Fourier Transform
FTIR	Fourier Transform Infrared Spectroscopy
FWHM	Full Width Half Maximum
GC	Gas Chromatography
GUI	Graphical User Interface
HRTEM	High Resolution Transmission Electron Microscopy
IDLH	Immediately Dangerous To Life Or Health
JCPDS	Joint Committee on Powder Diffraction Standards
LC_{50}	Lethal Concentration
LDA	Linear Discriminant Analysis
LDL	Lower Detection Limit
LPG	Liquified Petroleum Gas
MOS	Metal Oxide Semiconductor
NAAQS	National Ambient Air Quality Standard
NBE	Near Band Age
NDIR	Nondispersive Infrared
NIOSH	National Institute for Occupational Safety and Health
OAV	Odour Activity Value
OSHA	Occupational Safety and Health Administration
PEG	Polyethylene Glycol
PEN	Portable Electronic Nose
PL	Photoluminescence
PPM	Parts Per Million
QCM	Quartz Crystal Microbalance
ROS	Reactive Oxygen Species
SAED	Selected Area Electron Diffraction
SDS	Sodium Dodecyl Sulfate
TEM	Transmission Electron Microscopy
TGA	Thermogravimetric Analysis
TLV	Threshold Limit Value
TO	Transistor Outline
TWA	Time Weighted Average
UV-NBE	Ultraviolet Near Band Edge
UV-VIS	Ultraviolet Visible Spectroscopy
VLS	Vapour-Liquid-Solid
VOC	Volatile Organic Compound
WHO	World Health Organization
WMA	Win Muster Airsense
XPS	X-ray photoelectron spectroscopy
XRD	X-Ray Diffraction Analysis

Chapter 1

Introduction and scope of the thesis

This chapter is dedicated towards framing the problem statement for the dissertation, that deals with fabrication of sensor modules for detection of (a) carbon monoxide (CO) and (b) aroma volatiles emanated from black tea. In the process it identifies the problem areas through series of discussions on human olfaction system and its associated limitations, and thus establishes the relevance of the research program. The discussion then focuses on metal oxide semiconductors based chemiresistive sensors as rugged, reliable modules for detection of carbon monoxide. The next section not only justifies the choice of tin dioxide and zinc oxide as ideal materials for CO sensing, but also highlights the typical engineering performed on them to enhance their response. The discussion then introduces the second segment of the thesis which deals with aroma based tea quality monitoring. Conventionally, tea quality monitoring in industries is performed by dedicated human personnel called tea tasters who rely on their error prone organoleptic evaluations which lack scientific validation. Specifically, they identify subtle variation in the concentrations of key aroma volatiles for their evaluation process. Till date only a handful electronic prototypes incorporating nonspecific commercial sensors are utilized for aiding the tasters in their exertion. Therefore the motivation to fabricate specific sensor modules for these key volatiles is realized. The problem statement is framed accordingly and the scope of the thesis is elucidated.

List of Sections

1.1. Introduction

Human cognition or perception of worldly entities is primarily dependent on an assortment of natural sensors present within the body. These sensors help in identification and subsequent interpretation of an object or phenomenon through generation of physical or chemical stimuli, a process often termed as *transduction*. The stimuli is then perceived by the central nervous system and transmitted to the brain for mapping and generation of comprehensible information. All living beings including humans are endowed with selection of such sensory receptors. These receptors can be broadly classified into two separate divisions based on the function they perform. While some of the receptors are integral in monitoring the parameters key to human metabolism like osmolarity and pressure in blood vessels, others provide the necessary aid in cognition and reconstruction of an external entity in human brain. While the former group is intrinsic and requires medical intervention for maintaining their pristine self, humans have constantly strived to mimic the external sensory receptors and counter their associated limitations. The external receptors present in humans can be broadly classified into chemoreceptors (gustation and olfaction), photoreceptors (perception of light), mechanoreceptors (sound, strain & stress), nocireceptors (pain) and thermoreceptors (heat). These band of receptors are responsible for visual, auditory, olfactory, haptic (touch), and gustatory (taste) perceptions. Another form of sensors known as electroreceptors recognizing electronic stimulus are exclusive to marine life. The synergy of signals generated from the receptors stimulates human brain to provide a perception of the surrounding environment. Though every form of perception is important for the very existence of an individual, and atrophy of any cognitive process adversely affects the life’s balance, yet perhaps the most important among the sensory receptors are the chemoreceptors which are closely associated with the metabolic processes in humans. Chemoreceptors are responsible for an individual’s capability of identifying a particular taste and smell. Inbound molecules of a target analyte bind avidly with these chemosensors located in the gustatory or olfactory tracts and tranduces a recognizable electronic signal. While the sensors present in the mouth are responsible for detecting non-volatile portions, the aroma of an analyte is detected by the receptors present in the nose. The combined synergy of taste and aroma constitute the flavour of a particular component.

Thus the perception of aroma is largely decided by the sense of smell, formally known as olfaction, produced from the chemical binding of the volatiles within the analyte with the receptors. However the overall aroma can be further deconvoluted to be generated from contributions of two different modalities, namely “*orthonasal*” and *“retronasal”* olfaction.

While the former is produced from receptors located in the external nares or the nostrils due to volatiles travelling through the olfactory bulb, the later is generated from compounds reaching the receptors through the internal nares. The olfactory system of human is an organized entity of spatially correlated and functionally tuned smell receptors connected to brain through multiple nerve cells. The sense of olfaction is one of the most important perceptions in humans as it provides a preemptive estimate about critical issues including the quality of food to be ingested and empirical image about the presence of any hazardous toxins in the ambience, provided the gas has a perceptible odour threshold.

One important area where sense of smell plays a discerning role is the aroma based quality evaluation of agro products. One such important natural produce, where India is among the global leaders, is black tea whose aroma plays a significant role in determining the quality and subsequent commerciallization. To date, the quality evaluation of tea in industries is performed by dedicated human personnel known as tea tasters who evaluate a particular variety on the basis of their cognitive perception of smell and taste. Limitations associated with olfaction system often causes in false gradation of a batch and subsequently results in loss of revenue generated. Another important area where limitations of human olfaction system are overtly exposed is the detection of odourless toxic gases. Analytes on binding with the chemosensors produce action potential of different magnitudes. Only analytes which generate a high action potential are correctly mapped by the brain. These analytes are referred to possess a high Odour Activity Value (OAV). Odourless lethal gases do not produce any stimulus for the brain to act upon and if exposed for longer duration can cause severe health hazards. Fittingly, world health regulatory bodies observe strict mandates about maintaining a time weighted threshold limits of exposure towards these gases.

In this background, one part of this thesis aspires to counter the limitations of human olfactory system by describing the development of sensor modules capable of detecting low concentration of toxic gas, specifically carbon monoxide (CO), below its statutory limits. The statutory limits are prescribed by world health regulatory bodies who restrict the maximum exposure to this toxic gas on a time weighted scale. Carbon monoxide binds avidly with the haemoglobin and reduces blood’s oxygen carrying capacity. Owing to its high toxicity which can also surmount to fatalities if not monitored constantly, carbon monoxide has earned the trade name *“silent killer”*. Accentuating its danger further is its colourless and odourless features which make it imperceptible to human cognitive receptors. Threat associated with this gas has been recognised by researchers on a global scale and extensive research has been devoted in development of specific chemical sensors for detection of carbon monoxide.

Chemical sensors are dedicated units which allow inbound target analyte to undergo a chemical reaction on their surface, consequently changing one or more of its intrinsic parameters. Despite the commercial presence of CO detectors, constant research is being conducted globally to incrementally improve their performance, with the ultimate aim of fabricating fast and reliable sensors that can detect the presence of carbon monoxide below the prescribed limits. While improvement in data acquisition and associated sensor platform can enhance the performance upto a certain level, the main focus should be concentrated in the sensing material. In this regard, the current dissertation aspires to develop nanomaterials for cost-effective sensors with enhanced capability to detect carbon monoxide down to 1 parts per million (ppm) level which is considerably lower than the threshold limit value. The engineering process that augments the sensing parameters for the sensors shall be discussed in details.

Another section of the dissertation describes development of indigenous sensor modules for aroma based quality monitoring of black tea. Aroma in black tea is emanated as a function of synergistic contributions from several odour active volatiles. Few among them have a high action potential and influence the human organoleptic evaluation process considerably. The expert panel comprising of tea tasters which is conventionally employed in tea industries, investigates subtle variation in the concentration of these volatiles through their olfactory perception. However, the human organoleptic evaluation for gradation of individual batch of tea is error prone and depends on multiple influencing factors. The very subjective nature of human olfaction motivated this thesis to undertake development of an instrumental method specifically for detection of these key odour active volatiles. Considering the permutations of the odour active volatiles in creating a particular aroma, a discrete module shall not be able to comprehend the entire range of synergy.

The present chapter starts with an overview of human olfaction system and its application towards gathering information pertinent to odour of a target analyte. The discussion then veers towards limitations associated with human olfaction and their deficiencies in specific applications. In particular, two domains have been chosen where the limitation of human olfaction has serious implications. The focus is then concentrated in defining the necessity for carbon monoxide detectors by discussing the adverse effects of its accumulation on human metabolism. A comprehensive review then provides the different modalities of detection for this lethal gas. The advantages offered by metal oxide semiconductors as potent materials for fabricating sensors are discussed. A detailed discussion is then provided for the choice of two particular metal oxide semiconductors and their efficacy in detection of gases and volatiles.

The problem statement is framed next along with the hypothesis supported by a detailed literature survey. Finally, the scope of thesis is presented along with brief descriptions regarding the individual chapters.

1.2. The human olfaction system

The primary olfaction medium in humans consists of an olfactory bulb and an olfactory mucosa. The mucosa is the region of the nasal cavity that is specialized for detection of odorants. It comprises the olfactory epithelium and its underlying lamina propria where the sensing receptors are localized. Intriguingly, though human have a reduced dependence on smell compared to other modes of cognition, a substantial amount of almost one-thirtieth of the entire genome pool has been devoted for olfaction purpose [1]. The olfactory receptors are usually thin-walled pegs, cones, or plates with numerous pores through which airborne molecules diffuse. Dendrites of sensory neurons branch profusely within these pores and may respond to very low concentrations of detectable compounds. At this point it is worthy to note that "odour" is not an intrinsic feature imprinted on a molecule but rather a holistic experience. This can be further illustrated by the fact that identification of a particular smell remains same even with increasing concentration of the analyte. The chemoreceptors adopt a sensing mechanism which refrains from specific binding to an inbound odour molecule. Instead a target molecule binds with multiple receptors with varying affinities for the analyte. This result in conformal change among the receptors and subsequent activation of a guanine nucleotide-binding proteins (G-protein) coupled to the sensors on their cytoplasmic side (**Fig. 1.1**). The G-protein activation stimulates a chain of biochemical reaction that ultimately leads to generation of an action potential provided the odour activity value of the target molecule is beyond the perceptible threshold.

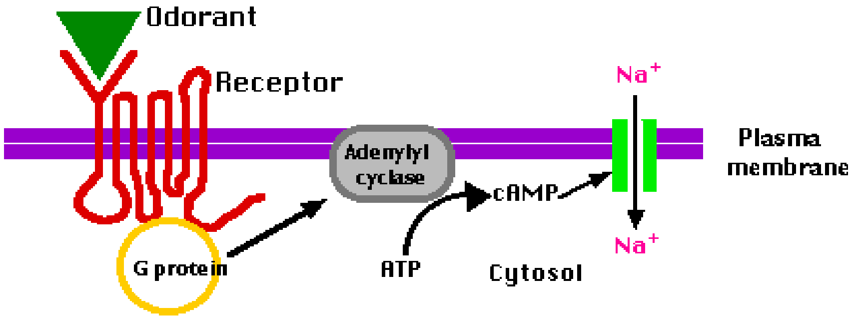

Fig. 1.1. *Sensing mechanism in the olfactory epithelium* [2]

Human olfaction system is endowed with approximately 900 olfactory receptor gene sequences, although 63% of them are non-decoding or "pseudogenes" [1] leaving about 300 active olfactory receptor genes. In comparison to the three genes allotted for vision and a single cochlear instrument dedicated for hearing, a large number of different odour receptors have been induced to provide a system for discriminating maximum permutations of odorants. Even then, the receptors are not tuned to specifically detect a molecule but rather show affinity towards divergent analytes at a different degree. This further enables the olfaction system to characterize smell that has never been encountered before. Moreover, for 80 % of the people, the nose is located slightly towards the right which helps to determine the possible source of a smell, as the lack of spatial uniformity permits a comparison. The olfaction system is versatile to have different detection threshold for individual molecule. For instance, the major aromatic constituent of bell pepper (2-isobutyl-3-methoxypyrazine) can be detected at a concentration of 0.01 nM. On the other hand, ethanol cannot be identified until its concentration reaches approximately 2 mM. Thus, the human beings are endowed with a fairly adaptive olfactory perception system and regularly apply their smell receptors for a preemptive quality evaluation of large number of food items on a regular basis.

Normal functioning of the olfaction system is crucial in detection of perceptible environmental hazards (e.g., spoiled foods, leaking natural gas, smoke and various airborne pollutants) and appreciation of foods, beverages, flowers and fragrances. Contrary to the clear guidelines provided for vision (390-750 nanometer wavelengths on the electromagnetic spectrum) and hearing (20-20,000 hertz), the units for olfaction is not well defined and the exact number of smells that human nose can distinctly recognise is highly debated. In fact, Bushdid and his colleagues had claimed through their experiments that human nose can detect more than one trillion different odours [3]. However, a recent rebuttal article shows that the claims were hypothetically incorrect and the actual amount might be much less to the order of a few thousand only. However this number is the permutation of few basic smells, and human nose are effective in distinguishing at most four different odours [4]. Similar to other cognition processes, the sense of smell is also prone to be affected by medical conditions, physical injuries, allergies and mental stability. Since olfaction is the least dependent mode of perception for humans, temporary reduction of its efficacy does not deter their daily operations significantly.

However, the scenario drastically alters when the olfactory performance\affects the livelihood of an individual. Tea tasters, for example rely on their sense of gustation and olfaction to assert the quality of black tea grades. They are dependent on their organoleptic evaluations which are prone to judgmental errors owing to temporal mood swings, deterioration of health, and changes in the environment. These assessments are further affected by a phenomenon otherwise known as *olfaction fatigue*. It is defined as the temporary, normal inability to distinguish a particular odour after a prolonged exposure to that airborne compound and occurs due to the constant adaptation of our sensory neurons towards similar volatiles. The symptom of olfactory fatigue is best illustrated through dairy professionals who often fail to discern the pungent odour emanated from dairy manures [5]. Another area where the limitation of human olfaction system is overtly exposed is in detection of imperceptible gases which does not elicit any considerable action potential and thus are not recognised by the brain. In worst situations where the gas is toxic, this has the possibility of causing severe health symptoms which can ultimately result in fatalities.

A standard technique for quantifying the efficiency of the olfaction system is threshold tests because of their intuitive appeal, their commercial availability and practical considerations. There are several types of olfactory thresholds, including detection thresholds, identification thresholds, and differential thresholds. The lowest concentration of an odorant that an individual can reliably detect (usually defined as that concentration where detection is midway between chance and perfect detection) is termed his or her *detection* or *absolute threshold*. The *recognition threshold* is defined as the lowest concentration where odour quality is reliably discerned. The *differential threshold* is the smallest amount by which a stimulus must be changed to make it perceptibly stronger or weaker. Pertinent to these standardization techniques are the terms Odour Activity Values (OAV) and Flavour Dilution (FD) factors. Between them, OAV is a measure of a specific compound's significance in the formation of the final odour, and is calculated as the ratio between the concentration of individual substance in a sample and its *absolute threshold*. In comparison, Flavour Dilution (FD) is defined as the highest dilution at which presence of a volatile can still be discerned. Despite the advent of these calibrating techniques, olfaction remains one of the weakest perceptions for humans and any form of instrumental technique with electronic interventions aiding the cognition process is beneficial.

1.3. Toxic gases and olfaction

Toxic chemicals are a range of volatiles or gases that can possibly be present in the ambience of an individual and if accumulated in the system through inhalation can affect the metabolism severely. The nature in which these toxins affect the physiology is as divergent as their sources. While instances of intentional dispensing of a range of toxins as a mark of bioterrorism or an act of war are sporadic, some other common form of these noxious derivatives are accumulated in the atmosphere from industrial wastes, as by-products of natural biochemical reactions and even through common household activities like cooking, air conditioners and water geysers. By definition, a volatile is deemed toxic if it has a median lethal concentration (LC_{50}) in air of more than 200 parts per million (ppm) but not more than 2,000 parts per million by volume of gas or vapour, towards albino rats within 200 to 300 grams inhaling them for 1 hour.

Widely considered as the world's biggest chemical disaster ever, the Bhopal gas disaster of 1984 that resulted in more than 25000 cumulative casualties stimulated the world health regulatory bodies to take note and postulate the permissible limits for these toxic gases. Accordingly, the world health regulatory bodies including Occupational Safety & Health Administration (OSHA), The National Institute for Occupational Safety and Health (NIOSH) and American Conference of Governmental Industrial Hygienists (ACGIH) identified approximately fifty gases to be highly detrimental for human health. They observed that these, either present in their natural state or as mixtures with other sources, are equally poisonous and should be avoided. The statutory norms for individual agency differ as they observe a difference in the exposure limits for almost every gas. However, the common parameter for the regulations is to maintain a limit much below the concentration that might affect human physiology on prolonged exposure.

Among the fifty chemical toxins, only a handful exists in the atmosphere in their natural forms. These common air pollutants include carbon monoxide (CO), nitrogen dioxide (NO_2), sulfur dioxide (SO_2) and hydrogen sulfide (H_2S), ammonia (NH_3), along with possible rare presence of germane (GeH_4), diborane (B_2H_6) and arsine (AsH_3) in areas where they are utilised for specific applications. Fortunately, almost all of these air contaminants are traceable through cognitive systems equipped to humans. While NO_x, SO_x, ammonia, arsine and H_2S can be identified by their characteristic noxious smells and associated asphyxiation, prolonged exposure to diborane beyond a threshold produces anomalies in form of skin blisters. The odour threshold for the common toxic gases along with their permissible exposure limits are presented in **Table 1.1**. A substantially lower odour threshold compared to the statutory limit implies that the presence of the hazardous gas in the ambience can be detected before its accumulation and necessary evasive actions might be taken. However, carbon monoxide is one highly toxic element that can gradually build up in ambient air without warning. The American Industrial Hygiene Association (AIHA) observes that carbon monoxide is colourless and odourless rendering it invisible to the organoleptic perceptions of vision and olfaction respectively. Additionally the lethal gas does not induce skin irritation making it imperceptible for the haptic mode of cognition.

__Table 1.1.__ Odour threshold and prescribed limits of exposure for common toxic gases

Chemical Name	**Time Weighted–Threshold Limit Value (TLV-TWA) (in ppm)**	**Immediately Dangerous to Life and Health (IDLH) (in ppm)**	**Warning Properties**	**Odour Threshold (in ppm)**
Ammonia	25	300	Adequate; Irritating pungent odour	5
Arsine (AsH_3)	0.05	3	Inadequate; Faint garlic-like or fishy smell	0.5
Boron trifluoride (BF_3)	1	25	Adequate; Extremely corrosive with pungent suffocating odour	Undetermined but 1.5 ppm can be recognized by smell
Bromine	0.1	3	Adequate; Red-brown liquid with irritating odour that causes choking and lacrimation	0.05-3.5
Carbon monoxide	25	1200	Inadequate; Odourless and colourless	-
Chlorine	0.5	10	Adequate; Greenish yellow gas with irritating odour	0.2-0.4
Chlorofluorocarbons	1000	2000	Inadequate; Almost odourless with slight irritating sensation	45
Diborane	0.1	15	Inadequate; Colourless with slight repulsive sweet odour	2-4
Formaldehyde	0.3	20	Adequate; Colourless with pungent odour	0.8
Germane	0.2	-	Inadequate; Colourless compressed gas with pungent odour	-
Hydrogen sulfide	10	100	Adequate; Characteristic pungent smell may result in olfactory fatigue	0.47×10^{-3} or 0.47 ppb

Nitrogen dioxide	3	20	Adequate; Red-brown gas with acrid odour	5
Phosgene	0.1	2	Inadequate; Colourless gas with sweet hay like odour at low concentration and pungent odour at higher levels	0.4-1.5
Phosphine	3	50	Inadequate; Colourless gas with nonirritating and garlic-like or fishy odour	0.15
Stibine	0.1	5	Adequate; Colourless gas with disagreeable odour	-
Sulfur dioxide	2	100	Adequate; Colourless gas with typical pungent odour	3-5

Carbon Monoxide – A Silent Killer

Apart from the socioeconomic opportunities available for the demography, the merit for inhabitancy of a metropolitan with more than 3,50,000 people is often measured by its environmental standards. The Air Quality Index (AQI) is one such metric used by government agencies to communicate with the public about the quality of ambient air. According to the Clean Air Act postulated in 1963, the population should have a clear idea about the air they are inhaling, and an increase in the concentration of a particular pollutant has to be duly informed to them. The information also highlights specific groups who might be prone to a deterioration of the air quality. An image of the Air Quality Index Map for India taken on 10th March, 2016 has been provided in **Fig. 1.2**. The AQI for an area is estimated based on the concentration of five major pollutants as per the clean air act: ground level ozone, sulfur dioxide, **carbon monoxide**, nitrogen dioxide and particulate matters. Increase in one or more of these pollutants in ambient air subjects the population at higher risk of health hazards. Interestingly, as per the guidelines delineated by the Environmental Protection Agency (EPA), carbon monoxide has a significant correlation with the air quality index [6]. Sub-indices of individual pollutants indicates that an accumulation of 30 ppm carbon monoxide can lead to serious aggravation of cardiovascular symptoms in heart patients and people are directed to take

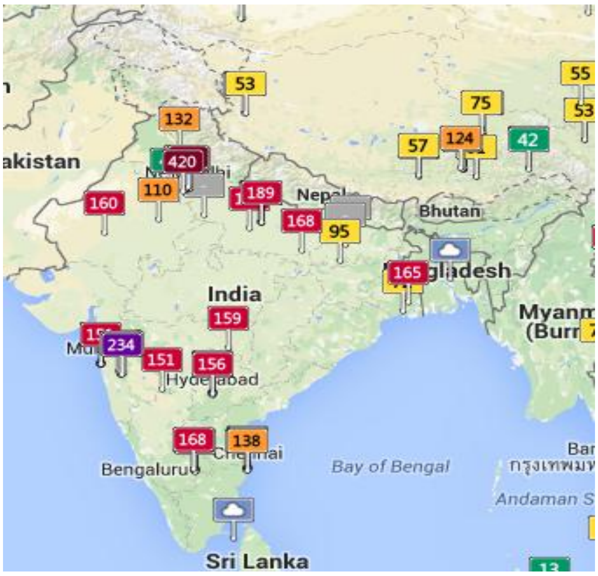

Fig. 1.2. *Air quality index map of India (on 10th March, 2016; source: http://aqicn.org/map/india/)*

evasive actions and avoid sources of CO. However, inability of human perceptions to intuit the presence of CO in their vicinity can potentially subject them to large dosage of this lethal gas. Since carbon monoxide is generated from incomplete combustion of hydrocarbons, the sources for this gas vary from traffic exhausts, outdoor campfires to more closer household appliances like water geysers, air coolers and cooking ovens.

Carbon monoxide (CO) poses a serious threat to health as it avidly binds with haemoglobin to form carboxyhemoglobin and thereby effectively reduces the oxygen-carrying capacity of blood [7]. This leads to severe impairment of tissues which suffers from acute hypoxia. Prolonged exposure to carbon monoxide have resulted in mortalities as well as morbidity as almost 50% individuals have been reported to suffer from neuro-cognitive sequelae [8]. The Centre for Disease Control (USA) estimates that CO poisoning claims nearly 3289 lives, and causes more than 50,000 visits to hospital emergency departments annually [9,10]. As a result, the recently promulgated National Ambient Air Quality Standard (NAAQS) by The U.S. Environmental Protection Agency (EPA) as well as the World Health Organization (WHO) have strictly mandated the maximum 8 hour time weighted average (TWA) exposure limit of carbon monoxide at 9 ppm [11]. Such harsh but necessary restrictions have prompted global researchers to aspire with renewed vigour for fast and reliable detectors for carbon monoxide that astute the presence of CO below the permissible limit. The limitations of human perception have necessitated development of electronic interventions in form of sensor modules that can detect low concentration of carbon monoxide.

Sensors are used in homes as a warning system to the otherwise undetectable carbon monoxide. Conventional sensors fall under two main categories; 'blob' sensors, and electrical sensors. 'Blob' sensors are essentially a patch of metal oxide salts that upon interaction with carbon monoxide reduces thus forming carbon dioxide in the process. The salt turns black when it is reduced with the colour change alerting the observer about the presence of the toxic fumes in ambience. Though cheap, the alerting system requires constant vigilance of the observer in order to distinguish the change in its colour. Given that at high concentration carbon monoxide causes dizziness and confusion, the occupant may be in no condition to readily observe this change. Electronic carbon monoxide sensors can further be subdivided into (a) thermistor type metal-oxide detectors that detect a change in heat when carbon monoxide lands on the oxide and reacts, (the change in temperature raising the alarm), and (b) an electrolytic detector that works by sensing the change in charge carriers in an electrolyte solution when carbon monoxide interacts with an electrode of the device.

1.4. Carbon monoxide sensors – a review

A sensor is defined as an object that reacts to the changes in its environment by transducing a corresponding change in one or more of its intrinsic parameters. These changes are usually of electrical form which can be calibrated to deliver a measure of the environmental change. Accordingly, cognitive limitations towards carbon monoxide have motivated researchers to opt for sensor modules which shall be fast, reliable and can detect carbon monoxide under the statutory limits repeatedly with confidence. Specific parameters determine the merit of a particular sensor in terms of their performance against the dispensed target analyte. These measurement specifications include *sensitivity, selectivity, response time and recovery time*. ***Sensitivity*** of a sensor defines its ability to instinctively react to a change in its ambience. Numerically, it is defined as the ratio between the change in electrical signal of a sensor and the signal it generates in absence of the analyte [12]. A calibration plot of sensitivity versus the analyte concentration helps in determining the degree of presence for the target gas. Although a high sensitivity is appreciated towards low ppm of the target, this simultaneously implies that the sensor saturates at relatively lower concentration levels, with no significant change in sensitivity with further accumulation of the gas molecules. ***Selectivity*** is an important criterion for sensor selection as this defines the ability of a sensor to specifically detect a target gas without being affected by the presence of other interfering gases. It is often represented as the ratio of the sensors response towards the target gas and the response towards an interfering volatile [13]. The ***Response time*** characterizes the speed of a sensor to respond towards an analyte and is defined as the time taken to produce 90% of the full-scale reading towards a target gas. Sensors with relatively low response time are appreciated as a quicker alert shall ensure timely evasive actions for individuals. ***Recovery time*** is a measure of how quickly a sensor gets ready for re-use after detection of an analyte and is defined as the time taken for a sensor to revert back to its 90% of the original scale once the gas is removed form its proximity. Additionally, another parameter namely ***periodical drift in base resistance*** finds importance for chemiresitive sensor. Drift sets in such sensors due to bulk diffusion of oxygen owing to a higher chemical potential in the atmosphere. This results in shift of the base resistance and a consequent anomaly in the measurement [14]. Sensors with minimal drift are appreciated for obvious reasons. Other significant parameters that characterise a sensor's dynamic performance are ***lower detection limit (LDL), resolution*** and ***linearity.*** For a sensor, LDL determines the lowest concentration of the targeted analyte it can detect with a considerable confidence. Resolution is defined as the unit change of the sensors parameter per unit change in the target concentration. A sensor with higher resolution provides better calibration at the lower concentrations of the gas. On the other hand, a linear plot of sensitivity against the concentration is aspired as this helps in possible extrapolation of the toxicity levels in the ambience based on the recorded response from the sensor.

Early versions of sensing instituted colorimetric changes as a preferred mode of detection as represented by 'blob' detectors. With an increase in CO poisoning incidents, the motivation for an audible sensing system which would not require constant observation was surmised. Accordingly a genesis of modules with the capability of electrical transduction on exposure to carbon monoxide was observed. The next few decades witnessed the inception and incremental optimization of different families of CO detectors. Although various sensing materials were explored, their mode of transduction mostly catered to one of the four mechanisms, namely i) optical ii) bio-mimetic iii) electrochemical and iv) chemiresistive semiconductor.

i) <u>Optical CO sensors</u>: The mode of operation for all sensors under this classification is essentially similar where a beam of light consisting of specific wavelengths is emitted from coherent source and is transmitted through two different paths towards a detector. While one of the paths consists of the target gas, the other chamber is filled with a reference gas which would allow undeterred transmission of the beam. The target gas on the other hand absorbs specific wavelengths causing attenuation at the detector site. The detector is affixed with a filter that passes only the wavelength that the target gas might absorb. The degree of attenuation for a specific wavelength determines the concentration of the target analyte. In fiber optic mode of detection, the emitter and the detector might be localized at the same site and the beam of light might be reverted back post interactions with the analyte [15]. The nondispersive infrared (NDIR) sensors however have dedicated channels for transmission of the reference and the attenuating beams. In fact Environmental Protection Agency recommends usage of NDIR sensors for CO detection primarily due to their specificity, and immunity towards temperature. Ideally, the CO molecules absorb wavelengths in the 4.6 μm region [16]. Though selective towards the target analyte this mode of detection suffers from limitations like complicated instrument set-up, low sensitivity and resolution. Additionally the optical sensors are generally deployed for detection of linear gas molecules and their veracity in detecting organic vapours is yet to be established. An alternate form of optical sensing, otherwise known as cataluminiscence (CTL) has also been foraying in the domain of gas detection. The mechanism is based on observation of luminescence due to catalytic oxidation of the target analyte on a sensing material and was initially observed for carbon monoxide by Brysee *et al.* In 1976 [17].

ii) Biomimetic CO sensors: Biomimetic sensors operate through a mechanism that is pertinent to the biotechnology field, where a gel form of synthetic haemoglobin darkens in the presence of CO and lightens in its absence [18]. An infrared light is passed across a filtering screen coated with the synthetic haemoglobin and is acquired by a detector. A darkened screen in presence of CO attenuates the intensity of the infrared reference beam and the extent of reduction can be used for calibrating the gas concentration. Typically, cyclodextrins coupled with chromophores are used as the coating material on the screen [19]. Although reliable and inexpensive, these sensors are prone to impairments in the recovery phase and are typically deployed in high-end applications primarily due to their immunity from generating false alarms. Additionally the advantage of a relatively low power requirement is countered by their susceptibility to high temperature and humidity.

iii) Electrochemical CO Sensors: This mode of detection found acceptance due to their tunable sensing parameters like high sensitivity, fast response time, high specificity and longer duration of operability. A prototype sensor system comprises of a sensing or working electrode, a counter electrode and an electrolyte in between. Additionally, the sensor is loaded with a hydrophobic porous membrane that allows the gas molecules to permeate while preventing the water molecule of the electrolyte to evaporate. The inbound carbon monoxide molecules diffuse through the porous membrane and get oxidized at the working electrode. Consequently, oxygen is taken up at the counter electrode which produces a measurable current. A load resistor connecting the electrodes externally and the conducting electrolyte ensures the continuous flow of the current. Either voltage measured across the load resistor or the current itself can be calibrated against the concentration of the target gas reacting at the working electrode. More often than not, the design of the electrochemical cells adopts a three electrode setup with an additional reference electrode which is placed in close proximity to the working electrode. The sole purpose of the third electrode is to maintain a constant voltage drive across the working electrode which might have deteriorated in the absence of the reference over prolonged electrochemical reaction on its surface. The reference electrode does not partake in any form of sensing or reactions. Though these sensors can be fairly tuned to be selective towards the target analyte they are prone to climate modulations and their performance is easily affected by changes in the ambient pressure and analyte temperature and require internal temperature-compensation modules. Yet a considerable bulk of the state-of-the-art CO detectors caters to this modality for the advantages specified above. An added advantage of these sensors can be considered to be the linearity they demonstrate in their response pattern against varying concentration of carbon monoxide. The electrochemical sensors are either *amperometric* or *potentiometric* in their modality. Commercial CO sensors implementing the electrochemical mode of detection have achieved coveted attributes like a resolution of 500 ppb [20] and sub-ppm sensitivity [21]. However, constant efforts are being vested in the field of research for improvement of the current norms. Most of these works are concentrated on exploring novel materials as the sensing electrode. For example, Li *et al.* have recently used C-loaded $PdCl_2$-$CuCl_2$ for detection of CO own to 1 ppm with an operational time of ~ 10 s, which is suitable for real field deployment [22]. Another investigation by Quesada *et al.* has revealed a higher response with the lower level of detection of 100 ppb [23]. They have strategically utilized Pt-catalyst on a carbon cloth and used the poisoning of the spluttered catalyst by CO to generate an enhanced electrical signal at low concentrations.

iv) Chemiresistive CO sensors: Often considered as a tributary of the electrochemical pedigree, chemiresistive sensors stand out due to their high sensitivity, non-complex operations, longevity and relatively faster response and recovery times. These types of sensors function through a simple mechanism where the intrinsic conductance of the sensing material changes upon contact with the target gas. While the bulk of these conductometric sensors are constituted by metal oxide semiconductors (MOS), other form of sensors like conducting polymers and low-D carbon based materials *viz.* carbon nanotube (CNT), graphene and fullerenes are also prominent members. Depending upon the nature of variation in the intrinsic conductance of the sensing material, a sensor can be either *n*-type (conductance increases upon exposure to carbon monoxide, e.g. SnO_2, ZnO) or *p*-type (conductance decreases, e.g. CuO, titania). Although the end result for each of these sensors is demarcated by a change in its conductance, the working principle differs significantly for each of them. For the conducting polymers, the polymeric chain generally contains a lone pair of electrons which might be donated to the inbound reducing analytes, ultimately leading to a formal change in conductance. This lone pair is transferred to the electron withdrawing carbon monoxide, which leads to possible formation of polarons and a corresponding increase in the resistivity [24]. Considering the scope of the present work, special emphasis in the form of a separate dedicated section discussing the growth of MOS sensors for carbon monoxide sensing has been presented.

1.5. Metal oxide semiconductor sensors

The inception of metal oxides as a plausible gas sensing material dates back by half a century when in 1962, Seyama demonstrated that ZnO thin films modulated their intrinsic conductivity in presence of propane at an elevated temperature of 485 ^{o}C [25]. Though the original discovery about semiconductors' ability to vary their properties aligned with changes in the ambience was made in The Bell laboratories in 1952 [26], systematic follow up investigations that could translate these findings into a technology were not undertaken. It was only when Taguchi demonstrated the efficiency of these materials and patented his technology, the research field gathered the necessary impetus [27]. The instated form of Taguchi sensors is still very much relevant to the present requirements. In fact, the first field deployed prototype was an SnO_2 sensor developed by Taguchi for detection of Liquified petroleum gas (LPG) leak which was on the rise in Japan in the 1960s owing to usage of bottled gases [28]. Constant progress made ever since in this domain of research witnessed the surge of various metal oxides as potent sensing materials. Among these, wide band gap semiconductors like tin dioxide (SnO_2) and zinc oxide (ZnO) found widespread acceptance mostly for their high sensitivity, thermal stability and tunable selective properties. In the early stages the specificity for these sensors towards an analyte was vitiated by large cross-sensitivities towards possible interfering analytes which limited their applicability. However, pioneering work from Shaver showed that the selectivity of a material can be enhanced by strategic incorporation of additives in the base material matrix. He introduced noble metals as additives to increase the sensitivity and selectivity towards hydrogen and other reducing gases [29]. Another material widely adopted was zinc oxide due to their unique physicochemical attributes. Apart for the features suitable for its scope as a sensing material, zinc oxide can be rendered definite morphologies [30]. The variation in morphologies offers the researchers an additional paradigm and prospect to investigate different superstructures and their associated changes in electronic attributes as sensing materials. Later, the operating temperature was also modulated to facilitate selective oxidation of the target analytes on the surface. Gradual progress has observed miniaturization of these sensor units where they have been transformed into planar platforms equipped with microheaters from the original Taguchi beds. This has lead to significant reduction in the power budget for the sensors [31]. Present day research has developed on the acquired knowledge base by coupling the innumerable prospects of nanotechnology which allows controlled manipulation of the material properties at molecular levels. Modern day scientists use nanoscience as a tool to churn out tailored materials of significantly smaller dimensions and higher surface to volume ratio which enables interaction with a higher number of target molecules. Yet another engineering often performed at the molecular level is the doping of the crystal lattice with acceptor or donor ions which can discretely tune the electronic properties of the sensor.

The detection mechanism for all metal oxide semiconductors is essentially similar, and depends on the amount of chemisorbed oxygen moieties on the sensor surface. Ideally, the metal oxide semiconductors are wide band gap materials effectively acting as insulators at room temperature. At elevated temperature though, electrons from the valence band make the transition to the conduction band, increasing the intrinsic conductivity. These free electrons are accepted by the ambient oxygen who themselves get chemisorbed on the sensor surface as adatom. The sensing of the material depends on the oxidation reaction of the probed gas by these adsorbates on the sensor surface. This motivates occasional sensitization of the sensor surface with sporadic distribution of catalyst nanoparticles which promotes the oxidation of the inbound target molecules. Considering the *n*-type materials, the adsorbates create a potential barrier at the grain boundaries by trapping free electrons and creating a depletion layer. The depletion layer subsequently enhances the energy requirement for an electron to flow through and increases the overall resistance of the material. This is signified by a noticeable band bending in the energy diagram across the grain boundaries. The adsorbates can be chemisorbed in different forms depending on the surface temperature. The major species within 300 ^{o}C is O_2^- while O^- is the dominant adatom within 300-450 ^{o}C [32]. However, at higher temperatures, a more unstable moiety in the form of O^{2-} becomes the dominant adsorbate. The O^{2-} species are highly unstable and do not affect the overall sensitivity in comparison to the more reactive O^- adsorbate. This is the reason that most of the MOS sensors have a working temperature in the range of 250-400 ^{o}C.

In presence of any reducing gas, e.g. CO, the O^- active species oxidizes the incoming volatile and liberates the entrapped electrons in the process (**Fig 1.3**). This is marked by a corresponding increase in the conductance of the base material. However, the influx of oxidizing gas molecules only enlarges the depletion layer, thereby increasing the resistance further. A converse mechanism holds true for *p*-type oxides where holes are the major carriers. Here, electron exchange due to interaction with a reducing gas and consequent increase in electron concentration leads to a decrease in the major carrier concentration and conductance, owing to electron-hole recombination. For an oxidizing gas which promotes further entrapment of electrons, the probability of recombination decreases, thus leading to an increase in the conductance [33]. However, a complete description of the gas-sensing mechanism can only be hypothesized taking into account all elementary steps (adsorptions, reaction, desorption, etc.) governing surface-gas target interactions leading to charge transfer [34].

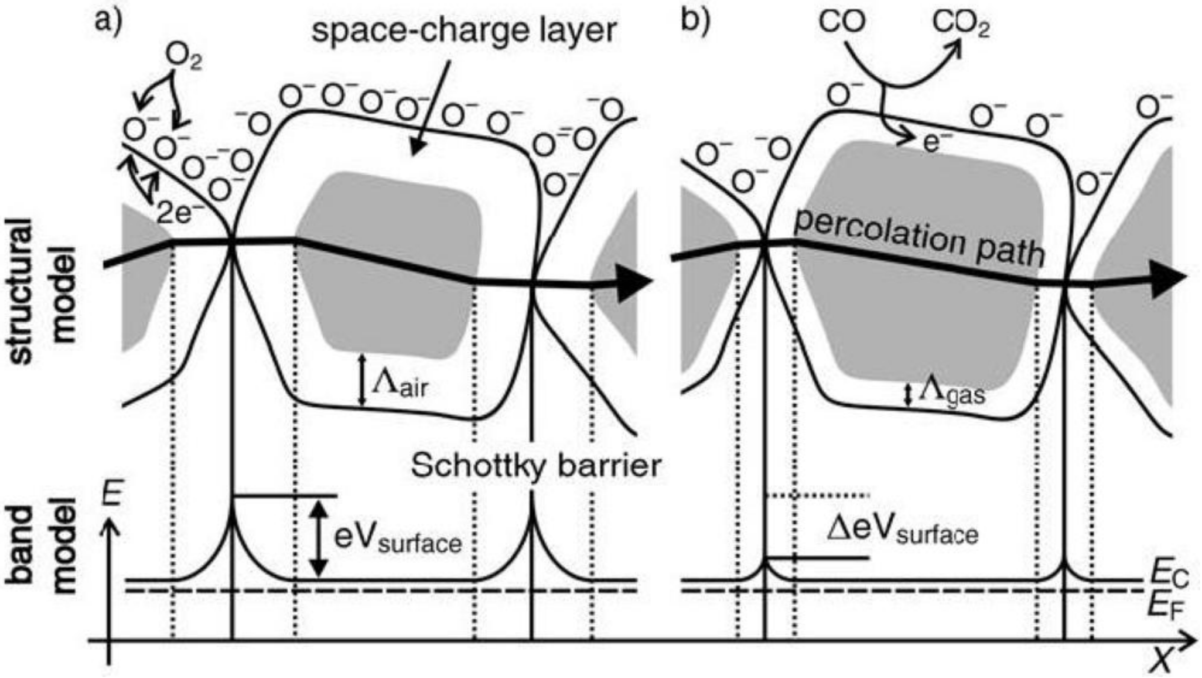

Fig. 1.3. *Structural and band models of conductive mechanism upon exposure to reference gas. (a) with or (b) without CO [32]*

The very fact that the sensing mechanism is dependent on the amount of oxygen chemisorbed on the surface provides an insight on the effects of the surface coverage for a sensor. A grain with smaller volume will have a higher specific surface area and will offer a greater space for the oxygen to chemisorb. Thus, crystals in nanoscale range have been effective in producing higher sensitivities [35]. Since sensing is primarily a surface phenomenon, it is influenced by the surface space charge created due to entrapment of free electrons. The depth of this depletion region determines the ultimate response pattern. Debye length is the distance which an electron can traverse without the probability of being impeded through collisions. It has been experimentally established that crystals with size about twice the Debye length exhibit high response [36]. This implies that the sensor performance is promoted by a decreasing crystal size and an increasing depletion layer as shown in **Fig. 1.4**. For a typical sensing material, SnO_2, produced with different grain sizes between 5 and 80 nm, simulations showed that the conductivity increases linearly with decreasing trapped charge densities and the sensitivity to the gas-induced variations in the trapped charge density increases too, in agreement with experimental findings [37]. For, SnO_2, the Debye length has been estimated as 3 nm, thus signifying a crystallite size of 6 nm to be ideal for the sensing purpose [38]. However, reducing the crystal size is but one of the techniques to improve sensing performance.

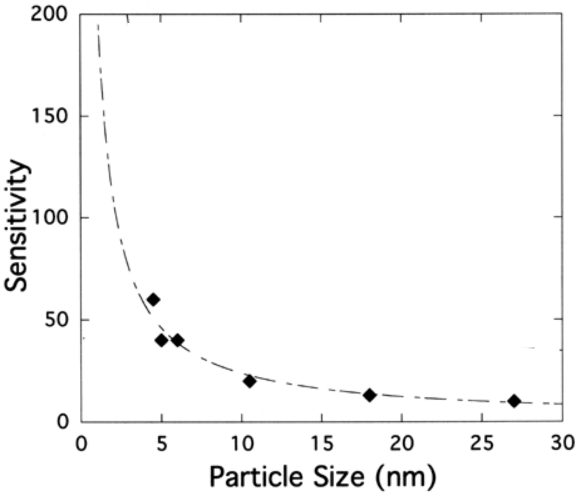

Fig. 1.4. *Plot showing that sensitivity drastically increase when the particle size is reduced below a range [35].*

Extensive research has been vested to investigate the scope of various metal oxide semiconductors as sensors. A pie chart showing the proportions of individual MOS materials contributions in the field of gas sensing, highlight SnO_2 and ZnO as the major leaders (**Fig 1.5**). Nevertheless, different MOS materials have been utilized for fabrication of CO sensors and have garnered acceptance for their simplistic approaches. Choice of a particular metal oxide often depends upon their adaptability towards the application they are deployed for. In the field of CO detection, bulk of the sensors has been fabricated either with SnO_2 or ZnO. The survey of these two oxides for CO detection deserves expansive literature survey which has been performed and provided through two tables (**Tables 1.2 and 1.3**). The engineering to tune these materials electronic properties can potentially initiate as early as the synthesis level and might extend through feature modulating steps like size variation, incorporation of additives right till the platform design stage.

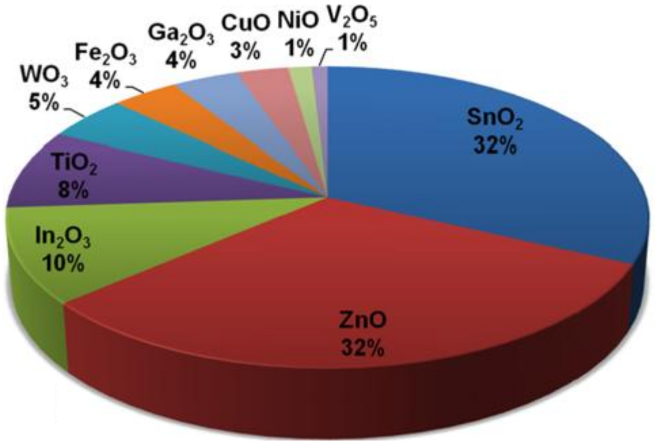

Fig. 1.5. *Individual contribution of metal oxide semiconductors in the domain of gas sensing [39]*

One of the pioneering investigations with MOS was performed by Okamoto *et al*. when he used zirconia to detect 100 ppm of carbon monoxide [40]. They used yttria as a stabilizer while Pt beads were sporadically dispersed on the surface to catalyse the oxidation reaction. Yttria stabilized zirconia was again used in conjunction with CdO and SnO_2 for detection and produced a linear calibration plot on the logarithmic scale for carbon monoxide within 20-400 ppm [41]. The same investigating group has recently improved the linearity across 20-800 ppm by using gold (Au) nanoparticles as catalysts deposited on the surface of zirconia electrodes [42]. Another metal oxide which has been used by researchers for sensing of different VOCs is indium oxide. However, In_2O_3 has been reported to demonstrate markedly low affinity towards carbon monoxide [43, 44] and therefore are used mostly for detection of volatile organic compounds. In contrast to the above observation, an interesting study was conducted with In_2O_3 by Neri and his group which showed indium oxide nanocrystals of 30 nm dimension detecting 50 ppm carbon monoxide [45]. Dispersed cobalt oxide on In_2O_3 have been found to be promoting the sensing response towards carbon monoxide [46,47]. Titania and tungsten oxide (WO_3) are the other oxides with citable footholds in the field of carbon monoxide detection. With tungsten oxide as the sensing material, a lower limit of detection of 14 ppm CO could be achieved [48]. Another advantage of working with tungsten oxide as reported by Fukuda *et al.* is its ability to detect low ppm CO (54 ppm) at a relatively low temperature (75 ^{o}C) [49]. Anatase phase of titania (TiO_2) on the other hand was used for detecting CO at a relatively higher level by Akbar and Younkman [50]. Anatase TiO_2 was also used by Dutta *et al.* for sensing carbon monoxide within 0-1400 ppm [51]. For the above investigation, while CuO was incorporated to enhance the sensitivity, presence of La_2O_3 ensured that the anatase phase could be maintained under all operating temperatures. Despite the sporadic researches performed with other MOS materials, sensing with tin dioxide and zinc oxide nanoparticles boast of a strong foundation and knowledge base. A comprehensive survey of the investigations performed on CO sensors with SnO_2 and ZnO has been presented in the following section.

1.5.1 Tin dioxide based CO sensor: Ever since tin dioxide was projected as a potent material for sensing of reducing gases, several research groups developed keen interest in using them for detection of carbon monoxide. One of the early comprehensive reports recognizing the veracity of SnO_2 as an effective CO sensing material was presented by Firth and his colleagues [52]. Later, Boyle and Jones purposely used TGS sensors for detection of 75 ppm and higher concentrations of CO [53]. But it was the detailed study performed by Windischmann and Jones that elucidated a comprehensive model of CO sensing mechanism, accounting for factors like the effect of CO partial pressure and humidity [54]. However, the first real account of introduction of catalytic oxidants into the SnO_2 matrix was given by Torvela when he intentionally used palladium for enhancing the response [55]. The promoting effect of palladium towards CO sensing was duly recognized and validated through similar works [56]. Since then the evolution of SnO_2 sensors for CO detection has been steady with the incorporation of different additives. A brief summary of the SnO_2 sensors implemented for detection of carbon monoxide is presented in **Table 1.2**. The thematic divisions for the literature survey have been made in cohesion with the scope of the urrent dissertation. Another mode of engineering often adopted for improving the sensitivity is rendition of distinct structures to the tin dioxide crystals. Considerable reduction in one or more lateral dimensions of the crystals to the nanoscale effectively increases the surface space region available for the entrapment of conduction band electrons. In this respect, 1-D and quasi 1-D structures of SnO_2 have been widely explored. Instinctive reactions of such structures make them natural candidates for a potential CO sensing material. Nanowires of SnO_2 were drawn by Kolmakov *et al.* for successful detection of low concentration of the toxic gas [57]. The next strategic step in the evolution of SnO_2 sensor was assembling a group of modules into an array for discrimination of CO among a permutation of different volatiles [58]. Such an array together with the interfacing circuitry is referred as an electronic nose system.

Table 1.2. *Brief review on tin dioxide based carbon monoxide sensors*

<table>
<tr><th colspan="7">Thematic Division: Initial phase of development</th></tr>
<tr><th>Sr. No.</th><th>Ref.</th><th>Material</th><th>Response (R_{air}/R_{gas})</th><th>Range / LDL of Detection (ppm)</th><th>Operating temperature (^oC)</th><th>Remarks</th></tr>
<tr><td>1</td><td>[52]</td><td>Stannic oxide (SnO_2)</td><td>~1.67</td><td>100</td><td>300</td><td>First article on stannic oxide based CO detection which hinted at modulating the operating temperature for increasing specificity.</td></tr>
<tr><td>2</td><td>[53]</td><td>TGS-SnO_2 sensor</td><td>~2</td><td>75</td><td>300</td><td>Standard commercial sensors were used for the first time for this study.</td></tr>
<tr><td>3</td><td>[54]</td><td>SnO_2</td><td>~1.25</td><td>50-500</td><td>350</td><td>This article presented the surface reaction occurring on the sensor and correlated the conduction of SnO_2 with partial pressure of CO</td></tr>
<tr><td>4</td><td>[59]</td><td>SnO_2</td><td>~10</td><td>1000</td><td>500</td><td>This report cited the development of a fast CO sensor with response and recovery time of 30 ms and 10 s respectively</td></tr>
<tr><td>5</td><td>[60]</td><td>SnO_2</td><td>-</td><td>10</td><td>300-900</td><td>This is the one of the first reports on integration of a sensor in a system. A gas valve is automatically shut off when the CO level crosses a threshold as detected by the sensor unit</td></tr>
<tr><th colspan="7">Thematic Division: Effect of particle size on sensing parameters</th></tr>
<tr><td>6</td><td>[35]</td><td>SnO_2 (5-30 nm)</td><td>60 for particles below 5 nm</td><td>800</td><td>300</td><td>This article clearly showed that particles with dimensions comparable to the Debye length produce exponentially enhanced sensitivities for CO</td></tr>
<tr><td>7</td><td>[36]</td><td>SnO_2 (68 - 236 nm)</td><td>32 for 50 ppm</td><td>4-50</td><td>420</td><td>This paper clearly highlighted that longer necks of polydispersed nanoparticles result in inferior response compared to monodispersed particles</td></tr>
<tr><td>8</td><td>[38]</td><td>SnO_2 (8 and 15 nm)</td><td>-</td><td>-</td><td>120 and 350</td><td>This report uses FTIR spectrometry to show that the smaller particles produce higher response towards CO</td></tr>
<tr><td>9</td><td>[61]</td><td>SnO_2 nanoparticles (19 nm)</td><td>Change in conductance - 300 x 10^{-8} Ω^{-1}</td><td>1000</td><td>50</td><td>Very well dispersed SnO_2 particles were used for detection of CO</td></tr>
<tr><td>10</td><td>[62]</td><td>SnO_2 nanoparticles</td><td>1.58</td><td>1000</td><td>175</td><td>This study investigated self heating property of the sensing film by passing a current through it. The current in turn promotes grain dispersion and porosity within the film</td></tr>
<tr><td>11</td><td>[63]</td><td>SnO_2 Quantum dots</td><td>147 at 225 ^oC</td><td>100-1000</td><td>25-300</td><td>The fabricated sensor is dual selective towards CO (under 300 ^oC) and methane (above 300 ^oC)</td></tr>
<tr><td>12</td><td>[64]</td><td>SnO_2 nanoparticles microspheres and micron-size</td><td>7 at 500 ^oC for 35 ppm CO</td><td>35</td><td>400-600</td><td>This article presented a contrasting result to the then reported studies, when agglomerated nanoparticles showed higher response compared to microspheres</td></tr>
</table>

Thematic Division : Effect of catalysts on sensing parameters						
Sr. No.	**Ref.**	**Material**	**Response (R_{air}/R_{gas})**	**Range / LDL of Detection (ppm)**	**Operating temperature (°C)**	**Remarks**
13	[65]	Au, Pd, Pt loaded SnO_2	13	500	375	This study established the efficacy of gold nanoparticles among noble metals as suitable catalyst for CO detection.
14	[66]	Au and Pt electrodes for SnO_2	Change in electrical current signal – 3 x 10^{-10} A	700	400	Study showed that unstable Au particles may diffuse from the electrodes and induce catalytic effects thus lowering the temperature of operation
15	[67]	9 different additives loaded SnO_2 compositions (Pt, La_2O_3, CuO, Pd, Sc_2O_3 TiO_2, WO_3 ZnO, Pd+ V_2O_5	80% at 1000 ppm for Pd+ V_2O_5 loaded SnO_2 sensor	0-5000	400	This report utilised a neural network to discriminate among the different target analytes.
16	[68]	Pt-SnO_2	450 at 160 °C for 400 ppm CO	50-400	400-650	Platinum incorporation resulted in lowering of the optimum temperature for operation
17	[69]	SnO_2-CeO_2-Pd	~125 at 120 °C for 250 ppm CO	40-250	120-180	High discrimination among interfering gas and optimum specificity towards CO
18	[70]	SnO_2 with Pt catalyst	10	50	300	Distributed Pt catalyst showed marked increase in sensor response with the possibility of detecting 100 ppb CO
19	[71]	Ceria seggregated on SnO_2	~25 for 250 ppm CO at 350 °C	250	300-400	This study reported on promoting effect of humidity on ceria towards catalytic oxidation of CO
20	[72]	$[RuO_2]@SiO_2$ on SnO_2	1.05	200	400	Ruthenium oxide layer induces on chip filtering of carbon monoxide through selective oxidation
21	[73]	V_2O_5 promoted SnO_2	~6.5 toards 500 ppm CO	50-500	175	Vanadium specied promoted the formation of O^- and O_2^- adatoms on the surface, which are critical in sensing and thus enhances response
22	[74]	Au/SnO_2	1.33	50	50	Gold nanoparticles seem to catalyze the oxidation of CO on sensor surface at relatively low operating temperatures
23	[75]	Pd-loaded SnO_2	Change conductance – 0.25 x 10^{-6} Ω^{-1} for 25 ppm CO	25-300	150	This article investigated the catalytic cycle of palladium as a catalyst in oxidation of carbon monoxide on sensor surface
24	[76]	Au/SnO_2 core–shell structure	28.57	1000	300	The Au-core adsorbs the inbound CO molecules and catalyzes their oxidation resulting in a high sensitivity thus increasing the sensitivity of the core-shell structure

Thematic Division: Effect of doping on sensing parameters						
Sr. No.	**Ref.**	**Material**	**Response (R_{air}/R_{gas})**	**Range / LDL of Detection (ppm)**	**Operating temperature (°C)**	**Remarks**
25	[77]	Cu-doped SnO_2	Change in voltage – ~2 V for 1000 ppm CO at 300 °C	400-1000	270-320	Copper doping enhanced the overall sensitivity towards carbon monoxide for SnO_2 films with Pt s catalyst
26	[78]	Fe-doped SnO_2	1.6	500	300-500	Iron doping resulted in decrease of senstitivity but improved the dynamic parameters like response and recovery times
27	[79]	Indium doped SnO_2	1.18 at 200 °C towards 1000 ppm CO	500-3000	50-250	Indium doping results in decreasein the grain size and a consequent increase in CO response
28	[80]	Au-doped SnO_2	2380 at 175 °C towards 2500 ppm CO	250-5000	150-350	Doping the tin dioxide crystal lattice with gold nanoparticles resulted in influencing the structural and sensing properties. Although no evidence of the dopant migrating and substituting tin ions from lattice is provided.
28	[81]	Fe-doped SnO_2	292 at 200 °C towards 1000 ppm CO	1000	150-250	Here iron doping actually increased the response towards CO along with the specificity, in contrast to the findings of [77] where the response reduced
29	[82]	Sm_2O_3 doped SnO_2	421 at 200 °C towards 300 ppm CO	300	50-400	Samarium oxide doping had a discerning effect on supprssion of crystallite growth
30	[83]	Sb-doped SnO_2	~2.2 at 250 °C towards 500 ppm	500	250	Antimony doping has a discerning effect on the sensitivity which increases with the dopant concentration

This thesis aspires to project cost effective group II elements as a suitable alternative to the noble metal additives. It has been established through previous reports that smaller particles produce improved response. Therefore group II elements, namely magnesium, calcium, strontium and barium have been incorporated in their oxide forms in the SnO_2 matrix in order to impede the crystal growth during sintering stage. The oxides are strategically placed on the grain boundaries and inhibit the characteristic neck-formation by which the crystals fuse and form bigger particles.

1.5.2. Zinc oxide based CO sensor: ZnO has been explored in tandem with other transition metal oxides for CO sensing. Boosted by its unique physicochemical properties of wide band gap (3.3 eV) and high carrier mobility ($1000 cm^2 V^{-1} s^{-1}$), they have been deployed for both lab scale and device fabrication of sensors. However, the properties are better manifested when the nanostructures are synthesized with controlled morphology for specific applications.

Rendition of such superstructures to ZnO crystals is relatively easier owing to the characteristic anisotropic *c*-axis oriented growth of the crystals, and presence of polar plane in the crystal. The polarity of the plane can be tactically capped by agents or utilized for anchoring oppositely charged crystals. Capping of the polar plane retards the *c*-axis oriented growth and favours the stacking of secondary planes with relatively lower growth rates. Effective control on the growth rates at different orientations results in formation of nanosheets, nanoflowers and nanoflakes morphologies. A table highlighting the genesis of zinc oxide as a potent CO sensing material has been presented (**Table 1.3**).

Table 1.3. *Brief review on zinc oxide based carbon monoxide sensors*

<table>
<tr><th colspan="7">Thematic Division: Initial phase of development</th></tr>
<tr><th>Sr. No.</th><th>Ref.</th><th>Material</th><th>Response (R_{air}/R_{gas})</th><th>Range / LDL of Detection (ppm)</th><th>Operating temperature (^{o}C)</th><th>Remarks</th></tr>
<tr><td>1</td><td>[84]</td><td>ZnO</td><td>-</td><td>-</td><td>25</td><td>First aticle to report that CO adsorbs on the surface of ZnO</td></tr>
<tr><td>2</td><td>[85]</td><td>Al_2O_3 and Li_2O doped ZnO</td><td>~3.5</td><td>800</td><td>300</td><td>One of the first reports on systematic doping of ZnO crytsal and their relative effect on sensing</td></tr>
<tr><td>3</td><td>[86]</td><td>ZnO</td><td>150% change in conductance</td><td>100</td><td>390</td><td>One of the initial reports to have used ZnO single crystals for producing a quantitatve measure of CO concentration</td></tr>
<tr><td>4</td><td>[87]</td><td>Pt/ZnO and pristine ZnO</td><td>18.6 towards 4000 ppm CO at 400 ^{o}C</td><td>400-4000</td><td>300-400</td><td>This article showed the enhanced oxygen adsorbtion capacity for Pt/ZnO and subsequent increase in their sensing</td></tr>
<tr><th colspan="7">Thematic Division: ZnO morphologies influenced sensing</th></tr>
<tr><td>5</td><td>[88]</td><td>Sheets, needle and spherical grains of ZnO</td><td>~4 for 500 ppm at 350 ^{o}C</td><td>50-500</td><td>350</td><td>This article showed the importance of controlling the faceted growth of ZnO particles. Larger particles calcined at higher temperatures produced inferior response</td></tr>
<tr><td>6</td><td>[89]</td><td>ZnO nanowires</td><td>2.32</td><td>500</td><td>320</td><td>Relatively inferior response at high concentration levels of carbon monoxide</td></tr>
<tr><td>7</td><td>[90]</td><td>Spherical, flower and star like ZnO nanoparticles</td><td>~11 for ZnO flowers</td><td>100-500</td><td>150-400</td><td>Among different morphologies explored for sensing applications, flower like ZnO showed maximum response towards CO</td></tr>
<tr><td>8</td><td>[91]</td><td>1-D nano assemblies of ZnO</td><td>~2 for 500 ppm at 200 ^{o}C</td><td>100-500</td><td>200</td><td>The sensing efficiency could be directly related to 1-D system morphology, and reduced lateral dimensions</td></tr>
<tr><td>9</td><td>[92]</td><td>Rods with differene surface area</td><td>~2</td><td>100</td><td>50-400</td><td>Surface area offered by the nanostructures for adsorption of CO play a discerning role in the response pattern</td></tr>
<tr><td>10</td><td>[93]</td><td>ZnO nanowirres</td><td>~6 fold change in drain</td><td>400-1600</td><td>Room temperature</td><td>This work utilized ZnO nanowires to adsorb CO even at room temperature and release electrons in the process</td></tr>
</table>

			current (I_{DS})			which translated into an enhanced drain current in the AlGaN/GaN high electron mobility transistors
11	[94]	Comb and nanobelts	1.4 for comb like structure	20000	75	Among the architectures, only comb like structure showed response towards very high concentration of CO
12	[95]	ZnO thin films with varying thickness	~2 for film thickness of 130 nm	1660	300	This article highlighted the correlation between point defects and CO sensing characteristics of ZnO crystals
13	[96]	ZnO nanoflowers	9 towards 1000 ppm at 200 ^{o}C	200-1000	150-400	ZnO nnoflowers built of thin nanorods as building blocks showed excellent response towards CO at the given range
14	[97]	Irregular ZnO nanoparticles within 100-150 nm	6.1 towards 1000 ppm at 400 ^{o}C	200-1000	150-400	The characteristic anisotropic growth along the *c*-axis was suppressed for the ZnO crystals which lead to formation of nanoparticles with higher sensitivities
Thematic Division: Additives influenced sensing of ZnO nanostructures						
Sr. No.	**Ref.**	**Material**	**Response (R_{air}/R_{gas})**	**Range / LDL of Detection (ppm)**	**Operating temperature (^{o}C)**	**Remarks**
15	[98]	Al-doped ZnO films	2.6 towards 1000 ppm CO at 400 ^{o}C	200-1000	100-500	The films fromed for the Al-doped ZnO crystals were flat and smooth with preferred (0001) oriented growth
16	[99]	Cu-doped ZnO films	2.7 towards 20 ppm CO at 350 ^{o}C	6-556	150-400	The Cu sites in ZnO columnar film adsorbed CO molecules by Cu-CO bonding through transfer of π-electrons from d-orbitals of Cu to CO resulting in enhancement of CO sensitivity
17	[100]	Au decorated ZnO nanowires	1.86 for Au-ZnO nanowires towards 50 ppm CO	5-100	25-350	Gold nanoparticle decorated ZnO crystals have been used to reduce the operating temperature for optimal sensing
18	[101]	Au nanoparticle decorated ZnO nanowires	~1.2 for 1000 ppm CO at room temperature	100-1000	Room temperature – 200	Au nanoparticles ionosorb oxygen adatoms even at room temperature and then induces spill-over effect to enhance response through chemical sensitization. Simultaneously Au-loading enables CO detection at room temperature
19	[102]	Al-doped ZnO films deposited on Au nanodots	6.4 towards 20 ppm CO at 250 ^{o}C	5-70	150-400	In this article Au nanodots primarily acted as a nucleation layer for ZnO crystals to render them distinct morphologies and increase their oxygen adsorption capacity
20	[103]	Pd nanoparticle decorated ZnO nanorods	~6 towards 200 ppm CO at 260 ^{o}C	10-600	260	The enhanced response for Pd/ZnO nanorods can be ascribed to their 3-D structure which allows CO to diffuse easily throughout the sensor
21	[104]	Pd-functionalized ZnO nanowires	1.02 towards 100 ppb CO	0.1-2	room temperature	This articel is one of the initial reports to show response of ZnO particles at room temperature towards sub-ppm concentrations of CO

This thesis investigates the morphological influence on carbon monoxide sensing where different hierarchical structures have been produced and investigated as probable sensing materials. A relatively new domain where templated synthesis of zinc oxide nanoparticles was undertaken and the resulting ceramic materials were availed for sensing. The templated synthesis offers a number of advantages as the nucleated crystals tend to imbibe the structure of the host template. This often allows formation of hollow shapes facilitating a greater surface coverage on either surface of the structure. Additionally, templated synthesis offers the benefit of relatively less agglomerated particles. This thesis presents protocols for synthesis of different superstructures including nanoflakes, nanosheets and nanoflowers of zinc oxide and studies their sensing characteristics. The analysis then veers towards templated synthesis where two different templates namely, egg shell membrane and layered double hydroxide have been used to anchor zinc oxide superstructures and their response towards carbon monoxide has been studied.

1.6. Tea tasting - an overview

India on a global scale features as the second largest producer of tea with production of around 960 M kg and yet faces a yearly deficit of 44 M kg. This can be explained by the popularity of tea as a domestic beverage as 85% of domestic household in India consume the brew. This in addition to the export of 193 M kg of tea accounts for an annual absorption which supersedes the amount produced and procured via import by 44 M kg [105]. The importance of the tea sector apart from generating revenue can be realized via the amount of employments it generates as Indian tea industries rely heavily on daily-wage workers. Under such a huge scenario, value addition to the sector from the scientific fraternity of any form should be beneficial.

To date the quality monitoring of black tea is executed through human perception in the industries. Tea industries traditionally employ human personnel to assess different batches of tea leaves, both produced as well as procured from small-holding cultivars. These dedicated personnel, referred as “tea tasters”, grade the tea on the basis of its quality attributes through manual inspection. Classifying the various tea grades, overseeing the fermentation process are some of the responsibilities performed by the dedicated human personnel. In order to assess the tea varieties, tea tasters depend upon their perceptions of smell, taste, touch and vision and grade the leaves accordingly. In a typical assessment, particular batch of tea sample is evaluated on the basis of their “leaf quality”,” infusion”, “liquor” and “aroma” based on the organoleptic perceptions and accordingly a score is allotted on a scale of 10. Normally a tea quality is estimated by a group of tasters comprising a “tasters panel”.

Among these, the aroma profile is of particularly importance for Indian black tea whose commercial value is determined by their olfactory impression. Being an organoleptic process, the evaluations are purely subjective and error prone, and varies with individual, place and time. Moreover, tea gardens in India are situated at dispersed geographic locations. This factor together with the subjective nature of human perception makes it difficult for the industries to set a common calibration scale for quality evaluation of their samples. Till date, no standard electronic prototype exists that can be used as a benchmark in aiding the tea tasters in their exertion and provide scientific validation to their efforts. It is the need of the hour to develop high-performance sensors which can help in classifying black tea grades based on aroma in a quantifiable and reliable manner.

1.6.2. Sensing of tea volatiles - prior art

Tea quality estimation has traditionally been a crucial determinant for industries in order to maximize the revenue a particular grade is expected to generate. Earlier conventions of 1960's used theaflavin content in black tea as the marker for quality evaluation of black tea in Northeast Indian as well as Central African tea. A direct correlation between the sensory evaluation and theaflavin content could be established [106]. Later, the use of theaflavin as the quality indicator was discarded owing to the method's poor reproducibility due to varying infusion conditions [107]. Initial scientific effort in quantifying black tea aroma saw the postulation of a couple of indexes, namely Wicremasinghe Yamanishi ratio based on the retention times of the gas chromatographic (GC) peaks of the black tea volatile organic compounds (VOCs), and Mahanta ratio based on desirability and undesirability of terpenoids and non-terpenoids respectively. While the former technique was dependent on the column packing material, the later calculated retention time of terpenoids in GC but lacked conviction due to the presence of desirable non-terpenoids in black tea aroma profile [108]. Two more indices, namely Owuor's Flavour Index and Yamanishi Botheju ratio were formulated in this regard and a study comparing the ratios performance was also reported [109-111].

While these indexes lacked conviction, the common base for them was projection of linalool as a key volatile compound. The black tea VOCs are normally classified into Group I and Group II [112] volatiles. While Group I elements primarily comprise VOCs with chromatograph elusion period shorter than linalool, the Group II members have longer durations. Another significant difference between the two groups is the undesirable grassy smell emanated from Group I constituents while a savoury sweet flowery aroma characterizes Group II affiliated VOCs. Several reports have been published on the concentration of VOCs in black tea [113,114]. Odour threshold and odour activity values were studied and reported for the major VOCs present in black tea by employing assessors [114]. The subtle variation in volatile concentrations result in a new synergy and a different aroma profile. The tasters perceive these subtle differences in the synergy through their orthonasal perceptions and grade the variety accordingly. Thus if the concentration of these volatiles could be monitored, the signature of detection pattern can lead to a precise quality estimation of black tea and subsequent classification among tea grades [115,116]. Among the VOCs, four major contributors that influence the tasters perception of the aroma through their relatively higher odour thresholds are trans-2-hexenal, linalool, geraniol and methyl salicylate [117].

The estimation of these volatiles was performed through complex chromatographic analysis and the present investigations aspire for advent of a more simpler method. However, the chormatographic analysis which gives a relatively accurate measure has been integrated on a device scale and has been commercialized as “zNose”. This prototype uses the Kovats indices relative to n-alkane vapour standards that have been implemented for black tea aroma quality detection [118].

1.6.3. State-of-the-art

Apart from the above techniques, a new paradigm focuses on prototype electronic noses (e-nose) for the classification of black tea aroma. However, all of the reported electronic noses serving this purpose contain commercially available sensors of Figaro (TGS) or of Win Muster Airsense (WMA) Analytics Inc., which are not specifically meant for the detection of VOCs in tea. The first reported electronic nose system for classification of black tea comprised TGS 880 (marketed for detection of cooking vapours), TGS 825 (marketed for detection of toxic gases), TGS 826 (marketed for detection of toxic gases) and TGS 822 (marketed for detection of organic solvents) [119]. A second prototype was reported for the purpose of classifying LongJing green tea that used a Portable Electronic Nose (PEN2) system from WMA Analytics Inc. Sensors used in this setup were W1C (marketed for detection of aromatics), W5S (marketed for detection of NOx), W3C (marketed for detection of ammonia and aromatic molecules), W6S (marketed for detection of hydrogen), W5C (marketed for detection of methane, propane and aliphatic non-polar molecules), W1S (marketed for detection of methane), W1W (marketed for detection of sulphur containing organics), W2S (marketed for detection of alcohols), W2W (marketed for detection of aromatics) and W3S (marketed for detection of methane and aliphatics) [120]. A separate report highlighted the implementation of TGS 823 (marketed for detection of organic solvent vapours), TGS 832 (marketed for detection of hydrocarbons), TGS 2600 (marketed for detection of air contaminants), TGS 2611 (marketed for detection of methane) and TGS 2610 (marketed for detection of general combustible gas) sensors as an array for black tea classification [121]. Yet another endeavour involved the use of TGS 821 (marketed for detection of hydrogen), TGS 824 (marketed for detection of ammonia), TGS 880 (marketed for detection of volatile vapours from food), TGS 822 (marketed for detection of toluene, xylene), TGS 822TF (marketed for detection of combustible gases), TGS 813 (marketed for detection of LPG), TGS 825 (marketed for detection of hydrogen sulfide) and TGS 812 (marketed for detection of propane, carbon monoxide) [122]. The performance of these electronic noses were enhanced by coupling them with various data pre-processing and classification techniques like Artificial Neural Network (ANN) [123,124] as well as by heating the headspace for emanation of larger amount of volatiles and physical raking of leaves [125]. A summary of the various electronic nose prototypes implemented for quality estimation of tea has been tabulated in **Table 1.4**.

Table 1.4. *Summary of electronic noses used for quality monitoring of tea*

Sr. No.	Reference	Sensors Used inthe array and their original targets	Category of Tea	No. Of different grades	Classification technique	Remarks
1	[119]	TGS 880 – Cooking vapours TGS 825 – Hydrogen sulfide TGS 826 – Ammonia vapours TGS 822 – Organic solvents	Tea samples varying in fermentation period	5	PCA, FCM, SOM, Neural Networks	Pioneering work on e-nose based quality monitoring of tea
2	[120]	W1C – Aromatics W5S – NO_x W3C – Ammonia vapours W6S – Hydrogen W5C – Methane W1S – Methane W2S – Alcohol vapours W2W – Aromatics W3S - Methane	LongJing green tea	4	PCA, LDA, ANN	This version of nose was instrumental in classifying green tea which has lower content of volatiles.
3	[121]	TGS 832 – Hydrocarbons TGS 823 – Organic solvent TGS 2600 – Air contaminants TGS 2611 – Methane TGS 2610 – Combustible gases	Black tea	4	PCA, BP-MLP, RBF, PNN	This effort was focussed on correlating the marks allotted by tea tasters with the data generated from the electronic nose
4	[122]	TGS 821- Hydrogen	Green tea	4	PCA, KNN,	This nose shows a

		TGS 824 - Ammonia vapours TGS 880 - Food volatiles TGS 822 - Toluene, xylene TGS 822TF - Combustible gases TGS 813 - LPG TGS 825 - Hydrogen sulfide TGS 812 - propane, carbon monoxide)			SVM	high discrimination among green tea grades through multifold cross validation

The drawbacks of the aforementioned electronic noses lie in not incorporating sensors specifically selective towards VOCs of tea. Therefore, if sensors can be tailor-made for detecting VOCs of tea, a much better classification of tea is expected by using them in electronic noses.

1.7. Problem statement and objective of the thesis

Two distinct applications which profoundly depend on the human olfaction have been identified. Limitations associated with the olfactory systems greatly influence either of these applications.

The limitations of human olfactory perception faced by the "taster panel" in their exertion to evaluate the aroma of a particular tea grade had motivated the advent of instrumental, objective and inexpensive means for tea quality evaluation in the form of electronic nose. It is to be noted that calibration of such prototypes were performed based on the knowledge base developed through feedback provided by the tea tasters. Such a knowledge base formed through the organoleptic estimations cannot be free from uncertainties and are susceptible to human errors. Another noteworthy point is the methodology adopted by the tea tasters for their evaluation where they actually distinguish among aromas through subtle variations in the odour active volatiles. Moreover, the prototype electronic noses developed thus far incorporate commercial sensors marketed for different toxic volatiles and air contaminants. The electronic noses function by gathering the synergy of these odour active volatiles, through the cross sensitivities of these sensors towards them. In order to solve this problem, dedicated sensor modules targeted towards detection of the influencing volatiles might be beneficial. If such sensors are incorporated in the array, the electronic nose prototype can provide more privileges in classification and quality monitoring of tea grades. It has been established through literature survey that the aroma emanated from Indian black tea is largely influenced through subtle variations in the concentrations of geraniol, linalool, methyl salicylate and trans-2-hexenal. On the basis of above propositions, the problem statement for a section of the dissertation may be framed as “The development of sensor modules for selective detection of major volatile organic compounds like linalool, geraniol, methyl salicylate and trans-2-hexenal in tea aroma.”

Thus the primary objective of one segment of the thesis is to develop sensor modules for specific detection of the aforementioned volatiles. Specifically chemiresistive type metal oxide semiconductor sensors shall be engineered for the purpose. Among the MOS materials, tin dioxide and zinc oxide have been adopted for the purpose citing their contributions in the field of volatile sensing. These composites shall be used in their pristine form or loaded with additives for detection of the tea aroma volatiles.

The other part of the thesis entails development of sensor modules for detection of carbon monoxide. Olfactory limitations restrict humans from establishing the presence of this toxic gas which can lead even to fatalities. The field of MOS based carbon monoxide sensor boasts of a strong knowledge base, with a variety of materials having already been explored. Metal oxide semiconductors offer a set of ubiquitous advantages over other mode of chemiresistive sensors that has been discussed. However, there is promising and necessary scope for research as most of the commercial sensors doesn’t detect below the statutory limits. The conventional MOS sensors also augment their performance through sporadic distribution of noble metal catalysts on their surface which inevitably adds to the overall cost of production. Thus the problem statement for this portion of the dissertation may be framed as “The development of MOS based sensor modules for selective and fast detection of carbon monoxide below their statutory limits with cost effective catalysts”.

This dissertation aspires to project an alternate group of cost effective additives that enhances the performance of the sensors at par to their commercial counterparts. These additives, specifically oxides of certain group II elements impedes crystal growth and produces smaller particles with higher specific surface area that bind a larger amount of target molecules.

1.8. Scope of the thesis

The current study intends to investigate two instances where human olfaction limitations can lead to economic and health related adversities. The limitations of human olfaction are countered through development of chemical sensors which transduces an electronic signal. More specifically, chemical sensors have been fabricated for detection of lethal carbon monoxide below the prescribed Threshold Limit Value (TLV) set by OSHA. Available commercial sensors often do not cater to these norms and therefore possibly subject the users to unwanted exposure to the toxic gas. The more accurate systems are highly expensive and therefore do not fulfil the need of the masses.

In another application sensor modules have been fabricated for detection of key volatiles within the black tea aroma, in order to assist the tea tasters in their exertion of quality monitoring of black tea grades.

Chapter 1 focuses on stating the problem to be countered. It is primarily based on literature survey, stating the techniques in use for detection of the analyte and their limitations. The human olfaction and the limitations associated with it is briefly discussed. Then the chapter details the necessity for carbon monoxide sensing in purview of the olfactory limitations to detect the toxic gas. A review of the different forms of carbon monoxide sensors has been presented with special emphasis being provided for chemiresistive type metal oxide semiconductor sensors. The choice of tin dioxide and zinc oxide among the MOS sensors has been delineated through literature review. The discussion then veered towards the second application within the scope of the thesis where the nuances of tea tasting have been presented. The state-of-the art electronic nose prototypes that have been used for providing an instrumental alternative for the human cognition have been detailed. The shortcomings of the conventional electronic noses have been recognised as they do not implement dedicated sensors but rely upon the cross-sensitivities of commercial modules towards the emanated aroma. The problem statements and the objectives in purview of the thesis have been clearly stated in this chapter.

Chapter 2 delineates the synthesis protocols adopted for producing the tin dioxide nanoparticles. In this respect, the advantages of opting for precipitation method have been discussed. However, precipitation of a precursor doesn't produce pristine SnO_2 crystals, but rather forms an interim oxide hydroxide phase which needs to be calcined at elevated temperatures. The phase transformation from the intermediate tin oxide hydroxide by calcination is a complex process which has been traced through X-ray diffraction and thermogravimetric analysis by collecting aliquots at different temperatures. The chapter then details the room temperature phase transformation of the interim product and subsequent production of tin oxide phases through a trade-off between kinetics and applied temperature. The chapter then highlights the necessity of sonication aided precipitation method for production of smaller particles. Additionally, an enticing synthesis technique where supplement of cations during sonication helps in production of requisite phases of tin oxide has been delineated in this chapter.

Chapter 3 details the implementation of the tin dioxide crystals for low concentration carbon monoxide detection. Performance of the sensors fabricated with the pristine form of SnO_2

was augmented through strategic incorporation of different cost-effective additives. Instead of noble metals conventionally used to improve the sensor performance, this chapter highlights the efficacy of oxides of certain group II elements (magnesium, calcium, strontium and barium) in the tin dioxide matrix for CO sensing. The chapter details the promising sensor performance demonstrated by these materials where carbon monoxide could be detected down to 1 ppm. Standard characterization which establish the discerning effects of these additives upon sensing mechanism have also been elucidated in this chapter.

Chapter 4 describes the formation of different nanostructures of zinc oxide and the effect of morphology in CO sensing. For this purpose, the chapter highlights the optimized synthesis of different zinc oxide superstructures *viz.* nanoflowers, nanoflakes, and nanosheets at room temperature through simple low power sonication method. This chapter also enlists the research performed with the sensors fabricated with these morphologies for CO detection. Additionally, another synthesis technique where dedicated templates were used to render ZnO crystals distinct morphologies has also been included in this module. The chapter concludes by highlighting the salient findings of templated ZnO sensors for CO detection.

Chapter 5 delineates the studies performed with the MOS based sensors (SnO_2 and ZnO) towards detection of volatile organic compounds within the emanated black tea aroma. Specifically, four volatiles were chosen based on literature survey, and optimized sensor compositions demonstrating partial selectivity towards these volatiles were developed. This chapter includes the different additives loaded onto the host systems (SnO_2 and ZnO) for enhancing their individual selectivity towards the volatiles. The optimised sensor compositions were then tested with the aroma generated from tea grades with known taster scores.

Chapter 6 outlines the salient observations made during the research program and also lists the scope for improvement. The chapter concludes by highlighting the new leads for future direction of research that shall result in incremental bolstering of the knowledge base.

References:

[1] G. Glusman, I. Yanai, I. Rubin, D. Lancet, “The complete human olfactory subgenome”, Genome Res., 11(2001) 685-702.

[2] http://users.rcn.com/jkimball.ma.ultranet/BiologyPages/O/Olfaction.html

[3] C. Bushdid, M.O. Magnasco, L.B. Vosshall, A. Keller, “Humans can discriminate more than 1 trillion olfactory stimuli”, Science, 343 (2014) 1370-1372.

[4] R.C. Gerkin, J.B. Castro, “The number of olfactory stimuli that humans can discriminate is still unknown”, eLife, 4 (2015) e08127(1-15).

[5] C.C. Stallings, J.W. Thomas, L.R. Prewitt, “Chemical treatment for odor abatement measured organoleptically in liquid dairy manure”, J. Dairy Sci., 61 (1978) 1509-1516.

[6] http://www3.epa.gov/ttn/caaa/t1/memoranda/rg701.pdf

[7] L. Zazzeron, C. Liu, W. Franco, A. Nakagawa, W.A. Farinelli, D.B. Bloch, R.R. Anderson, W.M. Zapol, “Pulmonary phototherapy for treating carbon monoxide poisoning”, Am. J. Respir. Crit. Care Med., 192(2015) 1191-1199.

[8] S.M. Motawei, S.M. El-Wasify, S.A. Eldakroury, A.M. Elmansoury, “Rhabdomyolysis complicating acute CO poisoning: a case study and a review”, Am. J. Med. Case Rep., 2 (2014) 232-236.

[9] http://www.cdc.gov/co/faqs.htm

[10] D. Roth, W. Schreiber, H. Herkner, C. Havel, “Prevalence of carbon monoxide poisoning in patients presenting to a large emergency department”, Int. J. Clin. Pract., 68 (2014) 1239-45.

[11] R.M. Hall, G.S. Earnest, D.R. Hammond, K.H. Dunn, A. Garcia, “A summary of research and progress on carbon monoxide exposure control solutions on houseboats” , J. Occup. Environ. Hygiene, 11 (2014) D92-D100.

[12] S. Pandey, G.K. Goswami, K.K. Nanda, “Nanocomposite based flexible ultrasensitive resistive gas sensor for chemical reactions studies”, Sci. Rep., 3 (2013) 2082(1-6).

[13] N.Yamazoe, G. Sakai, K. Shimanoe, “Oxide semiconductor gas sensors”, Catal. Surv. Asia, 7 (2003) 63-75.

[14] B. Kamp, R. Merkle, R. Lauck, J. Maier, “Chemical diffusion of oxygen in tin dioxide: Effects of dopants and oxygen partial pressure”, J. Solid State Chem., 178 (2005) 3027-3039.

[15] J. Hodgkinson, R.P. Tatam, “Optical gas sensing: a review”, Meas. Sci. Technol., 24 (2013) 012004(1-59).

[16] J. Yang, J. Zhou, Z. Lv, W. Wei, H. Song, “A real-time monitoring system of industry carbon monoxide based on wireless sensor networks”, Sensors, 15 (2015) 29535-29546.

[17] M. Breysse, B. Claudel, L. Faure, M. Guenin, R.J.J. Williams, T. Wolkenstein, “Chemiluminescence during the catalysis of carbon monoxide oxidation on a thoria surface”, J. Catal., 45 (1976) 137-144.

[18] O. Al-Araidah, M.A.K. Jaradat, W. Batayneh, “Using a fuzzy Poka-Yoke based controller to restrain emissions in naturally ventilated environments”, Expert Syst. Appl., 37 (2010) 4787-4795.

[19] L.Szente, J. Szejtli, “Non-chromatographic analytical uses of cyclodextrins”, Analyst, 123 (1998) 735-741.

[20] http://www.langan.biz/Site/T15n%20Specifications.html

[21] http://www.alphasense.com/WEB1213/wp-content/uploads/2015/04/COB41.pdf

[22] X. Li, T. Xuan, G. Yin, Z. Gao, K. Zhao, P. Yan, D. He, “Highly sensitive amperometric CO sensor using nanocomposite C-loaded $PdCl_2$–$CuCl_2$ as sensing electrode materials”, J. Alloys Compd., 645 (2015) 553-558.

[23] C. Quesada, T. Rockward, F. Garzon, D. Burleigh, R. Mukundan, “Demonstration of enhanced sensitivity to CO in H_2 fuel stream of an electrochemical analyzer”, ECS Trans., 58 (2014) 163-171.

[24] S. Radhakrishnan, S. Paul, “Conducting polypyrrole modified with ferrocene for applications in carbon monoxide sensors”, Sens. Actuators B: Chem., 125 (2007) 60-65.

[25] T. Seiyama, A. Kato, K. Fujiishi, M. Nagatani, “A new detector for gaseous components using semiconductive thin films”, Anal. Chem., 34 (1962) 1502-1503.

[26] W.H. Brattain, J. Bardeen, “Surface properties of germanium”, Bell Syst. Tech. J., 32 (1952) 1-41.

[27] N.Taguchi, “A metal oxide gas sensor” , Japanese Patent. No.45-38200, 1962.

[28] N.Taguchi, “Gas detecting device” , US Patent. No. 3631436 A, July 1962.

[29] P.J. Shaver, “Activated tungsten oxide gas detectors”, Appl. Phys. Lett., 11 (1967) 255-257.

[30] B. Shouli, C. Liangyuan, L. Dianqing, Y. Wensheng, Y. Pengcheng, L. Zhiyong, C. Aifan, C.C. Liu, "Different morphologies of ZnO nanorods and their sensing property", Sens. Actuators B: Chem., 146 (2010) 129-137.

[31] I. Simon, N. Bârsan, M. Bauer, U. Weimar, "Micromachined metal oxide gas sensors: opportunities to improve sensor performance", Sens. Actuators B: Chem., 73 (2001) 1-26.

[32] C. Wang, L. Yin, L. Zhang, D. Xiang, R. Gao, "Metal oxide gas sensors: sensitivity and influencing factors", Sensors, 10 (2010) 2088-2106.

[33] G. Neri, "First fifty years of chemoresistive gas sensors", Chemosensors, 3 (2015) 1-20.

[34] N. Yamazoe, K. Shimanoe, "Theory of power laws for semiconductor gas sensors", Sens. Actuators B: Chem., 128 (2008) 566-573.

[35] N. Yamazoe, "New approaches for improving semiconductor gas sensors", Sens. Actuators B: Chem., 5 (1991) 7-19.

[36] H. Keskinen, A. Tricoli, M. Marjamäki, J.M. Mäkelä, S.E. Pratsinis, "Size-selected agglomerates of SnO_2 nanoparticles as gas sensors", J. Appl. Phys., 106 (2009) 084316(1-8).

[37] A. Rothschild, Y. Komem, "The effect of grain size on the sensitivity of nanocrystalline metal-oxide gas sensors", J. Appl. Phys., 95 (2004) 6374-6380.

[38] M.I. Baraton, L. Merhari, "Influence of the particle size on the surface reactivity and gas sensing properties of SnO_2 nanopowders", Mater. Trans., 42 (2001) 1616-1622.

[39] K.J. Choi, H.W. Jang, "One-dimensional oxide nanostructures as gas-sensing materials: review and issues", Sensors, 10 (2010) 4083-4099.

[40] H. Okamoto, H. Obayashi, T. Kudo, "Carbon monoxide gas sensor made of stabilized zirconia", Solid State Ion., 1 (1980) 319-326.

[41] N. Miura, T. Raisen, G. Lu, N. Yamazoe, "Highly selective CO sensor using stabilized zirconia and a couple of oxide electrodes", Sens. Actuators B: Chem., 47 (1998) 84-91.

[42] Y. Fujio, V.V. Plashnitsa, M. Breedon, N. Miura, “Construction of sensitive and selective zirconia-based CO sensors using $ZnCr_2O_4$-based sensing electrodes”, Langmuir, 28 (2012) 1638-1645.

[43] S. Elouali, L.G. Bloor, R. Binions, I.P. Parkin, C.J. Carmalt, J.A. Darr, “Gas sensing with nano-indium oxides (In_2O_3) prepared via continuous hydrothermal flow synthesis”, Langmuir, 28 (2012) 1879-1885.

[44] M. Epifani, S. Capone, R. Rella, P. Siciliano, L. Vasanelli, G. Faglia, P. Nelli, G. Sberveglieri, “In_2O_3 thin films obtained through a chemical complexation based sol-gel process and their application as gas sensor devices”, J. Sol-Gel Sci. Technol., 26 (2003) 741-744.

[45] G. Neri, A. Bonavita, G. Micali, G. Rizzo, E. Callone, G. Carturan, “Resistive CO gas sensors based on In_2O_3 and $InSnO_x$ nanopowders synthesized via starch-aided sol–gel process for automotive applications”, Sens. Actuators B: Chem., 132 (2008) 224-233.

[46] H. Yamaura, K. Moriya, N. Miura, N. Yamazoe, “Mechanism of sensitivity promotion in CO sensor using indium oxide and cobalt oxide”, Sens. Actuators B: Chem., 65 (2000) 39-41.

[47] H.J. Lee, J.H. Song, Y.S. Yoon, T.S. Kim, K.J. Kim, W.K. Choi, “ Enhancement of CO sensitivity of indium oxide-based semiconductor gas sensor through ultra-thin cobalt adsorption”, Sens. Actuators B: Chem., 79 (2001) 200-205.

[48] A.M. Azad, M. Hammoud, “Fine-tuning of ceramic-based chemical sensors via novel microstructural modification: I: Low level CO sensing by tungsten oxide, WO_3”, Sens. Actuators B: Chem., 119 (2006) 384-391.

[49] H. Fukuda, R. Zohnishi, S. Nomura, “Highly sensitive metal-insulator-semiconductor field-effect transistor sensors for detecting carbon monoxide gas using porous platinum and tungsten oxide thin films”, Jpn. J. Appl. Phys., 40 (2001) 2782-2786.

[50] S.A. Akbar, L.B. Younkman, “Sensing mechanism of a carbon monoxide sensor based on anatase titania”, J. Electrochem. Soc., 144 (1997) 1750-1753.

[51] P.K. Dutta, A. Ginwalla, B. Hogg, B.R. Patton, B. Chwieroth, Z. Liang, P. Gouma, M. Mills, S. Akbar, “Interaction of carbon monoxide with anatase surfaces at high

temperatures: optimization of a carbon monoxide sensor", J. Phys. Chem. B, 103 (1999) 4412-4422.

[52] J.G. Firth, A. Jones, T.A. Jones, "Solid state detectors for carbon monoxide", Ann. Ocaip. Hyg., 18 (1975) 63-68.

[53] J.F. Boyle, K.A. Jones, "The effects of CO, water vapor and surface temperature on the conductivity of a SnO_2 gas sensor", J. Electron. Mater., 6 (1977) 717-733.

[54] H. Windischmann, P. Mark, "A model for the operation of a thin-film SnO_x conductance-modulation carbon monoxide sensor", J. Electrochem. Soc., 126 (1979) 627-633.

[55] H. Torvela, "Feasibility of using oscillatory catalytic oxidation phenomenon for selective carbon monoxide sensing", Active and Passive Elec. Comp., 12 (1987) 291-301.

[56] B.S. Chiou, J.J. Li, J.G. Duh, "Characteristics of Pd-doped tin oxide ceramics in response to CO gas", J. Electron. Mater., 17 (1988) 485-492.

[57] A. Kolmakov, Y. Zhang, G. Cheng, M. Moskovits, "Detection of CO and O_2 using tin oxide nanowire sensors", Adv. Mater., 15 (2003) 997-1000.

[58] V.V. Sysoev, B.K. Button, K. Wepsiec, S. Dmitriev, A. Kolmakov, "Toward the nanoscopic "electronic nose": hydrogen vs carbon monoxide discrimination with an array of individual metal oxide nano- and mesowire sensors", Nano Lett., 6 (2006) 1584-1588.

[59] H. Pink, L. Treitinger, L. Vite, "Preparation of fast detecting SnO_2 gas sensors", Jpn. J. Appl. Phys., 19 (1980) 513-517.

[60] K. Ihokura, K. Tanaka, N. Murakami, "Use of tin dioxide sensor to control a domestic gas heater", Sens. Actuators, 4 (1983) 607-612.

[61] C. Nayral, E. Viala, P. Fau, F. Senocq, J.C. Jumas, A. Maisonnat, B. Chaudret, "Synthesis of tin and tin oxide nanoparticles of low size dispersity for applications in gas sensing", Chem. Eur. J., 6 (2000) 4082-4090.

[62] A. Salehi, "A highly sensitive self heated SnO_2 carbon monoxide sensor", Sens. Actuators B: Chem., 96 (2003) 88-93.

[63] S.M. Sedghi, Y. Mortazavi, A. Khodadadi, “Low temperature CO and CH_4 dual selective gas sensor using SnO_2 quantum dots prepared by sonochemical method”, Sens. Actuators B: Chem., 145 (2010) 7-12.

[64] M.A. Andio, P.N. Browning, P.A. Morris, S.A. Akbar, “Comparison of gas sensor performance of SnO_2 nano-structures on microhotplate platforms”, Sens. Actuators B: Chem., 165 (2012) 13-18.

[65] A. Cabot, J. Arbiol, J.R. Morante, U. Weimar, N. Barsan, W. Gopel, “Analysis of the noble metal catalytic additives introduced by impregnation of as obtained SnO_2 sol–gel nanocrystals for gas sensors”, Sens. Actuators B: Chem., 70 (2000) 87-100.

[66] S. Capone, P. Siciliano, F. Quaranta, R. Rella, M. Epifani, L. Vasanelli, “Moisture influence and geometry effect of Au and Pt electrodes on CO sensing response of SnO_2 microsensors based on sol–gel thin film”, Sens. Actuators B: Chem., 77 (2001) 503-511.

[67] D.S. Lee, D.D. Lee, S.W. Ban, M. Lee, Y.T. Kim, “SnO_2 gas sensing array for combustible and explosive gas leakage recognition”, IEEE Sens. J., 2 (2002) 140-149.

[68] B. Esfandyarpour, S. Mohajerzadeh, S. Famini, A. Khodadadi, E.A. Soleimani, “High sensitivity Pt-doped SnO_2 gas sensors fabricated using sol–gel solution on micromachined (1 0 0) Si substrates”, Sens. Actuators B: Chem., 100 (2004) 190-194.

[69] I.J. Kim, S.D. Han, I. Singh, H.D. Lee, J.S. Wang, “Sensitivity enhancement for CO gas detection using a SnO_2–CeO_2–PdO_x system”, Sens. Actuators B: Chem., 107 (2005) 825-830.

[70] R. Dolbec, M.A. El Khakani, “Sub-ppm sensitivity towards carbon monoxide by means of pulsed laser deposited SnO_2 : Pt based sensors”, Appl. Phys. Lett., 90 (2007) 173114(1-3).

[71] F. Pourfayaz, Y. Mortazavi, A. Khodadadi, S. Ajami, “Ceria-doped SnO_2 sensor highly selective to ethanol in humid air”, Sens. Actuators B: Chem., 130 (2008) 625-629.

[72] V. Matsura, Y. Guari, C. Reye´, R.J.P. Corriu, M. Tristany, S. Jansat, K. Philippot, A. Maisonnat, B. Chaudret, [Ru(0)]@SiO_2 and [RuO_2]@SiO_2 hybrid

nanomaterials: from their synthesis to their application as catalytic filters for gas sensors, Adv. Funct. Mater., 19 (2009) 3781-3787.

[73] C.T. Wang, M.T. Chen, “Vanadium-promoted tin oxide semiconductor carbon monoxide gas sensors”, Sens. Actuators B: Chem., 150 (2010) 360-366.

[74] P. Manjula, S. Arunkumar, S.V. Manorama, “Au/SnO_2 an excellent material for room temperature carbon monoxide sensing”, Sens. Actuators B: Chem., 152 (2011) 168-175.

[75] W. Li, C. Shen, G. Wu, Y. Ma, Z. Gao, X. Xia, G. Du, “New model for a Pd-doped SnO_2-based CO gas sensor and catalyst studied by online in-situ x-ray photoelectron spectroscopy”, J. Phys. Chem. C, 115 (2011) 21258-21263.

[76] T. Yanagimotoa, Y.T. Yub, K. Kaneko, “Microstructure and CO gas sensing property of Au/SnO_2 core–shell structure nanoparticles synthesized by precipitation method and microwave-assisted hydrothermal synthesis method”, Sens. Actuators B: Chem., 166–167 (2012) 31-35.

[77] R.K. Sharmaa, P.C.H. Chan , Z. Tang, G. Yan, I.M. Hsing, J.K.O. Sin, “Sensitive, selective and stable tin dioxide thin-films for carbon monoxide and hydrogen sensing in integrated gas sensor array applications”, Sens. Actuators B: Chem., 72 (2001) 160-166.

[78] K. Galatsis, L. Cukrov, W. Wlodarski, P. McCormick, K. Kalantar-zadeh, E. Comini, G. Sberveglieri, “p- and n-type Fe-doped SnO_2 gas sensors fabricated by the mechanochemical processing technique”, Sens. Actuators B: Chem., 93 (2003) 562-565.

[79] A. Salehi, M. Gholizade, “Gas-sensing properties of indium-doped SnO_2 thin films with variations in indium concentration”, Sens. Actuators B: Chem., 89 (2003) 173-179.

[80] N.S. Ramgir, Y.K. Hwang, S.H. Jhung, H.K. Kim, J.S. Hwang, I.S. Mulla, J.S. Chang, “CO sensor derived from mesostructured Au-doped SnO_2 thin film”, Appl. Surf. Sci., 252 (2006) 4298-4305.

[81] S. Rani, S.C. Roy, M.C. Bhatnagar, “Effect of Fe doping on the gas sensing properties of nano-crystalline SnO_2 thin films”, Sens. Actuators B: Chem., 122 (2007) 204-210.

[82] S. Habibzadeh, A.A. Khodadadi, Y. Mortazavi, “CO and ethanol dual selective sensor of Sm_2O_3-doped SnO_2 nanoparticles synthesized by microwave-induced combustion”, Sens. Actuators B: Chem., 144 (2010) 131-138.

[83] P.S. Joshi, S.M. Jogade, P.A. Lohar, D.S. Sutrave, “Antimony doped tin oxide thin films: CO gas sensor”, J. Nano- Electron. Phys., 3 (2011) 956-962.

[84] T.S. Nagarjunan, M.V.C. Sastri, J.C. Kuriacose, “Simultaneous adsorption of hydrogen and carbon monoxide on zinc oxide”, J. Catal., 2 (1963) 223-229.

[85] Y. Takuma, M. Miyayama, H. Yanagida, “Effect of stepwise doping of Al_2O_3 and Li_2O on microstructure and electrical resistivity of ZnO ceramics”, Chem. Lett., 11 (1982) 345-348.

[86] B. Bott, T.A. Jones, B. Mann, “The detection and measurement of CO using ZnO single crystals”, Sens. Actuators, 5 (1984) 65-73.

[87] S. Saito, M. Miyayama, K. Koumoto, H. Yanagida, “Gas sensing characteristics of porous ZnO and Pt/ZnO ceramics”, J. Am. Ceram. Soc., 68 (1985) 40-43.

[88] H.W. Ryu, B.S. Park, S.A. Akbar, W.S. Lee, K.J. Hong, Y.J. Seo, D.C. Shin, J.S. Park, G.P. Choi, “ZnO sol–gel derived porous film for CO gas sensing”, Sens. Actuators B: Chem., 96 (2003) 717-722.

[89] T.J. Hsueh, Y.W. Chen, S.J. Chang, S.F. Wang, C.L. Hsu, Y.R. Lin, T.S. Lin, I.C. Chen, “ZnO nanowire-based CO sensors prepared on patterned ZnO:Ga/SiO_2/Si templates”, Sens. Actuators B: Chem.,125 (2007) 498-503.

[90] T. Krishnakumar, R. Jayaprakash, N. Pinna, N. Donato, A. Bonavita, G. Micali, G. Neri, “CO gas sensing of ZnO nanostructures synthesized by an assisted microwave wet chemical route”, Sens. Actuators B: Chem., 143 (2009)198-204.

[91] D. Barreca, D. Bekermann, E. Comini, A. Devi, R.A. Fischer, A. Gasparotto, C. Maccato, G. Sberveglieri, E. Tondello, “1D ZnO nano-assemblies by Plasma-CVD as chemical sensors for flammable and toxic gases”, Sens. Actuators B: Chem., 149 (2010) 1-7.

[92] S.K. Lim, S.H. Hwang, S. Kim, H. Park, “Preparation of ZnO nanorods by microemulsion synthesis and their application as a CO gas sensor”, Sens. Actuators B: Chem., 160 (2011) 94-98.

[93] S.C. Hung, C.W. Chen, C.Y. Shieh, G.C. Chi, R. Fan, S.J. Pearton, "High sensitivity carbon monoxide sensors made by zinc oxide modified gated GaN/AlGaN high electron mobility transistors under room temperature", Appl. Phys. Lett., 98 (2011) 223504(1-3).

[94] M. Amin, U. Manzoor, M. Islam, A.S. Bhatti, N.A. Shah, "Synthesis of ZnO nanostructures for low temperature CO and UV sensing", Sensors, 12 (2012) 13842-13851.

[95] S. Pati, S.B. Majumder, P. Banerji, "Role of oxygen vacancy in optical and gas sensing characteristics of ZnO thin films", J. Alloys Compd., 541 (2012) 376-379.

[96] P. Rai, Y.T. Yu, "Synthesis of floral assembly with single crystalline ZnO nanorods and its CO sensing property", Sens. Actuators B: Chem., 161 (2012) 748-754.

[97] P. Rai, Y.T. Yu, "Citrate-assisted hydrothermal synthesis of single crystalline ZnO nanoparticles for gas sensor application", Sens. Actuators B: Chem., 173 (2012) 58-65.

[98] J.F. Chang, H.H. Kuo, I.C. Leu, M.H. Hon, "The effects of thickness and operation temperature on ZnO:Al thin film CO gas sensor", Sens. Actuators B: Chem., 84 (2002) 258-264.

[99] H. Gong, J.Q. Hu, J.H. Wang, C.H. Ong, F.R. Zhu, "Nano-crystalline Cu-doped ZnO thin film gas sensor for CO", Sens. Actuators B: Chem., 115 (2006) 247-251.

[100] S.J. Chang, T.J. Hsueh, I.C. Chen, B.R. Huang, "Highly sensitive ZnO nanowire CO sensors with the adsorption of Au nanoparticles", Nanotechnology, 19 (2008) 175502(1-5).

[101] R.K. Joshi, Q. Hu, F. Alvi, N. Joshi, A. Kumar, "Au decorated zinc oxide nanowires for CO sensing", J. Phys. Chem. C, 113 (2009) 16199-16202.

[102] N.L. Hung, H. Kim, S.K. Hong, D. Kim, "Enhancement of CO gas sensing properties in ZnO thin films deposited on self-assembled Au nanodots", Sens. Actuators B: Chem., 151 (2010) 127-132.

[103] C.M. Chang, M.H. Hon, I.C. Leu, "Improvement in CO sensing characteristics by decorating ZnO nanorod arrays with Pd nanoparticles and the related mechanisms", RSC Adv., 2 (2012) 2469-2475.

[104] S.W. Choi, S.S. Kim, “Room temperature CO sensing of selectively grown networked ZnO nanowires by Pd nanodot functionalization”, Sens. Actuators B: Chem., 168 (2012) 8-13.

[105] N. Arya, “Indian tea scenario”, Int. J. Sci. Res. Publ., 3 (2013) 1-10.

[106] S.B. Deb, M.R. Ullah, “The role of theaflavins (TF) and thearubigins (TR) in the evaluation of black tea”, Two and a Bud, 15 (1968) 101-102.

[107] S.G. Reeves, F. Gone, P.O. Owuor, “Theaflavin analysis of black tea—Problems and prospects”, Food Chem., 18 (1985) 199-210.

[108] S. Baruah, M. Hazarika, P.K. Mahanta, H. Horita, T. Murai, “Effect of plucking intervals on the chemical constituents of CTC black teas”, Agric. Biol. Chem., 50 (1986) 1039-1041.

[109] P.O. Owuor, T. Tsushida, H. Horita, T. Murai, “Comparison of the chemical composition of black teas from main tea producing parts of the world”, Tea, 7 (1986) 71-78.

[110] T. Yamanishi, W.S. Botheju, M.J. De Silva, “An index for assessing the quality of Uva seasonal black tea”, Sri Lanka J. Tea Sci., 58 (1989) 40-49.

[111] P.O. Owuor, “Comparison of gas chromatographic volatile profiling methods for assessing the flavour quality of Kenyan black teas”, J. Sci. Food Agric., 59 (1992) 189-197.

[112] R. Ravichandran, R. Parthiban, “The impact of processing techniques on tea volatiles”, Food Chem., 62 (1998) 347-353.

[113] M. Zhu, E. Li, H. He, Determination of volatile chemical constitutes in tea by simultaneous distillation extraction, vacuum hydrodistillation and thermal desorption, Chromatographia, 68 (2008) 603-610.

[114] C. Schuh, P. Schieberle, “Characterization of the key aroma compounds in the beverage prepared from darjeeling black tea: quantitative differences between tea leaves and infusion”, J. Agric. Food Chem., 54 (2006) 916-924.

[115] C. Alasalvar, B. Topal, A. Serpen, B. Bahar, E. Pelvan, V. Gökmen, “Flavor characteristics of seven grades of black tea produced in Turkey”, J. Agric. Food Chem., 60 (2012) 6323-6332.

[116] Y. Liang, L. Zhang, J. Lu, “A study on chemical estimation of pu-erh tea quality”, J. Sci. Food Agric., 85 (2005) 381-390.

[117] P. Sharma, A. Ghosh, B. Tudu, L.P. Bhuyan, P. Tamuly, N. Bhattacharyya, R. Bandyopadhyay, U. Das, “A quartz crystal microbalance sensor for detection of geraniol in black tea”, IEEE Sens. J., 15 (2015) 1178-1185.

[118] E.J Staples, “The zNose, a new electronic nose using acoustic technology”, J. Acoust. Soc. Am. 108 (2000) 2495-2502.

[119] R. Dutta, E.L. Hines, J.W. Gardner, K.R. Kashwan, M. Bhuyan, “Tea quality prediction using a tin oxide-based electronic nose: an artificial intelligence approach”, Sens. Actuators B: Chem., 94 (2003) 228-237.

[120] H. Yu, J. Wang, “ Discrimination of LongJing green-tea grade by electronic nose”, Sens. Actuators B: Chem., 122 (2007) 134-140.

[121] N. Bhattacharyya, R. Bandyopadhyay, M. Bhuyan, B. Tudu, D. Ghosh, A. Jana, “Electronic nose for black tea classification and correlation of measurements with “tea taster” marks”, IEEE Trans. Instrum. Meas., 57 (2008) 1313-1321.

[122] Q. Chen, J. Zhao, Z. Chen, H. Lin, D.A. Zhao, “Discrimination of green tea quality using the electronic nose technique and the human panel test, comparison of linear and nonlinear classification tools”, Sens. Actuators B: Chem., 159 (2011) 294-300.

[123] J.W. Gardner, P. Boilot, E.L. Hines, “Enhancing electronic nose performance by sensor selection using a new integer-based genetic algorithm approach”, Sens. Actuators B: Chem., 106 (2005) 114-121.

[124] R. Kaur, R. Kumar, A. Gulati, C. Ghanshyam, P. Kapur, A.P. Bhondekar, “Enhancing electronic nose performance: A novel feature selection approach using dynamic social impact theory and moving window time slicing for classification of Kangra orthodox black tea (*Camellia sinensis* (L.) O. Kuntze)”, Sens. Actuators B: Chem., 166-167 (2012) 309-319.

[125] N. Bhattacharya, B. Tudu, A. Jana, D. Ghosh, R. Bandhopadhyaya, A.B. Saha, “Illumination heating and physical raking for increasing sensitivity of electronic nose measurements with black tea”, Sens. Actuators B: Chem., 131 (2008) 37-42.

Chapter 2

Optimization of synthesis for tin oxide nanoparticle

The work reported in this chapter highlights the various protocols adopted for synthesis of tin dioxide by researchers. Different synthesis processes adopted for production of tin oxide have been discussed before precipitation technique with its numerous advantages is projected as a preferred method. The phase transition of the precipitate traced by standard characterisation techniques helps in identifying the calcination temperature and the kinetics as the discerning parameters. A novel synthesis technique, where the requirement for the calcination process which is integral for obtaining phase pure tin dioxide after precipitation, could be mitigated. The room temperature synthesis technique which relies on ageing of the interim precipitate for production of distinct layers of stannous and stannic oxide has been delineated. The discussion then highlights the necessity of ultrasonication to produce relatively smaller crystals with larger specific surface area which is ideal for sensing applications. The chapter then discusses an alternate protocol where manganese is used as a catalyst during sonication aided precipitation method. This technique renders precise control on the production of distinct phases of stannous or stannic oxide. The chapter concludes by recognizing sonication aided precipitation method as the preferred mode of synthesis owing to its rapid and simple production of the desired phases.

List of Sections

Contents of this chapter are partially based on following publication

Saptarshi Ghosh, Somenath Roy, "Effect of ageing on $Sn_6O_4(OH)_4$ in aqueous medium—simultaneous production of SnO and SnO_2 nanoparticles at room temperature", Journal of Sol-Gel Science & Technology (Accepted, in press).

2.1. Introduction

Tin oxide (SnO_x), either in its stannous or stannic form, has intrigued the researchers with its unique physicochemical properties ever since its inception as a prominent Metal Oxide Semiconductor (MOS) material. It has evolved as an important entity in the ensemble of functional materials owing to its successful deployment in a varied field of applications and its comparatively simple production through a multitude of optimized synthesis protocols. The versatility of tin dioxide (SnO_2) integrates a wide band gap of 3.6 eV and low carrier density of 10^{19} –10^{21} cm^{-3} with a relatively high electron mobility of (~100-200 cm^2/Vs) [1]. In comparison, competence of stannous oxide (SnO) as a functional material is encoded in its unique electronic properties, which includes a field effect mobility of 5.59 cm^2/Vs [2]. As a result, these materials have found acceptance in domains of high criticality including gas sensing, coating material, catalysis and anode for lithium-ion battery [3-6]. A recent study also investigated SnO as dual channel transport where both *n* and *p*-channel were fabricated by the material [7]. The favourable intrinsic features can be further tailored through introduction of surface dwelling catalysts, or by doping its lattice to tune the electronic configuration. In addition, rendering distinct morphologies to the crystals have also been effective in tweaking the physicochemical properties.

Over the years, a range of application-oriented synthesis techniques have been adopted and optimized for producing SnO_2 crystals with specific attributes. The established processes can be broadly classified in two categories, namely conventional solid state and wet chemical synthesis techniques. Among the conventional solid state methods, vapour-liquid-solid (VLS) is particularly useful in synthesis of 1-D structures with high degree of confidence [8]. In contrast, another solid state technique, namely chemical vapour deposition (CVD) is more suitable for fabricating aligned arrays of SnO_2 nanorods [9]. A third technique, magnetron sputtering is mostly adopted for producing highly conductive thin films [10]. However, requirement for production of SnO_2 quantum dots, with dimensions below 5 nm, is often addressed by laser ablation technique [11], which is also capable of producing 1-D nanoribbons [12] and SnO_2 fractal patterns [13]. The solid state conventional techniques offer considerable advantages like production of pristine tin dioxide of desired dimensionality with considerable degree of confidence, along with the opportunity of *in-situ* doping of the crystal lattice [14]. Despite the advantages, the scope for these procedures is constricted by their requirement of complex and rugged setup, constant and precise monitoring of the entire procedure, and relatively larger synthesis period. On the contrary, wet chemical methods like precipitation, hydrothermal, spray pyrolysis, microemulsion, sonochemical and sol-gel routes provide a simple and uncomplicated approach for production of tin dioxide. These techniques not only ensure rapid kinetics in the liquid phase, but simultaneously allow production of SnO_2 crystals in different shapes and structures.

Among wet chemical approaches, the precipitation method is perhaps the oldest and most reliable for production of tin oxide due to its simple methodology, repeatability and rapid kinetics. The process relies upon providing an idealized ambience for nucleation and growth of tin oxide crystals. The procedure's inherent flexibility allows tweaking of certain growth parameters in order to customize the final product. For example, a slight change in the precursor concentration was enough to obtain different morphologies of SnO_2 with other parameters being kept constant [15]. Even the 1-D SnO_2 nanowires with high aspect ratio (~ 600:1), which are typically produced by conventional solid state techniques could be synthesized by a simple precipitation reaction [16]. These highly anisotropic crystals were later used to fabricate sensors for different gases where the anisotropy actually promoted sensing due to enhanced surface area and enlargement of facets which facilitated the adsorption of the inbound analyte molecules. Precipitation technique simultaneously allows addition of secondary components in the form of lattice dopants or surface catalysts which further optimizes the coveted sensing parameters of the base material. Although, whether an additive will migrate to the lattice and replace the Sn^{4+} depends on several factors including ionic radii compatibility, yet the microenvironment provided by the synthesis procedure plays a discerning role. Thus the exertion to grow tin dioxide crystals for developing sensors for tea aroma volatiles and carbon monoxide initiated through this simple yet reliable technique of precipitation.

2.2. Tin oxide – A brief review on physicochemical properties

Tin oxide's ascension, especially tin dioxide, as a marquee material in the field of gas sensing, stems from its endorsing physicochemical features that promote the detection mechanism. Since the MOS sensors detection is primarily a surface phenomenon, the chemisorbed oxygen adsorbates on tin dioxide play crucial role in the overall sensing. Though the dual valency of tin can tentatively result in a stoichiometric Sn^{4+} surface getting reduced into Sn^{2+} in presence of a reducing analyte depending on the oxygen chemical potential, yet this has limited impact on the sensing dynamics. Magnitude of band bending caused by variation in the depletion layer width at the grain boundaries in presence of the target moiety governs the overall performance of a SnO_2 based sensor. Thus, there is an apparent relationship among the electronic features of the material, the surface chemical activity and the gas sensing mechanism which shall be considered jointly and thus motivates a review on the established physical and chemical attributes of tin dioxide [17]. In most targeted applications one or multiple attributes of tin dioxide surface is modulated through introduction of additives. However, instances where rendition of distinct morphologies to the crystals have better manifested the electronic features are also reported [18].

An account of the physical properties for tin dioxide and tin monoxide has been summarised in **Table 2.1** [17]. Of particular importance for tin dioxide is the wide band gap of 3.6 eV which influence the transit of valence band electrons into the conduction band which eventually get entrapped by oxygen adsorbates at elevated temperature. The band gap is often tailored to improve the performance [19] of the fabricated gas sensors. The high melting point of >1900 ^{o}C and a high sublimation temperature of 1785 ^{o}C ensures operability of the SnO_2 based systems at elevated temperatures, although peritectic decomposition of SnO_2 at 1500 ^{o}C into SnO has been reported [20]. Since the bulk of MOS sensors work at a temperature range of 300-400 ^{o}C, the decomposition does not pose a serious threat in operation.

Table 2.1. *Physicochemical properties of stannous and stannic oxide*

	SnO	**SnO_2**
Mineral name	Romarchite	Cassiterite
Crystal structure	Tetragonal, litharge	Tetragonal, rutile
Space group	P4mnm	$P4_2mnm$
Lattice constants [nm]	a=b= 3.8029 A° c= 4.8382 A°	a=b= 4.738 A° c= 3.188 A°
Molar mass [g/mol]	134.70	150.71
Density [g/cm^3]	6.45	6.99
Melting point [^{o}C]	1080	>1900
Heat of formation [cal/mol]	-68	-138
Band gap [eV]	2.5 - 3	3.6

The high intrinsic conductivity of SnO_2 can be ascribed to the formation of oxygen vacancies and tin interstitials at lower energy in the crystal lattice. This produces conductive crystals albeit with an inherent non-stoichiometry in the form of SnO_{2-x} with the value of 'x' reaching a maximum of 0.03 at 900 ^{o}C [21]. The oxygen vacancy concentration is directly proportional with the ambient oxygen partial pressure and varies with a proportionality to the exponential reciprocal of a constant '*n*' whose value might vary within 5.7 and 8.3 for temperatures between 990 K and 720 K respectively. The nonstoichiometry can be increased by addition of extrinsic dopants thus further boosting the conductivity. For non-stoichiometric SnO_2, Kilic and Zunger showed that defect levels for oxygen vacancies lie just 114 meV below the conduction band minimum (CBM) and thus can be thermally ionized easily [22]. For Sn interstitials a level 203 meV above the CBM was found, implying a spontaneous donation of electrons into the conduction band. The extrinsic dopant is normally expected to have an extra electron compared to the cation in the SnO_2 lattice which might be donated to the conduction band upon substitutional replacement of the host cation. Additionally tin dioxide has a direct band gap with a dispersing conduction band (CB) along with high carrier mobility, which suggests a small change in the electron concentration in the CB shall be projected in the form of large conductance variation. Moreover, since the oxygen vacancies in SnO_2 lies just below the CBM, they can fill the conduction band with free electrons upon stimulation. The free electrons are trapped by chemisorbed oxygen facilitating a band bending in the near surface region. The band bending effect in presence of adsorbates alters the sheet conductance of the surface layer which might then be transduced for calibration. Therefore, adsorbate induced band bending causes major transduction in the electrical conductance in SnO_2 thus validating its candidature as a gas sensing material. This effect is even more profound for crystals with dimension comparable to the space charge region or the Debye length. Another relevant effect related to the observed near-surface band bending is the Schottky barrier an electron faces at the carrier depleted grain boundaries of polycrystalline films, which require an additional energy for the electron to cross over. The principle of operation for SnO_2 based modules is thus similar to that of conventional metal oxide semiconductors.

Extrinsic additives introduced into the SnO_2 might reside on the surface as sporadic clusters, or on rare occasions diffuse into the crystal lattice causing bulk doping through replacement of the host cation. The surface dwelling additives may induce one of the effects from catalytic (chemical) sensitization or electronic sensitization [23]. In chemical sensitization, the additives catalyze oxidation of the target analyte and reaction products subsequently spill-over from the clusters onto the semiconducting oxide support which effects the sensing. For electronic sensitization, usually noble metal nanoparticles are strategically localised on the surface. The interface between the metal particles and the semiconducting support effects an alignment of the fermi level and a subsequent bending of energy bands creating a modified Schottky barrier near the surface. The effective band bending is influenced in the presence of chemical adsorbates which enable the transduction in the variation of the sheet conductance. Under atmospheric conditions the additives are normally present in their oxide forms which reduce the conductivity of the SnO_2 owing to their superior work function. However in presence of a reducing analyte, the oxides are readily reduced to their metallic counterparts, leaving a reduced work function and a decrease in the degree of band bending.

The knowledge base representing standard properties for stannous oxide is a bit fuzzy compared to their tetravalent counterpart. For example, the band gap of stannous oxide is still not established and is expected to lie in between 2.5-3 eV. Absence of single crystals for stannous oxide further limits the scope for proper characterization of the material [17]. Moreover, stannous oxide is susceptible to oxidation at relatively low temperatures [24], which renders them unsuitable for sensing applications. Despite the lack of a strong knowledge base about the inherent properties for the stannous oxide, the crystal structures for both the bivalent and tetravalent oxide states of tin are well documented. While tin dioxide has a rutile structure, stannous oxide is mostly available in their litharge form. Though stannous and stannic are the more prevalent forms, less common interim structures, where Sn is composed of non-stoichiometric mixtures of Sn(II) and Sn(IV), like Sn_3O_4 and Sn_2O_3 have also been reported [25,26]. The heats of formation for stannous and stannic oxides at 298 K were determined to be $\Delta H = -68$ cal/mol and $\Delta H = -138$ cal/mol, respectively, thus leaving a $\Delta H = -70$ cal/mol for the oxidation of SnO to SnO_2 at elevated temperatures.

Stannic oxide (SnO_2) has a rutile structure with a tetragonal unit cell and has been represented in **Fig. 2.1(a)**. The tetragonal unit cell is slightly elongated compared to stannous oxide with lattice constants of a=b= 4.738 A˚ and c= 3.188 A˚ with a space-group symmetry of P4$_2$/mnm [27]. In the bulk all Sn atoms are sixfold coordinated to threefold coordinated oxygen atoms. The litharge structure of stannous oxide (SnO) with a tetragonal unit cell is shown in **Fig. 2.1(b)**. It has a P4/nmm symmetry space group and lattice constants a=b= 3.8029 A˚ and c= 4.8382 A˚. Each Sn and O atom is fourfold coordinated with a bond length of 2.23 A˚ and a van-der-Waals gap between two

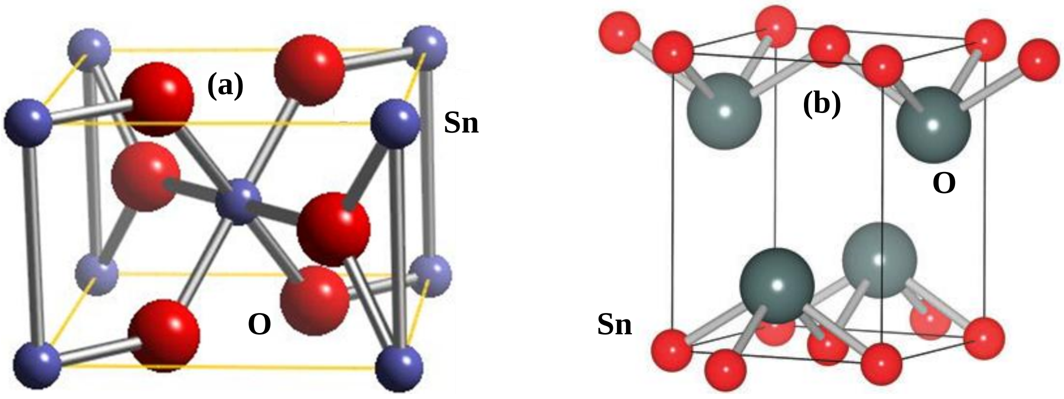

Fig. 2.1. *Crystal structures of **(a)** rutile tin dioxide (SnO_2) [28] and **(b)** litharge tin monoxide [29].*

adjacent Sn planes of 2.52 A°. The positive charge of the Sn^{2+} ions is screened by electron charge clouds between the Sn planes, thus reducing the Coulombic repulsion between adjacent Sn layers. These charge clouds, or charge hats, arise from Sn5s electrons that do not participate in the bonding for Sn(II) and thus can be described as a lone pair.

2.3. Synthesis techniques commonly used for tin dioxide

Tin dioxide crystals have mostly been implemented in their nanoscale for sensing applications simply to exploit the additional surface coverage available for such low dimensional particles. As such, tin dioxide nanoparticles have been synthesized through a variety of protocols, with the intrinsic attributes differing for each of the methods. Techniques like laser ablation, precipitation and hydrothermal are more common in the laboratory scale. In contrast controlled schemes like vapour-liquid-solid (VLS) and chemical vapour deposition (CVD) offer precise monitoring of the growth conditions at additional complexity. Two standard approaches have been recognized thus far for synthesis of the nanomaterials, namely top-down and bottom-up techniques. The choice of a particular approach depends on the degree of requisite control on the size, shape, and crystalline structure of the end product. The top-down approach involves the division of a massive solid into smaller portions, successively reaching to nanometer size. This approach is way more complicated and require precise monitoring to achieve the ultimate objective, thus making it unsuitable for bulk production. On the other hand, bottom-up approach involves the condensation of atoms or molecular entities in a gas phase or in solution with further self assembly process leading to the formation of nanostructures. The physical forces operating at nanoscale are used to combine basic units into larger stable structures. There are several standard methods grouped under this approach, including hydrothermal, sol-gel, microemulsion, assembly of quantum dots and precipitation. Among these, precipitation technique, especially aided with sonication, shall be discussed in detail as the materials for the present dissertation were produced through this simple yet effective technique. However, brief summary of other synthesis techniques for production of SnO_2 shall be beneficial to envisage the choice of precipitation method, and thus has been provided here.

(i) **Atomic Layer Deposition (ALD):** The method attracts researchers due to the possibility of obtaining highly conformal materials through layer-by-layer build up with thickness in the nanometer range. An ideal ALD growth proceeds by exposing the substrate surface alternatively to the different precursors strictly separated from each other in the gas phase. However the slow kinetics of the iterative surface reaction and subsequent adsorption is a deterrent in its ubiquitous acceptance. Nevertheless, this technique has been adopted for synthesis of tin dioxide thin films with excellent thickness and composition controllability [30,31].

(ii) **Chemical Vapour Deposition (CVD):** The method is ideal for production of thin films and relies on reaction of precursors in the gaseous phase and their deposition. Though the principle is similar, CVD differs from ALD as it is a continuous process in contrast to the cyclic nature of the ALD method. The CVD technique is often coupled with microfabricated patterns for deposition of targets. The thickness of the deposits can vary from angstroms to millimeters. Researchers have been intrigued with this method for production of SnO_2 thin films as slight modifications of the growth conditions have drastically changed the features [32,33]. Additionally CVD method empowers the researchers to dope the host lattice at their discretion [34].

(iii) **Vapour-Solid (VS):** This technique is particularly useful for production of 1-D and quasi 1-D structures of tin dioxide [35,36]. In a typical synthesis process, a precursor of tin is kept at one end of a tube furnace which is evaporated through high temperatures. The metal vapours are flown to the other end of the tube by a flow of oxidizing gas mixture. The flow rate determines the length of the nanowires being formed. A thermal gradient is maintained across the tube furnace ensuring condensation of the metallic vapours in their oxide forms towards the relatively cooler end of the channel, where a substrate is placed for deposition.

(iv) **Electrodeposition:** The principle of electrodeposition induces chemical reactions in an aqueous electrolyte solution with the help of an applied voltage. Ions in the solution are deposited onto the negatively charged cathode at a relatively cheap and fast rate. Controlling the current density and the iteration count allows monitoring of the thickness of the deposited layer. The precursor analyte typically contains the supplement of the target ions which are electrophoretically transferred on the electrode for deposition. The electrochemical technique is particularly important in simple production of SnO_2 nanotube architecture [37,38].

(v) **Sol-gel:** The sol-gel process is an efficient wet chemical technique which involves conversion of a system from a colloidal sol into a semi-solid gel phase. With advantages encompassing production of highly porous materials, low processing temperature, and molecular level control over the composition, this method has intrigued researchers since its inception. The sol is produced through hydrolysis and polycondensation reaction of a tin precursor salt following which it is converted into a gel through casting and ageing. The gel can be utilized to produce nanomaterials of differing porosity by regulating the amount of liquid in the system through thermal treatment. The porosity in the developed materials help in adsorption of a greater amount of target molecules thus producing a high response [39,40].

(vi) **Hydrothermal:** This mode of synthesis is particularly useful for synthesis of nanomaterials with complex 2-D or 3-D morphologies. The reacting precursors are placed in an autoclave and subjected to extreme conditions including high temperature and pressure which if controlled manifests different structures. The temperature in the autoclave can be raised above the boiling point of water, reaching the pressure of vapour saturation. Regulation of the solution composition, reaction temperature, pressure, solvent properties, additives and ageing time allows control over the grain size, particle morphology, crystalline phase and surface chemistry. This has been widely used for production of SnO_2 particles with different superstructures which have then been deployed for sensing applications [40,41].

(vii) **Microwave Assisted:** This is a relatively new technique but has found acceptance among researchers due to fast production of pure phase tin dioxide and elimination of the calcination process integral for most of the other techniques. Microwave energy surrogating the thermal treatment through focused local heating for shorter synthesis period generally leads to a very fine particle in the nanocrystalline regime. Though primarily employed for production of SnO_2 quantum dots [42], this process has been slowly gathering momentum in production of other nanostructures [43].

2.4. Synthesis of tin dioxide by precipitation method

Precipitation is effectively a solution phase reaction between two precursors that produces a precipitate as the product and has been largely accepted for its uncomplicated methodology. The product formed can then be utilized in its pristine form or thermally processed to produce a new phase. In the production of tin dioxide, a typical precipitation procedure involves addition of an alkali to a precursor stannous salt which produces stannous oxide hydroxide ($Sn_6O_4(OH)_4$) as an interim product. The interim product is then transformed to tin dioxide through calcination at an elevated temperature [44]. One of the common tin precursors used for synthesis of tin dioxide is $SnCl_4{\cdot}5H_2O$ where Sn is already in tetravalent oxidation state.. However $SnCl_4{\cdot}5H_2O$ has the tendency of forming adducts with ammonia which has been chosen as the precipitating agent. The complex subsequently requires a relatively higher reaction temperature for dissociating [45]. In contrary, the ionic nature of $SnCl_2$ facilitates the precipitation process and thus has been used as the precursor in the present studies involving production of SnO_2.

In a typical synthesis process, 0.1 M $SnCl_2 \cdot 2H_2O$ (Sigma Aldrich, ACS reagent, 98%) was dissolved in 150 mL DI water forming a milky white solution. The procedure was performed with a small concentration (~ 4 ml) of hydrochloric acid (Merck Millipore, ACS, ISO, Reag. Ph Eur, 37%) to deter hydrolysis of $SnCl_2$ (equation 2.1) and subsequent formation of insoluble Sn(OH)Cl [3]. The addition of 4 mL HCl (35%) shifted the equilibrium of equation 2.1 to the left in accordance with Le Chatelier's principle. The amount of HCl to be added is critical as excess HCl beyond the optimized level of 4 mL tends to oxidize the stannous precursor into its stannic counterpart.

$$SnCl_2 \cdot 2H_2O + H_2O \rightarrow Sn(OH)Cl + HCl \qquad (2.1)$$

This resulted in a clear acidic solution (pH ~ 2) to which NH_4OH (Sigma Aldrich, AR Grade, ~25%) was added drop wise, effecting precipitation to occur as the pH gradually increased to 9. White precipitate, thus obtained was filtered out and washed with deionized water to remove any chloride ions, excess NH_4OH and other by-products like NH_4Cl. A standard silver nitrate and nitric acid test, often used for assessing the presence of halide ions, was performed on the supernatant liquid post centrifugation, to ensure complete removal of chloride ions. Filtered sample was then dried in freezing condition (7 ^oC) to mitigate the possibility of any structural or electronic transition that might have occurred from thermal energy applied for drying. The dried sample was subsequently calcined at 850 ^oC to produce crystalline SnO_2 particles.

2.4.1. Phase transition studies with XRD analysis and thermogravimetric plots

The prevention of hydrolysis for stannous chloride in water through addition of HCl promote formation of the following species, of which the trimer is the most feasible and dominant moiety [46].

$$Sn^{2+} + H_2O \leftrightharpoons Sn(OH)^+ + H^+ \qquad (2.2.a)$$

$$2Sn^{2+} + 2H_2O \leftrightharpoons Sn_2(OH)_2^{2+} + 2H^+ \qquad (2.2.b)$$

$$3Sn^{2+} + 4H_2O \leftrightharpoons Sn_3(OH)_4^{2+} + 4H^+ \qquad (2.2.c)$$

Initially, in the lower pH range (2-2.5), addition of ammonia results in rapid consumption of the H^+ radicals marked by an increase in the system's pH. Subsequent addition of ammonia facilitates the condensation of the existing moieties into $Sn_6O_4(OH)_4$ through the following reaction:

$$2[Sn_3(OH)_4]^{2+} + 4OH^- \rightarrow Sn_6O_4(OH)_4 + 4H_2O \qquad (2.3)$$

The as-synthesized material, after complete drying in refrigerator, was phase-profiled through X-Ray Diffraction Analysis (XRD) with an D8 advanced Davinci (Bruker) XRD system using CuK$_\alpha$ radiation (0.15418 nm). The XRD analysis of the dried sample, whose plot has been shown in **Fig. 2.2**, revealed the formation of a pure phase tin (II) oxyhydroxide ($Sn_6O_4(OH)_4$) [JCPDS part No. #84-2157]. Slightly broad peaks visible in the X-Ray profile implies moderate degree of crystallinity for the synthesized material. The average crystallite size for $Sn_6O_4(OH)_4$ as deduced from the Scherrer equation was 19.4 nm. This interim product has been reported in earlier literature [44] and is required to be calcined at elevated temperatures in order to render distinct phases of tin oxide. However, nanoparticles with higher surface energy tend to coalesce and form agglomerates which minimize the effective surface coverage and calcining at lower temperatures might lead to impure phases, Thus to find the precise temperature range at which the calcinations should occur, the effect of the temperature gradient on $Sn_6O_4(OH)_4$ was studied to comprehend the phase transition which the interim product undergoes.

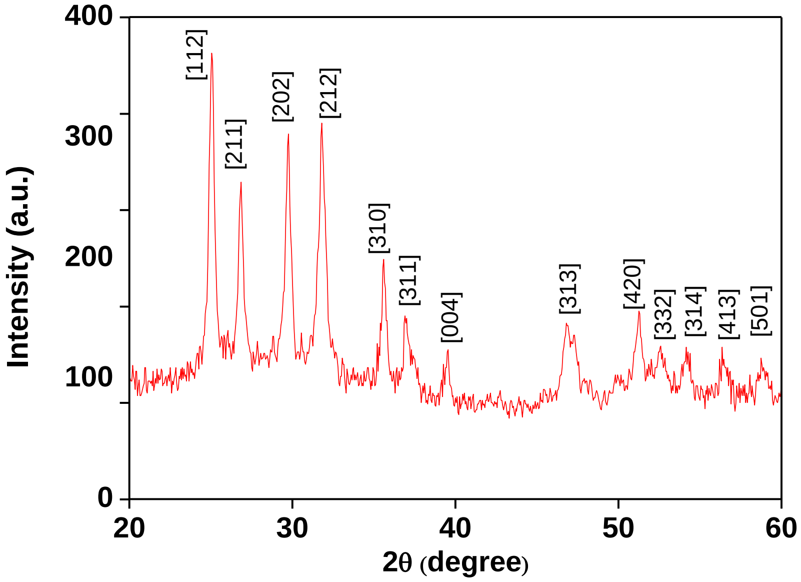

Fig. 2.2. *XRD plot of room temperature synthesized tin oxide hydroxide ($Sn_6O_4(OH)_4$)*

Thermogravimetric analysis (TGA) provides an empirical idea about the phase transition a system undergoes by providing the change in sample mass under a temperature gradient. Thermogravimetric analysis of the as synthesized $Sn_6O_4(OH)_4$, after drying in the refrigerator, was carried out in presence of 80% nitrogen and 20% air on a STA 499 Netzsch instrument and is shown in **Fig. 2.3(a)**. The sample for this experiment, measured precisely at 1 g, was subjected upto 1000 ^oC temperature with a thermal ramp of 5 ^oC/min. Initial reduction in weight till 120 ^oC was ascribed to the loss of physisorbed water and initiation of the decomposition process of $Sn_6O_4(OH)_4$ to form SnO [47]. The plot continued to show a monotonic loss in weight with temperature, with a minima occurring at 235°C. Beyond this temperature there was a constant gain in weight upto 500 °C, followed by a saturation region with minuscule loss in mass. There has been a dearth in detailed discussions about crystallographic phase evolution of tin oxide correlating with this complex weight loss and gain processobserved in the thermogravimetric analysis. In order to have a clearer scientific understanding of the phase evolution, differential scanning calorimetry (DSC) was performed on the precipitate to find the possible points of phase transformations, and is shown in **Fig. 2.3(b)**.

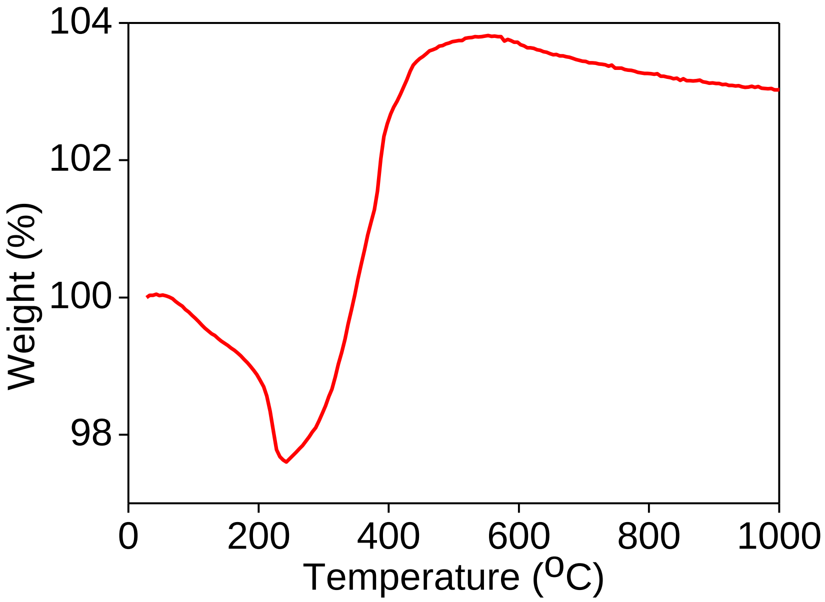

Fig. 2.3(a). *Thermogravimetric plot of as prepared tin oxide hydroxide*

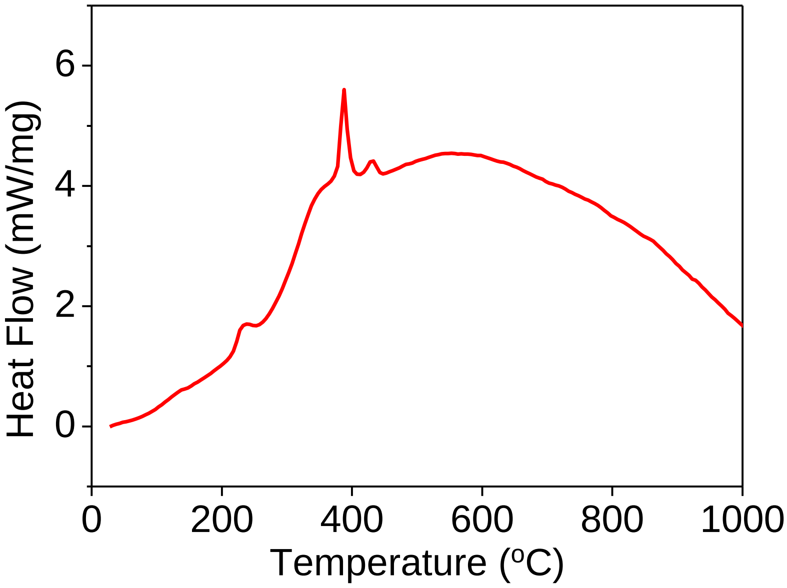

Fig. 2.3(b). *Differential Scanning Calorimetry (DSC) plot of as prepared tin oxide hydroxide*

Aliquots were collected at regular intervals along the TGA trace, as well as from temperature zones with plausible information about phase transitions. Since significant variations in sample weight were observed for the temperatures 100, 200, 235, 245, 300, 500, 600 and 950 ^{o}C, aliquots were collected at these temperatures. X-Ray Diffraction analyses (**Fig. 2.4**) on the collected aliquots were performed to profile their phases. The first noticeable change in the XRD pattern was observed for the sample heated at 200 ^{o}C, where a small but discernible peak appeared at 33.7^{o}, followed by new shoulder peaks appearing at 29.2^{o} and 26.4^{o} for the sample heated upto 235 ^{o}C. The new peaks correspond to the oxide phases (II and IV) of tin, thus indicating at nominal presence of SnO and SnO_2. This observation confirms the initiation of the dehydration process of $Sn_6O_4(OH)_4$ to stannous oxide as represented in equation (2.4).

$$Sn_6O_4(OH)_4 \rightarrow 6SnO + 2H_2O \qquad (2.4)$$

Simultaneously this observation also hints at a concurrent oxidation process where the SnO has started converting to SnO_2. Upon calcining beyond 235 ^{o}C, the peaks corresponding to SnO gradually decreased in intensity, while those for SnO_2 showed a contrasting trend, implying the growth of tin dioxide planes through phase transition. Further calcination resulted in an increase in phase purity of tin dioxide, and beyond 500 ^{o}C, no other peaks corresponding to any other phase of tin oxide remained. Calcination also resulted in sharpening of the peaks suggesting a growth in the size a well as crystallinity of the SnO_2 grains with temperature.

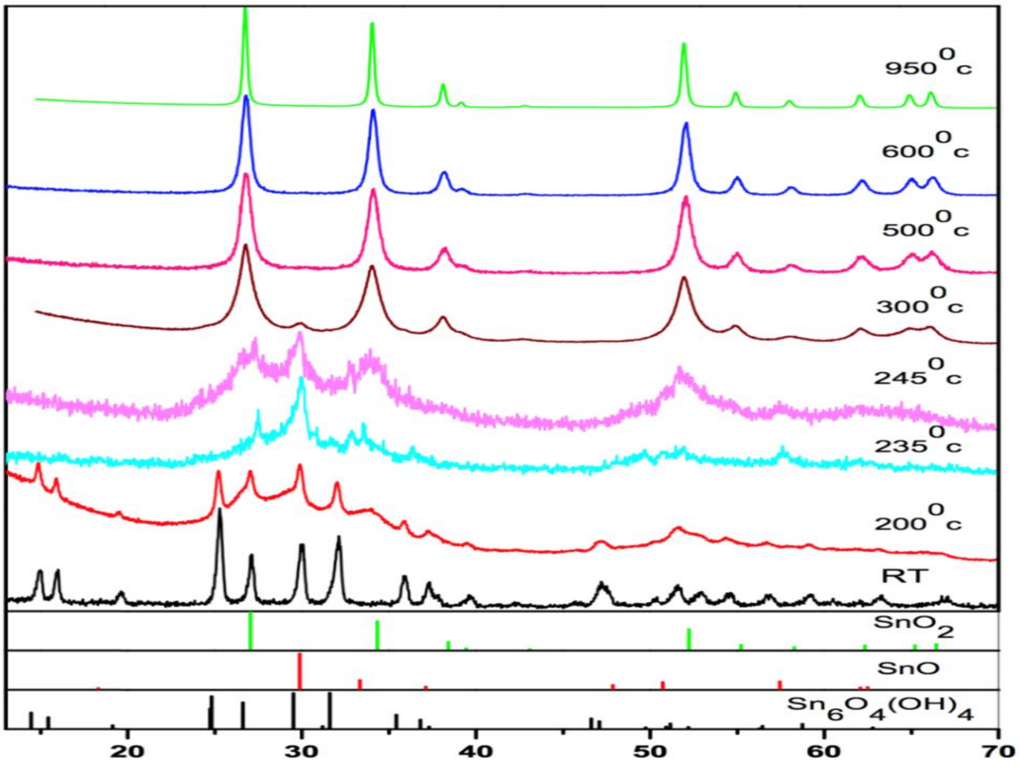

Fig. 2.4. *XRD patterns highlighting the phase evolution of* SnO_2 *from* $Sn_6O_4(OH)_4$

In order to assess the quantitative phase compositions of $Sn_6O_4(OH)_4$, SnO and SnO_2 at different temperature zones, standard Rietveld refinement technique was implemented on the XRD data obtained for calcined samples. While the as synthesized precipitate composed exclusively of tin oxide hydroxide ($Sn_6O_4(OH)_4$) [JCPDS part No. #84-2157], the samples heat treated at 200 and 235 ^oC showed considerable presence of other oxide phases. The sample calcined above 500 ^oC had exclusive presence of stannic oxide. A comprehensive account of the phases at different temperatures has been presented in **Table 2.2**.

Table 2.2. *Percentage of different phases of tin oxides at different temperature zones*

	As-synthesized (RT)	200 ^oC	235 ^oC (0.976 g)	500 ^oC (1.037 g)
$Sn_6O_4(OH)_4$	100	43.5	-	-
SnO	-	18	60	-
SnO_2	-	38.5	40	100

2.4.2. Correlating phase evolution of SnO_2 with thermogravimetric analysis

At this point it is imperative to correlate the salient findings of XRD analysis with the nature of the TGA curve demonstrated by the as prepared $Sn_6O_4(OH)_4$ under a thermal gradient. It is to be noted that the sample used for TGA was precisely measured at 1 g. The weight of the sample at the minima corresponding to 235 ^oC of the TGA curve was found to be 0.976 g, while that of beyond 500 ^oC and complete conversion to SnO_2 was 1.037 g signifying a slight gain in weight. A mathematical approach, summarized in **Table 2.3**, was adopted in order to understand the nature of TGA curve using the observations from XRD analysis. To simplify the approach, the entire thermal range from room temperature till complete conversion to stannic oxide, was divided in three regions.

Zone 1: (RT-200 ^oC):

As deduced from the X-Ray refinement (**Table 2.2**), a total of 43.5% of the initial weight of $Sn_6O_4(OH)_4$ remained unconverted at 200^oC, signifying conversion of 0.56 g into other phases. The converted amount of 0.56 g can approximately produce 0.54 g of SnO through equation (2.4), thus implying a loss of 0.02 g as physically adsorbed water. However, the refinement data revealed presence of only 0.18 g SnO, which hints at simultaneous conversion of the rest stannous phase into stannic form through oxidation. Therefore approximately 0.36 g SnO was oxidized thus producing 0.40 g SnO_2 or 40% of the initial weight. The calculated value suggesting presence of 40% SnO_2 in the calcined sample is in close approximation with the refinement derived data provided in **Table 2.2**. In absence of any form of external impetus and under inert atmosphere, the oxidation of SnO is a spontaneous process and follows the established disproportionation reaction [48]. Initially

SnO gets converted to metallic Sn and Sn_2O_3, followed by oxidation to SnO_2, rendering the stannic oxide to be most stable thermodynamically. The phase transformation process has been represented through equation (2.5(a)-(b)).

$$4SnO \rightarrow Sn + Sn_3O_4 \tag{2.5.a}$$

$$4Sn_3O_4 \rightarrow SnO_2 + Sn \quad \Delta G^{o}_{298} = -5.9\ kJmol^{-1} \tag{2.5.b}$$

However, in presence of oxygen, a normal oxidation process has been reported to be more feasible and is represented via equation (2.6) [48].

$$4SnO + ½\ O_2 \rightarrow SnO_2 \quad \Delta G^{o}_{298} = -262.9\ kJmol^{-1} \tag{2.6}$$

Therefore, considering the evaluated amounts of the initially formed $Sn_6O_4(OH)_4$, different phases of tin oxides and the loss of loosely bound water, the total weight of the sample at 200°C can be approximated as 0.99 g (99% of the total weight). The small aberration of calculated weight loss (1%) from the actual weight loss (1.17% as observed from TGA curve at 200°C from **Fig. 2.3(a)**) might be attributed to the loss of chemically adsorbed water which is not accounted for in the calculations pertinent to the dehydration process.

Zone 2: (200-235°C):

In the temperature zone 200-235 °C, a complete absence of $Sn_6O_4(OH)_4$ signifies conversion of the rest 43% that remained till 200 °C. Interestingly, an endothermic peak is observed in the DSC plot (**Fig. 2.3(b)**) centred at 234 °C, which signifies the complete conversion of $Sn_6O_4(OH)_4$ into SnO. This would produce around 0.42 g SnO and simultaneously release 0.015 g loosely bound water. Considering the 0.18 g unreacted stannous oxide derived from zone 1, approximately 0.60 g of SnO can be estimated to be present at 235 °C. This is in close agreement with the information acquired from the phase analysis that stated SnO to constitute 60% of the total sample mass. This finding also suggests that no significant amount of oxidation of stannous oxide into its stannic counterpart occurred. This is further corroborated as the estimated mass of 0.40 g SnO_2 from zone 1 is in agreement with the percentage composition of 40% obtained for SnO_2 from zone 2 (from **Table 2.2**), suggesting no further supplement in stannic oxide in between the two zones. The net weight for this zone can be estimated at 0.985 g by considering the oxide phases and the loss of physisorbed water.

Zone 3: (235-500°C):

The TGA plot shows a monotonic increase beyond 235 °C which can be explained through complete conversion of remaining 0.60 g SnO into 0.67 g of SnO_2. Taking into account the SnO_2 present after calcination at 235 °C, net weight of the stannic oxide amounts to 1.07 g, which explains the observed weight gain from the TGA plot.

Table 2.3. *Summary of the thermogravimetric analysis correlated with the Rietveld analysis*

		Zone 1 (g)	Zone 2 (g)	Zone 3 (g)
$Sn_6O_4(OH)_4$	C	0.57	0.43	-
	NC	0.43	-	-
SnO	C	0.36	0	0.60
	NC	0.18	0.60	-
SnO_2		0.40	0.40	1.07
H_2O released		0.02	0.015	-
Total weight		0.99	0.985	1.07

*C – Converted; NC – Non converted

2.4.3. Calcination kinetics – An influencing parameter

Information compiled from XRD analysis and TGA plot revealed the phase transitions undergone by the as-formed tin oxide hydroxide after precipitation stage during the formation of SnO_2. It was observed that calcination temperature plays a discerning role in effecting these transitions. Along with the thermal energy, the dehydration process of interim $Sn_6O_4(OH)_4$ is simultaneously dependent upon the period for which the precipitate has been subjected to the applied temperature. In order to resolve the effect of kinetics on phase transition, as synthesized $Sn_6O_4(OH)_4$ was subjected to calcination at 200, 420, 600 and 680 ^oC for 2 h under normal atmospheric conditions. Diffraction spectra shown in **Fig. 2.5** for these samples revealed a distinct deviation from that obtained for samples calcined for 1 h. The observed peaks for the former are well resolved and relate to phase pure materials mostly. Sample calcined at 200 ^oC for 2 h showed diffraction peaks corresponding to the planes exclusively of stannous oxide with no presence of the as-synthesized $Sn_6O_4(OH)_4$. The intensity of the peaks decreased for samples calcined at 420 ^oC, but still showed maximum presence of SnO [JCPDS part No. #06-0395]. This observation was subsequently corroborated through TGA analysis which showed the stability of SnO upto around 420 ^oC. In addition to the diminishing peaks for SnO nanoparticles, a new peak corresponding to the [110] plane of SnO_2 appeared in the XRD spectrum. Following which, the XRD plots revealed presence of phase pure rutile tetragonal SnO_2 at higher calcination temperatures [JCPDS part No. # 41-1445]. The sharpness for individual peaks also increased at higher temperatures owing to a growth in crystal size. However these findings point at calcination kinetics as another influencing parameter for the phase transitions to occur. Thus an inference can be drawn on the influencing nature of the synergy of calcination temperature and calcination kinetics in formation of the tin dioxide, and thus controlled tuning of either parameter can engineer the growth of SnO_2 crystals. An inference could be drawn from this observation that the necessity for thermal energy might be mitigated provided the kinetics is favourably modulated.

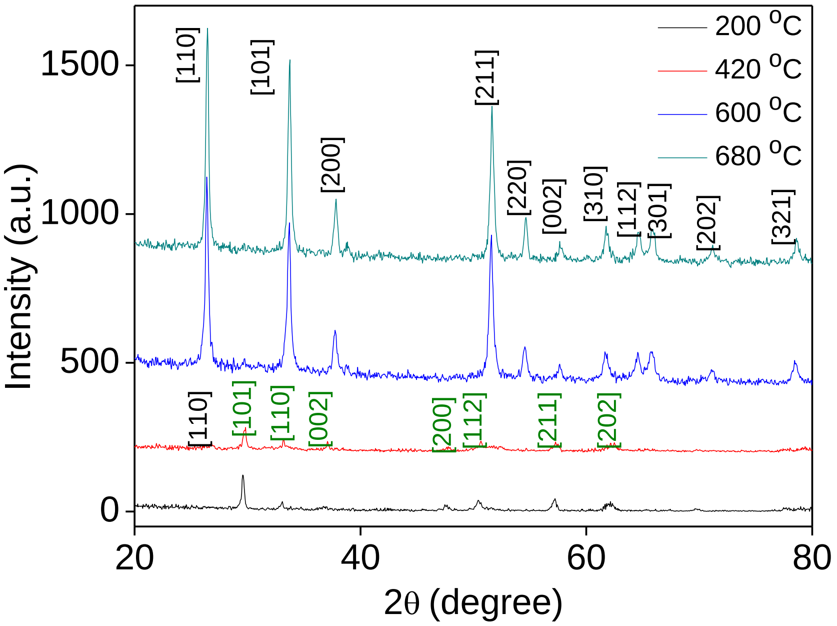

Figure 2.5. *Calcination period for longer duration shows improved phase purity*

2.5. Room temperature synthesis of tin oxide (SnO and SnO_2)

According to previous reports, the dehydration of interim $Sn_6O_4(OH)_4$ to form stannous oxide is preferred at temperature range within 90-100 °C [49,50] while pure stannic phase is obtained above 600 °C. Along with the thermal energy, the dehydration process of interim $Sn_6O_4(OH)_4$ is simultaneously dependent upon the duration of applied temperature. These two parameters are instrumental in determining the structural and electronic attributes of the ensuing tin oxide nanocrystals post dehydration. While ageing the $Sn_6O_4(OH)_4$ sol for 24 h at 60 °C resulted in interwoven SnO matrix, dehydrating the same sol within an hour under similar conditions produced SnO flowers [51]. The variation in crystal quality as a function of ageing duration was evident from their differing morphologies and reflections of the planes in X-Ray spectra. The interwoven SnO nanoribbons produced through ageing for 24 h was elongated along the <100> direction, in contrast to the broadened <110> peak observed for the flowers formed within 1 h [52]. Another report detailed formation of stannous oxide from $Sn_6O_4(OH)_4$ at a relatively lower temperature of 40 °C [53]. Here, $Sn_6O_4^+$ ions were produced through dissolution of $Sn_6O_4(OH)_4$, which then reacted with hydrazine in presence of NaOH to recrystallize into nanosheets of SnO. Despite the reduced reaction temperature, the process required drying of the as-obtained precipitate at a temperature of 60 °C for 24 h thus indicating a discerning role of the ageing process. However, the observations from previous section suggested that a trade-off between the kinetics and the applied temperature is possible.

In the present study the thermal requirement was further reduced and distinct layers of stannous and stannic phases of tin oxide could be produced in the same aqueous medium at room temperature (25 ^{o}C) through simple ageing of the interim $Sn_6O_4(OH)_4$. The tin oxide hydroxide was synthesized by a simple precipitation method and the sol was aged for twelve days at room temperature to produce distinct separable layers of SnO and SnO_2. The layers were extracted and profiled for their phase and morphological attributes implementing standard characterization tools. Additionally, in order to perceive whether the system's pH has any influence in the growth kinetics, the synthesized material was divided in multiple aliquots with the pH for each aliquot being controlled by addition of a basic, acidic or neutral media.

2.5.1. Procedure for room temperature production of SnO_x layers

The interim product of tin oxide hydroxide was prepared in accordance to the standard procedure delineated in section 2.4. However, instead of drying the $Sn_6O_4(OH)_4$, the mixture was homogenized by stirring for 15 min, before transferring 5 mL aliquot to an open-mouth glass vial. The vial was then stored in a vacuum oven at 25 ^{o}C and aged for 12 days. The white sol containing $Sn_6O_4(OH)_4$ was then stirred for 15 min before distributing it equally in 13 glass vials (5 mL in each). The vials were then kept for ageing at room temperature with an open mouth for air to circulate. 1 mL of different concentrations [0.1, 0.2 0.5 and 1 M] of ethanol, ammonia, and HCl were added to alter the pH and growth condition in 12 vials while the solution in the 13th vial was used as control. Upon successful conversion of the interim product into distinct layers of tin oxides, a similar experiment was performed in a separating glass funnel to extract the layers for phase analysis. The separated layers were dried without any increase in temperature to mitigate any thermal influence on the phase profile of the compositions.

Upon ageing the precipitate for twelve days, three distinguishable layers were observed, with a black layer forming at the bottom and a yellow layer at the top of the initially formed $Sn_6O_4(OH)_4$. A real-time picture (**Fig. 2.6**) depicts the three distinct layers for the aliquot aged for twelve days. A similar experiment was performed within a separating glass funnel to extract the different layers and assess them for their phase profile through XRD analysis. The XRD plot for the nanoparticles obtained from the differentiated layers is shown in **Fig. 2.7** which indicates at coexistence of three different phases at three observed layers for the sample. While the topmost yellow layer was inferred to be SnO_2, the black layer at the bottom was ascribed to stannous oxide and the white sol was observed to be remnant $Sn_6O_4(OH)_4$. The average crystallite sizes as deduced by implementing the Scherrer equation for the stannous and stannic oxide were 26 nm and 14 nm respectively

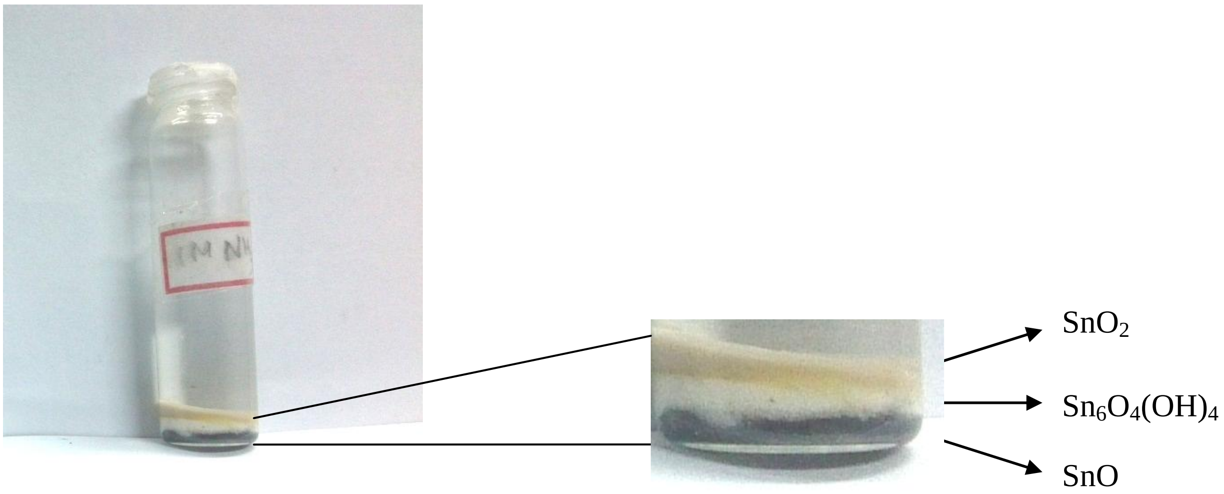

Fig. 2.6. *Distinct separation of tin oxide layers after 12 days of ageing of the interim precipitate*

.

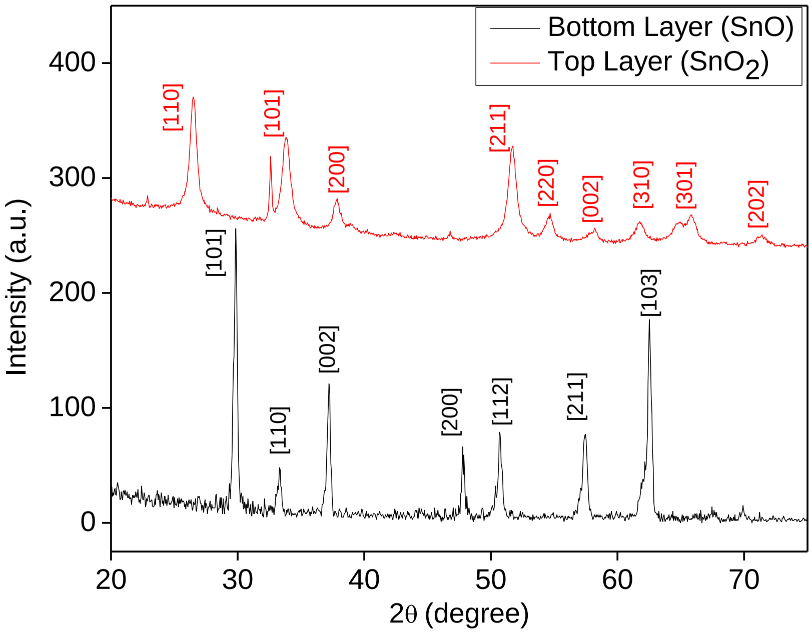

Fig. 2.7. *XRD plots of layers separated after 12 days of ageing showing formation of distinct stannous and stannic oxide*

Calcination of the interim $Sn_6O_4(OH)_4$ at an elevated temperature of 850 ^{o}C produced SnO_2 crystals of 35 nm [3]. Therefore, an apparent reduction in size for the pristine SnO_2 particles could be obtained by minimizing the thermal requirement. Additionally, electron microscopic studies on the SnO nanoparticles extracted from the bottom layer was performed on a Carl Zeiss-Supra 35VP FESEM system. The microscopic analysis depicted in **Fig. 2.8(a)** conforms to the estimation of dimension made through XRD analysis, as spherical particles in the range of 25-30 nm were observed in the images. The thermal stability of the stannous oxide nanoparticles was further probed by subjecting them to thermogravimetric analysis at a rate of 5 °C/min in oxidizing atmosphere. The study, highlighted in **Fig. 2.8(b)**, highlights that the produced stannous oxide is stable up to around 410 °C, beyond which it starts oxidizing to its stannic form. This observation is in agreement with the findings from **Fig. 2.5** suggesting that stannous oxide is stable upto around 420 °C. Apparently the pH of the system did not influence the phase transition as the samples kept in the neutral and basic media converted in 12 days. However, the aliquot kept in acidic media dissolved, thus mitigating the probability of further investigations.

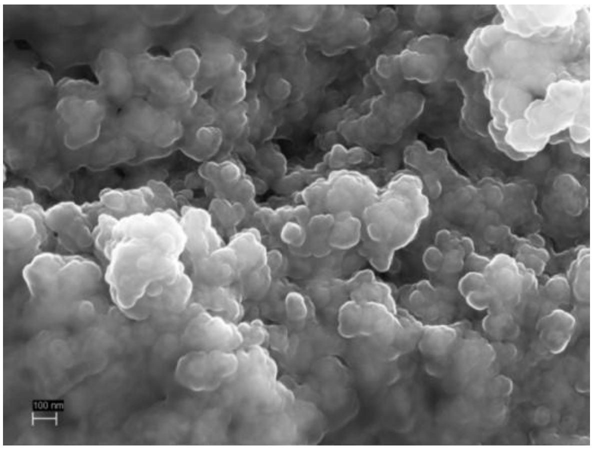

Fig. 2.8(a). FESEM images of as-obtained SnO crystals

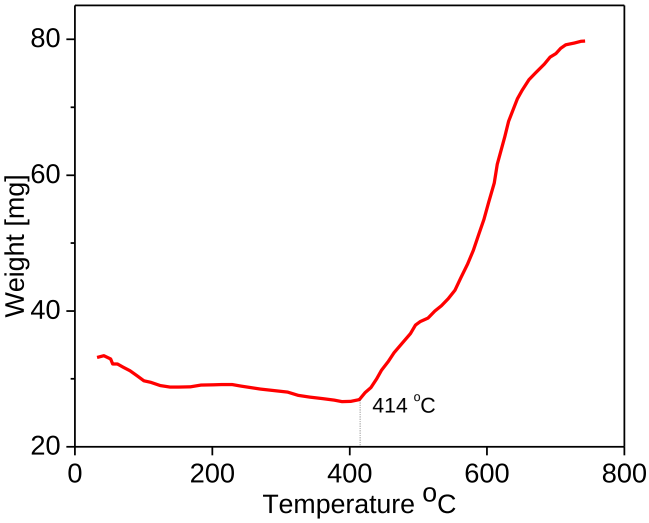

Fig. 2.8(b). Thermo gravimetric analysis of the as-obtained stannous oxide sample, showing the thermal stability for the material upto 410 °C.

2.5.2. Formation mechanism

It was inferred from previous reports that calcination temperature as well as kinetics plays discerning roles in the phase evolution of tin oxide from its precipitated state [51,52]. The overall process of phase transition is a dehydration reaction with water as a product and was illustrated through equation 2.4. Unavailability of external thermal impetus results in continuous removal of water from the system through evaporation. This in turn shifts the equilibrium of the equation 2.4 towards right and drives the reaction forward. Earlier reports had mentioned that an increasing ratio of Sn^{2+} and OH^- is necessary for the decomposition reaction to be feasible [47]. To achieve this, biasing of the cationic to anionic ratio through introduction of metallic supplements were found to be beneficial for production of SnO. However, in the present scenario, a flagging water volume increases the cationic ratio and no such need for the use of cationic supplements was observed. Also, the excess ammonia left after complete precipitation is emanated from the system, thus tilting the equilibrium of equation 2.4 further right. In conjunction with the above mechanism, formation of stannic oxide within the same system might be explained by reaction of the stannous oxide in aqueous medium with water [47]:

$$6SnO + 2H_2O \rightarrow SnO_2 + H_2 \qquad (2.7)$$

This explains the formation of the yellowish layer of pure tin dioxide at room temperature in the system after twelve days of ageing.

2.6. Ultrasonication assisted precipitation

Thus far, the temperature requirement for production of SnO_2 could be mitigated and the kinetics could be successfully altered. Though the novel method presented an alternate energy-efficient route for synthesis of tin dioxide, the time required for the process to complete was the limiting and decisive factor. Moreover, the separation of individual layer produced is another challenging task. In contrast, the samples produced through normal precipitation followed by calcination ensured relatively rapid production of SnO_2 nanocrystals. The phase purity for the samples calcined above 650 ^oC was established through XRD analysis. The X-Ray plots also revealed information about the average crystallite size of the particles through Debye-Scherer equation. Although effective at times the average crystallite size can only give empirical values, and the actual size can be measured by more specific analysis like Transmission Electron Spectroscopy (TEM). It is to be noted at this point that the synthesized materials are to be adopted for sensing applications and therefore a smaller particle size with high specific surface area is desired. A higher specific surface area would inadvertently mean more active sites for binding of target analytes on the surface.

The TEM analysis on the phase pure SnO_2 crystals formed through calcination of the interim tin oxide hydroxide at 850 ^oC was performed on a Tecnai G^2 30ST (FEI) High Resolution Transmission Electron Microscopy instrument. The TEM images provided in **Fig. 2.9**, reveal that the particles are rather large, with dimensions well above 50 nm. Ideally, smaller SnO_2 particles with dimensions in close proximity to the Debye length show maximum sensitivity due to the high surface area to volume ratio [54]. For larger particles, the sensing phenomenon is dominated through bulk interactions, which is minimal as dispensed gas might not be able to penetrate beyond the surface. On the contrary, surface interactions govern the sensing process among smaller particles where the dimension is comparable to the Debye length. In order to reduce the size of the particles so as to enhance their efficiency in sensing applications, an alternate route of synthesis was adopted. The new approach implemented ultrasound energy in cohesion with the precipitation method, to produce particles of smaller dimensions. The sonication aided precipitation method has been used earlier to produce SnO_2 particles with high specific surface area [50]. A detailed discussion about the sonochemical technique and its role in controlling the particle size has been presented in the following section.

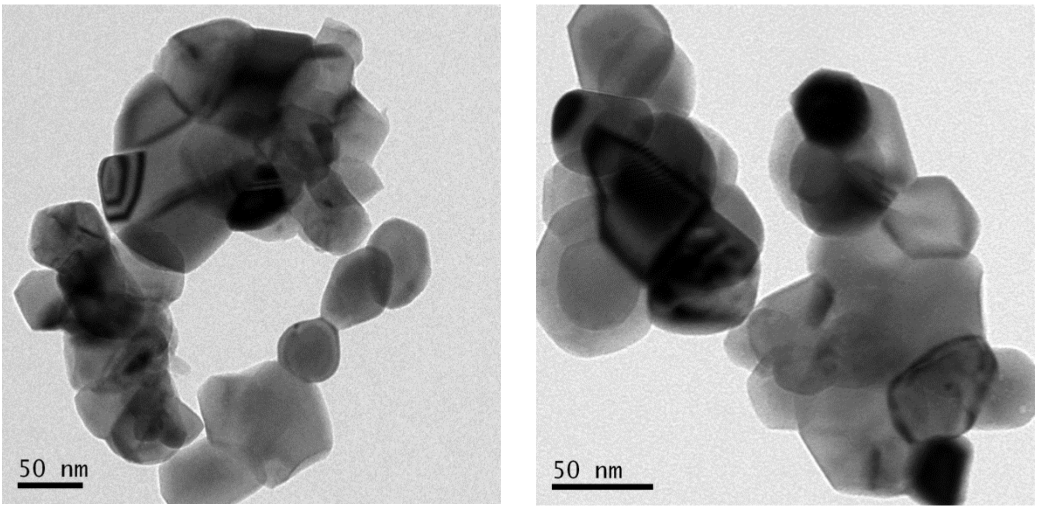

Fig. 2.9. *Simple precipitation produces* SnO_2 *crystals of dimension greater than 50 nm*

Sonochemical technique

Ever since Suslick showed a separate avenue for production of nanomaterials with the help of ultrasound, the sonication technique has established itself as an important candidate in energy-efficient, fast synthesis of nanomaterials [55]. The sonication process is based on the acoustic cavitation phenomenon which involves the formation, growth, and collapse of many bubbles in the aqueous solution. Basically ultrasound waves, like sound waves, consist of cycles of compression and expansion. Compression cycles exert a positive pressure on the liquid, pushing the molecules together, expansion cycles exert a negative pressure, pulling the molecules away from one another. In order for a cavity to form, a large negative pressure associated with the expansion cycle of the sound wave is needed to overcome the liquid's tensile strength. During the expansion cycle, a sound wave of sufficient intensity can generate cavities. Since the amount of gas that diffuses in or out of the cavity depends on the surface area, diffusion into the cavity during expansion cycles will be slightly greater than diffusion out during compression cycles. For each cycle of sound, then the cavity expands a little more than it shrinks. Over many cycles of cavities will grow slowly. The growing cavity can eventually reach a critical size where it will most efficiently absorb energy from the ultrasound. At this point the cavity can grow rapidly in the course of a single cycle of sound. Once a cavity has experienced a very rapid growth caused by the high intensity ultrasound, it can no longer absorb energy as efficiently from the sound waves. Without this energy input the cavity can no longer sustain itself. The liquid rushes in and the cavity implodes. Near a solid surface, bubble collapse becomes non spherical, driving high-speed jets of liquid into the surface and creates shockwave damage to the surface. During this process, bubble collapse produces intense local heating and high pressure of very short lifetimes and these transient, localized hot spots drive high-energy chemical reactions. Extreme reaction conditions can be created at localized spots. Assisted by the extreme conditions, for example, at temperature greater than 5000 K, pressure larger than 500 atm, and cooling rate higher than 1010 K/s, nanostructure of metal oxides can be formed via chemical reactions.

Microscopic images (**Fig. 2.10**) for the particles synthesized with sonochemical technique performed with a Sonics, Vibra-Cell, VCF 1500 ultrasonic processor shows a reduction in particle size. The power induced by an ultrasonic processor into the system is influenced by many a factors, especially the horn dimension and the amplitude. In addition, the duty cycle and the material viscosity also affect the gross power levels. Considering the above parameters and the fact that the experiments were conducted in 1 atmospheric pressure and without flow, the power levels for the ultrasonic processor in this experiment could be calculated as 600 W.While the normally synthesized particles were around 50 nm in size, the dimension for the sonochemically synthesized particles catered within 35 nm.

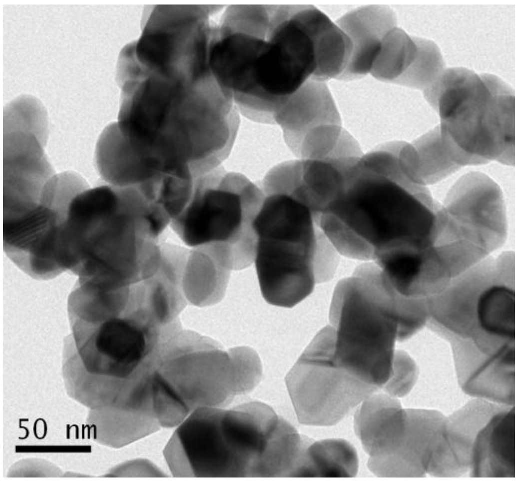

Fig. 2.10. *Sonication aided precipitation method reduces the particle size to 35 nm*

2.7. Incorporation of manganese for precise control on tin oxide synthesis

Although with sonication, the reduction in particle size could be achieved along with faster kinetics compared to the ageing process, the as-prepared product again required calcination at elevated temperature for producing SnO_2 nanocrystals. Since through separate experiments it was deduced that a higher cationic ratio is favourable in limiting the thermal requirement, and that sonication helps in producing smaller crystals, the next obvious strategic step was to merge these two techniques. Thus the cation concentration was supplemented within the system with influx of Mn^{2+} ions in presence of sonication and studied its effect in the phase evolution of SnO_2 particles. The precipitation process was catalysed by Mn^{2+} ions to produce phase pure pristine tin monoxide and tin dioxide without the production of the intermediate tin oxide hydroxide ($Sn_6O_4(OH)_4$), normally associated with the precipitation method. The as-synthesized material was characterized for their morphological attributes by Field Emission Scanning Electron Microscopy (FESEM) studies while Transmission Electron Microscopy (TEM) studies and Selected Area Electron Diffraction (SAED) studies revealed the cuboidal structure of the nanostructure. In a relevant study, Ning *et al*. had reported on different cations (M^{n+}) mediated formation of SnO [47] where they investigated the dehydration of $Sn_6O_4(OH)_4$ in presence of positive ions. But while they ascribed the ratio between Sn^{2+} and water as an important parameter in formation mechanism, the clarity of the roles played by the cations remained fuzzy. In order to investigate the more precise effect of Mn^{2+} in the process, XPS studies was performed on the synthesized material to determine the oxidation states of the catalyst and the host composite, and infer the significance of manganese in the process.

Manganese ion supplemented synthesis of tin oxide

The core steps for the precipitation synthesis procedure resulting in formation of the interim tin oxide hydroxide were elucidated in section 2.4. Prior to the precipitation process, 10 mL manganese chloride [$MnCl_2 \cdot 4H_2O$, Sigma-Aldrich, ACS reagent, ≥98%] was prepared by dissolving varying weight percent of the precursor in deionized (DI) water. Different proportions [0, 1, 2, 5 wt%] of manganese chloride was introduced into the system and their effects on the structural and phase evolution of ensuing crystals were studied. The solutions, namely the stannous and manganese chloride precursors dissolved in water, were mixed and homogenized by stirring for 30 minutes. Upon homogenization, liquor ammonia was added to the mixture under sonication to facilitate precipitation until a pH value of 9 was attained. An ultrasonic processor (Sonics, Vibra-Cell, VCF 1500) was intermittently operated for introducing the ultrasound energy into the system. The estimated power level was approximately 600 W. The as prepared material was centrifuged, washed several times with DI water for removal of trace chlorine ions and dried at 70 ^{o}C for 12 hours in a vacuum oven. Standard structural and phase characterization techniques were utilized to affirm the oxidation states of the final products and infer the discerning role of the cationic supplements.

Structural and phase analysis of the final products

When manganese was loaded on to the surface of tin oxide, it got segregated on the surface and no evidence for doping of Mn^{m+} ions in the crystal lattice was found. Since no peak shifts are observed for the XRD spectra, it is inferred that the additives have not substituted tin ions at the lattice points. An apparent absence of lattice substitution might be ascribed to the mismatch in the ionic radii of tin (0.69 Å) with manganese (0.83 Å). The XRD spectra for the materials synthesized with different concentrations of manganese as additive have been shown in **Fig. 2.11**. The plot shows the formation of different phases of tin oxides formed exclusively as a function of manganese loading percentage. The XRD plots of separately synthesized tin dioxide [JCPDS part No. # 41-1445 and tin monoxide [JCPDS part No. #06-0395] have been provided in the two lower panels for ready referencing. While absence of any Mn^{m+} ions produces the expected $Sn_6O_4(OH)_4$ phase as the interim product, an interesting phenomenon is observed in presence of additives. Upon loading of 1 wt% manganese the precipitate is asserted as phase pure stannic oxide (SnO_2) as the XRD plot is devoid of any peaks pertinent to tin oxide hydroxide or SnO and only peaks relevant to SnO_2 are visible. Increasing the catalyst concentration effects a phase transition where a loading of 3 wt% results in formation of mixed phases of SnO and SnO_2.

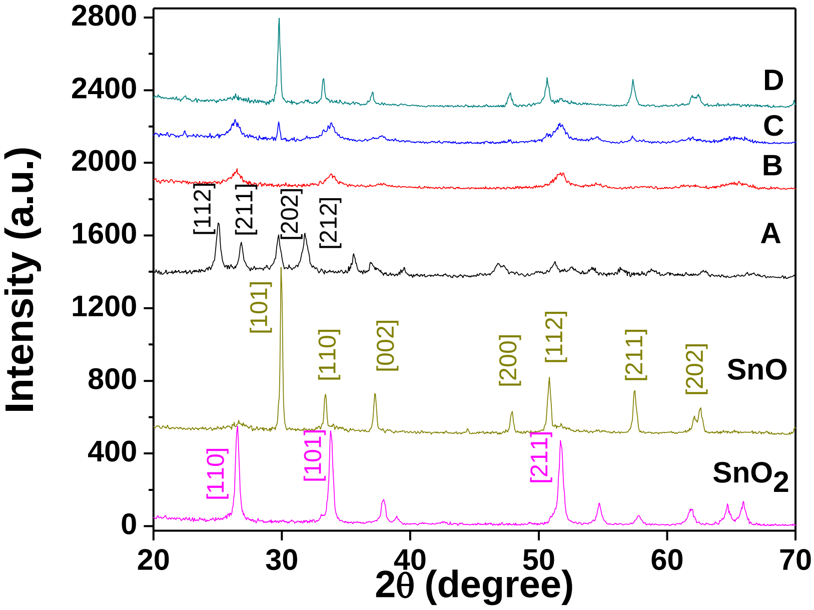

Fig 2.11. *XRD plots for samples synthesized with* ***A.*** *0 wt%* ***B.*** *1 wt%* ***C.*** *3 wt%* ***D.*** *5 wt% of manganese loading. XRD plots for separately prepared Tin (II) and Tin (IV) oxides have also been provided for referencing.*

However, the material is clear of normally formed $Sn_6O_4(OH)_4$ and comprise solely of the tin oxide phases. The phase transition is even more visible when the loading concentration for manganese was increased upto 5 wt%. At this loading level, peaks pertinent exclusively to SnO were observed, signifying that the precise control on generation of different phases for tin oxides can be administered through modulation of cationic percentage in the system. The advantage of this protocol was embedded in its **i)** thermal requirement mitigation coupled with **ii)** precise control on the rapid formation of tin oxides through variation of additives.

Morphological studies on the room temperature synthesized tin oxides were performed through FESEM images provided in **Fig. 2.12**. While the 1 wt% manganese loaded SnO_2 and 3 wt% loaded mixed phase stannous and stannic oxides fail to show any distinct morphologies, the 5 wt% loaded pure phase SnO demonstrate tendency to form nanocubes.

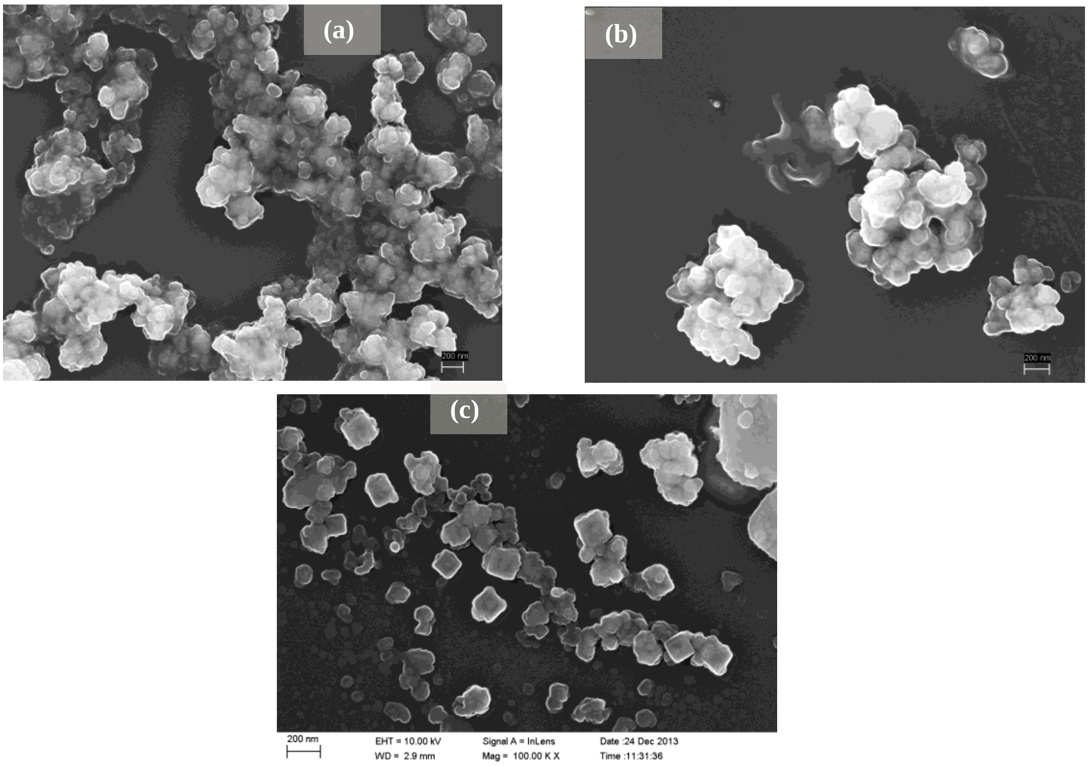

Fig. 2.12. *FESEM images for different loading concentrations **(a)** 1 wt%, **(b)** 3 wt% and **(c)** 5 wt% of manganese showing tendency to form nanocubes*

The FESEM images show that the dimensions of the SnO nanocubes vary within 100 nm to 400 nm along with the presence of smaller particles. This is further corroborated by TEM images, depicted in **Fig. 2.13** which clearly highlights the cubic nature of the crystals for 5 wt% loading.

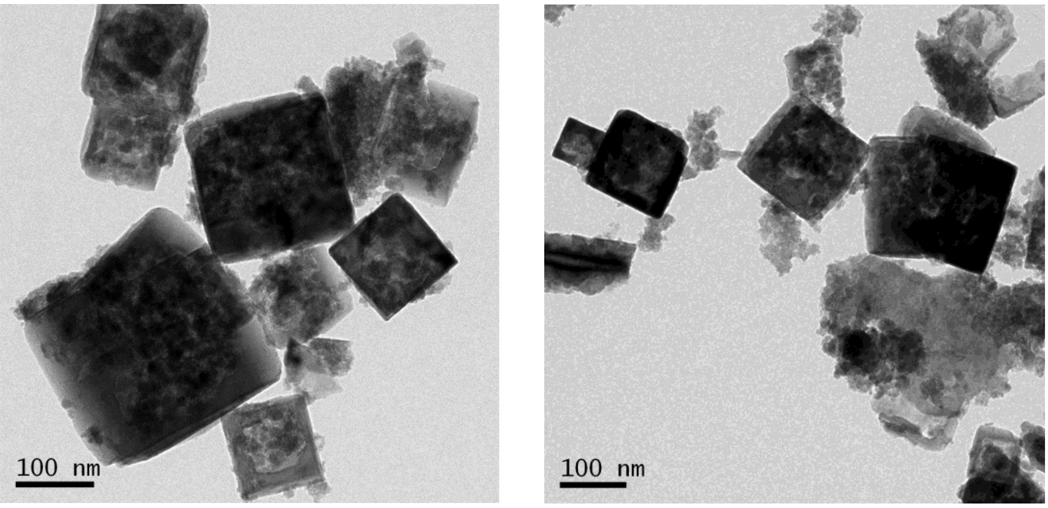

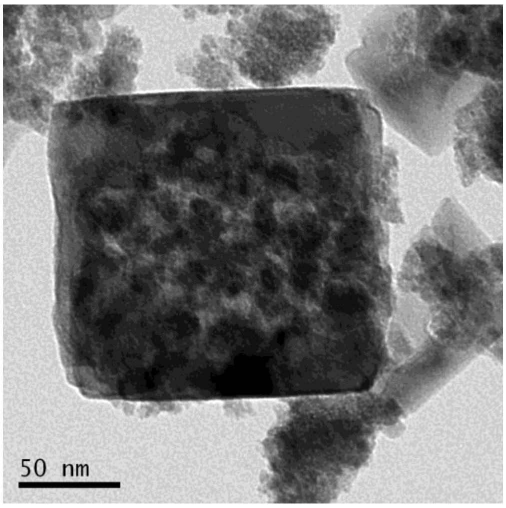

Fig. 2.13. *TEM images corroborating the formation of SnO nanocubes*

Each cube is approximately 100 nm in dimension which correlates with the findings of FESEM analysis. The morphological attributes of the 5 wt% Mn-loaded SnO crystals were further probed through High Resolution Transmission Electron Microscopy (HRTEM) analysis which validated the presence of stannous oxide (SnO) through a *d*-spacing of 0.29 nm corresponding to its [101] plane [56] as shown in **Fig. 2.14(a)**. Additionally, the analysis also reveled presence of an adjacent plane with a *d*-spacing of 0.22 nm which correlates to the [002] plane of manganese oxide (MnO) [57].

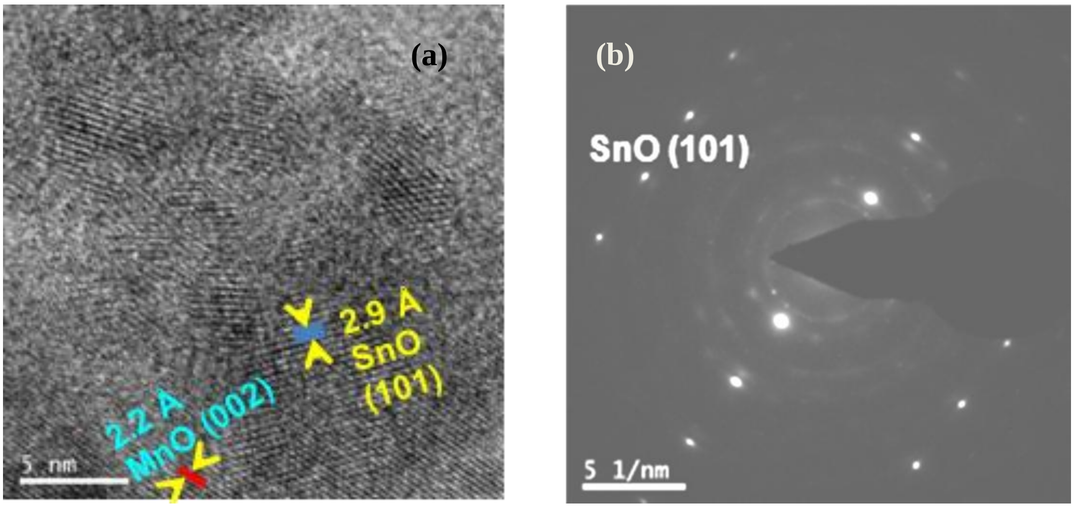

Fig. 2.14(a). *High resolution TEM images showing dual presence of SnO and MnO lattices* ***(b)*** *SAED pattern confirming the single crystallinity of SnO phase*

The Selected Area Electron Diffraction (SAED) pattern obtained for the 5 wt% Mn-loaded SnO presented yet another notable observation and has been shown in **Fig 2.14(b)**. It has been mentioned previously that the proper characterization of stannous phase is impeded due to absence of single crystals [17]. However, the SAED pattern clearly shows parallel fringes which suggest that the material is mostly single crystalline though some degree of polycrystalline nature with a dominant [101] facet may be observed from the concentric circles. However, the present thesis aspires to develop SnO_2 based sensors and therefore further research with stannous oxide remains beyond the scope of this dissertation. However the X-ray photoelectron spectroscopy (XPS) analysis for the material was performed in conjunction with the structural characterization to ascertain the phase of the catalyst. The XPS spectra for the SnO nanoparticles are presented through **Fig. 2.15** and have been used to assert the valence state of manganese.

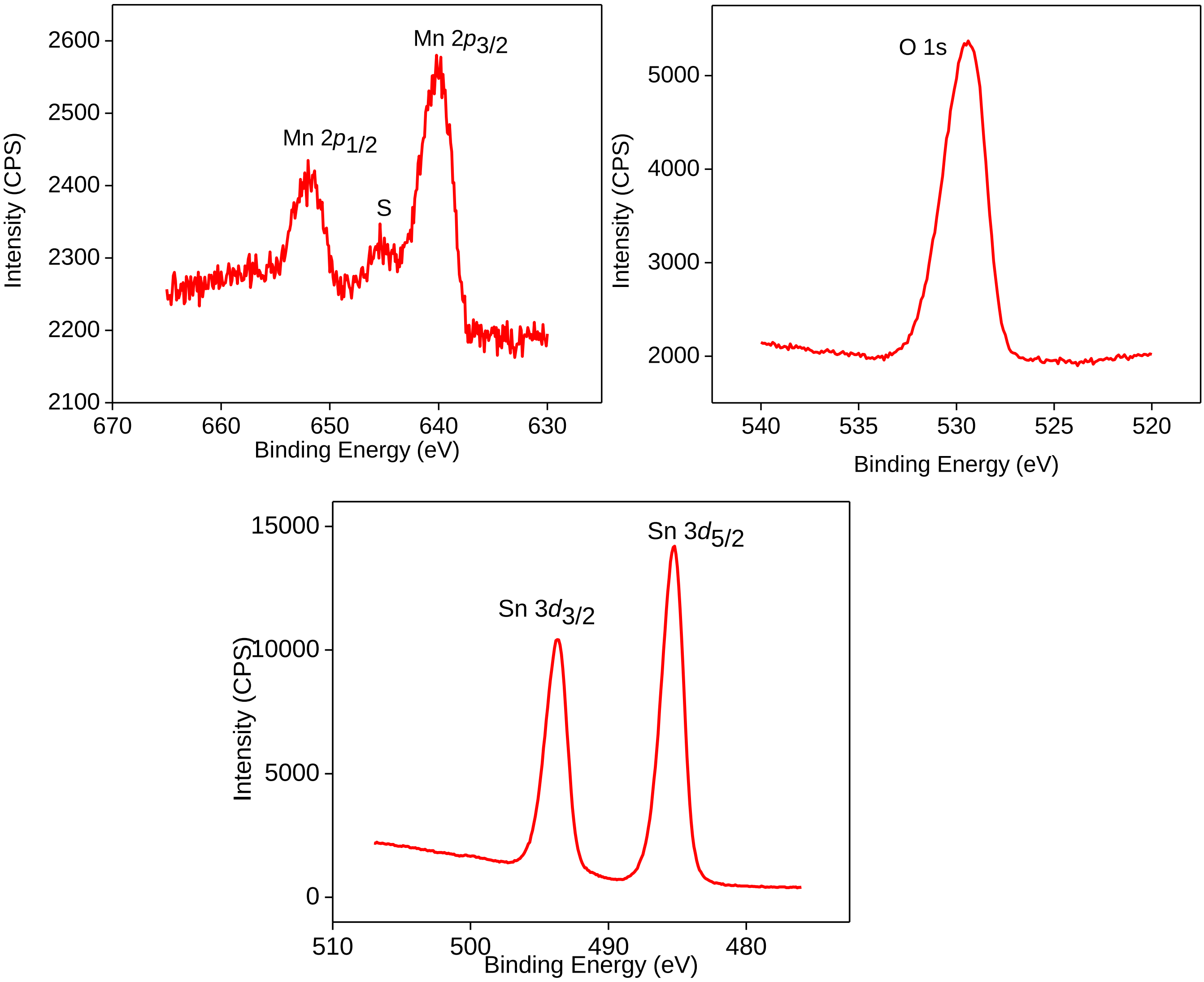

Fig. 2.15. *XPS spectra for 5 wt%-SnO showing bivalent oxidation states for tin and manganese*

The peak corresponding to Mn $2p_{3/2}$ located at 640.4 eV correlates with the MnO state (CAS registry No. 1344-43-0) which was further validated by a satellite peak at 645.4 eV and a Mn $2p_{1/2}$ peak at 652.0 eV. The O 1s peak located at 529.4 eV also pointed towards a +2 oxidation state for manganese. The bivalent state for tin was concurrently established through peaks corresponding to $3d_{5/2}$ at 485.2 eV and $3d_{3/2}$ at 493.6 eV of the spectrum (CAS registry No. 21651194).

2.8. Conclusion

This chapter was dedicated solely for presenting the different protocols adopted for synthesis of tin dioxide. The advantages offered by simple precipitation technique motivated in adopting this particular mode for synthesis of the nanomaterial. However, the phase transition studies revealed that kinetics as well as the applied temperature plays crucial roles in decomposition of the interim precipitate and subsequent formation of SnO_2. This facilitated the synthesis of SnO and SnO_2 phases through simple ageing at room temperature. The alternate approach, though novel, required twelve days for complete transformation of the interim product into different oxide phases. The synthesis period limits the scope for this approach even though the thermal budget could be minimized. Moreover, simple precipitation method produced crystals with dimensions over 50 nm. The crystal size could be reduced to 35 nm through the introduction of sonication during the precipitation reaction. In the next strategic step, an effort was made to produce tin oxide crystals rapidly at room temperature. Thus cationic catalysts in the form of manganese oxide were introduced during the precipitation in presence of sonication. The variation in the catalyst concentration rendered precise control over the production of different tin oxide phases. The summary of the investigations has been presented through a schematic (**Fig. 2.16**). Though incorporation of cationic catalyst empowers synthesis of tin oxide phases at ones discretion, the objective of the present dissertation was to develop SnO_2 based sensors for detection of carbon monoxide and volatiles. The presence of manganese on the surface as verified through XPS analysis might be a deterrent as the composition of the nanomaterial is changed. Therefore the

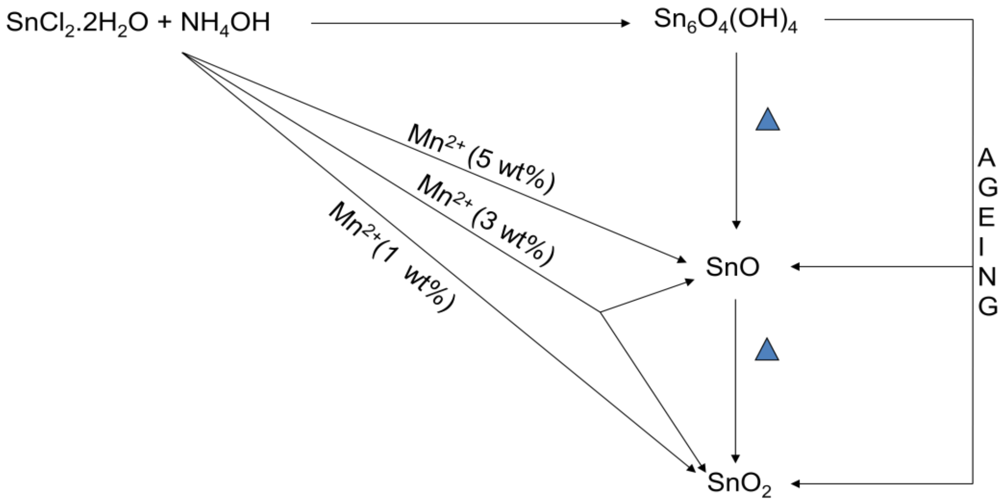

Fig. 2.16. *Schematic representing the protocols investigated for synthesis of tin dioxide*

sonication aided precipitation technique followed by calcination of the interim product has been adopted for the synthesis of SnO_2 nanoparticles in the subsequent chapters.

Reference:

[1] H.N. Lee, B.J. Song, J.C. Park, "Fabrication of p-channel amorphous tin oxide thin-film transistors using a thermal evaporation process", J. Disp. Technol., 10 (2014) 288-292.

[2] P. Zhao, H. Sun, L. Tian, B. Wang, F. Liu, , P. Sun, G. Lu, "Interfacial engineering and configuration design of bilayered photoanode consisting of macroporous tin dioxide/titanium dioxide for high performance dye-sensitized solar cells", Electrochimica Acta., 176 (2015) 845-852.

[3] S. Ghosh, M. Narjinary, A. Sen, R. Bandyopadhyay, S. Roy, "Fast detection of low concentration carbon monoxide using calcium-loaded tin oxide sensors", Sens. Actuators B: Chem., 203 (2014) 490-496.

[4] K. Peters, P. Zeller, G. Stefanic, V. Skoromets, H. Němec, P. Kužel, D. Fattakhova-Rohlfing, "Water-dispersible small monodisperse electrically conducting antimony doped tin oxide nanoparticles", Chem. Mater., 27 (2015) 1090-1099.

[5] K. Saxena, C.S. Bisaria A.K. Saxena, "Synthesis and characterization of some novel silicon esters and their application as lubricant base stock solution", Appl. Organomet. Chem., 23 (2009) 535-540.

[6] F. Mueller, D. Bresser, V.S.K. Chakravadhanula, Stefano Passerini, "Fe-doped SnO_2 nanoparticles as new high capacity anode material for secondary lithium-ion batteries", J. Power Sour., 299 (2015) 398-402.

[7] P.K. Nayak, J.A. Caraveo-Frescas, Z. Wang, M.N. Hedhili Q.X. Wang H.N. Alshareef, "Thin film complementary metal oxide semiconductor (CMOS) device using a single-step deposition of the channel layer", Sci. Rep., 4 (2014) 4672(1-5).

[8] J.H. He, T.H. Wu, C.L. Hsin, K.M. Li, L.J. Chen, Y.L. Chueh, L.J. Chou, Z.L. Wang, "Beaklike SnO_2 nanorods with strong photoluminescent and field-emission properties", Small, 2 (2006) 116-120.

[9] Z. Zhang, R. Zou, G. Song, L. Yu, Z. Chen, J. Hu, "Highly aligned SnO_2 nanorods on graphene sheets for gas sensors", J. Mater. Chem., 21 (2011) 17360-17365.

[10] N. Oka, S. Yamada, T. Yagi, N. Taketoshi, J. Jia, Y. Shigesato, “Thermophysical properties of SnO_2-based transparent conductive films: Effect of dopant species and structure compared with In_2O_3-, ZnO-, and TiO_2-based films”, J. Mater. Res., 29 (2014) 1579-1584.

[11] M.K. Singh, M.C. Mathpal, A. Agarwal, “Optical properties of SnO_2 quantum dots synthesized by laser ablation in liquid”, Chem. Phys. Lett., 536 (2012) 87-91.

[12] J.Q. Hu, Y. Bando, Q.L. Liu, D. Golberg, “Laser-ablation growth and optical properties of wide and long single-crystal SnO_2 ribbons”, Adv. Funct. Mater., 13 (2003) 493-496.

[13] Z. Chen, C.H. Shek, C.M.L.Wu, “Insights from investigations of tin dioxide and its composites: electron-beam irradiation, fractal assessment, and mechanism”, Nanoscale, 7 (2015) 15532-15552.

[14] Q. Wan, E.N. Dattoli, W. Lu, “Transparent metallic Sb-doped SnO_2 nanowires”, Appl. Phys. Lett., 90 (2007) 222107(1-3).

[15] A. Esmaeili-Bafghi-Karimabad, D. Ghanbari, M. Salavati-Niasari, L. Nejati-Moghadam, S. Gholamrezaei, “Photo-catalyst tin dioxide: synthesis and characterization different morphologies of SnO_2 nanostructures and nanocomposites”, J. Mater. Sci.: Mater. Electron., 26 (2015) 6970-6978.

[16] D. Chu, Y.P. Zeng, D. Jiang, Y. Masuda, “In_2O_3–SnO_2 nano-toasts and nanorods: Precipitation preparation, formation mechanism, and gas sensitive properties”, Sens. Actuators B: Chem., 137 (2009) 630-636.

[17] M. Batzill, U. Diebold, “The surface and materials science of tin oxide”, Prog. Surf. Sci., 79 (2005) 47-154.

[18] H. Wang, K. Dou, W.Y. Teoh, Y. Zhan, T.F. Hung, F. Zhang, J. Xu, R. Zhang, A.L. Rogach, “Engineering of facets, band structure, and gas-sensing properties of hierarchical Sn^{2+}-doped SnO_2 nanostructures”, Adv. Funct. Mater., 23 (2013) 4847-4853.

[19] A. Tricoli, M. Righettoni, S.E. Pratsinis, “Minimal cross-sensitivity to humidity during ethanol detection by SnO_2-TiO_2 solid solutions”, Nanotechnology, 20 (2009) 315502(1-10).

[20] E.R. Leite, J.W. Gomes, M.M. Oliveira, E.H. Lee, E. Longo, J.A. Varela, C.A. Paskocimas, T.M. Boschi, F.Lanciotti Jr., P.S. Pizani, P.C. Soares Jr., "Synthesis of SnO_2 nanoribbons by carbothermal reduction process", J. Nanosci. Nanotechnol., 2 (2002) 125-128.

[21] B. Kamp, R. Merkle, R. Lauck, J. Maier, "Chemical diffusion of oxygen in tin dioxide: Effects of dopants and oxygen partial pressure", J. Solid State Chem., 178 (2005) 3027-3039.

[22] Ç. Kılıç, A. Zunger, "Origins of coexistence of conductivity and transparency in SnO_2", Phys. Rev. Lett., 88 (2002) 095501(1-4).

[23] N. Yamazoe, Y. Kurokawa, T. Seiyama, "Effects of additives on semiconductor gas sensors", Sens. Actuators, 4 (1983) 283-289.

[24] C.G. Fink, C.L. Mantell, "Some physico-chemical properties of stannous oxide", J. Phys. Chem., 32 (1928) 103-112.

[25] F. Lawson, "Tin oxide—Sn_3O_4", Nature, 215 (1967) 955-956.

[26] P. Sarker, M.N. Huda, "Understanding the thermodynamic pathways of SnO-to-SnO_x phase transition", Comput. Mater. Sci., 111 (2016) 359-365.

[27] J. Duan, Q. Cao, S. Yang, H. Huang, X. Zhao, R. Zhang, G. Cheng, "Preparation and characterization of rectangular tin dioxide microtubes", J. Cryst. Growth, 289 (2006) 164-167.

[28] S.C. Wang, M.O. Shaikh, "A room temperature H_2 sensor fabricated using high performance Pt-loaded SnO_2 nanoparticles", Sensors, 15 (2015) 14286-14297.

[29] A. Walsh, D.J. Payne, R.G. Egdell, G.W. Watson, "Stereochemistry of post-transition metal oxides: revision of the classical lone pair model", Chem. Soc. Rev., 40 (2011) 4455-4463.

[30] L. Niinistö, M. Nieminen, J. Päiväsaari, J. Niinistö, M. Putkonen, M. Nieminen, "Advanced electronic and optoelectronic materials by Atomic Layer Deposition: An overview with special emphasis on recent progress in processing of high-k dielectrics and other oxide materials", Phys. Status Solidi, 201 (2004) 1443-1452.

[31] J. Heo, A.S. Hock, R.G. Gordon, "Low temperature atomic layer deposition of tin oxide", Chem. Mater., 22 (2010) 4964-4973.

[32] M. Kwoka, N. Waczyńska, P. Kościelniak, M. Sitarz, J. Szuber, "X-ray photoelectron spectroscopy and thermal desorption spectroscopy comparative studies of L-CVD SnO_2 ultra thin films", Thin Solid Films, 520 (2011) 913-917.

[33] M. Kwoka, L. Ottaviano, N. Waczyńska, S. Santucci, J. Szuber, "Influence of Si substrate preparation on surface chemistry and morphology of L-CVD SnO_2 thin films studied by XPS and AFM", Appl. Surf. Sci., 256 (2010) 5771-5775.

[34] J. Suffner, P. Ágoston, J. Kling, H. Hahn, "Chemical vapor synthesis of fluorine-doped SnO_2 (FTO) nanoparticles", J. Nanoparticle Res., 12 (2010) 2579-2588.

[35] S.K. Sinha, S. Ghosh, "Catalyst-free growth of Al-doped SnO2 zigzag-nanobelts for low ppm detection of organic vapours", Physica E, 84 (2016) 434–443.

[36] Y.J. Hsu, S.Y. Lu, "Vapor−Solid growth of Sn nanowires: growth mechanism and superconductivity", J. Phys. Chem. B, 109 (2005) 4398–4403.

[37] M. Lai, J.H. Lim, S. Mubeen, Y. Rheem, A. Mulchandani, M.A. Deshusses, N.V. Myung, "Size-controlled electrochemical synthesis and properties of SnO_2 nanotubes", Nanotechnology, 20 (2009) 185602(1-6).

[38] S.L. Chou, J.Z. Wang, H.K. Liu, S.X. Dou, "SnO_2 meso-scale tubes: One-step, room temperature electrodeposition synthesis and kinetic investigation for lithium storage", Electrochem. Commun., 11 (2009) 242-246.

[39] M. Huebner, D. Koziej, M. Bauer, N. Barsan, K. Kvashnina, M.D. Rossell, U. Weimar, J.D. Grunwaldt, "The structure and behavior of platinum in SnO_2-based sensors under working conditions", Angew. Chem., 50 (2011) 2841-2844.

[40] P.R. Ohodnicki Jr., S. Natesakhawat, J.P. Baltrus, B. Howard, T.D. Brown, "Characterization of optical, chemical, and structural changes upon reduction of sol–gel deposited SnO_2 thin films for optical gas sensing at high temperatures", Thin Solid Films, 520 (2012) 6243-6249.

[41] H. Wang, Q. Liang, W. Wang, Y. An, J. Li, L. Guo, "Preparation of flower-like SnO_2 nanostructures and their applications in gas-sensing and lithium storage", Cryst. Growth Des., 11 (2011) 2942-2947.

[42] L. Xiao, H. Shen, R.V. Hagen, J. Pan, L. Belkoura, Sanjay Mathur, "Microwave assisted fast and facile synthesis of SnO_2 quantum dots and their printing applications", Chem. Commun., 46 (2010) 6509-6511.

[43] Y.T. Yu, P. Dutta, "Synthesis of Au/SnO_2 core–shell structure nanoparticles by a microwave-assisted method and their optical properties", J. Solid State Chem., 184 (2011) 312-316.

[44] J.R. Partington, J.W. Moser, "Red stannous oxide", Nature, 154 (1944) 643-643.

[45] A. Sharma, D. Prakash, K.D.Verma, "Optical characterization of hydrothermally grown SnO_2 nanocrystals", J. Optoelectron. Adv. Mater., 11 (2009) 331-337.

[46] C.A. Ibarguen, A. Mosquera, R. Parra, M.S. Castro, J.E. Rodríguez-Páez, "Synthesis of SnO_2 nanoparticles through the controlled precipitation route", Mater. Chem. Phys., 101 (2007) 433-440.

[47] J. Ning, Q. Dai, T. Jiang, K. Men, D. Liu, N. Xiao, C. Li, D. Li, B. Liu, B. Zou, G. Zou, W.W. Yu, "Facile synthesis of tin oxide nanoflowers: a potential high-capacity lithium-ion-storage material", Langmuir, 25 (2009) 1818-1821.

[48] M.S. Moreno, G. Punte, G. Rigotti, R.C. Mercader, A.D. Weisz, M.A. Blesa, "Kinetic study of the disproportionation of tin monoxide", Solid State Ion., 144 (2001) 81-86.

[49] G. Saito, S. Hosokai, M. Tsubota, T. Akiyama, "Influence of solution temperature and surfactants on morphologies of tin oxide produced using a solution plasma technique", Cryst. Growth Des., 12 (2012) 2455-2459.

[50] D.N. Srivastava, S. Chappel, O. Palchik, A. Zaban, A. Gedanken, "Sonochemical synthesis of mesoporous tin oxide", Langmuir, 18 (2002) 4160-4164.

[51] H. Uchiyama, H. Imai, "Tin oxide meshes consisting of nanoribbons prepared through an intermediate phase in an aqueous solution", Cryst. Growth Des., 7 (2007) 841-843.

[52] H. Uchiyama, H. Ohgi, H. Imai, "Selective preparation of SnO_2 and SnO crystals with controlled morphologies in an aqueous solution system", Cryst. Growth Des., 6 (2006) 2186-2190.

[53] C.S. Moon, H.R. Kim, G. Auchterlonie, J. Drennan, J.H. Lee, "Highly sensitive and fast responding CO sensor using SnO_2 nanosheets", Sens. Actuators B: Chem., 131 (2008) 556-564.

[54] C. Wang, L. Yin, L. Zhang, D. Xiang, R. Gao, “Metal oxide gas sensors: sensitivity and influencing factors”, Sensors, 10(2010) 2088-2106.

[55] K.S.Suslick, “Sonochemistry”, Science, 247 (1990) 1439-1445.

[56] J.A. Caraveo-Frescas, H.N. Alshareef, “Transparent p-type SnO nanowires with unprecedented hole mobility among oxide semiconductors”, Appl. Phys. Lett., 103 (2013) 222103(1-5).

[57] T. Wang, Z. Peng, Y. Wang, J. Tang, G. Zheng, “MnO nanoparticle@mesoporous carbon composites grown on conducting substrates featuring high-performance lithium-ion battery, supercapacitor and sensor”, Sci. Rep., 3 (2013) 2693(1-9).

Chapter 3

Grain growth inhibition of SnO_2 by Group II elements for fast detection of carbon monoxide

This chapter elucidates the development of tin dioxide based sensors for carbon monoxide sensing. Performance of tin dioxide as a sensing material is often augmented through introduction of noble metal catalysts which adds to the final cost of individual units. In the present work, an alternate group of cost-effective additives, affliated to the group II of periodic table have been used as performance enhancing agents for tin dioxide. These additives induce a phenomenon known as the grain growth inhibition during the sintering process which impedes formation of larger crystals. The additives have been shown to reside at the grain boundaries in their oxide form through sophisticated microscopic analysis. The resultant crystals are smaller in dimension as compared to the pristine tin dioxide particles produced barring the grain growth inhibitors. The chapter then highlights the dynamic carbon monoxide sensing characterisation performed with the grain growth inhibited crystals. The developed sensors are observed to have excellent sensitivity along with fast response and recovery times.

List of Sections

Contents of this chapter are partially based on following publication

S. Ghosh, M. Narjinary, A. Sen, R. Bandyopadhyay, S. Roy, "Fast detection of low concentration carbon monoxide using calcium-loaded tin oxide sensors", Sensors and Actuators B: Chemical, vol. 203 (2014) pp. 490-496.

3.1. Introduction

Chapter 2 of this dissertation was dedicated for discussing the optimized protocol for synthesizing tin dioxide. Among the different methods, sonication aided synthesis followed by calcination of the precipitate produced phase pure tin dioxide with about 35 nm size distribution. Additionally, simultaneous introduction of cationic catalyst (Mn^{2+}) in presence of sonication facilitated precise control over production of stannous or stannic oxide at room temperature. Though the scholastic information acquired was novel, yet it deviated from an original mandate of fabricating quality sensors for carbon monoxide. But the crux of the information gathered was instrumental in conceiving the subsequent research work. Sensors fabricated with smaller particles have been reported to demonstrate considerable increase in their response pattern [1,2]. Thus smaller particles with dimension close to the Debye length enhances the prospect for detection of low concentration of gases like CO and methane that can penetrate into the bulk and react with chemisorbed oxygen on the inner grain boundaries [3]. Moreover, selectivity of the MOS sensors is improved through catalytic oxidation of the target analyte, effected by presence of a catalyst at the grain boundaries or on the surface [4,5]. Alternately, doping the SnO_2 lattices with either donor or acceptor elements that modify the overall electronic configuration to favour the sensing of CO is another frequently adopted approach by researchers [6]. Thus an entity, which can simultaneously induce size reduction of the tin dioxide crystals and promote catalytic oxidation of carbon monoxide on the sensor surface, is perceived to be effective in fabricating a state of art CO sensor. As stated through the review of existing literature in Chapter 1, researchers have mostly utilized noble metals as catalysts on the SnO_2 matrix. These metals activate the sensor surface either through chemical or electronic sensitization by their presence. In rare instances, the metal particles can also drift to the lattice and introduce oxygen vacancies through possible doping and substitution of the host cation. In this respect, gold [7], iridium [8], platinum [9] and palladium [4] have been extensively used for sensitizing SnO_2 based sensors for CO detection.

However, incorporation of noble metals often increases the preconditioning time and introduces a drift in baseline properties of the sensors. In addition to the use of expensive precursors, the complexity associated with these methods resulted in advent of another technique where small crystals of SnO_2 with large specific surface area are produced by grain growth inhibition [10]. Though grain growth inhibition can be attained in multiple ways, most common method involves impeded growth of SnO_2 crystals by deliberate loading of certain elements, which prevents the characteristic neck formation during the sintering stage.

The prospect of using these relatively smaller particles as sensor materials has generated considerable interest among researchers [11]. In a recent study, Illyaskutty and his colleagues explored the tin dioxide crystals, grain growth inhibited by combinations of oxides of copper, lanthanum and antimony as prospective materials for carbon monoxide sensing. However, the concentration of carbon monoxide detected by these sensor modules was much higher than the permissible limits [12].

In the present chapter, various group II elements (namely, calcium, barium, strontium and magnesium) were loaded onto the tin dioxide matrix and the resulting materials were investigated for their response towards carbon monoxide. In their oxide forms, the elements have been reported to reside on the grain boundaries, causing a limiting effect on the grain growth, and impeding the characteristic neck formation of tin oxide crystals during the sintering process. Moreover, a few of the group II oxides (calcium and magnesium) are known to promote catalytic oxidation of carbon monoxide [13]. Thus if the tin dioxide matrix could be loaded with these entities while *in-situ* synthesis, a standard carbon monoxide sensor could be fabricated. A secondary reason for investigating these materials as additives is the lucrative prospect of devising a cost-effective sensor module. Normally, tin oxide crystals are laced with noble metal catalysts, which augment the price of the final sensor module. However, the group II oxides are devised from economic precursors and introduction of them doesn't add up to the final cost significantly.

3.2. Group II elements as grain growth inhibitors

Grain growth inhibition is a simple yet effective technique often adopted in the field of material science to produce crystals of small dimensions. Grain growth is an intrinsic phenomenon that occurs post nucleation and is promoted through applied thermal impetus in ceramics. Materials researcher had long derived the basic driving force for grain growth and formulated the relevant kinetics. They identified reasons for the growth at different sintering zones and also protocols for limiting it. While boundary mobility was utilised as limiting parameter at lower annealing temperatures and in nonporous materials, porosity control governed the same for higher annealing temperatures. But it was perhaps the pioneering study by Yamazoe [14], establishing the direct correlation between decreasing particle size and increasing sensor response, which inculcated real interest in limiting the grain growth for gas sensing materials. While the influence of grain size on sensing response has been extensively studied by scientists thereafter [15], most have opted for varying the sintering time and temperature in order to produce a grain size distribution. However, grain growth inhibition with dopants for certain refractories has been investigated, whose mechanical properties would otherwise diminish upon sintering at high temperatures due to unrestricted growth. Though grain growth inhibition can be attained in multiple ways, most common method involves impeded growth of the nucleated crystals by strategic loading of certain elements, which prevents the characteristic neck formation during the sintering stage.

The inception of Grain boundary "pinning" for tin dioxide crystals with secondary materials was presented by Wu *et al.* [16], where silica was used for the purpose. They demonstrated that the "pinned" nanoparticles had considerably smaller size (~ 2 nm) and large surface area. The group also showed considerable improvement in carbon monoxide (500 ppm) sensor performance for the small particles. Several metal oxides have since then been investigated as potential grain growth inhibitors for the tin dioxide crystals. For example, varying concentrations of scandia were observed to have a discernable effect on grain growth inhibition of tin oxide crystals [17]. When calcined at 800 ^{o}C, a retarded grain distribution with a maximum size of 11 nm could be achieved through loading of scandia in tin dioxide, while the pristine SnO_2 crystals grew upto 30 nm. Additionally, introduction of scandia enhanced the sensitivity towards carbon monoxide, albeit in a concentration range much higher (1000 ppm) than permitted by OSHA (9 ppm). In comparison, nanoparticles of further reduced dimension of 8 nm could be produced by loading tin dioxide matrix with Nb_2O_5, and the resultant composite showed excellent response towards ethanol vapours [18]. Often the metal oxide loaded SnO_2 composites are further sensitized by sprinkling noble metal catalysts on the surface. For example, an SnO_2-In_2O_3 composite with a cationic ratio of 3 (Sn/In ~ 3) and particle size as low as 6 nm, was laced with Au and Pd nanoparticles. This was observed to have a profound effect on the CO sensitivity at a concentration level of 500 ppm. Apart from the inhibitory effect, any alteration even in the nanoscopic range in the neck region enhances the response significantly as the the neck dimensions are commensurate with the space-charge thickness of SnO_2

Despite the considerable reduction in grain size and effective increase in specific surface area, all the aforementioned composites detected carbon monoxide at a higher concentration level compared to the permissible limit as elucidated in chapter 1. This prompted the idea of identifying a suitable secondary metal oxide that might catalyse carbon monoxide oxidation on sensor surface, in addition to grain boundary pinning. In this respect, a notable work from Min and Choi had shown the inhibitory effect of calcium oxide (CaO) on SnO_2 crystals [19]. They had ascribed the restricted surface diffusion and sublimation of SnO_2 due to the presence of surface dwelling calcium oxide, for the reduced crystal size. Similarly, MgO is another group II metal oxide which has been reported to impose inhibitory effects on crystal growth of SnO_2 particles [20]. Coupled with the fact that these two group II metal oxides have catalytic effects on the oxidation of CO [13,21], they pose as potent candidates as additives in the SnO_2 matrix for carbon monoxide sensing.

In this study, magnesium, calcium, strontium and barium were exclusively loaded in their oxide form onto SnO_2 crystals and the grain growth inhibitory effects for these elements were studied. While magnesia and calcia are established growth inhibitors in the field of ceramics, discerning roles of strontium [22] in controlling the growth kinetics among SnO_2 crystals have recently been projected. However, the role of barium still remains fuzzy as it has often been referred to either promote [23] or impede [24] grain growth in different chemical forms. The growth limited crystals were characterised for their structural and electrical attributes and were then used to device sensors for detecting carbon monoxide in sub-TLV concentration.

3.3. Synthesis procedure for grain growth inhibition technique

Tin dioxide loaded with either of the Group II elements was synthesized by ultrasonication assisted co-precipitation method as explained in chapter 2. The sonochemical route for synthesis induces a unique microenvironment through liquid bubble implosion producing acoustic cavitations for nanomaterials to nucleate and grow [25]. The basic steps for the synthesis procedure have already been delineated in chapter 2. In order to introduce the additives into the system, 10 mL solutions of nitrates of the group II elements (calcium nitrate (Sigma Aldrich, puriss. p.a., ACS reagent, 99-103%), barium nitrate (Sigma Aldrich, ACS reagent, ≥99%), magnesium nitrate (Sigma Aldrich, puriss. p.a., ACS reagent, 98.0-102.0%) and strontium nitrate (Sigma Aldrich, puriss. p.a., ACS reagent, ≥99.0%) were procured and used without any further purification) were prepared according to the weight percent of the additives (1, 5 and 10 wt%) to be loaded in the SnO_2 matrix. The two precursor solutions containing the stannous chloride and soluble nitrates of the additives were mixed and ammonium hydroxide was added drop wise under sonication till a pH value between 9 and10 was achieved. The sonochemical synthesis was carried out by an ultrasonic processor (Sonics, Vibra-Cell, VCF 1500) for one hour, with an intermittent cooling period of 5 minutes after every 15 minutes of sonication. The power induced into the reaction was estimated to be close to 600 W. The precipitate was centrifuged, washed multiple times with deionized water for removal of trace chlorine and dried at 70 ^{o}C for 12 h in an oven. The dried sample was calcined at 850 ^{o}C for 1 h to enhance crystallinity and to obtain phase-pure SnO_2.

Standard structural and electronic characterization necessary for profiling the individual products were performed on the instruments mentioned in chapter 2. The nitrogen adsorption and desorption isotherms at 77 K were measured using a NOVA® Surface Area Analyzer system. The samples were outgassed at 300 °C for 2h in vacuum. The data analysis was performed using Quantachrome NOVAWin software version 10.01.

The calcined tin oxide based powders were used to fabricate sensor modules. A thick paste of pristine or loaded SnO_2 powder was prepared by mixing it with isopropyl alcohol (Merck). Around 50 μm thick layers were coated on hollow tubular alumina substrates and cured at 600 ^oC for 1 hour. The operating temperature of the sensors was varied by changing the current driven through the Ni-Cr wire inserted in the hollow alumina tube. A series of mass flow controllers were deployed for dispensing a desired concentration of the respective target gases diluted in a carrier gas. The sensor under test was exposed to the target gas at 1 atmospheric pressure and at a flow rate of 50 sccm. The change in resistance of the active metal oxide layer in presence of gas was measured using an Agilent B2901A source-meter and was recorded using a LabView-based graphical user interface (GUI).

3.4. Morphological and compositional analysis

Incorporation of group II elements in the tin dioxide matrix might have dual possibilities depending on the sonication time, calcinations temperature and solid solubility of the additive. Each of the additives and their morphological effects on the overall compositions is considered in the following sections.

3.4.1. Calcium-added SnO_2

When calcium is used as an additive in tin oxide, the calcium ions may occupy the substitutional sites in the SnO_2 matrix or get segregated at the grain boundaries as CaO phase. A considerably larger ionic radius of Ca^{2+} (1.14 Å) compared to that of Sn^{4+} (0.83 Å) suggests a nominal substitution of Ca^{2+} ions in the SnO_2 matrix [19]. It is possible that beyond the solubility limit, calcium is dispersed on the surface of the SnO_2 crystals as free calcium oxide. The XRD plots for the pure and 5 wt% Ca-loaded SnO_2 powders are shown in **Fig. 3.1**. The observed peak positions were matched with the reference (JCPDS part no. 041-1445) and were correlated with different crystal planes of SnO_2 (**Fig. 3.1(a)**). The absence of any peak corresponding to CaO may be attributed to its low abundance, which was beyond the detection limit of X-ray. The broadening of peaks is presumably due to grain boundary pinning by CaO, leading to grain growth inhibition of SnO_2 particles during calcination and consequent retention of fine-grained structure [26]. In addition, a closer look into the XRD spectra reveals a distinct shift in the peak positions for the samples (5 wt%) where Ca^{2+} replaced Sn^{4+} in the lattice, with respect to pristine SnO_2 (**Fig. 3.1(b)**). The peak shifts can be attributed to the distortion/stress introduced into the lattice due to presence of relatively large Ca^{2+} ions in the substitutional sites. The direction of the shifts, which depend on the relative size of the host and substitutuing ions are in accordance to earlier reports [27,28]. Using the

Scherrer formula, the average crystallite size of Ca-SnO_2 nanoparticles (calcined) was estimated to be about 23 nm.

The growth inhibition property of calcium oxide for SnO_2 nanoparticles was also evident in the TEM studies. **Fig. 3.2(a)-(b)** represent the images of pristine and calcium added SnO_2 after calcination at 850 °C respectively, while the HRTEM image showing the presence of CaO in the grain boundaries of SnO_2 nanoparticles have been shown in **Fig. 3.2(c)-(d)**. While the pure form of SnO_2 samples composed of particles even greater than 50 nm, the TEM on Ca-loaded samples showed particles of smaller size (20–25 nm). The energy dispersive X-Ray analysis (EDAX) spectrum for Ca-SnO_2 nanoparicles corroborates the presence of calcium in the system as shown in **Fig. 3.2(e)**. A smaller particle size implies higher surface to volume ratio, which is favourable for gas sensor applications. An estimation of the specific surface area was obtained by BET (Brunauer–Emmett–Teller) method. Analysis of the isotherms for the SnO_2 nanoparticles yielded an average BET surface area of 5.0 m^2/g, while that for the 5 wt% and 10 wt% Ca-loaded samples was calculated to be 7.3 m^2/g and 19.9 m^2/g, respectively.

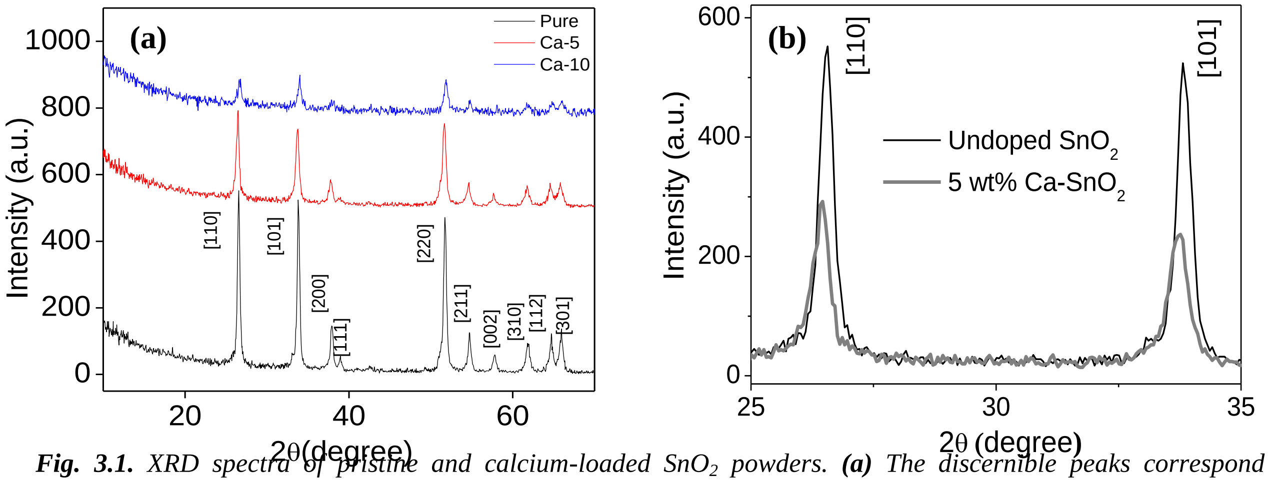

Fig. 3.1. XRD spectra of pristine and calcium-loaded SnO_2 powders. (a) The discernible peaks correspond to different crystal planes of SnO_2 without showing any pronounced peak for calcium related phases. (b) Peak shifts between pure and calcium loaded samples, indicating lattice distortion due to substitution of Sn^{4+} by Ca^{2+} ions.

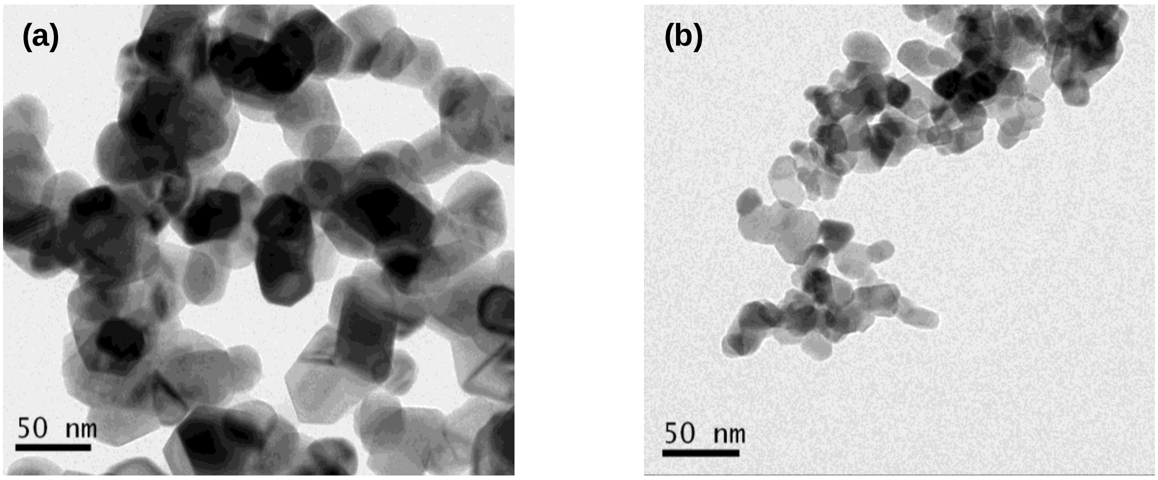

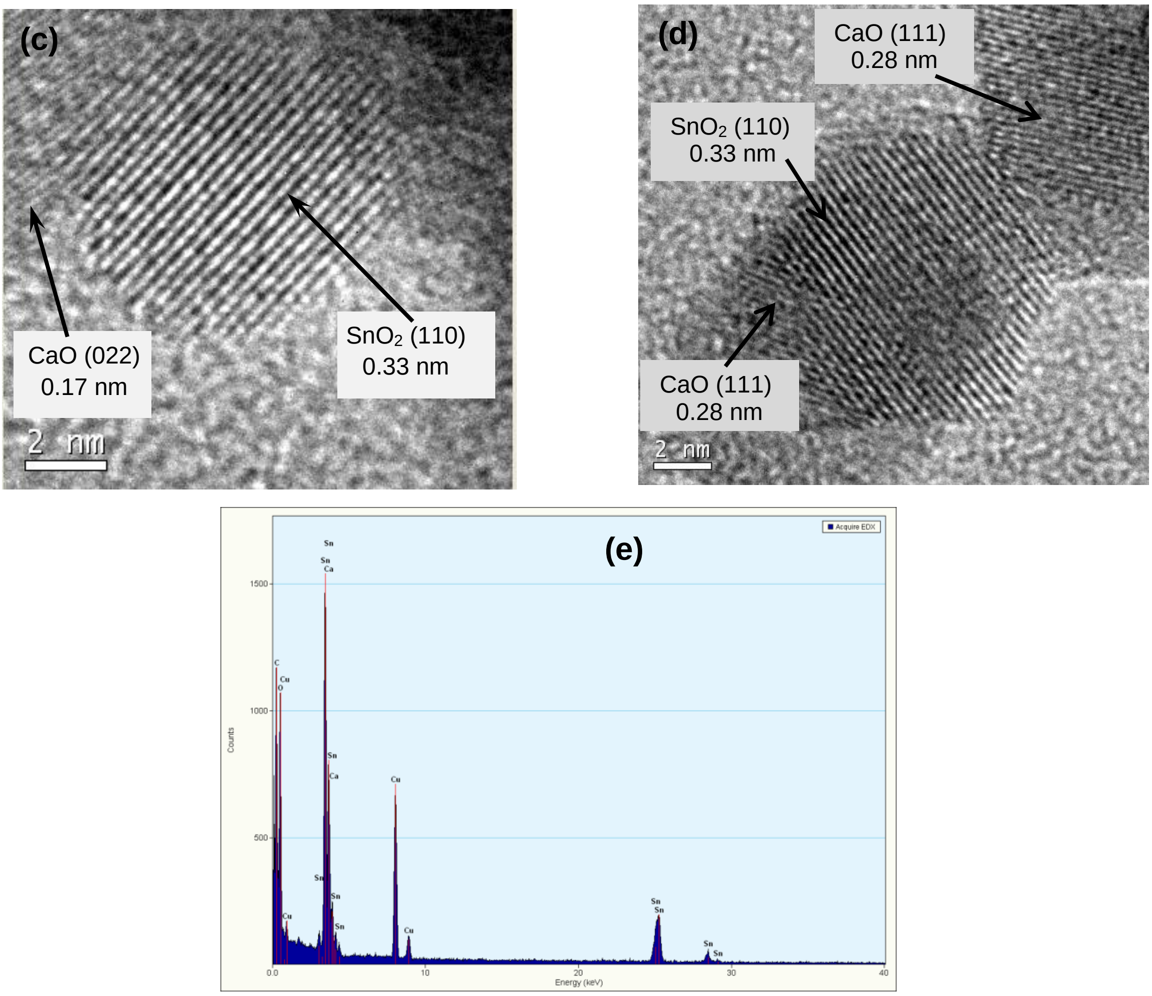

Fig. 3.2. *TEM images of* ***(a)*** *pure and* ***(b)*** *5 wt% Ca-loaded SnO_2 powders after calcination at 850 ^{o}C. The role of calcium as a grain growth inhibitor is evident.* ***(c)*** *and* ***(d)*** *present HRTEM images of SnO_2 particles, where the presence of CaO is shown at the grain boundaries and on the surface of SnO_2, respectively.****(e)*** *EDX spectrum for Ca-SnO_2 nanoparticle showing the presence of calcium*

In addition to a high specific surface area, oxygen vacancy is another factor that governs the response properties of gas sensors. The presence of oxygen vacancies in Ca-doped SnO_2 matrix was apparent in photoluminescence (PL) studies. The PL spectra were recorded for undoped and Ca-doped SnO_2 samples with an excitation wavelength of 300 nm (**Fig. 3.3**). A dominant peak at around 390 nm (3.2 eV) was observed for all the samples which are in agreement with previous reports [29]. The emission spectra showed two other broad peaks at around 570 nm (2.2 eV) and 590 nm (2.1 eV), respectively. Since the energy corresponding to the PL peaks are much lower than the bandgap energy of SnO_2 (3.6 eV), the visible emissions cannot be correlated to the direct recombination of the conduction band electrons with the valence band holes. Hence, the observed emissions at longer wavelengths may be associated with defect energy levels, present within the band gap of SnO_2 [30]. Oxygen vacancies are known to be the most common defects in oxides and usually act as radiative centres in the luminescence process. In oxide semiconductors, oxygen vacancies can be present in three different charge states, neutral ($V_O^{\times}$), monovalent positively charged ($V_O^{\bullet}$) or divalent positively charged ($V_O^{\bullet\bullet}$), with respect to the normal $O^{2\square}$ state. The energy level of the neutral oxygen vacancy is close to the conduction band edge due to correlation energy of two electrons [31]. Hence the emission of photons with an energy 3.2 eV (390 nm) is likely to be associated with the presence of $V_O^{\times}$ in SnO_2 matrix, which may be converted to ionized vacancies [32,33]. The other two broad peaks might have appeared due to charged oxygen vacancies $V_O^{\bullet}$ and $V_O^{\bullet\bullet}$, respectively, whose energy levels are located deep in the band gap

The nature of emissions as a function of calcium doping in SnO_2 was studied. It was found that with the increase in calcium concentration, the intensity of the primary peak changed marginally, while the two broader peaks at higher wavelengths became more pronounced. In fact, as a Ca^{2+} is substituted for a Sn^{4+}, an oxygen ion site is left vacant to maintain the cation-anion site relationship of 1:2. Using Kröger-Vink notation, this can be presented as –

$$\mathrm{CaO}(s) \xrightarrow{\mathrm{SnO_2}} \mathrm{Ca_{Sn}}'' + \mathrm{O}^{x} + V_O^{\bullet\bullet} \tag{3.1}$$

Thus, within the solubility limit, calcium doping increased charged oxygen vacancies in the SnO_2 matrix, which was manifested in the PL spectra.

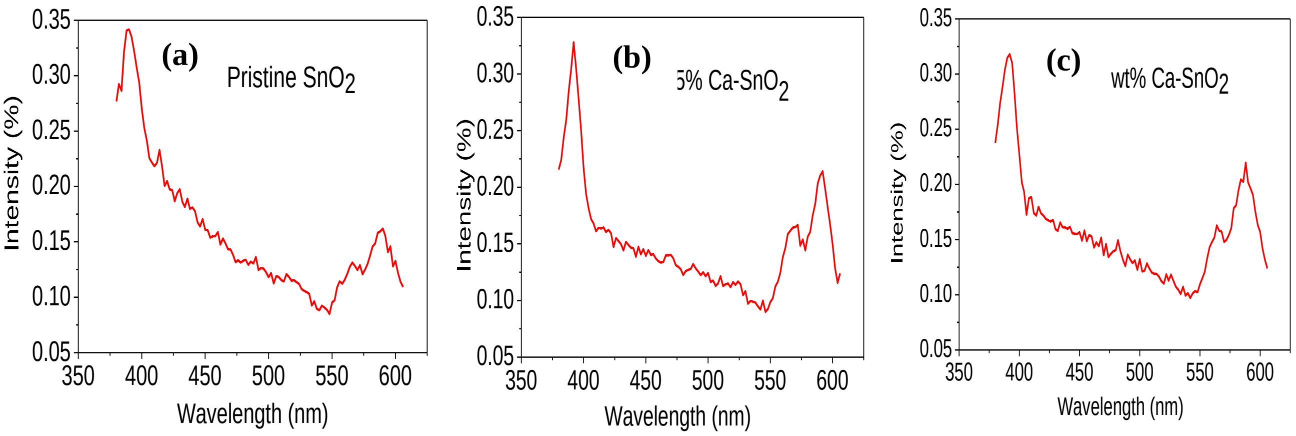

Fig. 3.3. Photoluminiscence spectra of ***(a)*** *pure,* ***(b)*** *5 wt% and* ***(c)*** *and 10 wt% Ca-loaded SnO_2 nanopartciles, respectively. The excitation wavelength is 300 nm. The emission peaks appearing at wavelengths much higher than that corresponds to SnO_2 band gap and hence correlated with the defect states, primarily oxygen vacancies.*

Additionally, Fourier Transform Infrared spectroscopy (FTIR) was performed on the Ca-loaded SnO_2 to envisage the molecular signature of the bond structures and has been highlighted in **Fig. 3.4**. The metallic bonds always occur within 400-800 cm^{-1} and are visible in the infrared spectrum for the synthesized 5 wt% Ca-SnO_2 [34]. The band with an absorption peak centred at 616 cm^{-1} might be attributed to the Sn-O stretching mode, while the small undulation at 420 cm^{-1} can be ascribed to the metallic Ca-O bond of calcia. This peak is relatively low in intensity primarily due to the low abundance of calcia in the SnO_2 matrix. The absence of any distinct peak at 1620 cm^{-1} might be attributed to the complete loss of water of coordination from the composite. This was expected as the system was heat treated to 850 °C and the water of coordination is lost beyond 500 °C as observed from Chapter 2. Similarly the peak at 3443 cm^{-1} corresponding to O-H bending is suppressed in the heat treated ceramic sample.

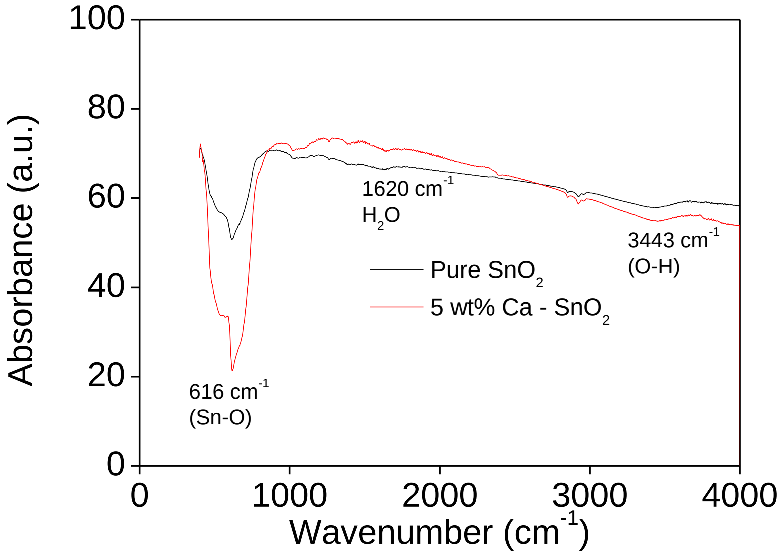

Fig. 3.4. *FTIR spectra for 5 wt% Ca-SnO_2 plotted against the spectra for pristine SnO_2*

3.4.2. Magnesium-added SnO_2

The X-Ray Plots for SnO_2 crystals with 5 wt% and 10 wt% magnesium loadings of different additives are shown in **Fig. 3.5(a)**, while **Fig. 3.5(b)** illustrates the peak shift observed for the 5 wt% loaded particles. As observed for calcium loadings, the spectra does not reflect any phases corresponding to MgO or any other tin oxide form other than the rutile tetragonal phase of SnO_2 crystals [JCPDS part no. 041-1445]. No phase corresponding to either elemental or oxide form of the additives was observed, perhaps due to the low amount of magnesium incorporated. However, closer inspection reveals distinct shifts in X-Ray profile for the loaded materials, from the peaks corresponding to pristine SnO_2.

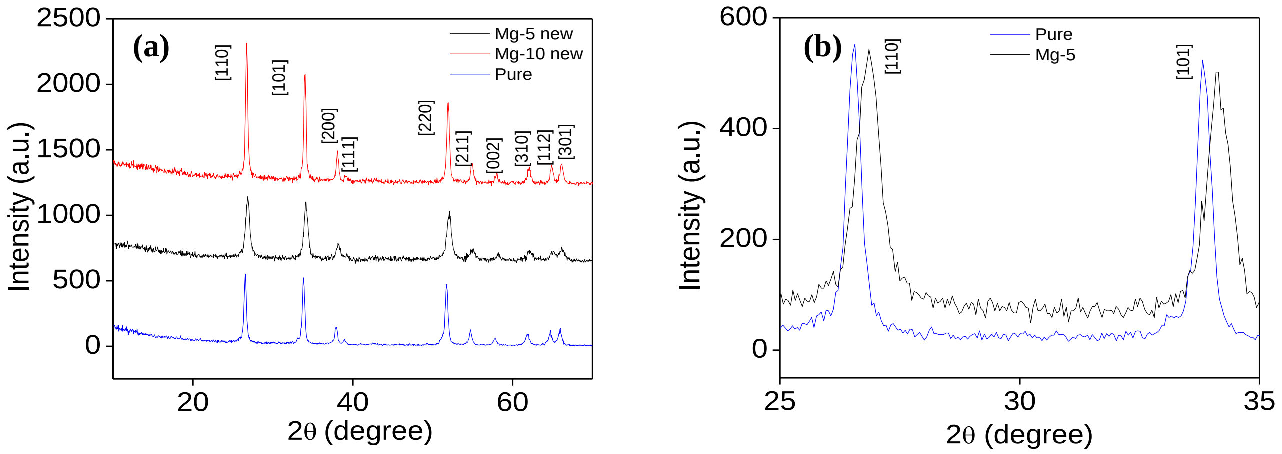

Fig. 3.5. XRD spectra of pristine and magnesim-loaded SnO$_2$ powders. ***(a)*** *The discernible peaks correspond to different crystal planes of SnO$_2$. Magnesium loading caused a broadening of peaks signifying production of smaller crystals.* ***(b)*** *A closer look reveals peak shifts between pure and magnesium loaded samples*

Peak shifts are clear indications of possible doping through ionic substitution leading to deformation of crystal lattice, where direction of the shift is dependent on the ratio between ionic radii of the dopant and Sn^{4+} [35]. Similar shifts in peaks for calcium loaded SnO$_2$ crystals owing to slight solid solubility of calcium in tin dioxide were found. In addition, the peak broadenings can be function of strains generated by variation in crystallite size [36] and defects in the system [37] and thus the possibility of doping shall be corroborated through photoluminescence spectrum analysis. Magnesium loaded nanoparticles have broad peaks of diminished intensity, implying a decrease of particle size for these materials.

Bright Field (BF) TEM images of varying magnification (**Fig. 3.6(a-b)**) for 5 wt % magesium loaded crystals corroborates the perception of grain growth inhibition as the crystals loaded with Mg are relatively smaller and are mostly distributed under 20 nm. This suggests that tin dioxide crystals, which in their pristine form grow to approximately 35 nm upon calcination (**Fig. 3.2(a)**), have indeed been size restricted. Similar inhibitory effects from calcium loading in the previous section which restricted the crystal growth below 25 nm were presented.

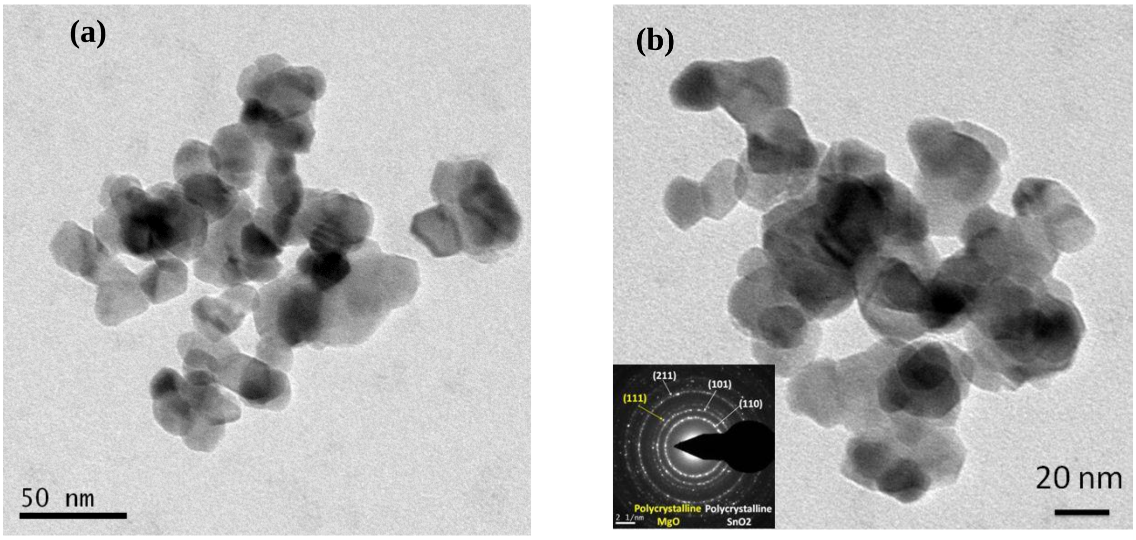

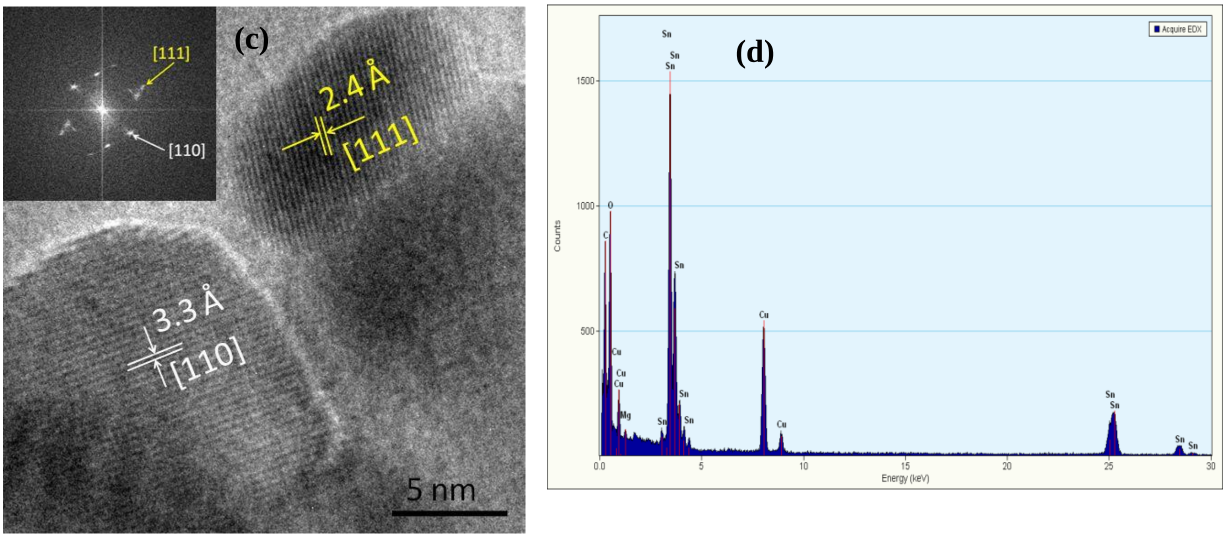

*Fig. 3.6(a). Bright Field TEM Images for the grain growth limited 5 wt% Mg-SnO$_2$ particles **(b)** Higher magnification images showing particle size within 20 nm **(c)** Presence of MgO particles ([111] lattice plane) adjacent to the grain boundaries of SnO$_2$ crystals and **(d)** EDAX spectrum showing the presence of magnesium.*

The magnesium loaded crystals with lower particle size offer higher surface coverage and are expected to yield better response towards carbon monoxide. However, though the BF-TEM images portray the diminished size of synthesized crystals, it still requires corroborating data to establish the grain growth inhibition originating from the additives. High Resolution TEM (HRTEM) and Selected Area Diffraction (SAED) studies are thus performed in tandem with bright field analysis at greater magnification to confirm presence of inhibiting additives on the periphery of SnO$_2$ crystals. The HRTEM analysis performed on magnesia loaded SnO$_2$ particles revealed the [111] plane corresponding to MgO with lattice fringes spaced at 0.24 nm [38] and is shown in **Fig 3.6(c)**. This is further validated by the SAED analysis depicted in the inset of the higher magnification bright field image (**Fig 3.6(b)**) and the Fast Fourier Transform (FFT) function performed on the high resolution microscopic images, which simultaneously confirms the [111] plane of MgO in cohesion with the planes relevant to tin dioxide.

Once the effect of the magnesium loading on SnO$_2$ grain inhibition is established, their influence in profiling the defect states in the base crystal is examined by photoluminescence studies. The plot comprising PL spectrum for 5 wt% of magnesium loaded SnO$_2$ crystals is shown in **Fig 3.7**. The spectrum is characterised by one broad peak at around 370 nm (3.35 eV) in association with two sharp peaks at 422 nm (2.93 eV) and 485 nm (2.55 eV). Since bulk SnO$_2$ is characterised by a band gap of 3.6 eV, therefore, the broad peak around 370 nm cannot arise from direct recombination of free electrons in the Sn 4p conduction band to holes in the O 2s valence band. Moreover, a restricted particle size can only result in expansion of the band gap beyond 3.6 eV due to quantum confinement effect, thus mitigating the scope for radiative recombination of electron hole pairs through Near Band Edge (NBE) transitions. The band gap expansion due to quantum confinement is generally manifested by a blue shift in UV-visible spectrum [39].

Therefore, the broad peak centred at 364 nm is ascribed to the synergistic contributions from radiative recombination of surface localised free excitons and transition of the excitons to neutral oxygen vacancy levels (V_o^0) [40]. Since the V_o^0 is a very shallow donor, it is likely to exist as its singly charged counterpart (V_o^+) at room temperature. Therefore the major contribution in formation of the broad band centred at 364 nm can be ascribed to the activities of the free surface excitons. The shoulder peaks appearing at higher wavelengths are results of luminescence centres generated by tin interstitials (Sn_i) (422 nm) and presence of charged oxygen vacancies [41]. The broadness of the peak located at 485 nm is another evidence of grain inhibition as this is often observed for SnO_2 quantum dots [42,43]. However, a relatively lower amplitude of photoinduced luminescence at higher wavelengths suggest that contributions from surface defects are more pronounced rather than the oxygen vacancies.

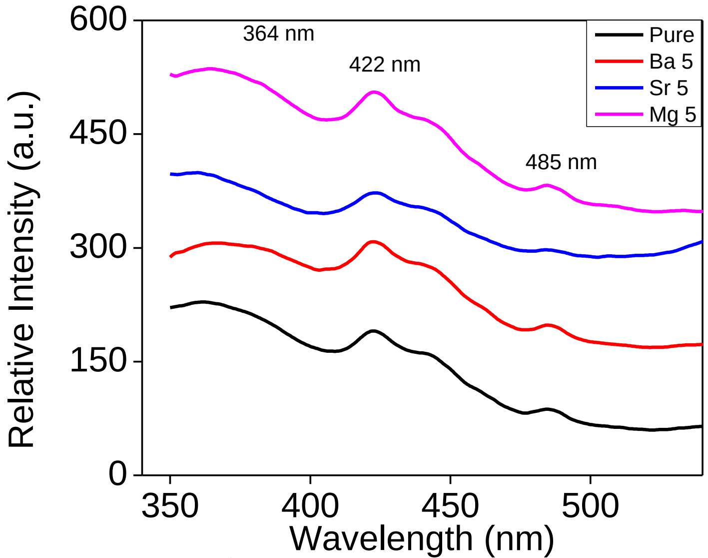

Fig. 3.7. *Photoluminescence spectra for the 5 wt% magnesium, barium and strontium loaded SnO_2 nanocrystalsin comparison with the pure tin dioxide.*

Combining the information gathered from structural and optical characterization for the magnesium loaded SnO_2 crystals, it can be inferred that similar to calcium, the additive does replace some of the host tin cations from their position in the lattice. The Kröger-Vink representation for doping is valid for magnesium ions as well and can be represented as

$$MgO(s) \xrightarrow{SnO_2} Mg_{Sn}'' + O^x + V_O^{\bullet\bullet} \tag{4.2}$$

The grain growth inhibition along with the doping of the lattice brings about a discernable effect on sensing phenomenon as shall be seen subsequently.

3.4.3. Strontium-added SnO_2

The x-ray spectrum for strontium loaded SnO_2 crystals depicted in **Fig. 3.8(a)** show similar features alike the Mg and Ca loaded spectra as all peaks conform to the rutile tetragonal phase of tin dioxide [JCPDS part no. 041-1445]. Absence of any phases corresponding to SrO may be ascribed to the nominal amount of the additive introduced. However, the characteristic peak shifts visible for the previous specimens are also present for strontium loaded crystals. This observation points towards a tendency of group II elements to dope the crystal lattice of tin dioxide. Though the shift in peak for the strontium loaded crystals is maximum (**Fig. 3.8(b)**), signifying a greater magnitude of lattice distortion, yet the Full Width Half Maximum (FWHM) value is smaller compared to magnesium loaded counterpart. This hints at a possible larger crystals compared to Mg-SnO_2.

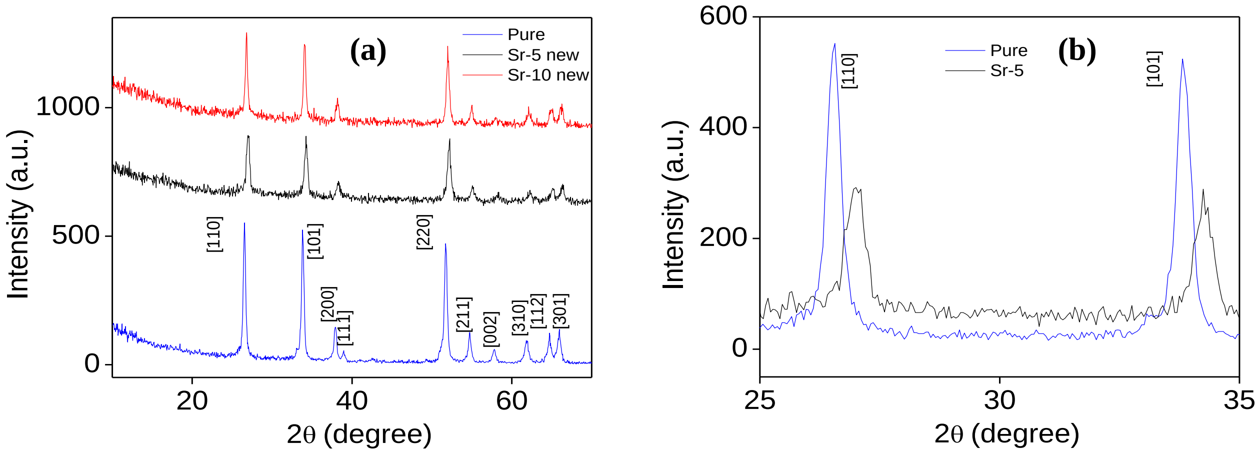

Fig. 3.8. *XRD spectra of pristine and strontium-loaded SnO_2 powders.* ***(a)*** *The discernible peaks correspond to different crystal planes of SnO_2.* ***(b)*** *A closer look reveals maximum peak shifts between pure and strontium loaded samples among SnO_2 crystals synthesized with group II additives.*

The possibility of larger crystals is validated through bright field TEM images which show presence of crystals in the range of 20-30 nm (**Fig. 3.9(a-b)**). The SAED pattern shown in the inset of **Fig. 3.9(b)** highlights the nanopolycrystalline nature of the composite where planes for SrO and SnO_2 are observed simultaneously in the inverse lattice plane. This is further highlighted by HR-TEM images where fringes with *d*-spacing of 0.26 nm corresponding to [200] plane of SrO [44] were observed adjacent to the SnO_2 particles. This again validates the boundary dwelling nature of the group II additives in their oxide form and their corresponding limiting effect on the grain growth.

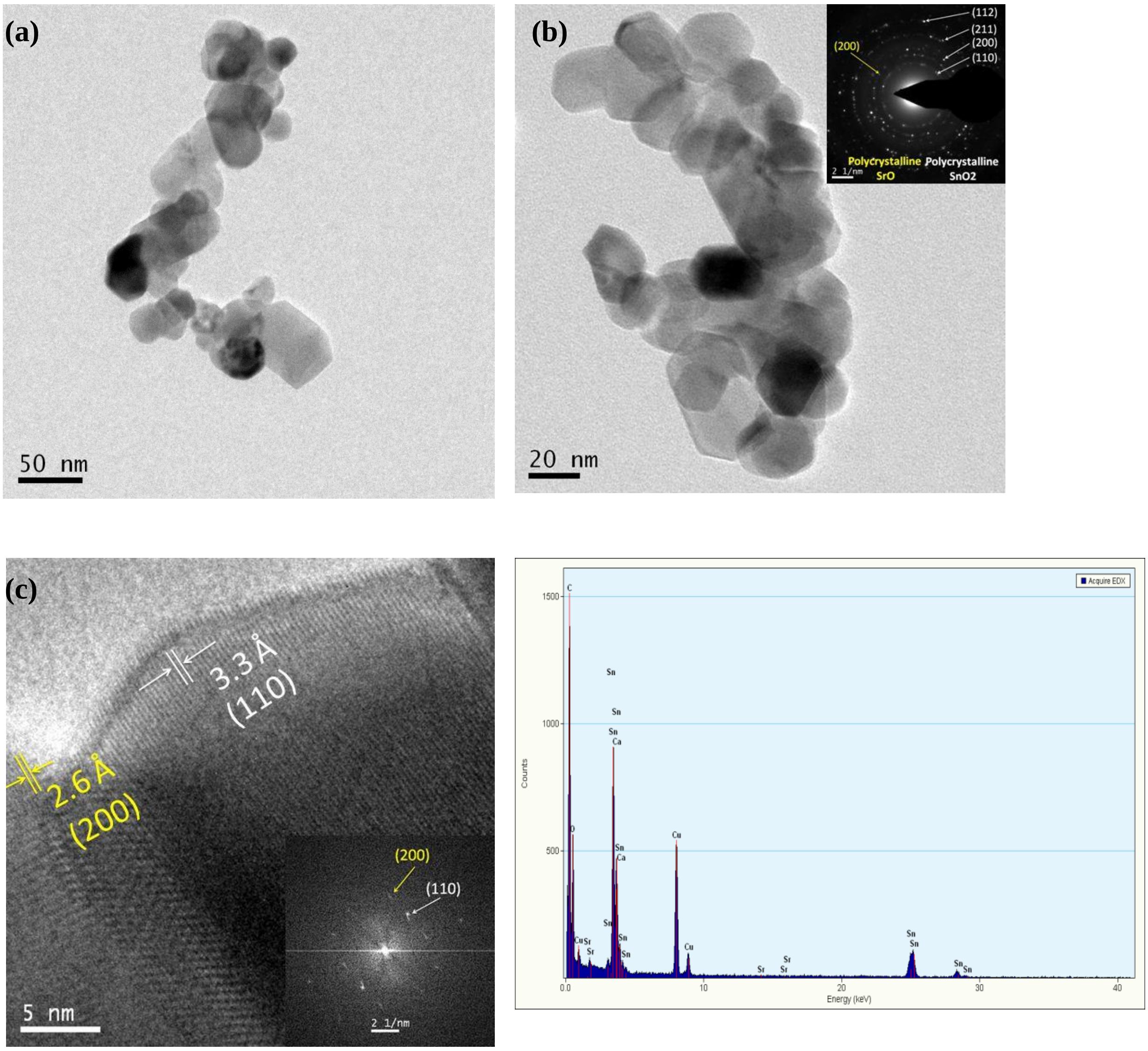

Fig. 3.9(a). *Bright Field TEM Images for the grain growth limited 5 wt% Sr-SnO$_2$ particles* ***(b)*** *Higher magnification images showing particle size in the 20-30 nm* ***(c)*** *Presence of SrO particles ([200] lattice plane) adjacent to the grain boundaries of SnO$_2$ crystals and* ***(d)*** *EDAX spectrum for SrO loaded SnO$_2$ crystals confirming the presence of strontium*

The photolumiscence spectrum for strontium loaded crystals yields similar features compared to the magnesium and calcium loaded crystals. However, the Sr-SnO$_2$ room temperature PL spectra highlights contours with diminished magnitudes. The reduced PL peak intensity might be correlated with the greater amplitude of peak shift in the x-ray spectrum which indicated at a higher lattice distortion. Such strained lattice produces greater amount of non radiative emission. The photoluminiscence peak intensity decreases on the occurrence of non radiative recombination and also on account of an increased defects (oxygen vacancies) [46].

3.4.4. Barium-added SnO$_2$

A reversible effect on introduction of barium into the matrix was observed, as the grain growth was promoted in contrast to the limiting effect demonstrated by the other group II additives. An empirical assumption about the grain promoting effects of barium loading can be made from the highly sharp features of the XRD peaks illustrated in **Fig 3.10(a)**. Characterised by a relatively low FWHM values these peaks indicate towards an anomaly to the hypothesis of grain inhibition by group II elements. Another striking dissimilarity from other additives is the absence of any peak shift as observed through the plot of **Fig 3.10(b)**, implying the absence of lattice substitution. The salient information decoded from the XRD plot was corroborated by the bright field TEM image of the Ba-SnO$_2$ crystals (**Fig. 3.11(a-b)**). The particle size for the composite was larger than 50 nm and therefore was expected to produce inferior sensing response compared to the other nanocrystalline materials.

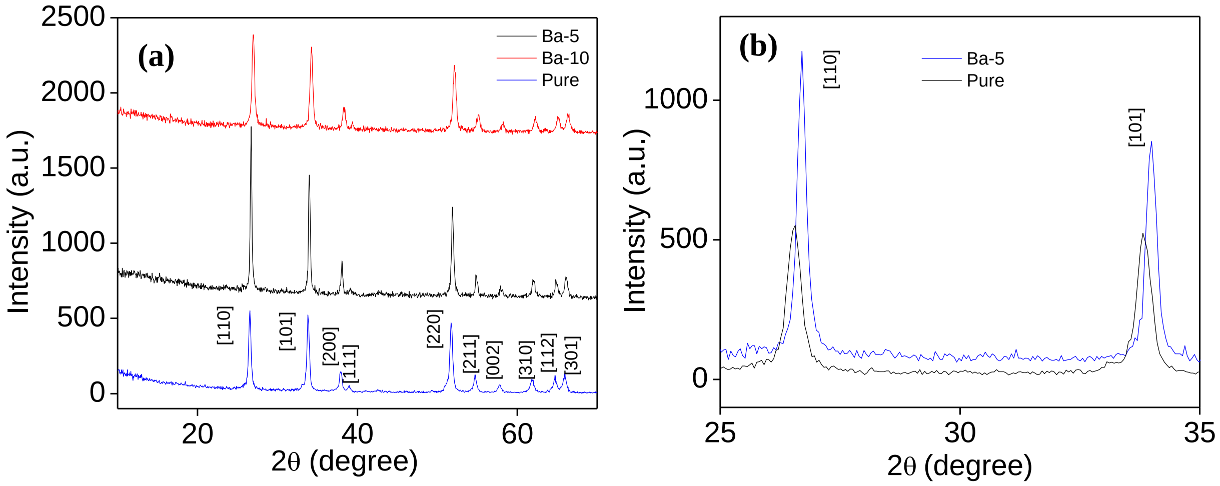

Fig. 3.10. *XRD spectra of pristine and barium-loaded SnO$_2$ powders.* ***(a)*** *The discernible peaks correspond to different crystal planes of SnO$_2$.* ***(b)*** *A closer look reveals maximum peak shifts between pure and strontium loaded samples among SnO$_2$ crystals synthesized with group II additives.*

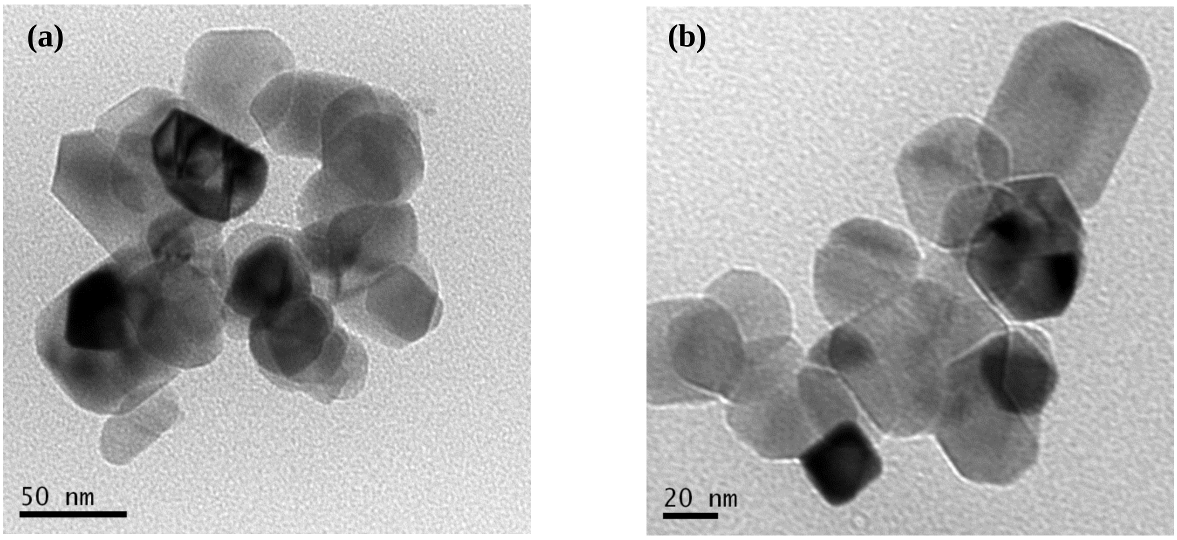

Fig. 3.11(a). *Bright Field TEM Images for the grain growth limited 5 wt% Ba-SnO$_2$ particles* ***(b)*** *Higher magnification images showing particle size larger than 50 nm*

The photoluminescnece spectra for the barium loaded particles conformed to the spectra generated by magnesium and strontium loadings. However, the higher peak intensity suggested a lack of oxygen vacancy related defects in the lattice. The larger dimensions of the barium loaded crystals deem it unsuitable for CO sensing application and therefore its application was limited as a comparative material.

3.5. Gas sensing characterisation

Thick film sensors were fabricated with the group II loaded tin dioxide nanocrystals for detection of low concentration carbon monoxide. Among them, calcium and magnesium loaded crystals were expected to demonstrate superior response than the rest due to prominent grain inhibition effect which allows the crystals to offer higher specific surface area. Additionally, both MgO and CaO have established catalytic influence towards oxidation of carbon monoxide which might be helpful in enhancing the sensor response. Barium loaded crystals were comparatively larger and thus should have shown inferior sensing pattern. This was indeed the scenario as calcium and magnesium loaded crystals showed much improved response. The dynamic carbon monoxide sensing characterization has thus been presented from the perspective of Ca-SnO_2 sensors. The performance of the Ca-SnO_2 sensor acts as the benchmark while the response patterns for the rest sensors have been presented as a comparative analysis with it.

3.5.1. Gas sensing for Ca-SnO_2 sensors

Calcium-loaded SnO_2 sensors, with favourable attributes like high specific surface area and charge-trapping oxygen adsorbates, were tested for detection of carbon monoxide. **Fig. 3.12(a)** depicts normalized resistance values (sensor response) of the Ca-SnO_2 sensors when exposed to CO concentrations in the range of 1 – 30 ppm. In the calibration plot, R_{air} and R_{CO} denote sensor resistances in air and in the presence of carbon monoxide, respectively. A good linearity could be observed over the entire range of measurement. From the slope of the calibration curve the sensitivity was calculated to be 0.028 ± 0.003 ppm^{-1}. The lower limit of detection (LOD) of the developed sensor, which is 1 ppm, is comparable or superior to the commercial sensors in the same genre. Further, dynamic response characteristics of the sensors were recorded in presence of a series of gas pulses. **Fig. 3.12(b)** depicts such a representative curve, which was obtained for a pulse train of 1 ppm CO in air and at an operating temperature of 350 ^{o}C. Pulse duration was made variable to preserve the generality in the response pattern. From the series of dynamic response curves two important sensor parameters were deduced - response time and recovery time. Response time (τ_r) is defined as the time required by the sensor to attain 90% of its saturation resistance value after being exposed to the target gas. While, the recovery time (τ_o) is characterized as the time lag to reach its baseline value (90%) after the stimuli are withdrawn. From the set of transient response patterns the values of τ_r were calculated to be in the range of 10 – 12 s and that of τ_o varied between 30 and 45 s (for different concentrations of CO). The values of τ_r and τ_o obtained in this study were compared with those reported for commercial metal-oxide sensors and found the former to be superior in most of the cases. The working temperature of a metal-oxide gas sensor plays a pivotal role in determining the sensitivity. Usually a high operating temperature is required for the surface reactions to take place and for showing an appreciable sensitivity. On the flip side, a prolonged operation in an elevated temperature induces grain growth by coalescence and hence causes a drift in the sensor response patterns. Thus an optimization of temperature is required both for the sake of material stability and power consumption. The Ca-loaded SnO_2 sensors were characterized at different temperatures ranging from 150 to 400 ^{o}C (**Fig. 3.12(c)**). A steady increase in response was observed which gradually reached saturation at 350 ^{o}C, the temperature at which all the subsequent studies were performed. Further increase in operating temperature did not yield a remarkable improvement in sensor response. The shape of the response versus temperature curve can be explained by the competition between slow kinetics at relatively low temperatures and enhanced desorption at higher temperatures [4].

The influence of calcium loading concentration on the CO response properties of the sensors was also investigated. In fact, base resistance of the sensors were found to be a function of Ca-loading in SnO_2 (**Fig. 3.12(d)**). An eventual increase in Ca-loading led to higher base resistance due to decrease in grain size and consequent enhancement in grain boundary scattering. An estimation of the crystallite size could be obtained from the XRD spectra using Scherrer formula. For pure samples, the average crystallite size was calculated to be 27 nm, while for 5 wt% and 10 wt% calcium-loaded SnO_2 powders the average crystallite size was 23 nm and 18 nm, respectively. As illustrated in **Fig. 3.13(a)**, with increased calcium loading, initially the response increases and reaches a saturation value at around 5 wt% calcium in the SnO_2 matrix. With further enhancement in calcium concentration, the response drops. Due to the limited solid solubility in the tin oxide matrix, calcium gets segregated at the grain boundaries, as is evident in the HRTEM image (**Fig. 3.2(c**)). The presence of calcium oxide at the grain boundaries inhibits the growth of tin oxide nanocrystals (Fig. 2b) and thereby increases the effective surface area, which was evident from BET studies. The higher effective surface area promotes enhanced surface coverage of oxygen adsorbates and the response increases, as is apparent in the case of 5 wt% loading of calcium. Additionally, the sporadic deposition of calcium oxide on the SnO_2 particle surface can contribute to sensor response via catalytic activities. Calcium oxide has been reported to provide active sites for

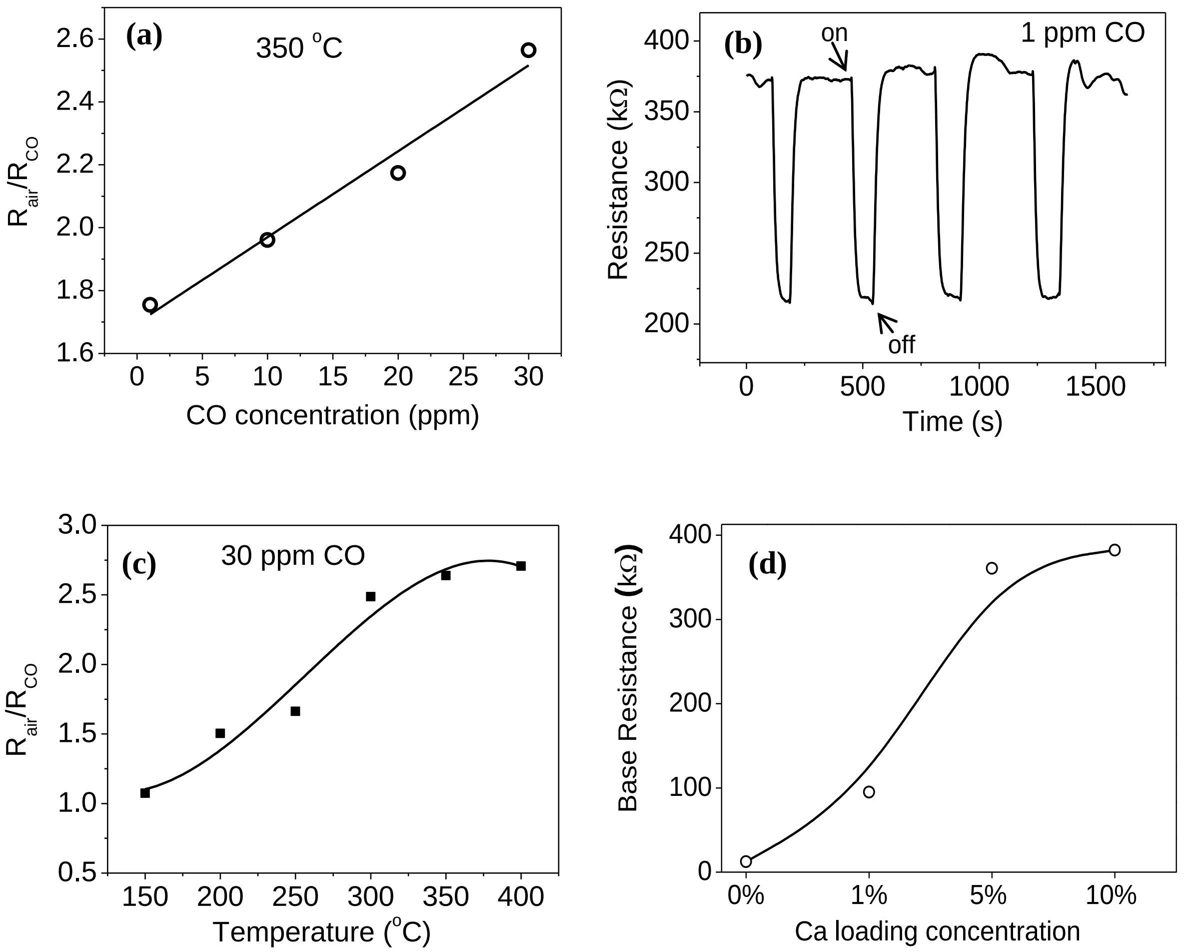

Fig. 3.12. *Response characteristics of 5 wt% Ca-loaded SnO_2 sensors.* ***(a)*** *Calibration curve drawn over the dynamic range of 1 – 30 ppm CO* ***(b)*** *Dynamic response characteristics of 1 ppm CO at 350 °C.* ***(c)*** *Sensor response as a function of temperature, which shows saturation at 350 °C.* ***(d)*** *Sensor base resistance as a function of Ca loading.*

oxygenation of carbon monoxide and thus is expected to promote CO sensitivity [13]. In fact, an increase in sensor response (at a given temperature) or a reduction in operating temperature (for an identical sensor response) was seen when SnO_2 is loaded with calcium. For 30 ppm CO, while an pure SnO_2 sensor generated a response value (R_{air}/R_{CO}) of 1.5 at 350 °C, the similar response for 5 wt% Ca-loaded SnO_2 sensors could be obtained at much lower temperature (200 °C). However, when the calcium loading in SnO_2 is substantially high (say, 10 wt%) the response decreases, which may be attributed to the eventual blocking of surface adsorption sites on the SnO_2 nanocrystals [46]. For noble metal catalysts the reduction in sensitivity beyond a threshold is imposed by the exceeding of the percolation threshold [47] due to formation of conducting metallic clusters on the surface. Calcium oxide being an electrical insulator in its pristine form, does not adhere to this process. Referring to the HRTEM image in **Fig. 3.2(d)**, for 10 wt% loading, there is an abundant deposition of calcium oxide at the grain boundaries as well as on the surface of SnO_2 nanocrystals.

It is important to draw a comparative picture of response between Ca-SnO_2 and noble metal-loaded SnO_2 sensors, which is presented in **Fig. 3.13(b)**. In each case, the loading concentration was chosen on the basis of maximum response to 30 ppm CO. Interestingly, in terms of sensor response, the Ca-loaded SnO_2 sensors either outperformed the noble-metal loaded sensors or showed a comparable property. While the noble metals in SnO_2 primarily induce surface sensitization effects, calcium loading has an additional benefit in terms of grain growth inhibition, which is a favourable attribute for enhanced sensitivity. Additionally, the base resistance of Ca-SnO_2 sensors was highly stable over a long period of operation (as discussed in the subsequent section). Finally, when it comes to production cost, the precursors for calcium loading are economically much more viable than their noble metal counterparts. Selectivity of any chemical sensor is one of the most important parameters to be considered or field deployment. **Fig. 3.14(a)** reflects the degree of selectivity achieved with the Ca-SnO_2 sensors when operated at 350 ^{o}C. A closer look at the bar chart reveals that even a 10-fold higher concentration of a VOC (ethanol) or a 32-fold higher concentration of a hydrocarbon (methane) resulted in lower sensor responses compared to that obtained for 10 ppm CO in air. Additionally, the reproducibility of the devices was checked by applying a random sequence of pulses of different gases and VOC.

The dynamic response pattern is presented in **Fig. 3.14(b)**, which reveals that the responses for the identical pulses of CO was congruent, even after exposing the sensor to varying CH_4 and CO concentrations in between two similar CO pulses. The above observation suggests that the Ca-SnO_2 sensors have a minimal or no memory effect.

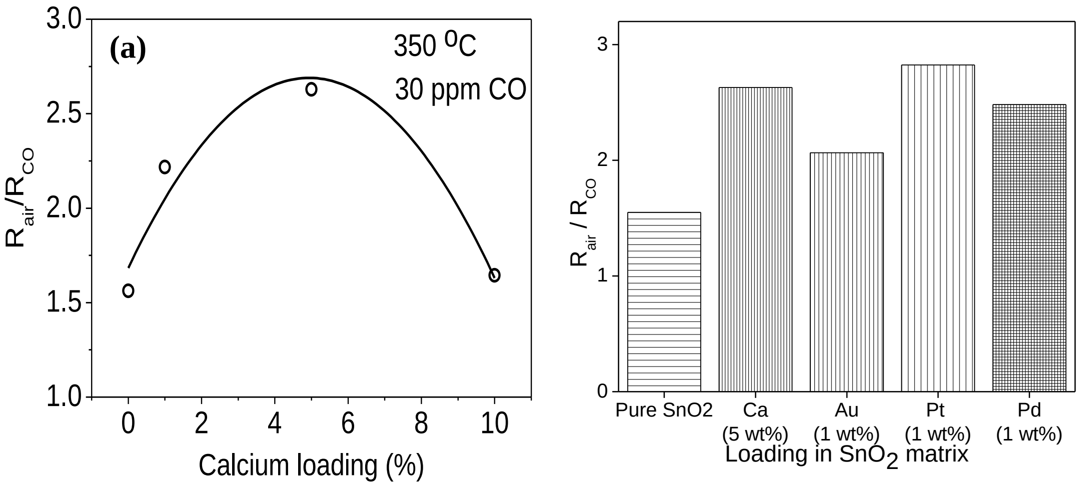

Fig. 3.13: *Effect of loading on the sensor response characteristics.* ***(a)*** *With an increase in calcium loading concentration in the SnO_2 matrix, the sensor response increases, eventually reaches a saturation value and then starts decreasing.* ***(b)*** *Comparison of calcium with noble-metal catalysts in SnO_2.*

Ambient humidity is a factor that influences the sensitivity of metal-oxide sensors to specific gases. The interaction between surface-adsorbed oxygen and water molecules modulates the baseline properties of the sensors, which in turn affects the sensitivity. **Fig. 3.14(c)** presents the response of the Ca-SnO_2 sensors towards saturated moisture. It is to be noted that CO

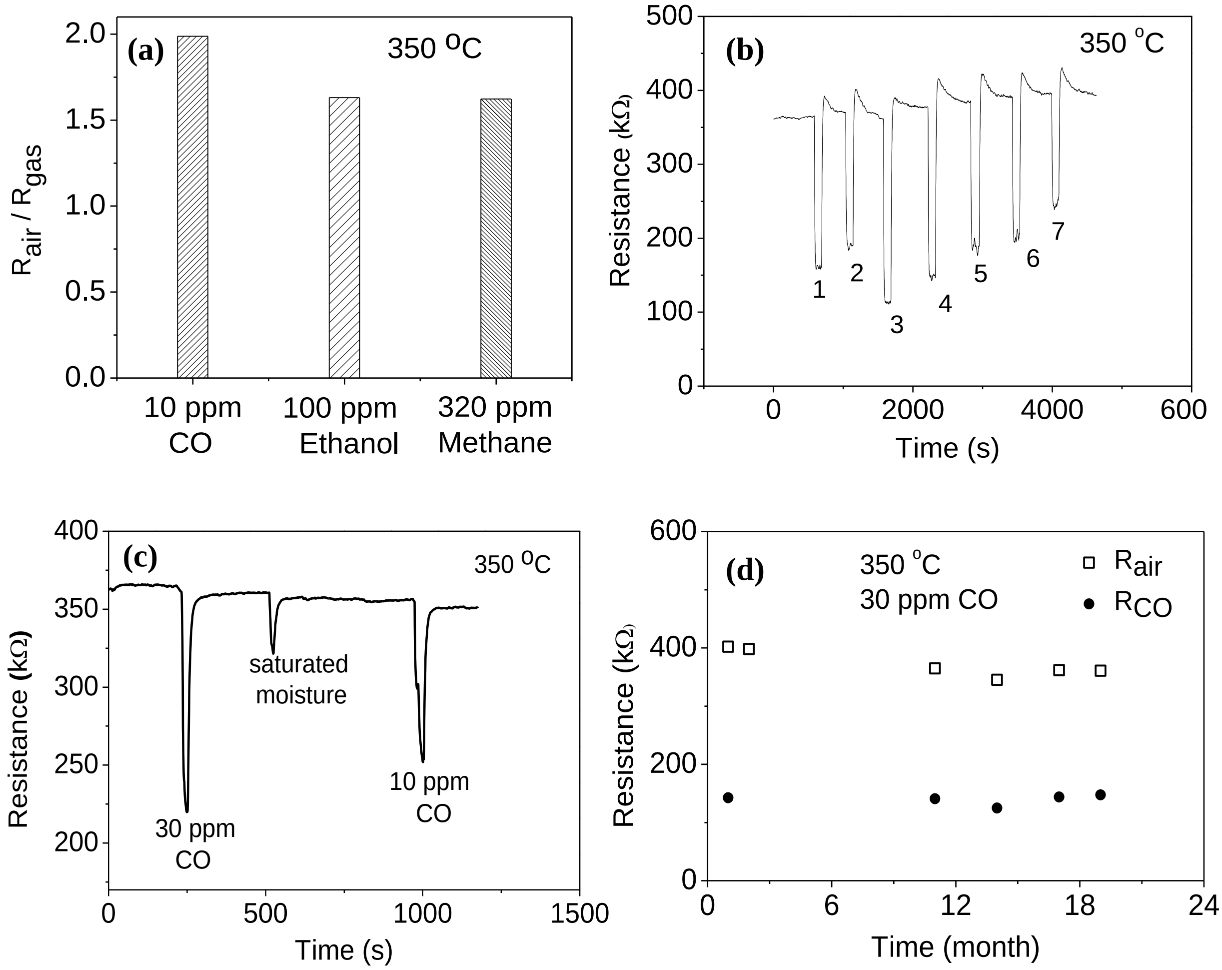

Fig. 3.14. *Selectivity and stability of Ca-loaded SnO_2 sensors.* ***(a)*** *Cross-sensitivity of the sensors in presence of high concentrations of other VOC and hydrocarbon.* ***(b)*** *Random pulses of varying concentrations of various gases show the repeatability and the ruggedness of the sensor. [1] 1000 ppm CH_4, [2] 10 ppm CO, [3] 3000 ppm CH_4, [4] 30 ppm CO, [5] 1000 ppm CH_4, [6] 10 ppm CO, [7] 320 ppm CH_4* ***(c)*** *Effect of saturated moisture on the CO response.* ***(d)*** *Long term stability of Ca – SnO_2 sensors.*

pulses were given to a sensor kept at 350 °C in laboratory ambient with about 68% RH at 26 °C. Between two CO pulses of varying magnitude, the sensor was exposed to a pulse of saturated moisture. Though a discernible sensor response was observed, the contribution of 100% humidity was manyfold inferior even to a 10 ppm CO pulse. The above observation suggests that CO response of the Ca-SnO_2 sensors was not overwhelmed by the presence of moisture in air. A nominal drift due to humidity can, however, be handled by a simple compensation circuit.

A drift in sensor properties, as a sequel of high temperature operation, is a common phenomenon with metal-oxide sensors. As mentioned above, enhanced mass transport at elevated temperatures causes sintering of the metal-oxide nanoparticles and consequently the sensor parameters keep changing with time. Calcium loading, beyond the solubility limit in SnO_2 matrix, plays a crucial role. Segregation of calcium at the grain boundaries, as evidenced in TEM studies, mitigates the grain growth and stabilizes the base resistance to a significant extent. As presented in **Figure 3.14(d)**, 5 wt% Ca-loaded SnO_2 sensors exhibited steady values of response over an extended period of time after fabrication. Interestingly, significant drift of the baseline resistance of the Ca-SnO_2 sensors over a period of 19 months have not been observed (maximum length of time studied so far). For 30 ppm CO, the calculated values of sensor response (R_{air}/R_{CO}) over the entire period of test showed a mean of 2.64 and a standard deviation of 0.16. Besides long term stability, activation time of the CO sensors was also investigated. For Ca-SnO_2 sensors, it took about 2 h before the baseline reached a stable value with 2% overall drift. In contrary, indigenously fabricated 1 wt% Pt-loaded SnO_2 sensors showed more than 30% drift in baseline resistance over an identical period of 2 h. The above observation suggests that the replacement of noble metal catalysts by calcium not only reduces the fabrication cost, but also helps in stabilizing the sensor properties at high temperatures.

3.5.2. Gas sensing for Mg-SnO_2 and Sr-SnO_2 sensors

The grain growth inhibited particles of SnO_2, with oxides of magnesium or strontium in their periphery, were exposed to varied concentrations of carbon monoxide. The change in their intrinsic conductance in presence of the toxic gas was assessed to calibrate the concentration of carbon monoxide. Barium loaded crystals were excluded from the sensing studies as it contradicted with the basic mandate and showed promoting effects instead of limiting the crystal growth. The calibration plots for the Mg-SnO_2 and Sr-SnO_2 sensors have been depicted in **Fig. 3.15(a)** along with the calibration curve of Ca-SnO_2 sensors for comparative purposes. As observed from the calibration plot, Ca-SnO_2 sensors demonstrate better sensitivity towards carbon monoxide with its higher R_{air}/R_{CO} ratio. On the other hand strontium loaded crystals have least sensing response among the group II incorporated SnO_2 nanoparticles. Interestingly, Mg-SnO_2 has matching response pattern to that of the Ca-SnO_2 sensors with marginal decrease in sensitivity. However, the linearity in calibration plot, an important and sought feature for any MOS sensor is more prominent in Mg-SnO_2 as compared to its calcium loaded counterpart.

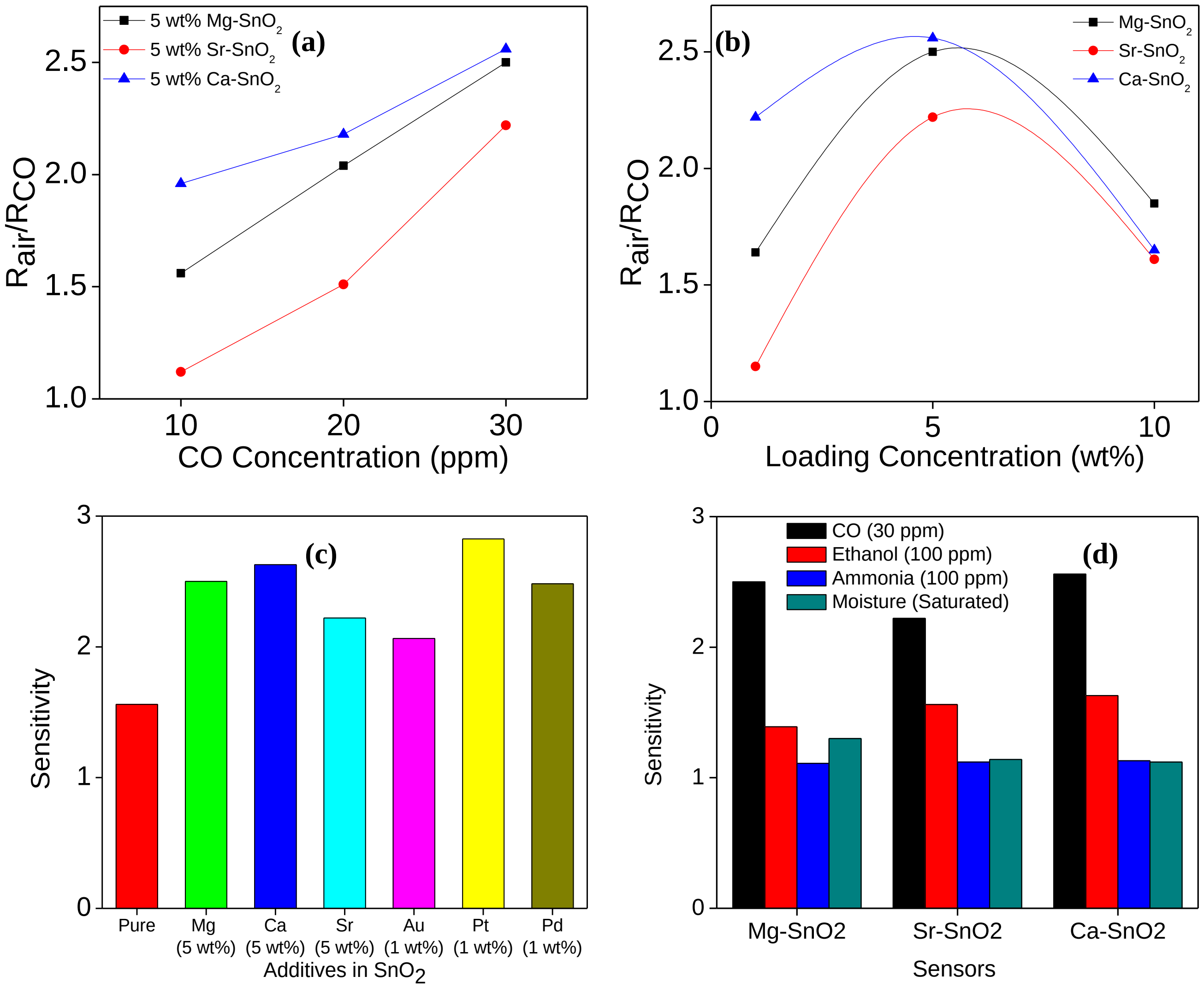

Fig. 3.15(a). *Comparative calibration plots and* ***(b)*** *Comparative loading plot for grain inhibited crystals* ***(c)*** *Resposne plot towards 30 ppm CO for the grain inhibited SnO2 sensors against other noble metal sensitized sensors* ***(d)*** *Cross sensitivity plot for the sensors showing higher affinity towards carbon monoxide*

Moreover, the resolution of the sensors, defined as the change in R_{air}/R_{CO} per unit change in analyte concentration, is also higher for the Mg-SnO$_2$ sensors. While the resolution for Mg-SnO$_2$ is 0.047 ppm^{-1}, the value for Ca-SnO$_2$ is much less at 0.017 ppm^{-1}. Strontium loaded crystals, despite their inferior response pattern, shows a relatively higher resolution of 0.055 ppm^{-1}. Despite its inability to restrict the grain growth, barium loaded SnO$_2$ crystals were also examined for their sensor response. As expected, the sensitivity towards different concentrations of carbon monoxide was observed to be abysmally low for this sensor. The effect of loading concentration on the response pattern was also investigated and the relevant plot has been shown in **Fig. 3.15(b)**. The common trend for each plot of shows an increase in sensitivity till 5 wt%, followed by a gradual decrease in response. The grain inhibitory effects for the additives increases with loading concentration as smaller particles are produced. However, beyond an optimum loading level of 5 wt%, the sensitivity decreases owing to presence of dielectric CaO regions in between SnO$_2$ grains which result in poor conductive pathway [48]. Since the group II additives are being promoted as efficient replacements for surface sensitizing noble metals [49], it was imperative to compare the response towards carbon monoxide for the two categories of sensors

A comparative assessment of the performances involving sets of group II additive loaded sensors and noble metal sensitized modules is provided in **Fig. 3.15(c)**. The comparison reveals that the response pattern for magnesium and calcium loaded SnO_2 sensors are at par or even better towards carbon monoxide than their noble metal loaded counterparts. It simultaneously shows the enhanced response over sensors developed with pristine form of tin dioxide. Coupled with the fact that precursors of magnesium and calcium are far inexpensive than those for noble metals, these sensor modules offer a cost efficient solution for detecting the lethal gas. The cost effectiveness, low detection limit, fast response as well as recovery of around 12 s and 45 s respectively, and minimum acclimatization period of only 2 hours, project these sensor modules as suitable alternates to the existing commercial products. A summary of performance parameters for the indigenous Ca-SnO_2 sensor against the datasheets of carbon monoxide sensors designed by reputed firms has been presented in **Table 3.1**. Apart from the grain inhibitory effects that produce SnO_2 nanocrystals with high specific surface area, another possible reason for the Mg-SnO_2 and Ca-SnO_2 modules to demonstrate high sensitivity is that both MgO and CaO are established catalysts for oxygenation of CO [13]. The sporadic distribution of the grain inhibitors on crystal periphery catalyses the oxidation of the dispensed carbon monoxide by the oxygen adsorbates on the sensor surface.

Table 3.1. *Comparison of performance parameters of 5 wt% Ca-SnO_2 sensors and commercial modules*

Parameters	TGS 2600 (Figaro USA Inc.)	MQ-7 (Hanwei Electronics Co., Ltd)	Ca-SnO_2 sensors
Sensitivity (30 ppm CO)	42%	N.A.	**61%**
LOD	30 ppm	20 ppm	**1 ppm**
Activation time	2 days	2 days	**2 h**
Response time	3 min	60 s	**10-12 s**
Recovery time	10 min	90 s	**35-40 s**

The cross-sensitivity for any field deployed sensor towards interfering analytes is another parameter that is closely monitored. The cross-sensitivity for the developed sensor modules by studying their response in ethanol and ammonia was determined. The concentration of ethanol and ammonia were maintained at 100 ppm which is much higher than that present in indoor ambient air [50,51]. In fact, the concentrations for the interfering analytes were maintained multifold compared to carbon monoxide to highlight the affinity of the sensors exclusively towards the toxic gas. The plot showing the response of the developed sensor modules in presence of the cross-interfering gases is presented in **Fig. 3.15(d)**. Affinity of the developed sensors towards carbon monoxide might be partly ascribed to the catalytic influence of surface dwelling grain inhibiting oxides towards oxidation of carbon monoxide. A measure of selectivity for individual sensor, defined by the relative ratio of sensitivities demonstrated towards CO and another cross-interfering analyte is provided in **Table 3.2**. A higher ratio of sensitivities for a particular sensor inevitably implies greater affinity of that module towards carbon monoxide compared to the interfering analyte. As such, Mg-SnO_2 and Ca-SnO_2 shows higher levels of separation among sensitivities in comparison to the Sr-SnO_2 counterpart.

Table 3.2. *A measure of selectivity for the developed sensor modules*

Sensors	R_{CO}/R_{EtOH}	$R_{CO}/R_{Ammonia}$	$R_{CO}/R_{Moisture}$
Mg-SnO_2	1.80	2.25	1.92
Sr-SnO_2	1.42	1.98	1.95
Ca-SnO_2	1.57	2.26	2.28

Another noteworthy aspect for the developed sensors is their minimal association with moisture. As performance of MOS sensors is often adversely affected in presence of moisture, the sensors presented in this study have the potential to excel in such scenarios.

3.6. Conclusion

This study investigated the role of group II elements, *viz.* magnesium, strontium, barium and calcium as possible performance enhancing additives in tin dioxide matrix for detection of sub-TLV concentration of carbon monoxide. While magnesium, calcium and strontium were observed to limit the grain growth and produce smaller SnO_2 crystals with high specific surface area, barium actually enhanced the grain growth and produced large crystals inefficient for sensing applications. The sensor modules developed with the smaller SnO_2 crystals laden with oxides of Ca, Mg or Sr showed considerable sensitivity and selectivity towards low concentration of carbon monoxide. The lower detection limit for the fabricated sensors could be pushed down to 10 ppm which is considerably below the statutory limit prescribed by world health regulatory bodies. In fact, discerning features for the fabricated sensors like the LDL, response and recovery time as well as the overall acclimatization period were observed to be at par or superior to the commercial carbon monoxide detectors available in market. Additional benefits like inexpensive precursors and selective affinity towards the target analyte make these sensors as suitable candidates for possible field trials and subsequent commercialization.

References:

[1] Y. Liu, E. Koep, M. Liu, “A highly sensitive and fast-responding SnO_2 sensor fabricated by combustion chemical vapor deposition”, Chem. Mater., 17 (2005) 3997–4000.

[2] A. Rothschild, Y. Komem, “The effect of grain size on the sensitivity of nanocrystalline metal-oxide gas sensors”, J. Appl. Phys., 95 (2004) 6374-6380

[3] G.G. Mandayo, E. Castaño, F.J. Gracia, A. Cirera, A. Cornet, J.R. Morante, “Strategies to enhance the carbon monoxide sensitivity of tin oxide thin films”, Sens. Actuators B: Chem., 95 (2003) 90–96.

[4] A. Kolmakov, D.O. Klenov, Y. Lilach, S. Stemmer, M. Moskovits, “Enhanced gas sensing by individual SnO_2 nanowires and nanobelts functionalized with Pd catalyst particles”, Nano Lett., 5 (2005) 667–673.

[5] A.R. Phani, S. Manorama, V.J. Rao, “Effect of additives on the response of sensors utilizing semiconducting oxide on carbon monoxide sensitivity”, Appl. Phys. Lett., 66 (1995) 3489-3491.

[6] A.A. Zhukova, A.N. Shatokhin, F.N. Putilin, I.A. Petukhov, M.N. Rumyantseva, A.M. Gaskov, Effect of surface modification with palladium on the CO sensing properties of antimony doped SnO_2 whiskers, Inorg. Mater., 49 (2013) 1005-1010.

[7] P. Manjula, S. Arunkumar, S.V. Manorama, “Au/SnO_2 an excellent material for room temperature carbon monoxide sensing”, Sens. Actuators B: Chem., 152 (2011) 168-175.

[8] Y. Ozaki, S. Suzuki, M. Morimitsu, M. Matsunaga, “Temperature-humidity dependence and stability of SnO_2-based CO gas sensors improved by surface modification with platinum and iridium”, Electrochemistry, 68 (2000) 694-701.

[9] M. D'Arienzo, L. Armelao, A. Cacciamani, C.M. Mari, S. Polizzi, R. Ruffo, R. Scotti, A. Testino, L. Wahba, F. Morazzoni, "One-step preparation of SnO_2 and Pt-doped SnO_2 as inverse opal thin films for gas sensing", Chem. Mater., 22 (2010) 4083-4089.

[10] N. Lavanya, S. Radhakrishnan, C. Sekar, "Fabrication of hydrogen peroxide biosensor based on Ni doped SnO_2 nanoparticles", Biosens. Bioelectron., 36 (2012) 41-47.

[11] A. Tricoli, M. Graf, S.E. Pratsinis, "Optimal doping for enhanced SnO_2 sensitivity and thermal stability", Adv. Func. Mater., 18 (2008) 1969-1976.

[12] N. Illyaskutty, J. Knoblauch, M. Schwotzer, H. Kohler, "Thermally modulated multi sensor arrays of SnO_2/additive/electrode combinations for enhanced gas identification", Sens. Actuators B: Chem., 217 (2015) 2-12.

[13] M. Bailes, F.S. Stone, "The reaction of oxygen with CO complexes on calcium oxide and magnesium oxide", Top. Catal., 11/12 (2000) 213–222.

[14] N. Yamazoe, "New approaches for improving semiconductor gas sensors", Sens. Actuators B: Chem., 5 (1991) 7-19.

[15] G. Korotcenkov, S.D. Han, B.K. Cho, V. Brinzari, "Grain size effects in sensor response of nanostructured SnO_2- and In_2O_3-based conductometric thin film gas sensor", Crit. Rev. Solid State Mater. Sci., 34 (2009) 1-17.

[16] N.L. Wu, S.Y. Wang, I.A. Rusakova, "Inhibition of crystallite growth in the sol-gel synthesis of nanocrystalline metal oxides", Science, 295 (1999) 1375-1377.

[17] G. Xu, Y.W. Zhang, X. Sun, C.L. Xu, C.H. Yan, "Synthesis, structure, texture, and CO sensing behavior of nanocrystalline tin oxide doped with scandia", J. Phys. Chem. B, 109 (2005) 3269–3278.

[18] E.R. Leite, I.T. Weber, E. Longo, J.A. Varela, "A new method to control particle size and particle size distribution of SnO_2 nanoparticles for gas sensor applications", Adv. Mater., 12 (2000) 965-968.

[19] B.K. Min, S.D. Choi, "Role of CaO as crystallite growth inhibitor in SnO_2", Sens. Actuators B: Chem., 99 (2004) 288–296.

[20] S.D. Choi, D.K. Lee, "CH_4 sensing characteristics of K-, Ca-, Mg impregnated SnO_2 sensors", Sens. Actuators B: Chem., 77 (2001) 335–338.

[21] R.M. Morris, K.J. Klabunde, “Formation of paramagnetic adsorbed molecules on thermally activated magnesium and calcium oxides. Further studies of carbon monoxide”, J. Am. Chem. Soc., 105 (1983) 2633-2639.

[22] N. Jaiswal, D. Kumar, S. Upadhyay, O. Parkash, Ceria co-doped with calcium (Ca) and strontium (Sr): a potential candidate as a solid electrolyte for intermediate temperature solid oxide fuel cells, Ionics, 20 (2014) 45-54.

[23] W.J. Borland, S. Suh, J.P. Maria, J.F. Ihlefeld, I. Burn, “Glass flux assisted sintering of chemical solution deposited thin dielectric films”, US Patent 8183108 B2, May 22, 2012.

[24] S.R. Dhage, V. Ravi, O.B. Yang, “Varistor property of SnO_2·CoO·Ta_2O_5 ceramic modified by barium and strontium”, J. Alloys Compd., 466 (2008) 483-487.

[25] C. Wang, H. Cheng, Y. Sun, Q. Lin, C. Zhang, “Rapid sonochemical synthesis of luminescent and paramagnetic copper nanoclusters for bimodal bioimaging”, ChemNanoMat, 1 (2015) 27-31.

[26] M.M. Bagheri-Mohagheghi, M. Shokooh-Saremi, “Electrical, optical and structural properties of Li-doped SnO_2 transparent conducting films deposited by the spray pyrolysis technique: a carrier-type conversion study”, Semicond. Sci. Technol., 19 (2004) 764-769.

[27] P. Barpanda, N. Recham, J.N. Chotard, K. Djellab, W. Walker, M. Armand, J.M. Tarascon, “Structure and electrochemical properties of novel mixed Li $(Fe_{1-x}M_x)$ SO_4F (M= Co, Ni, Mn) phases fabricated by low temperature ionothermal synthesis”, J. Mater. Chem., 20 (2010) 1659-1668.

[28] M. Schumm, M. Koerdel, S. Müller, H. Zutz, C. Ronning, J. Stehr, D.M. Hofmann, J. Geurts, “Structural impact of Mn implantation on ZnO”, J. Appl. Phys., 108 (2010) 044910(1-7).

[29] T.W. Kim, D.U. Lee, Y.S. Yoon, “Microstructural, electrical, and optical properties of SnO_2 nanocrystalline thin films grown on InP (100) substrates for applications as gas sensor devices”, J. Appl. Phys., 88 (2000) 3759-3761.

[30] J.H. He, T.H. Wu, C.L. Hsin, K.M. Li, L.J. Chen, Y.L. Chueh, L.J. Chou, Z.L. Wang, “Beaklike SnO_2 nanorods with strong photoluminescent and field-emission properties”, Small, 2 (2006) 116-120.

[31] A.V. Dijken, E.A. Meulenkamp, D. Vanmaekelbergh, A. Meijerink, “Identification of the transition responsible for the visible emission in ZnO using quantum size effects”, J. Lumin., 90 (2000) 123-128.

[32] A.R. Babar, S.S. Shinde, A.V. Moholkar, C.H. Bhosale, J. H. Kim, and K.Y. Rajpure, “Physical properties of sprayed antimony doped tin oxide thin films: The role of thickness”, J. Semicond., 32 (2011) 053001(1-8).

[33] D.A. Popescu, J.M. Herrmann, A. Ensuque, F. Bozon-Verduraz, “Nanosized tin dioxide: Spectroscopic (UV-Vis, NIR, EPR) and electrical conductivity studies”, Phys. Chem. Chem. Phys., 3 (2001) 2522-2530.

[34] Y. Liu, Y. Jiao, Z. Zhang, F. Qu, A. Umar, X. Wu, “Hierarchical SnO_2 nanostructures made of intermingled ultrathin nanosheets for environmental remediation, smart gas sensor, and supercapacitor applications”, ACS Appl. Mater. Interfaces, 6 (2014) 2174-2184.

[35] S.S. Pan, S. Wang, Y.X. Zhang, Y.Y. Luo, F.Y. Kong, S.C. Xu, J.M. Xu, G.H. Li, “p-type conduction in nitrogen-doped SnO_2 films grown by thermal processing of tin nitride films”, Appl. Phys. A, 109 (2012) 267-271.

[36] K.M. Reddy, S.V. Manorama, A.R. Reddy, “Bandgap studies on anatase titanium dioxide nanoparticles”, Mater. Chem. Phys., 78 (2002) 239-245.

[37] U. Manzoor, D.K. Kim, “Synthesis and enhancement of ultraviolet emission by post-thermal treatment of unique zinc oxide comb-shaped dendritic nanostructures”, Scr. Mater., 54 (2006) 807-811.

[38] M.R. Carrott, P. Carrott, M.B.D. Carvalho, K.S.W. Sing, “Ex-hydroxide magnesium oxide as a model adsorbent for investigation of micropore filling mechanisms”, J. Chem. Soc. Faraday Trans., 87 (1991) 185-191.

[39] J. Du, R. Zhao, Y. Xie, J. Li, “Size-controlled synthesis of SnO_2 quantum dots and their gas-sensing performance”, Appl. Surf. Sci., 346 (2015) 256-262.

[40] S. Mohapatra, N. Bhardwaj, A. Pandey, “MeV ion irradiation induced evolution of morphological, structural and optical properties of nanostructured SnO_2 thin films”, Mater. Res. Express, 2 045013(1-9).

[41] A.R. Babar, S.S. Shinde, A.V. Moholkar, C.H. Bhosale, J.H. Kim, K.Y. Rajpure, “Sensing properties of sprayed antimony doped tin oxide thin films: solution molarity”, J. Alloys Compd., 509 (6) 3108-3115.

[42] S. Sharma, A.K. Srivastava, S. Chawla, “Self assembled surface adjoined mesoscopic spheres of SnO_2 quantum dots and their optical properties”, Appl. Surf. Sci., 258 (2012) 8662-8666.

[43] Y.L. Shi, J. Wang, H.L. Li, “Photoluminescence behavior of purpose-built ZnO arrays on different growth substrates”, Appl. Phys. A, 79 (2004) 1797-1799.

[44] H.A. Hamedani, N.K. Allam, M.A. El-Sayed, M.A. Khaleel, H.G. Faisal, M. Alamgir, “An experimental insight into the structural and electronic characteristics of strontium-doped titanium dioxide nanotube arrays”, Adv. Funct. Mater., 24 (2014) 6783-6796.

[45] P. Chetri, A. Choudhury, “Investigation of optical properties of SnO_2 nanoparticles”, Phys. E, 47 (2013) 257-263.

[46] M.E.M. Hassouna, A.M. El-Sayed, F.M. Ismail, M.H. Khder, A.A. Farghali, S.M. Yakout, “Investigation on the structure, electrical conductivity and ethanol gas sensitive properties of Ce-doped SnO_2 nanoparticles sensors”, Int. J. Nanomater. Biostruct., 2 (2012) 44-49.

[47] G. Halek, I.D. Baikie, H. Teterycz, P. Halek, P. Suchorska-Woźniak, K. Wiśniewski, “Work function analysis of gas sensitive WO_3 layers with Pt doping”, Sens. Actuators B: Chem., 187 (2013) 379-385.

[48] C. Jiang, S. Xu, G. Zhang, L. Li, Y. Yang, K. Shi, “Facile synthesis of CaO–SnO_2 nanocrystalline composite rods by electrospinning method with enhanced gas sensitive performance at room temperature”, CrystEngComm, 15 (2013) 2482–2489.

[49] I. Kocemba, J. Rynkowski, “The influence of catalytic activity on the response of Pt/SnO_2 gas sensors to carbon monoxide and hydrogen”, Sens.Actuators B: Chem., 155 (2011) 659-666.

[50] E. Gallego, X. Roca, J.F. Perales, X. Guardino, Determining indoor air quality and identifying the origin of odour episodes in indoor environments, J. Environ. Sci., 21 (2009) 333-339.

[51] T. Lindgren, A case of indoor air pollution of ammonia emitted from concrete in a newly built office in Beijing, Build. Environ., 45 (2010) 596-600.

Appendix: Sensor Fabrication

The nanomaterials developed were deposited on a standard Taguchi type sensor substrate for fabrication of sensing units. The process details have been represented in **Fig. 3.16**. The sensor substrates are hollow cylinders of alumina of approximately 1 mm external diameter. A nichrome wire is passed through the hollow cylinder specifically to achieve the elevated operating temperature. A current flown accross the wire effects a rise in temperature through Joule heating which implies that operating temperature can be achieved through modulating the current.

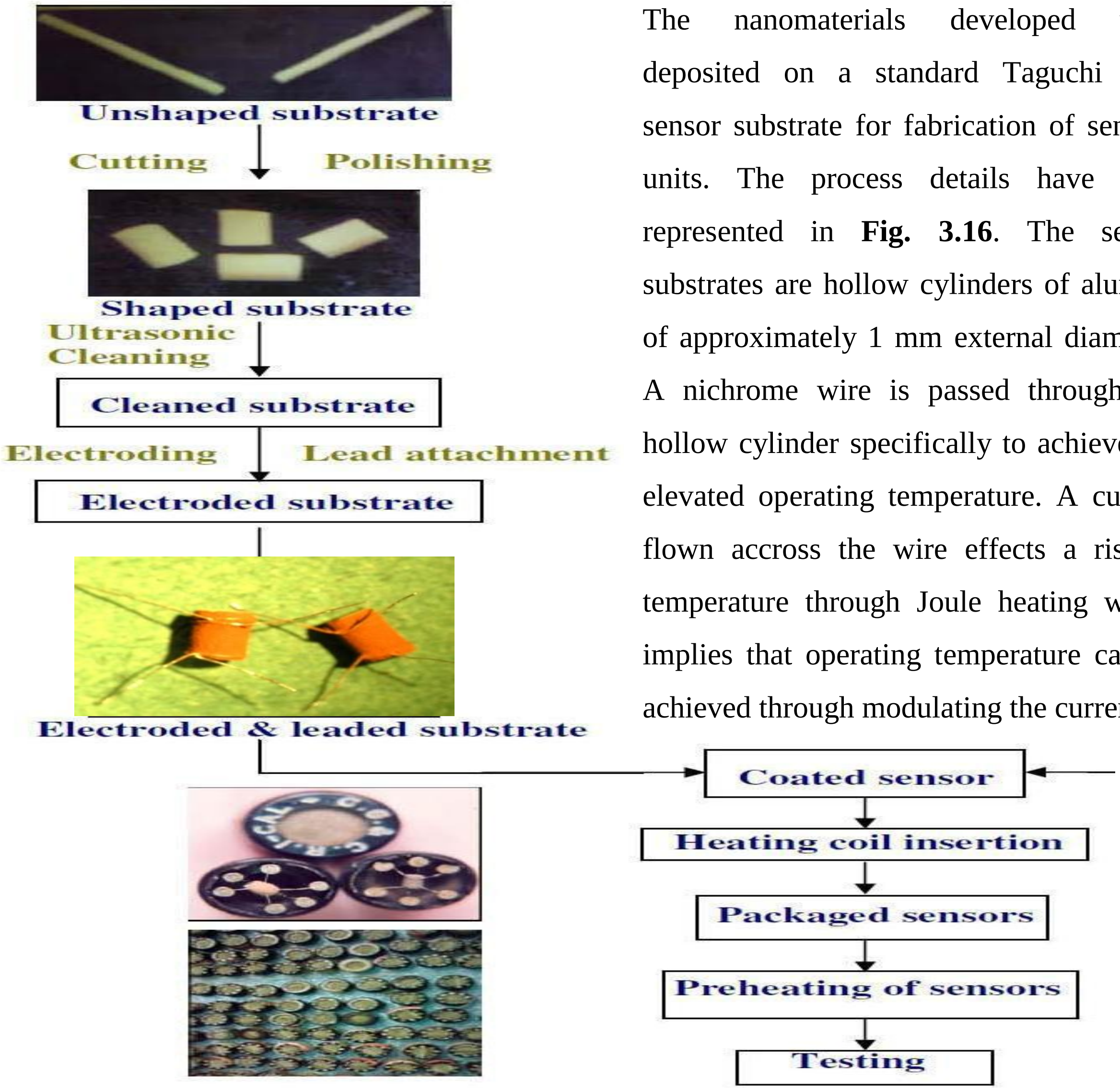

Fig. 3.16. *Details of sensor fabrication steps after development of the tailored nanomaterial*

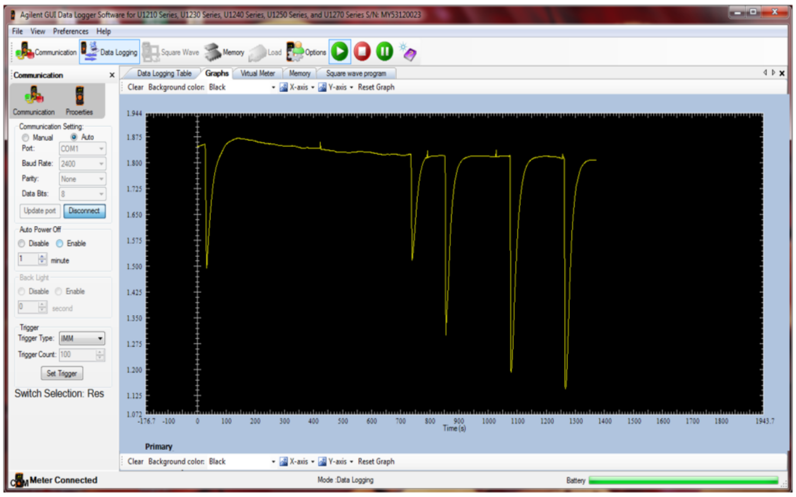
Agilent GUI Data Logger Software for U1210 Series, U1230 Series, U1240 Series, U1250 Series, and U1270 Series S/N: MY53120023

Communication Setting: ○ Manual ● Auto
Port: COM1
Baud Rate: 2400
Parity: None
Data Bits: 8
Auto Power Off: ○ Disable ● Enable
1 minute
Back Light: ○ Disable ○ Enable
0 second
Trigger Type: IMM
Trigger Count: 100
Switch Selection: Res
Background color: Black
Meter Connected
Mode :Data Logging

Fig. 3.17. *Graphical user interface (GUI) for data logging of the sensors*

Chapter 4

Creation of exotic morphologies of ZnO and their carbon monoxide sensing

This chapter introduces the second sensing material, namely zinc oxide through its physicochemical properties adopted from literatures. Zinc oxide is a versatile material whose electronic properties can be better manifested through rendition of distinct morphologies to its crystals. The chapter delineates the sonochemical synthesis approach for production of different superstructures of zinc oxide. The chapter then delves into the mechansim working behind formation of such morphologies. The sensing performances of the superstructures are then discussed which were found to be inadmissible in comparison to the tin dioxide based sensors elucidated in the previous chapter. An alternate approach, namely templated syntehsis of zinc oxide crystals was adopted with two different templates which yielded a slightly better results. Some of these ZnO superstructures were subsequently utilized for detection of volatile organic compounds, to be described in the next chapter.

List of Sections

Contents of this chapter are partially based on following publication

[1] S. Ghosh, D. Majumder, A. Sen, S. Roy, "Facile sonochemical synthesis of zinc oxide nanoflakes at room temperature", Materials Letters vol. 130 (2014) pp. 215-217.

4.1. Introduction

The previous chapter elucidated development of tin dioxide based carbon monoxide sensors. The efficient modules could detect carbon monoxide down to 1 ppm which is significantly below the statutory limits prescribed by different health regulatory bodies. However, sensing properties of metal oxide semiconductors are better manifested when the nanostructures are synthesized with controlled morphology for specific applications. Rendition of such unique superstructures is relatively simpler for zinc oxide owing to its distinctive lattice properties. Along with the presence of an unique polar plane which can be deliberately modulated to form various heterostructures, zinc oxide (ZnO) as a material of special interest has coveted optical, semiconducting and piezoelectric properties for sensor applications. While, a direct wide band gap of ZnO (~3.3 eV) is favourable for making semiconductor sensor modules, the electron mobility as high as 1000 $cm^2V^{-1}s^{-1}$ is ideal for fabricating nanoscale field-effect transistors [1]. The prospect of tuning these properties through a mere change in the morphology intrigues materials researchers as the requirement for introduction of external impurities is mitigated. For example, a dye-sensitized solar cell with its photoanode made up of ZnO nanoflowers exhibited 90% superior power conversion efficiency compared to that based on ZnO nanorod arrays [2]. In another study, clusters of ZnO nanosheets in a flowerlike configuration have been found suitable for chemical sensor applications [3]. The inherent property of zinc oxide to morph into two- or three-dimensional superstructures has been widely investigated and specific structures have been observed to be ideal for different applications.

Creation of such exotic morphological features, by tweaking growth parameters, often renders in tuned physicochemical properties that can be deployed for specific applications [4,5]. In this respect, one-dimensional (1-D) and quasi one-dimensional structures of ZnO, for example, nanowires, nanorods, nanobelts and nanorings, are perhaps the most widely explored variants of ZnO superstructures. A comprehensive survey on diverse techniques adopted for producing 1-D ZnO crystals has been summarised by Wang in his review article [6]. Apart from 1-D structures, distinct assemblies of two dimensional (2-D) and hierarchical three dimensional (3-D) ZnO structures have also grabbed special attentions due to their enhanced application specific attributes [7]. While nanoflowers and nanosheets are the more conventional superstructures, other types of morphologies, like nanotowers and nanovolcanoes also exist [8]. Additionally, unconventional nanostructures resembling combs, bowling pins, bottles, arrows, and nails have also been produced [9].

While the tailored synthesis of one- or multi-dimensional ZnO structures has generated special interest, it is also important to investigate the morphological transitions among these hierarchical structures. For example, by changing precursor concentrations, materials of varying dimensionality could exclusively be developed [10,11]. Additionally, optimization of growth criteria, like electrodeposition time, was found to be decisive in thickening of nanoplates and consequent formation of zinc oxide nanowalls [12]. In a separate study, Sounart *et al*. investigated secondary nucleation on primary ZnO crystals to generate hierarchical nanostructures [13]. In the aforesaid literature, one- or multi-dimensional superstructures were produced by modifying synthesis parameters, or through hierarchical growth approach, where higher-order morphology was achieved through augmentation of an existing structure. Nonetheless, an investigation of the interstructural transformation, where an initial 3-D structure is demolished to create new 2-D morphology from the remnants, has seldom been reported.

This chapter has thus been dedicated to elucidate the development of two- and three-dimensional hierarchical structures of zinc oxide through an optimised sonochemical method. Sonication technique used for implementing the structural evolution offers a range of advantages, like efficient conservation of energy and faster kinetics [14,15]. Additionally, the sonochemical technique facilitates the entire evolution to occur at room temperature, thereby rendering it as a green approach. At this point, it is imperative to mention the ability of sonochemistry to produce 1-D and 2-D ZnO nanostructures [16,17]. Jung *et al.* altered sonication time along with precursor concentration and capping agent to either promote or impede the inherent anisotropic growth of zinc oxide, and therefore could produce a variety of one- or multi-dimensional structures [18]. In a similar investigation, Zak and his colleagues produced hierarchical ZnO flowers from conglomerates of nanorods by varying the time for synthesis [15]. Sonication time was further proved to be crucial when multiple nanorods aggregated in presence of ultrasound energy to produce pin-cushion, cactus and nanopencils, thus rendering it as a key factor for structural transitions [19]. Although the aforementioned studies highlighted sonication-aided transformation of nanostructures, these were mostly confined to the transition of 1-D to 2-D structures. To date the evolution of a 3-D zinc oxide nanostructure into a 2-D arrangement is not known to be reported. In this chapter, a detailed account of sonochemical evolution of zinc oxide nanoflowers into nanoflakes, is reported which is a deviation from the standard hierarchical growth model. Interestingly, the entire process could be executed at room temperature. A plausible mechanism for the structural evolution process of ZnO is proposed.

However, the proposed nanostructures were observed to be limited in their applicability for detection of carbon monoxide due to high base resistance, ultimately making them unsuitable for electronic interfacing. Therefore an alternate approach of templated synthesis zinc oxide superstructures was also explored and has been presented in the later sections of this chapter. Templating is one of the most important techniques for the controlled synthesis of nanostructured materials. This powerful tool uses a pre-existing guide with desired nanoscale features to direct the formation of nanomaterials into forms that are otherwise difficult to obtain. As a result, templated synthesis is capable of producing nanostructures with unique structures, morphologies and properties. The general route for templated synthesis of nanostructured materials includes the following steps: (1) template preparation, (2) directed synthesis of target materials using the template, and (3) template removal (if necessary). Herein two non-colloidal templates were utilized for zinc oxide nanostructure development. The templates either act as platforms for anchoring the exotic nanostructures or impose its own morphology on the nucleated particles. An added advantage of templated synthesis is the achievable dispersion of the nanostructures. The de-agglomerated crystals offer larger surface area for the target analyte to transduce a greater signal.

4.2. Zinc oxide – a brief review of physicochemical properties

The physical properties for bulk zinc oxide crystals has been summarised in a tabular form and presented in **Table 4.1**. The parameter that enables its claim as a pertinent member of gas sensitive materials is its high electron mobility of 200 cm^2/V.s. However this value is pertinent to single crystals while the number is less than 100 cm^2/V.s for polycrystalline [20].

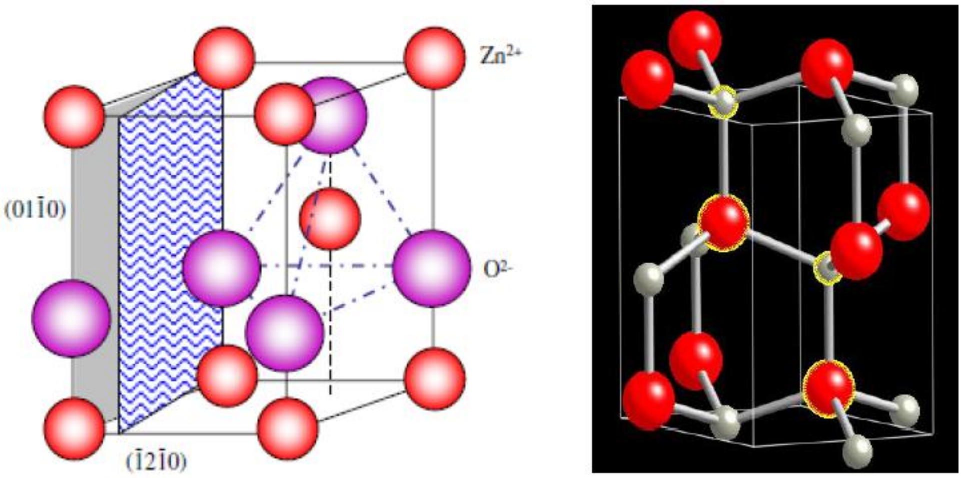

Fig. 4.1(a). *The hexagonal wurtzite structure model of ZnO and* ***(b)*** *tetrahedral coordination of Zn-O*

Additionally a high melting point in tandem with the wide band gap (3.4 eV) deems it suitable for applications at elevated temperature. Another attribute that aids precise characterization of ZnO nanoparticles is its high exciton binding energy of 60 meV. The high exciton energy compared to conventional semiconductors like gallium nitride (21 meV) and zinc selenide (20 meV) projects zinc oxide as a potential functional material with excellent optical properties [21]. However, these values are typical for single crystal and perturbations of the crystals morphology provide the opportunity to tailor some of these attributes without introduction of external additives. This is critical in maintaining the pristine nature of the ZnO crystals so as to load them with catalytic additives fit for improving the sensing response. For example, Al-Gaasani and his group observed a prominent change in the optical gap among different synthesized superstructures [22]. Such deviation allows the sensors fabricated with them to be operated at different temperatures and enhance the selectivity towards the target. The change in these exotic structures can be imposed through different approaches, although owing to the simultaneous presence of polar and non-polar lattice planes, a simple change in the growth ambience during the nucleating stage has been observed to be enough.

Table 4.1. *Physicochemical properties of zinc oxide*

Property	**Value**
Molecular formula	ZnO
Molar mass	81.40 g/mol
Density	5.606 g/cm^3
Melting point	1975 °C
Solubility in water	0.16 mg/100 mL
Refractive index	2.0041
Lattice Constants	a_o = 0.32469 Å c_o = 0.52069Å
Relative Dielectric Constant	8.66
Energy Gap	3.37 eV Direct
Intrinsic Carrier Concentration	< 10^6 /cc
Exciton Binding Energy	60 meV
Electron mobility (at 300 K)	200 cm^2/V.s.
Hole mobility (at 300 K)	5-50 cm^2/V.s

Zinc oxide crystallizes into either of a more common wurtzite form or adopts a zincblende structure. The wurtzite structure has a hexagonal packing (space group C6mc) with lattice parameters a = 0.3296 and c = 0.52065 nm. A ratio c/a ~ 1.6 further indicates at an ideal hexagonal lattice [23]. The structure of ZnO is formed by number of alternating planes composed of tetrahedrally coordinated O2$^-$ and Zn^{2+} ions, stacked alternately along the c-axis

(Figure 4.1). The tetrahedral coordination in ZnO results in non-centrosymmetric structure which produces a polar surface is the basal plane. The oppositely charged ions produce positively charged Zn-(0001) and negatively charged O-$(000\bar{1})$ surfaces, resulting in a normal dipole moment and spontaneous polarization along the *c*-axis as well as a divergence in surface energy. To maintain a stable structure, the ZnO- ±(0001) polar surfaces generally have facets that are atomically flat, stable and without surface reconstruction. The other two most commonly observed facets for ZnO are $\{2\bar{1}\bar{1}0\}$ and $\{0\bar{1}10\}$, which are non-polar surfaces and have lower energy than the {0001} facets [6].

What make the formation of different heterostructures possible for zinc oxide are the anisotropic growth rates for different facets. Under normal conditions, ZnO crystals undergo anisotropic growth oriented along the *c*-axis to form nanorods[24]. Even the growth rates for aligned basal planes differ as the positively charged direction has a faster growth kinetics compared to the negative polar plane. A faster kinetics implies that the plane vanishes faster and therefore gives rise to nanopencils [25]. However, in presence of proper capping agents which might impede the characteristic growth along *c*-axis, the kinetics of other planes take over and accordingly a different superstructure is obtained. The growth rates of different zinc oxide planes can be summarised as $v(0001)>v(01\bar{1}\bar{1})>v(01\bar{1}0)>v(01\bar{1}1)>v(000\bar{1})$ [25]. This particular methodology has been adopted by researchers to produce different self assembled morphologies. The self-assembly often visible for ZnO crystals can be perceived as their effort to reduce the surface energy.

4.3. Sonication aided synthesis of ZnO nanostructures

Different structures of zinc oxide were produced by either impeding or promoting the growth rates along different planes. For the purpose, different surfactants of varying ionic nature were implemented. For generation of different shapes, zinc nitrate hexahydrate [$Zn(NO_3)_2{\cdot}6H_2O$, Sigma Aldrich, reagent grade, 98%], potassium hydroxide (KOH, Sigma Aldrich, ≥85%) were procured from Sigma Aldrich, Germany and used without further purification. While cetyltrimethylammonium bromide (CTAB, Sigma Aldrich, AR ≥99%) was used as a cationic surfactant, sodium dodecyl sulfate (SDS, Sigma Aldrich, AR ≥99%) role as anionic surfactant brought major transformation in the ZnO morphology. Polyethylene glycol (PEG, M.W. 4000) was used as a nonionic surfactant for modulating the growth pattern of different planes. Deionized (DI) water was collected from an ultrapure type I water purification system (Sartorius Stedim Biotech, Germany, model: arium® 611UF). Different amounts (0.5-1.0 g) of $Zn(NO_3)_2{\cdot}6H_2O$ and KOH were dissolved in 250 ml of DI water, followed by addition of a 10 ml of surfactant solution to the initial mixture. In presence of excess KOH, the solution lost its turbidity to become transparent, signifying the formation of tetrahydroxozincate $[Zn(OH)_4]^{2-}$, the basic growth unit of ZnO. Ultrasound energy, generated from a vibrational tip sonicator (Hielscher Ultrasonics GmbH, Germany, model: UP 200S, 200W, 24 kHz), was then imparted into the system for definite timeframes (3, 8 and 15 minutes) to facilitate precipitation. Another sample devoid of any surfactant was also precipitated as reference. The precipitate obtained at the end of each reaction period was sampled and characterized. The morphology of the ZnO structures was studied using FESEM (Carl Zeiss, Germany, model: Supra 35VP). The transitions among the hierarchical structures, manifested by preferential growth of crystalline planes, were probed by XRD (Bruker Corporation, MA, USA, model: D8 Advance, Cu K_α line). The optical properties of the ZnO structures were investigated by photoluminescence [Photon Technology International, NJ, USA,model: QuantaMaster™ 40], FTIR [Perkin Elmer, MA, USA, model: 1615 FTIR spectrophotometer] and UV-visible spectroscopy [Shimadzu Corporation, Japan, model: UV-2450 spectrophotometer].

4.4. Role of surfactants in generating different morphologies of ZnO

The evolution of different ZnO architectures depend upon the nature of mediating surfactant as well as on the amount of sonication energy imparted in the system. The qualitative measure of the sonication energy can be estimated from the quantum time frames for which the ultrasound energy was exposed to the system. It was observed that a mere change in the sonication period could transform a 3-D nanoflowers formed just after 3 minutes into 2-D nanoflakes after 15 minutes. The discerning role of surfactant lies not only as a pivotal surface directing agent but also in reducing the free energy of the system and facilitating nucleation. Additionally, surfactant reduces the surface tension of the medium and promotes easy transport of growth units. However, the surfactants mediated growth produce different hierarchical structures under similar growth conditions and therefore require individual assessment.

4.4.1. Cationic surfactant (CTAB) mediated growth

4.4.1.1. Variation in surfactant concentration

The influence of variation in growth parameters on the final morphology was analysed by exclusively varying the surfactant concentration and the sonication period. Morphological analyses of the as-synthesized ZnO materials were performed by FESEM studies. The representative SEM images are shown in **Fig. 4.2**, which reveal the role of surfactant in the evolution of microstructures. **Figure 4.2(a)** presents densely packed clusters of ZnO nanoflakes, which were synthesized at room temperature (27 °C) after 15 min of ultrasonication of the precursor in presence of 10 mM CTAB (surfactant). A magnified image (**Fig. 4.2(b)**) helps in size estimation of the nanoflakes, which are apparently 200 – 400 nm wide and a few nm thick [26].

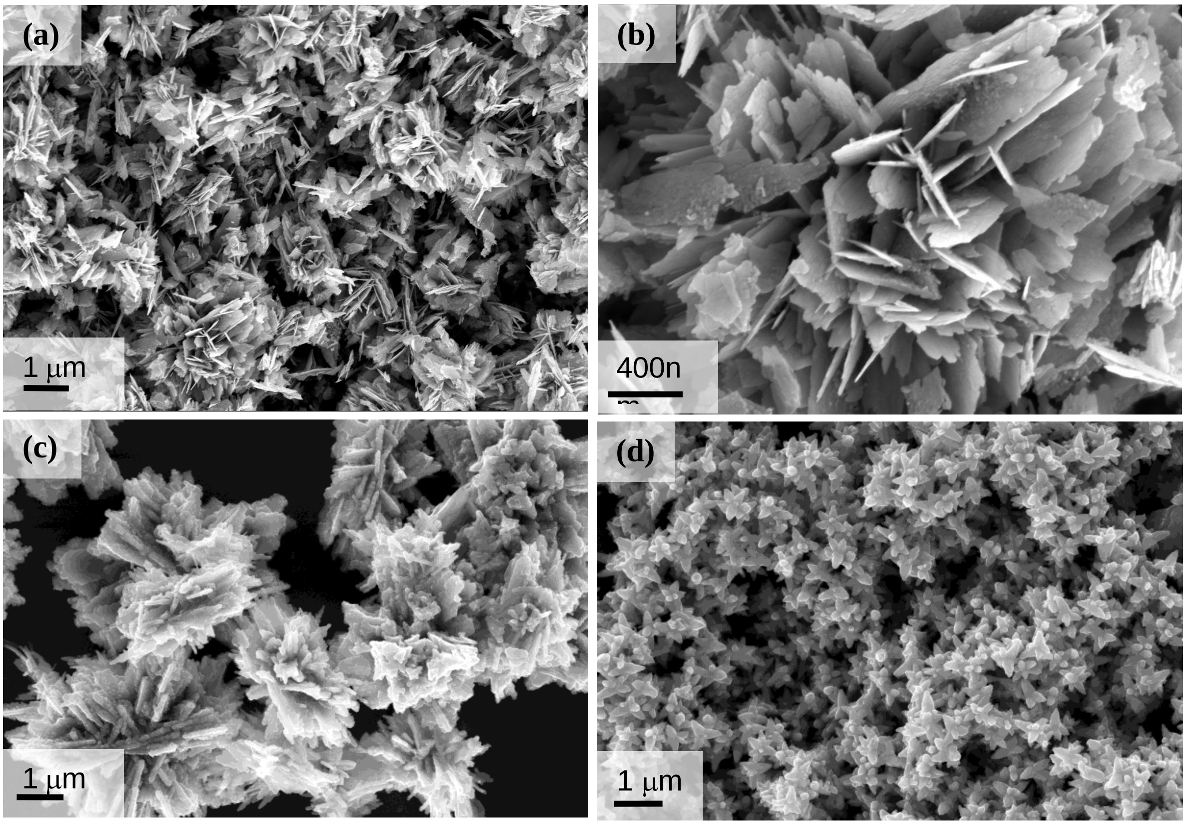

Figure 4.2. *FESEM images of sonochemically synthesized ZnO nanostructures for varying concentration of surfactant:* ***(a)*** *10 mM CTAB,* ***(b)*** *higher magnification image of a,* ***(c)*** *15 mM CTAB and* ***(d)*** *no CTAB. The precursor concentration and sonication time remain constant in all case*

Most of the flakes are vertically aligned and have a tendency to form clusters. It is worth mentioning that the surfactant plays a pivotal role in governing the reaction kinetics, the microstructures and the crystallinity of the synthesized material. As recently reported by Zhang et al., in absence of a surfactant, it may take up to 24 h for sonochemical synthesis of ZnO nanosheets from identical precursors [27]. The presence of CTAB (a cationic surfactant) reduces the surface tension of the solution. This decreases the activation energy for forming the new phase, and therefore ZnO nanostructures could be synthesized faster at a lower supersaturation temperature [28]. The formation of ZnO nuclei can be described by the following set of equations:

$$Zn^{2+} + 2OH^{-} \rightarrow Zn(OH)_2 \tag{4.1}$$

$$Zn(OH)_2 + 2OH^{-} \rightarrow [Zn(OH)_4]^{2-} \tag{4.2}$$

$$[Zn(OH)_4]^{2-} \rightarrow ZnO + H_2O + 2OH^{-} \tag{4.3}$$

Referring to equation 4.1, the Zn^{2+} and OH^- ions are generated from the hydrolysis of $Zn(NO_3)_2$ and KOH, respectively. In presence of excess OH^- ions, $Zn(OH)_2$ produces tetrahedral zincate ions (equation 4.2), which is the basic growth unit for ZnO crystal. The CTA^+ cations in the solution, generated by hydrolysis of the surfactant CTAB, electrostatically attract $[Zn(OH)_4]^{2-}$ anions to form complexing agents. The adsorption of these complexing agents on the periphery of the ZnO nuclei results in generation of active sites on the surface [29]. Thus, even at room temperature (27 °C) and within a short time (as low as 3 min), ZnO nanostructures can grow on those active sites. It is apparent that CTAB acts as a transporter of growth units and accelerate the formation of ZnO nanostructures. When the concentration of the surfactant was increased (15 mM), much wider and thicker plates for an identical synthesis time of 15 min were obtained, as shown in **Fig. 4.2(c)**. Also, an enhanced clustering of the plates, an effort to further decrease their surface energy in presence of excess CTAB, is apparent from the SEM image. On the other hand, when no surfactant is used, star-like 3D structures with smaller dimension were seen for a similar growth period of 15 min (**Fig. 4.2(d)**). It is interesting to note that identical starlet morphology could be observed for CTAB-mediated synthesis in an initial phase (3 min). The above observation suggests that a morphology evolution likely takes place from stars to flakes under ultrasonication and simultaneously ratifies the role of CTAB as a growth accelerator. The crystallinity and phase purity of the as-synthesized ZnO nanostructures were characterized by X-ray diffraction spectra. The influence of surfactant concentration on the crystallinity of the ZnO nanostructures is presented in **Fig. 4.3**. As presented in **Fig. 4.3**, all peaks could be indexed to hexagonal wurtzite ZnO crystal with a lattice constant of a = 3.25 Å and c = 5.21 Å (JCPDS Card #36-1451). No characteristic peak from any other material or impurity could be detected, thus ensuring the formation of pure phase ZnO at room temperature. Noticeably, the peaks corresponding to (101) plane are stronger than those associated with the (002) plane, implying a retarded growth along [001] orientation. Due to preferential growth along the *c*-axis, the reflections from the (002) plane should be strongest, as is observed for rod or wire-like structures of ZnO. However, in the present case, reflections from the lateral surface planes like (101) and (100) predominate over the (002) plane, indicating a departure from the *c*-axis growth. It is apparent that introduction of CTAB reduces the degree of crystallinity, which may be attributed to the expedited nucleation and growth as discussed above. For the samples synthesized with CTAB, the XRD spectra also reveal a shift in peaks (~ 0.25°), which might be a result of enhanced residual stress and defect concentration.

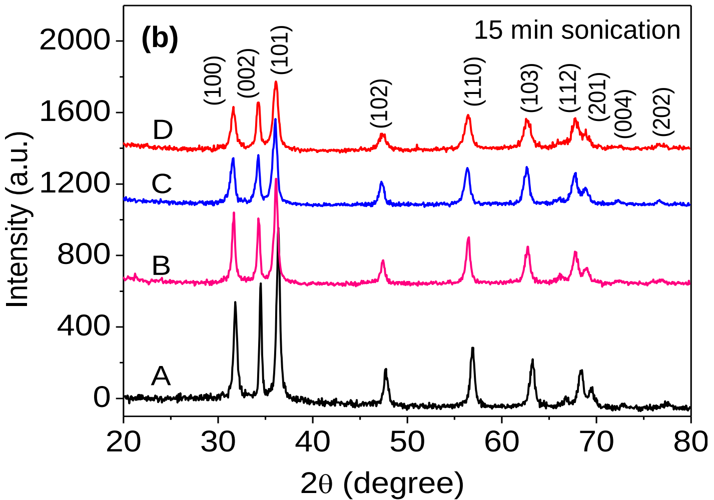

Fig. 4.3. *X-ray diffraction patterns of as-synthesized ZnO nanostructures for varying concentration of CTAB (A-D: 0, 5, 10 and 15 mM, respectively) for 15 min ultrasonication*

The room temperature UV-vis absorption spectrum of the sonochemically synthesized ZnO flakes is depicted in **Fig. 4.4**. The spectrum recorded for the particles dispersed in DI water reveals a characteristic peak of ZnO at wavelength 364 nm (equivalent to 3.4 eV), which can be assigned to the intrinsic band-gap absorption of ZnO as a result of the electron transitions from the valence band to the conduction band (O2p → Zn3d) [26]. The bandgap, E_g, from the UV spectrum was determined using the equation

$$\alpha h\nu = B\,(h\nu - Eg)^{n} \qquad (4.4)$$

where hν is the photon energy, α the energy absorption coefficient, B the absorption edge width parameter, E_g the band gap, and the exponent *n* depends on the type of optical transition in the gap region. Typically, n is ½, 3/2, 2, and 3 for transitions being direct and allowed, direct and forbidden, indirect and allowed, and indirect and forbidden, respectively. For ZnO, the band-gap is direct and transition is allowed and hence the value of exponent *n* should be ½. The intercept of the $(\alpha h\nu)^2$ vs. hν plot gives us an estimate of the band gap as 3.37 eV, which is consistent with that usually reported for ZnO.

To obtain the molecular fingerprint of the synthesized material, FTIR analysis was performed in the transmittance mode (**Fig. 4.5**). Two absorption peaks were observed at 425 cm^{-1} and 570 cm^{-1}, respectively, which correspond to the Zn-O bond. Based on the theory of average dielectric constant Vergés *et al.* proposed that, for 2D morphologies of ZnO, two peaks would appear at 406 cm^{-1} and 580 cm^{-1}, while a single peak would be observed for spherical structures [30]. In the present study, the appearance of two peaks is in good agreement with the observed flake-like 2D morphologies (**Fig. 4.2(a)** and **4.2(b)**). The absorption peaks at 1385 cm^{-1} and 1447 cm^{-1} might arise from CH_3 bending and CH scissoring, respectively. Additionally, the peaks at 2858 cm^{-1} and 2930 cm^{-1}, corresponding to the stretching modes of methylene groups, originate from the residual CTAB in the as-synthesized sample [26]. The band between 3300 cm^{-1} and 3600 cm^{-1} might be associated with the stretching vibration of the hydroxyl (O-H) bond, while that observed at 1640 cm^{-1} corresponds to the bending vibration of the H-O-H bond, representing adsorbed water molecules on the ZnO surface. Small undulations observed at 1040 cm^{-1} should relate to O-O bonds originated from the adsorbed oxygen species [31].

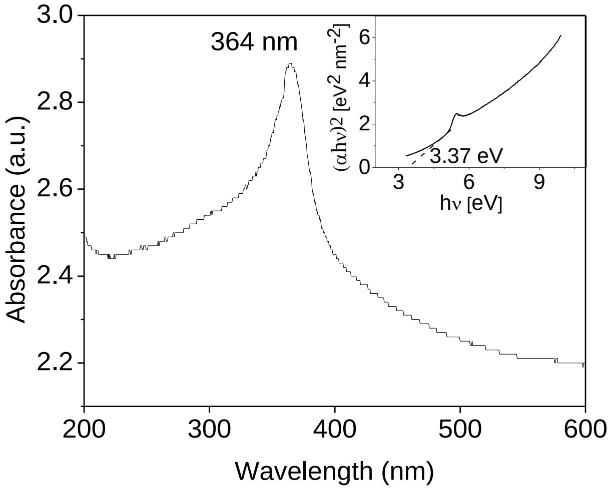

Fig. 4.4. *UV-Vis spectrum for the as-synthesized ZnO nanoflakes. Inset: changes of $(a\,hv)^2$ as a function of hv*

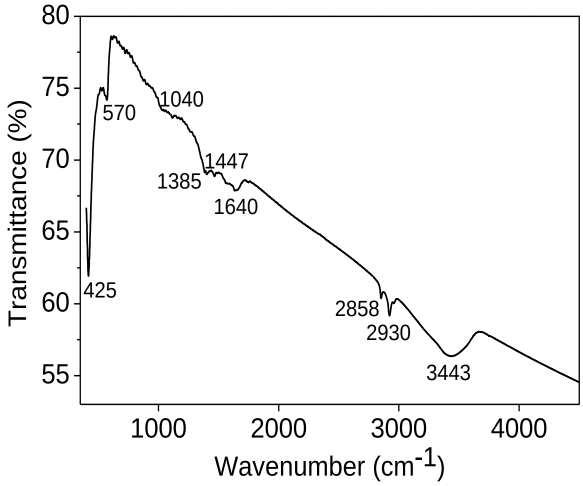

Fig. 4.5. *FTIR plot for the as-synthesized ZnO nanoflakes*

4.4.1.2. Variation in sonication period

The sonochemical method, deployed in the present study for implementing the structural evolution, offers a range of advantages, like efficient conservation of energy and faster kinetics. Additionally, the sonochemical technique facilitates the entire evolution to occur at room temperature, thereby rendering it as a green approach. A change in the sonication time seems to drastically modify the morphologies of the precipitate. In fact, sustained sonication causes a structural evolution from 3-D nanoflowers to 2-D ZnO nanoflakes. The structural evolution of ZnO nanoflowers to nanoflakes is presented in the FESEM images of **Fig. 4.6**. It can be seen that the nanoflowers [**Fig. 4.6 (a)** and **(b)**], formed within 3 minutes, gave way to the conglomerates of nanosheets [**Fig. 4.6 (c)** and **(d)**] when the sonication was continued for 8 minutes. On sustained sonication, two dimensional nanoflakes were obtained after 15 minutes [**Fig. 4.2(a)** and **(b)**]. While the tailored synthesis of one- or multi-dimensional ZnO structures has generated special interest, it is also important to investigate the morphological transitions among these hierarchical structures. Despite the keen interest in multidimensional structures of zinc oxide, an investigation of the interstructural transformation, where an initial 3-D structure is demolished to create new 2-D morphology from the remnants, has seldom been reported. Here a plausible mechanism of such morphological transition as a function of sonication time has been proposed. Thus a detailed account of sonochemical evolution of zinc oxide nanoflowers into nanoflakes, which is a deviation from the standard hierarchical growth model, has been provided.

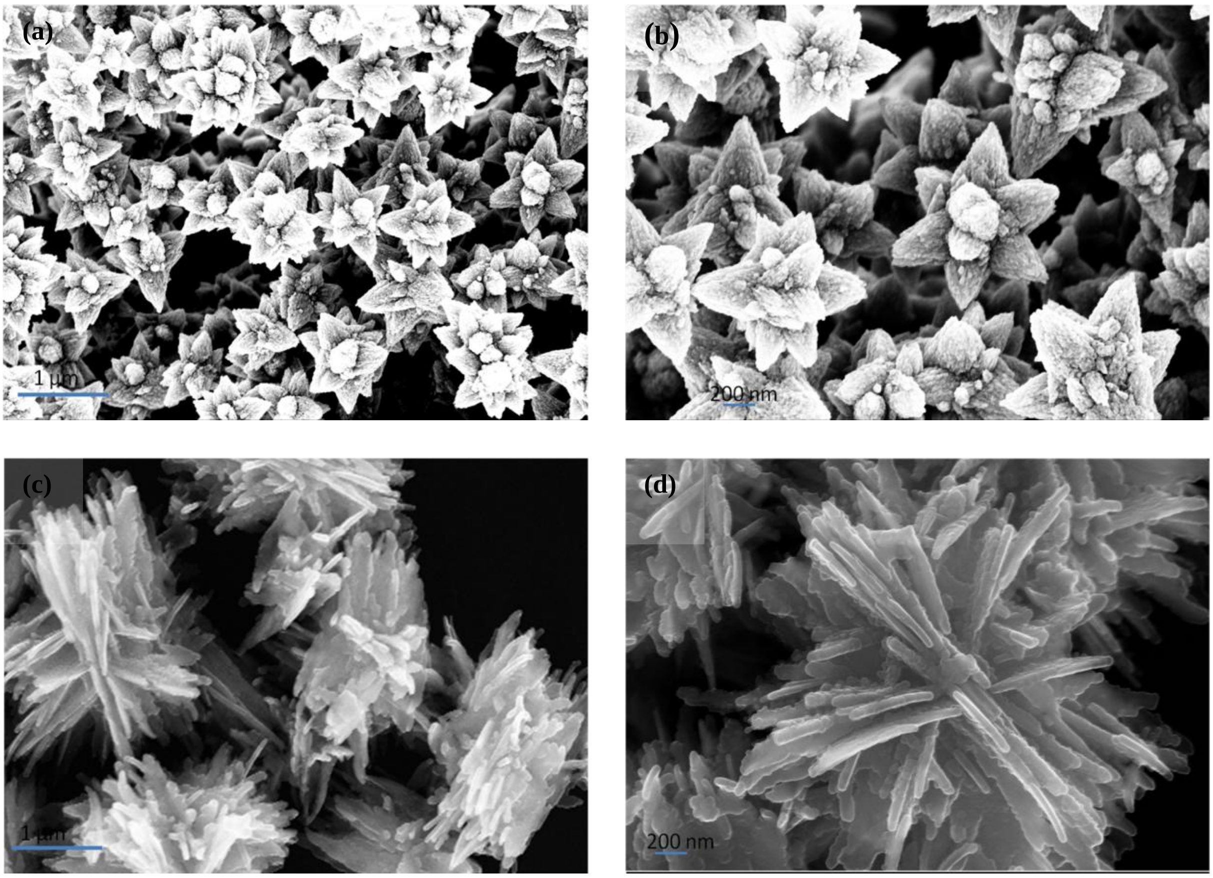

Fig. 4.6. *Ultrasound energy assisted room temperature structural evolution of ZnO* ***(a-b)*** *zinc oxide nanoflowers formed after 3 minutes, into* ***(c-d)*** *conglomerates of nanosheets formed after 8 minutes*

Structural Evolution from 3-D ZnO Nanoflowers to 2-D Nanoflakes

The first candidate in the series of the exotic hierarchical structures is the ZnO nanoflowers [**Fig. 4.6 (a)** and **(b)**], the formation of which from the zinc nitrate precursor in an alkaline medium is primarily governed by equations 4.1 – 4.3. According to equation 4.3, imparted ultrasonic energy at room temperature surrogates the requirement for thermal impetus, otherwise necessary for dehydration of the zincate ions and subsequent nucleation of ZnO crystals [28]. The temperature of the system was constantly monitored during sonication and was observed to be restricted within 27 ^{o}C. In addition, the presence of a cationic surfactant (CTAB) ensures rapid kinetics by maintaining a low supersaturation level. The surfactant lowers the free energy of the system and facilitates nucleation of ZnO seeds at lower supersaturation. Additionally, a reduced surface tension of the system eases the transport of growth units to nucleation sites by electrostatic pairing of CTA^+ and $[Zn(OH)_4]^{2-}$ ions [28]. Subsequently, post nucleation growth is governed by diffusion and accumulation of zincate ions on the surface of already nucleated particles [32].

To comprehend the effect of sonication, zinc oxide was simultaneously synthesized by heat induced precipitation at 70 °C for 15 min, thus negating the effect of ultrasound energy. Morphological comparisons between the samples prepared by the two methods revealed that ultrasound energy plays an influencing role in formation of distinct structures. The nanoflowers generated after 3 min of sonication resemble a natural flower (daffodil) with more prominence than the thermally precipitated samples. Even the kinetics for the ultrasound aided process is faster as sustained sonication for 15 min produced nanoflakes as the third product of evolution timeline. While nanoflowers were produced after 3 min for sonochemically synthesized samples, irregular structures, somewhat resembling flowers, could only be formed after 15 min for the other method. The XRD plot along with the FESEM images for the thermally precipitated samples are provided in **Fig. 4.7(a)-(b)**.

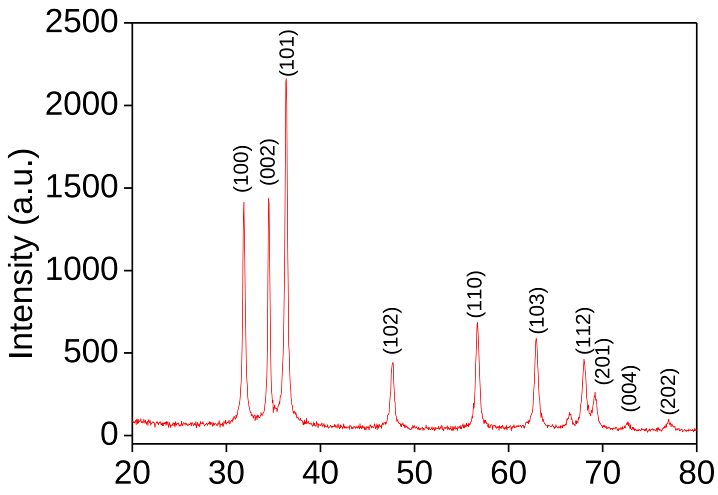

Fig. 4.7(a). *X-ray diffraction patterns of as-synthesized ZnO structures prepared by thermal precipitation at 70 °C for 15 minutes*

Inclination of ZnO crystals to form flowers can be derived from their tendency to twin along certain planes and form fourling structures. Fuller was the first to deduce that four acicular spines of zinc oxide tend to conjoint at equal angles, often resemble a star or flower shape [33]. While each spine signify a single ZnO crystal elongated along its respective *c*-axis, the twinning primarily occurs along (112) plane during the crystal growth phase to form the superstructures [34]. In addition, the acicular spines are webbed by interspatial nanosheets forming in between them. These intermediate sheets contribute significantly to the number of spines radiating from the base nucleus as well as provide supplements for increasing the girth of the existing spines. This occurs till the reactant concentration declines below a critical concentration, at which the growth of the hierarchical structure ceases with the onset of the solubility limit [32]. Beyond the solubility threshold, the dissolution/reprecipitation phenomenon governs the structural evolution of the zinc oxide crystals. The acicular spines get their tapered structure through local dissolution at their tips [35].

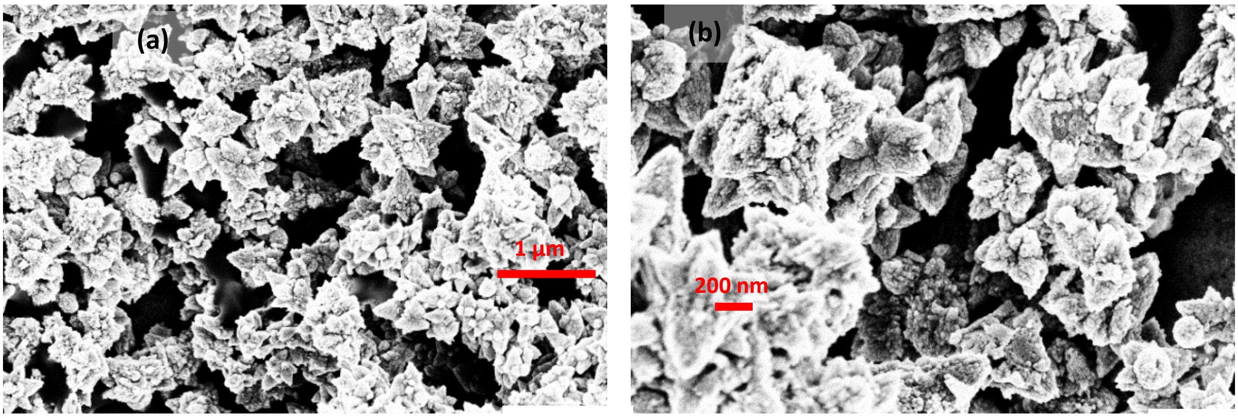

Fig. 4.7(b). *FESEM images of ZnO hierarchical structures synthesized by thermal precipitation depicting irregular and immature shapes of nanoflowers*

A basic understanding of the flower formation mechanism provides a better platform for envisaging the evolution trajectory. The second candidate in the evolution ladder is the ZnO nanosheets which form after 8 minutes of sustained sonication. An increase in ZnO flowers in the system manifests two exclusive phenomena; i) cessation of further nucleation due to monotonic decrease in the precursor concentration and ii) advent of a counteractive dissolution process, which causes disbanding of the flowers beyond the solubility limit. In the initial stage, the dissolution kinetics, represented by equation 4.5, is weak compared to the rate of nucleation and thus remains dormant while the nanoflowers are being formed [36]. But a rise in ZnO level beyond the solubility limit simultaneously recede equation 4.3, while promoting the dissolution process. The dehydration and dissolution processes marked in equation 4.3 and equation 4.5, respectively, are laced with spontaneous release of two hydroxyl ions into the system. Accumulations of these anions, in addition to the hydroxyl ions present due to excess KOH, enhance the basicity of the solution and promote the dissolution process further. Thus, under sustained sonication, as the rate of dissolution supersedes the rate of formation, the ZnO nanoflowers disband to regenerate zincate ions.

$$ZnO + H_2O \rightarrow Zn^{2+} + 2OH^- \tag{4.5}$$

$$Zn^{2+} + 4OH^- \rightarrow [Zn(OH)_4]^{2-} \tag{4.6}$$

A closer look at equation 4.3 and equation 4.5 reveals that these are counterproductive in nature. In other words, an increase in ZnO concentration would simultaneously promote equation 4.5 and impede equation 4.3, while the vice versa can be achieved through a rise in zincate ions. Thus, when continued dissolution increases Zn^{2+} concentration beyond a threshold within the system, sustained sonication re-triggers the kinetics for second phase nucleation of ZnO crystals (equation 4.6).

The interim ZnO nanosheets formed after 8 minutes of sonication, is seen through FESEM micrographs [**Fig. 4.6(c)** and **(d)**], where the images clearly depict a deviation from the original nanoflowers produced after 3 minutes [**Fig. 4.6(a)** and **(b)**]. The width of the sheets is largely regular, varying from 50 to 60 nm while the length and breadth of the sheets span within 200 and 600 nm. The affinity of ZnO nanosheets to form self-assembly might be perceived as their tendency to reduce the surface energy.

The nanosheets are basically the product of second phase nucleation and subsequent growth of ZnO crystals. In fact, both dissolution and re-nucleation processes further enriched the concentration of hydroxyl ions within the system. The excess OH^- ions eventually subdue the declining $[Zn(OH)_4]^{2-}$ concentration and get adsorbed in abundance on the Zn^{2+} plane through competitive binding [37]. The anionic OH^-, upon binding to the polar [001] plane, neutralizes the positive charge. Otherwise, negatively charged zincate ions would have attached to the Zn^{2+} plane, causing an anisotropic growth along the *c*-axis ([001] plane) and eventual formation of ZnO flowers with acicular spines. Since the preferred anisotropic growth is impeded by the abundant hydroxyl ions, the nonpolar planes with relatively higher growth rate, aided by imparted sonication energy, starts developing [38]. Retarded growth along *c*-axis coupled with developed nonpolar side planes results in the formation of nanosheets. A schematic diagram representing the entire evolution process has been shown in **Fig. 4.8**. when sonication was continued for 15 minutes [**Fig. 4.2(a)-(b)**].

The final member in the evolution series, self-assembled zinc oxide nanoflakes, was obtained when sonication was sustained for 15 minutes. The impression of the nanosheets can be observed in the nanoflakes through their similar dimensions, with an exception in the thickness of the two structures. While the thickness of the ZnO sheets ranged from 50 to 60 nm, the flakes appeared to be far more nimble with a thickness of few nanometers. This observation indicates that the dissolution phenomenon continued after formation of nanosheets, and resulted in corrosion of the ZnO nanosheet surfaces, thus decreasing the width.

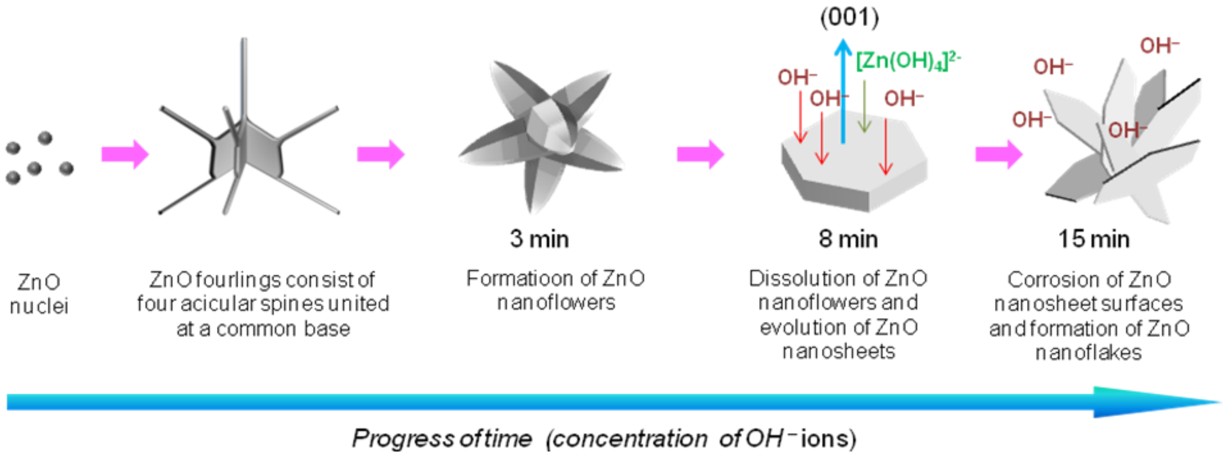

Fig. 4.8. *Schematic diagram representing formation of ZnO nanosheets from nucleation process*

Structural and optical characterization

Quality of the nanocrystals in terms of their phase purity and crystallinity was analysed by X-ray diffraction spectra, as shown in **Fig. 4.9**. All the peaks of the nanostructures conformed to wurtzite hexagonal ZnO crystal (JCPDS card No. # 36-1451), without any trace of probable intermediates or impurities. An increase in degree of crystallinity of the superstructures with sonication time is apparent from the gradually enhanced peak intensities (**Fig. 4.9**). With higher sonication time, the relative intensity of the (101) peak becomes stronger suggesting a gradually diminished growth along the (002) plane. Relative peak intensities corresponding to [101] plane is observed to be least for ZnO nanoflowers, while those generated from nanosheets and flakes show much higher values. This is expected as the nanosheets and flakes were produced by promoting growth along the [101] plane, and simultaneously impeding growth along the *c*-axis [001] direction. Moreover, full width at half maximum (FWHM) values for [101] plane decreases with sonication time and reaches minimum for nanosheets implying an improved crystal quality [39].

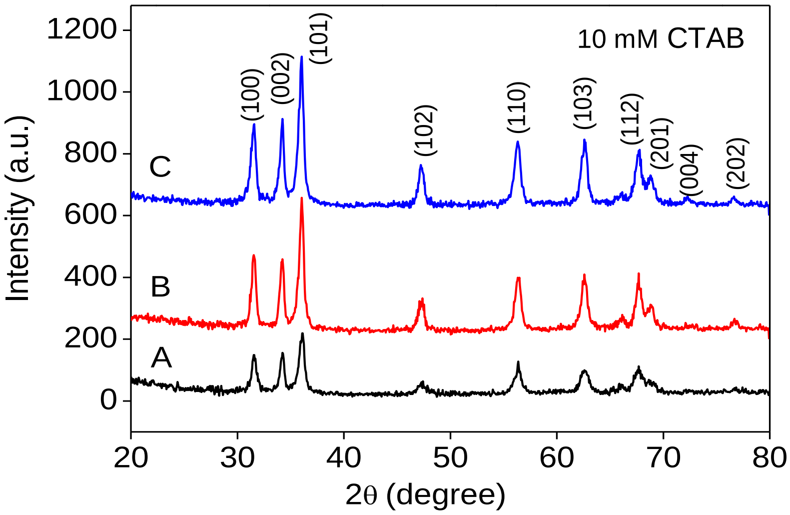

Fig. 4.9. *X-ray diffraction patterns of as-synthesized ZnO nanostructures for varying sonication time (A-C: Nanoflowers, nanosheets and nanoflakes respectively) with 10 mM surfactant*

Thereafter, the FWHM value increases for the flakes, indicating a decrease in crystallinity, probably due to the dissolution that occurs on the nanosheets surface. Simultaneously, a maximum value of 0.445^{o} along the [001] plane for nanosheets corroborates the retarded growth along this direction. The FWHM values for the synthesized nanomaterials and the corresponding crystallite size, as calculated from the Scherer equation, are provided in **Table 4.2**. The contrast between the sizes of observed particles in FESEM images (**Fig. 4.2** and **Fig. 4.6**) and the deduced crystallite size from XRD analysis infers that each particle consists of multiple crystallites, and thus possesses multiple grain boundaries. These grain boundaries along with corners and edges in the superstructure provide active sites for the dissolution to initiate [35].

Table 4.2. *Comparison of the crystallite size calculated from the XRD analyses with the observed dimensions in microscopic images for the ZnO superstructures*

Morphology	FWHM (101)	FWHM (001)	Crystallite size (nm) (XRD)	Particle Size (nm) (FESEM)	Microstrain (ε_{str})
Nanoflowers	0.569	0.391	15.33	600	0.0076
Nanosheets	0.443	0.445	19.71	300	0.0059
Nanoflakes	0.537	0.399	16.25	200	0.0072

The UV-Vis spectra for the ZnO structures obtained during the evolution process are presented in **Fig. 4.10**, where all the superstructures are observed to yield an absorption band centred around 360 nm. The maximum absorbance for the flakes and flowers occurs at 364 nm while the peak corresponding to the nanosheets is slightly blue shifted to 358 nm. All three absorption bands demonstrate a subtle blue shift from bulk ZnO, which has a characteristic optical band gap of 3.37 eV and an absorption peak around 367 nm. This blue shift can be directly related to the size-quantization effect owing to a reduction in crystallite size [40]. The relatively sharper peaks for nanosheets and nanoflakes signify an enhanced crystal quality [41]. The above observations are in good agreement with the inferences drawn from XRD analysis, which exhibited an increase in degree of crystallinity with sonication time. The band gaps for the superstructures were found to be greater than the typical value of 3.2 eV for bulk ZnO, in coherence with the demonstrated blue shift. While the nanoflakes and nanosheets provide a band gap of 3.37 eV, the nanoflowers had a slightly higher energy gap of 3.42 eV.

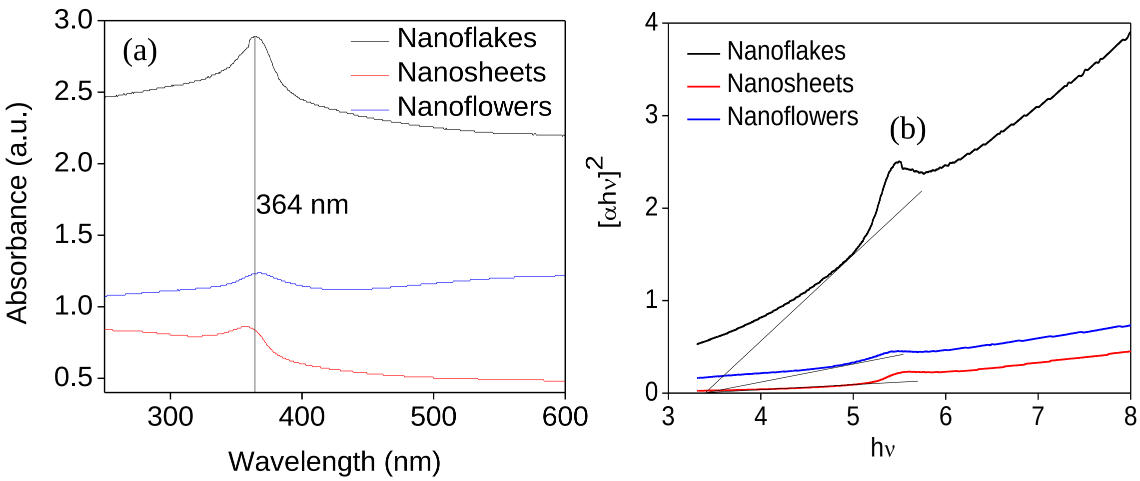

Fig. 4.10. *UV-Visible spectra for the synthesized ZnO structures showed a blue shift of 25 nm from bulk ZnO with the absorption peak centred around 360 nm*

The visible spectrum photoluminescence spectroscopy for the synthesized ZnO structures was carried out within a range of 350 to 650 nm with 360 nm excitation wavelength at room temperature. In general, the PL spectra of ZnO nanostructures comprises a UV-Near Band Edge (UV-NBE) band, and a broad green emission band in the visible range (400 to 750 nm) otherwise known as Deep Level Emissions (DLE). The DLE band arises due to the intrinsic defects present in the material, but the width of the band limits the identification of individual contribution from these defects [42]. In the present study, the characteristic UV-NBE band is observed to have undergone red shift for all the materials (**Fig. 4.11**). Plausible origin for the NBE band is the recombination of free excitons through interim collisions. In comparison, the visible band is better resolved and comprises an additional blue emission band centred at 470 nm along with the characteristics DLE related green emission band (550 nm) [30]. The blue band emission is ascribed to the donor-acceptor pair transition involving deep levels. However, the higher wavelength green emission band is sourced from interstitial oxygen and doubly charged oxygen vacancies [42].

Molecular fingerprints for the synthesized nanocrystals are obtained through FTIR analysis performed in the range of 400 to 4000 cm^{-1}. Since the spectra for the nanoflakes and nanosheets are similar, a representative FTIR spectrum of the nanoflakes has been shown in **Fig. 4.12**. The spectra for the 2-D structures differ from that obtained for the 3-D nanoflowers. Markedly, an extra absorbance peak, in addition to the common peak at 415 cm^{-1}, appears at 573 cm^{-1} for both the two dimensional morphologies. Based on the theory of average dielectric constant, this observation is in agreement with the FESEM images as 2-D slab like morphologies (sheets and flakes in the current study) are expected to generate dual peaks [30]. The synthesized materials showed remnants of CTAB, identified by small absorption peaks within 2820 cm^{-1} and 2980 cm^{-1}, indicating stretching of methylene groups present in the cationic surfactant [26].

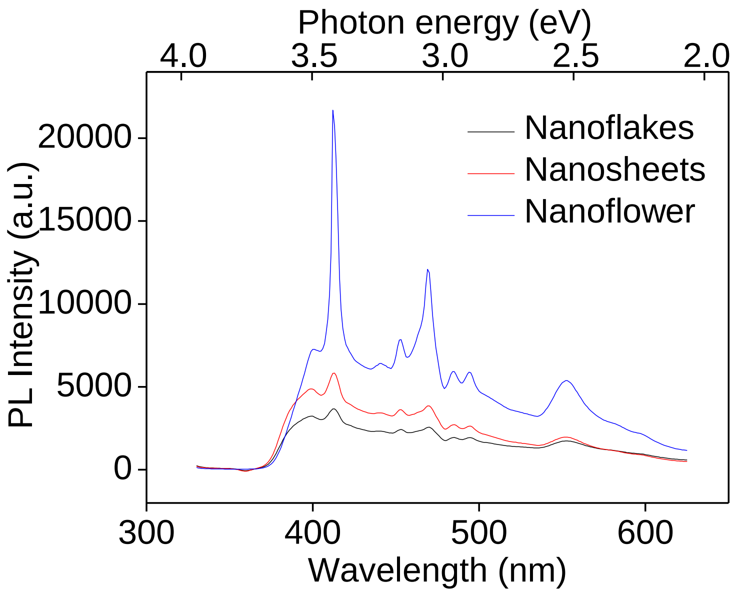

Fig. 4.11. *Photoluminescence spectra highlighted an additional blue band emission in addition to the characteristics UV-NBE band and green emission band in the DLE region*

Additionally, allied peaks at 1040 cm^{-1} and 900 cm^{-1} signify C=C stretching mode vibration, and thus further corroborates the miniscule presence of CTAB. The aforementioned peaks pertaining to the cationic surfactant are relatively intense for nanoflowers than their 2-D successors, thus implying a more prominent role of surfactant in the formation of flowers than flakes. The peaks appearing at about 1385 cm^{-1} and 1447 cm^{-1} may be linked to the C-H scissoring and CH_3 bending respectively [26]. The broad absorption band within 3300 cm^{-1} and 3600 cm^{-1} can be associated with the stretching mode vibration of O-H groups present on the surface. A relatively strong peak for the nanoflowers indicates the presence of higher number of functional hydroxyl groups on its surface than those on the nanoflakes. This might be explained by the fact that water molecules adsorb dissociatively on polar [001] surface and partly dissociatively on nonpolar [101] surface of zinc oxide, giving rise to dangling hydroxyl groups [43]. Since the nanoflakes are devoid of a distinct polar (001) facet, owing to the loss of intrinsic polarity through charge neutralization of Zn^{2+} plane by hydroxyl ions, the signal generated for hydroxyl groups in the IR spectra is relatively smaller for them. The weak band centered at 1610 cm^{-1} may be ascribed to the H-O-H bending vibration arising mainly due to the adsorbed molecules of water on zinc oxide surface [44].

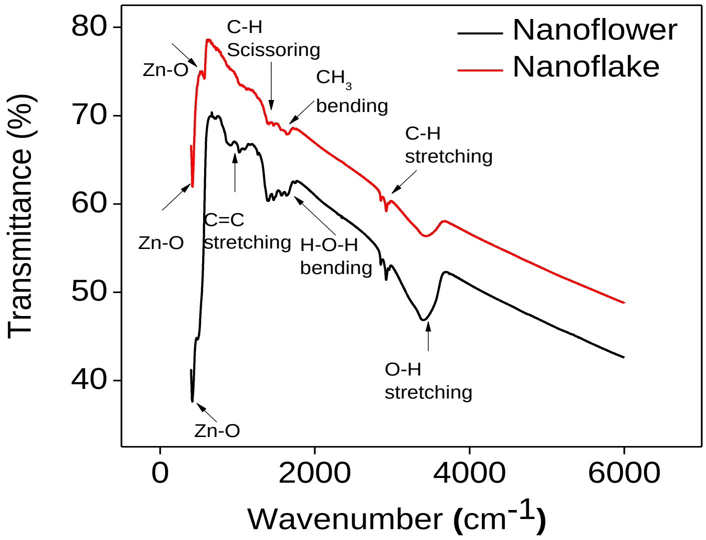

Fig. 4.12. *Molecular fingerprint of the nanostructures obtained via FTIR revealed distinct features between the nanoflakes and nanoflowers in terms of additional peaks and absorbance intensity*

4.4.2. Nonionic surfactant (PEG) mediated growth

Nonionic surfactants are mostly utilised for wrapping ceramic nanoparticles and disperse them uniformly. The wrapping aids in prevention of the agglomeration among nanoparticles. Additionally, the surfactant backbone possibly acts as nucleation centres for bigger zinc oxide particles. Polyethylene glycol with a molecular weight of 4000 was used as a surfactant in synthesis of zinc oxide nanoparticles. When the concentration of the surfactant was varied, exotic nanoflowers were obtained for a precise amount of 1 g, while irregular cones of zinc oxide were obtained for other PEG quantities. This observation is in agreement with the findings of Li *et al.* who proposed that specific concentration of PEG produced definite morphology while all other amounts reuslted in irregular crystals [45]. The entire range of superstructures produced through variation of the surfactant amount has been depicted in **Fig 4.13(a)-(f)**. While the irregular nanocones are much smaller with dimensions well below 100 nm, the flowers pose a much larger expanse of about 3 micrometer while the girth of the basal nodule was observed to be approximately 500 nm. Such large assemblies, though exotic in their structural features, are unsuitable for sensing applications. Closer inspection of magnified images reveal the nanoflowers to be self assemblies of ZnO nonorods that have fused together to optimize their surface energy.

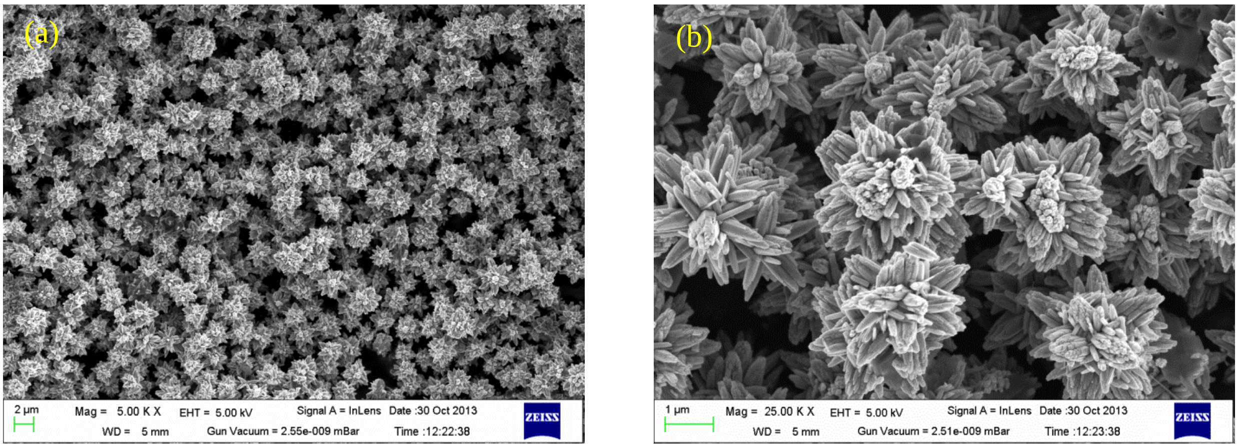

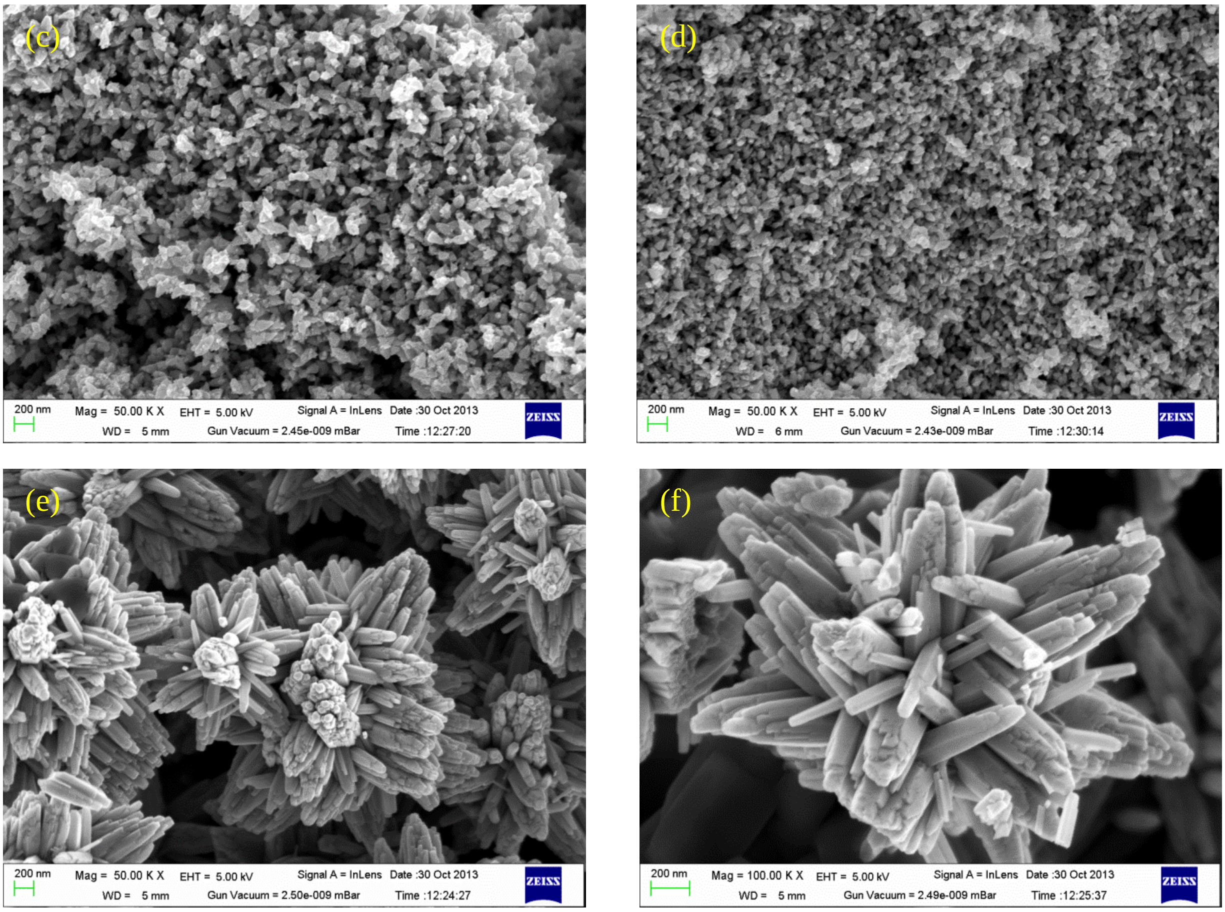

***Fig. 4.13.** Microscopic images for nonionic surfactant mediated synthesis of ZnO crystals with **(a)-(d)** 1 g PEG **(e)** 0.5 g PEG and **(f)** 1.5 g PEG*

The phase purity of the synthesized particles was established through XRD analysis which has been presented in **Fig. 4.14**. As observed previously, precipitation under sonication does not produce any undesired phases of zinc oxide. All the peaks presented in **Fig. 4.14** conform to wurtzite hexagonal structure of zinc oxide. However, the variation in the relative peak intensities clearly indicates at different degree of crystallinity. While the nanoflowers comprising of fused nanorods are highly crystalline with an intense [002] plane, the smaller nanocones are characterised with relatively broader peaks and lower intensities.

The UV-visible plot for the different shapes of ZnO nanoparticles have been presented in **Fig. 4.15**. The plots for all the superstructures have a characteristic absorbance peak centred at 364 nm corresponding to approximately 3.40 eV. An interesting observation from the UV-plot is the diminished peak intensity for the nanoflowers which correlates with the salient findings from the x-ray spectra about a high degree of crystallinity for this composite. This is compounded by a relatively sharper peak observed for the nanocones which suggest inferior crystallinity for them.

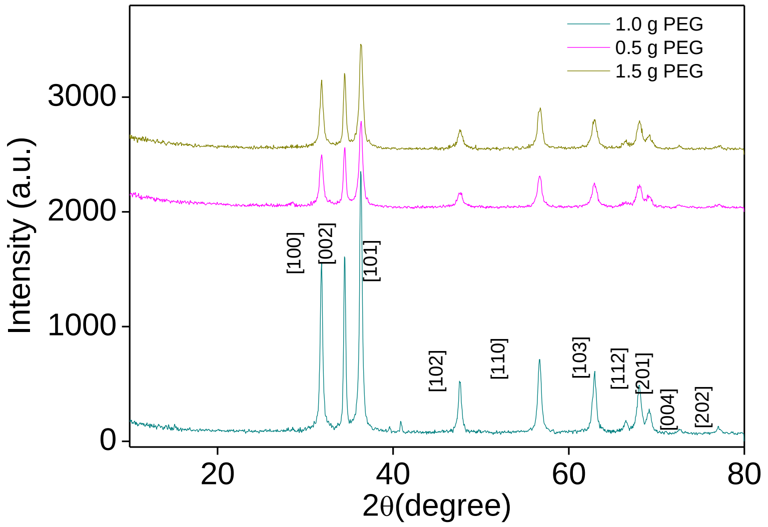

Fig. 4.14. X-Ray spectra for PEG mediated synthesis of ZnO crystals

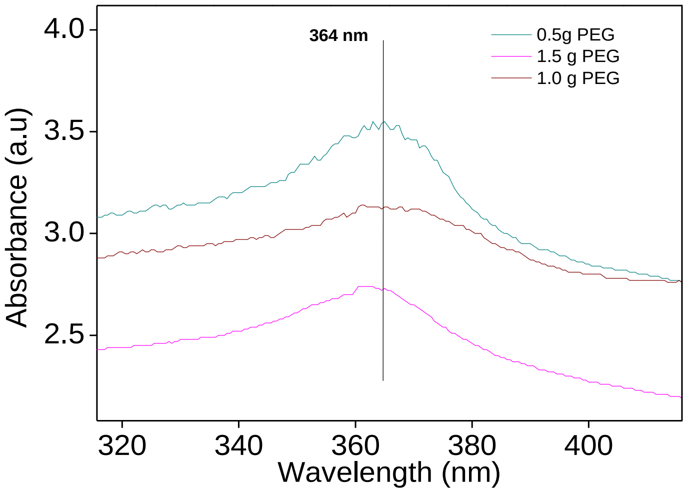

Fig. 4.15. UV-Visible plots for the PEG mediated synthesis of ZnO nanocrystals

The formation mechanism of PEG mediated ZnO nanoflowers can be ascribed to the tendency of polyethylene backbone to form coils in presence of OH^- ions which are provided by the initial KOH. In presence of zinc nitrate this coils form tubular shapes, with PEG chains wrapping each other along with the intermediate metal oxide colloids [46]. In presence of sonication energy these tubular shapes coalesce to portray the image of self assembled flowers of nanorods. This is done as an attempt to optimize the surface energy acquired from sustained sonication. An additional role for PEG is to facilitate easy transportation of the zincate growth units by adsorbing them on the oxygen species of its C-O-C skeleton [47].

4.4.3. Anionic surfactant (SDS) mediated growth

The anionic surfactants are laced with a negatively charged head which is often used as a capping agent on the [001] plane of zinc oxide to impede its growth. Sodium dodecyl sulfate has been used as the capping agent for the present scenario. The anionic surfactant mediated synthesis produced the standard zinc oxide hexagonal platelets, along with particles with different number of edges [**Fig. 4.16**].

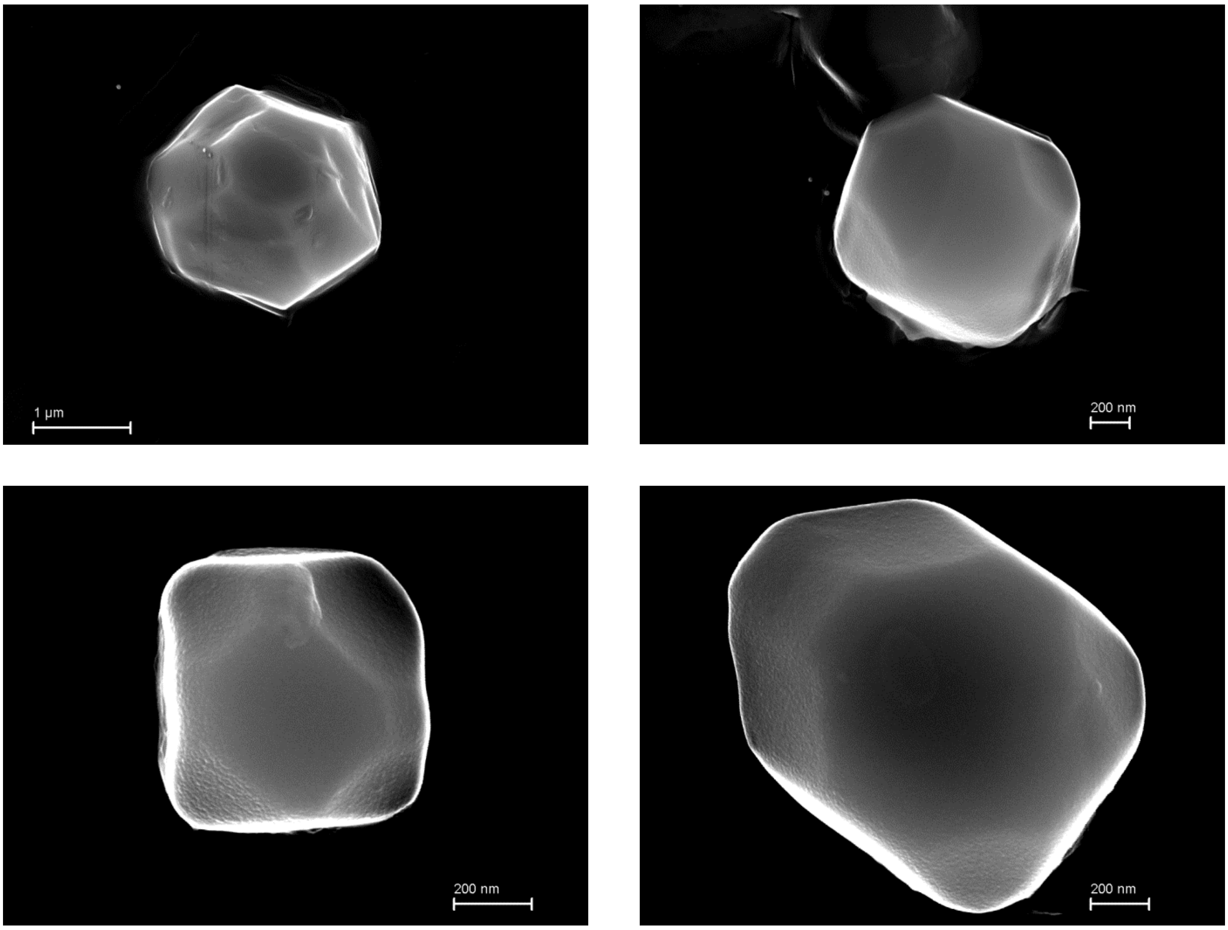

Fig. 4.16. *Anionic surfactant (SDS) mediated growth of zinc oxide nanocrystals*

Each of the structures span from 1 to 2 micrometers with contours of the nanoparticles presenting well defined edges. It is presumed that SDS in their exertion to cap crystal planes actually adsorbs on multiple facets with different degree. The adsorption on the [001] plane is much stronger due to the coulombic interaction between the negative sulphate ends of SDS and positively charged polar plane thus limiting any anisotropic growth along the *c*-axis [48]. However, SDS limits other growth directions by adsorbing on them through simple van der Waals interaction, thus producing crystals with different vertices.

4.5. Carbon monoxide sensing with ZnO nanostructures

Although the surfactant mediated synthesis of zinc oxide crystals produced exotic structures, which might be noble and arouse interests from material perspective, their applicability for carbon monoxide sensing was limited. For compliance with the TLV mandates, carbon monoxide is required to be detected below 35 ppm for all practical purposes. Unfortunately the exotic structures failed to detect CO below the statutory limits. Though limited in their applicability for CO sensing, these structures could be effectively used for detection of volatile organic compounds, to be presented in the next chapter.

As the ZnO superstructures were unable to produce results in detecting carbon monoxide, an alternate approach was undertaken. A possible alternate strategy would be to load the zinc oxide crystals with specific additives for improving their response. An effort was made to load the zinc oxide nanoflower crystals with the calcium oxide, which loaded on SnO_2 crystals had significantly improved their response. The FESEM images presented in **Fig 4.17** show complete replacement of the 3-D nanoflowers structure with agglomerated calcium-loaded zinc oxide composite which were found to be unresponsive towards CO.

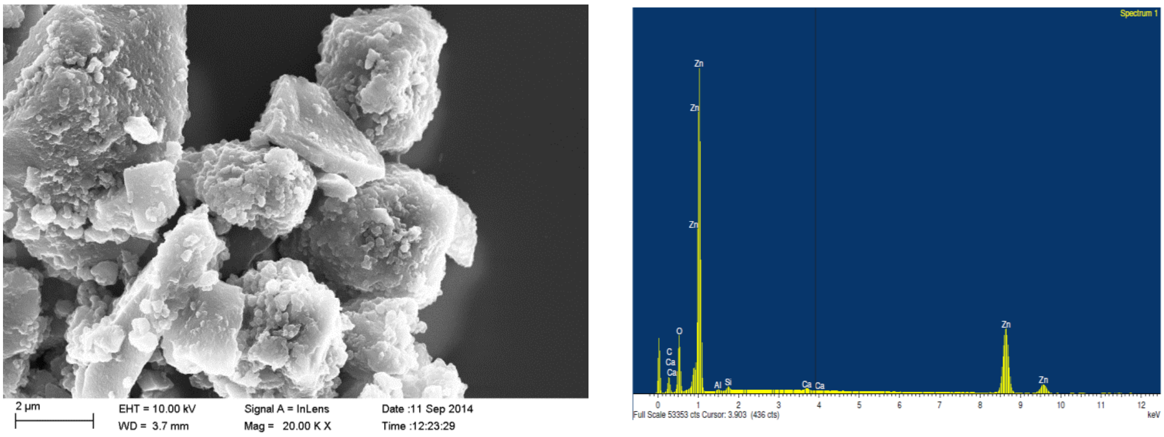

Fig. 4.17. *FESEM image of calcium loaded zinc oxide agglomerates with the EDX spectrum confirming the presence of calcium*

The observations with different morphologies regarding poor carbon monoxide sensitivity instigated to adopt a different methodology, where definite templates that act as structure directing agents for zinc oxide nanoparticles were used.

4.6. *In-situ* grown ZnO nanostructures on different templates for CO detection

The drive towards templated synthesis of ceramic materials has gained momentum over the last decade and currently boasts of a strong knowledge base [49,50]. More often than not, this approach has proven to be environmentally benign, exploiting the pertinent techniques of green synthesis. Zinc oxide, with its exclusive range of piezoelectric, optical and semiconducting properties, has not eluded the purview of this approach [51,52]. Different entities have either been strategically implemented or successfully mimicked [53] while producing this versatile metal oxide.

4.6.1. Growth of ZnO nanoflowers on egg shell membrane

While an immense number of natural products has been utilized as precursors in zinc oxide's production, an independent field of bio-inspired synthesis simultaneously investigated biomaterials as soft templates for nucleation and growth of ZnO nanoparticles [54,55]. Usually, biotemplated synthesis of zinc oxide implies that a naturally occurring substance has either been chemically modulated or utilized at its pristine self, on which metal oxide crystals are incubated. In the now-established biomorphic mineralization approach, which combines the nature optimized geometry with structural chemistry, the pertinent biomaterial acts as a structure directing agent and imposes the zinc oxide crystals nucleated upon it to imitate its dimension [56]. Employing sacrificial template is another prevalent modality in the domain of biotemplated synthesis. Investigations with different biomaterials as templates for producing zinc oxide crystals projected avian eggs as a resourceful alternative, with its surface dwelling functional moieties capable of anchoring the nanoparticles. Avian eggs are cheap, environmentally benign and naturally available which do not require any form of pre-processing. Shoeb et.al. produced phase pure zinc oxide nanoparticles by using egg albumen as biotemplate, and simultaneously investigated the superior anticandidal effects of the reactive oxygen species (ROS) released in presence of the synthesized nanoparticles [57]. But considering the high cytotoxicity demonstrated by ZnO nanoparticles towards zebra fish embryo models [58], the scope of this technique might be limited as production of zinc oxide would inevitably cause damage to the life-form.

Alternatively, shells are natural waste products from eggs which are disposed once the necessity of the egg has been met, either naturally or commercially. Therefore, implementing egg shells as biotemplates can be envisaged as analogous to recycling a waste product for a beneficial purpose. An exciting study was reported by Lee et.al. which explored egg shell membranes for synthesis of ZnO nanocrystals and investigated the resultant structures for their photocatalytic activities [59]. ESM was also used as a sacrificial template for synthesis of interwoven zinc oxide structures which preserved their morphology once the substrate was pyrolysed at elevated temperature [60]. Intrinsic to all these studies is the undisputed influence of ESM on ZnO morphology as the nanocrystals were imposed to follow the template’s structure. This in process limited the scope of tailoring the final structure of the synthesized ZnO crystals. It is well known that ZnO nanocrystals can be rendered different shapes and each of these morphologies exhibit varying attributes which might be exploited for range of potential applications. Thus, if the membrane could be used exclusively for nucleation, while the ZnO morphology could be tailored during crystal growth, it would retain the intrinsic properties of the particular morphology while simultaneously providing a soft backbone to the synthesized material. A relevant study was reported by Xu et.al. where ZnO nanoflowers were implanted on silk fibroin fibers [61]. Additionally, if the in-situ implantation is transpired at room temperature by effective implementation of sonochemical technique, it would be beneficial to establish the overall efficacy of the process.

In this study, sonochemically engineered room temperature nucleation and growth of zinc oxide nanoflowers on ESM biotemplate is reported. The ESM collagen fibers provide a stable platform for controlled incubation of ZnO particulates. The spatially located particles develop nanoflowers under sonication. The structural and optical properties of the templated nanomaterial have been investigated. A mechanism involving the synergistic contributions from the synthesis parameters, imparted ultrasonic energy and the surfactant has been proposed.

Synthesis process

Sonochemical technique was implemented for nucleating zinc oxide crystals on the ESM backbone following which the imparted ultrasound energy monitored the growth of the crystals into nanoflowers at room temperature In a typical synthesis, equal amounts of $Zn(NO_3)_2 \cdot 6H_2O$ and KOH were dissolved in 250 ml de-ionized water forming a transparent solution implying the formation of tetrahydroxozincate ($[Zn(OH)4]^{2-}$) complex. Additionally, 1 g cationic surfactant (CTAB) was added to the mixture. A acetic acid extracted native ESM section (1" x 1") was immersed in the solution following which the ultrasound energy was imparted into the system by an ultrasonic processor (Hielscher UP200S, 200W, 24kHz). The output energy for sonication was fixed at 60% of the maximum power and the intermittent pulse duration was preset at 3 min followed by 5 min of interval. Following three cycles of sonication (9 minutes), the immersed ESM section gathered white precipitate on its surface. The section was then taken out and studied for structural augmentations under an FESEM system. The ESM/ZnO section was simultaneously analysed for crystallinity and phase purity by X-Ray diffraction. Optical properties, which might be beneficial in deducing the application specificity of the ESM/ZnO, were analysed in the UV and IR range.

Anchored ZnO nanoflowers

Representative FESEM images of varied magnifications of the synthesized ESM/ZnO are shown in (**Fig 4.18(a)-(c)**). The images clearly depict anchored ZnO nanoflowers spatially located on the ESM strands. The images clearly highlight that the nucleation had transpired exclusively on the polymer fibers as all the flowers are evidently located on the network and not on vacant spaces. Closer assessment of a singly located nanoflower (**Fig 4.18(c)**) shows its diameter to be approximately 2 µm and comprising of multiple nanosheets fused together. The ZnO nucleation promoting role of CTAB and in the subsequent development of ZnO flakes/sheets was investigated. An additional role for CTAB can be assessed as CTA^+ forms an ionic pair with $[Zn(OH)_4]^{2-}$ ions. Under system's reduced surface tension the ionic pair moves to the ESM backbone and implants the primary growth unit for ZnO formation on the fibers. Following which, the imparted sonochemical energy is utilized by the zincate ions to dehydrate and nucleate as ZnO nanocrystals at room temperature.

Under sustained sonication, the crystals would have developed nanorods due to the characteristic anisotropic growth of ZnO crystals along *c*-axis. However, the formation of nanoflowers comprising an assembly of nanosheets might be inferred from the sonication aided precipitation-dissolution process illustrated in the scheme of **Fig. 4.8**. To establish the role of CTAB in implanting the flowers, a control experiment was conducted where non-ionic polyethylene glycol (PEG) replaced the cationic surfactant, with all other parameters remaining constant. The FESEM image (**Fig 4.18(d-e)**) for the nanoflowers produced with the control experiment portray a differing scenario from its previous counterparts. The images show that ZnO nanoflowers produced with PEG are not anchored to the ESM backbone, while they are completely rooted to the collagen fibers when CTAB is used. Therefore, the cationic surfactant is inferred to have a discerning role in anchoring the particles. The disparity among the ESM anchored nanoflowers synthesized with CTAB or PEG originates from the isoelectric point of the ESM network. The extremely basic environment created due to the KOH employed for synthesis renders the system's pH to cater around 10. The high value of pH implies a negatively charged surface for the ESM network [62] which attracts the ionic pair of CTA^{+}-$[Zn(OH)_4]^{2-}$ and anchors the moiety on the surface. Trace of the remnant CTAB on the ESM/ZnO surface was found from FTIR studies which corroborates the above observations. An extremely relevant study in this field has been reported by Li et.al. which suggests CTAB as a remedy to anchor zincate ions on negatively charged surface of silk templates [63]. An imperative clause for successful engineering of nanomaterials is the congruency among characterization techniques. The mandate is realized in the present investigation by correlating the FEEM images with XRD analysis (**Fig. 4.19**). As expected, the plot clearly signifies a hybrid structure and contains peaks pertinent to the ESM network and the ZnO crystals. The broad peak at 20^{o} might be ascribed to the sequence and conformations of amino acids present in an otherwise amorphous ESM network [64].

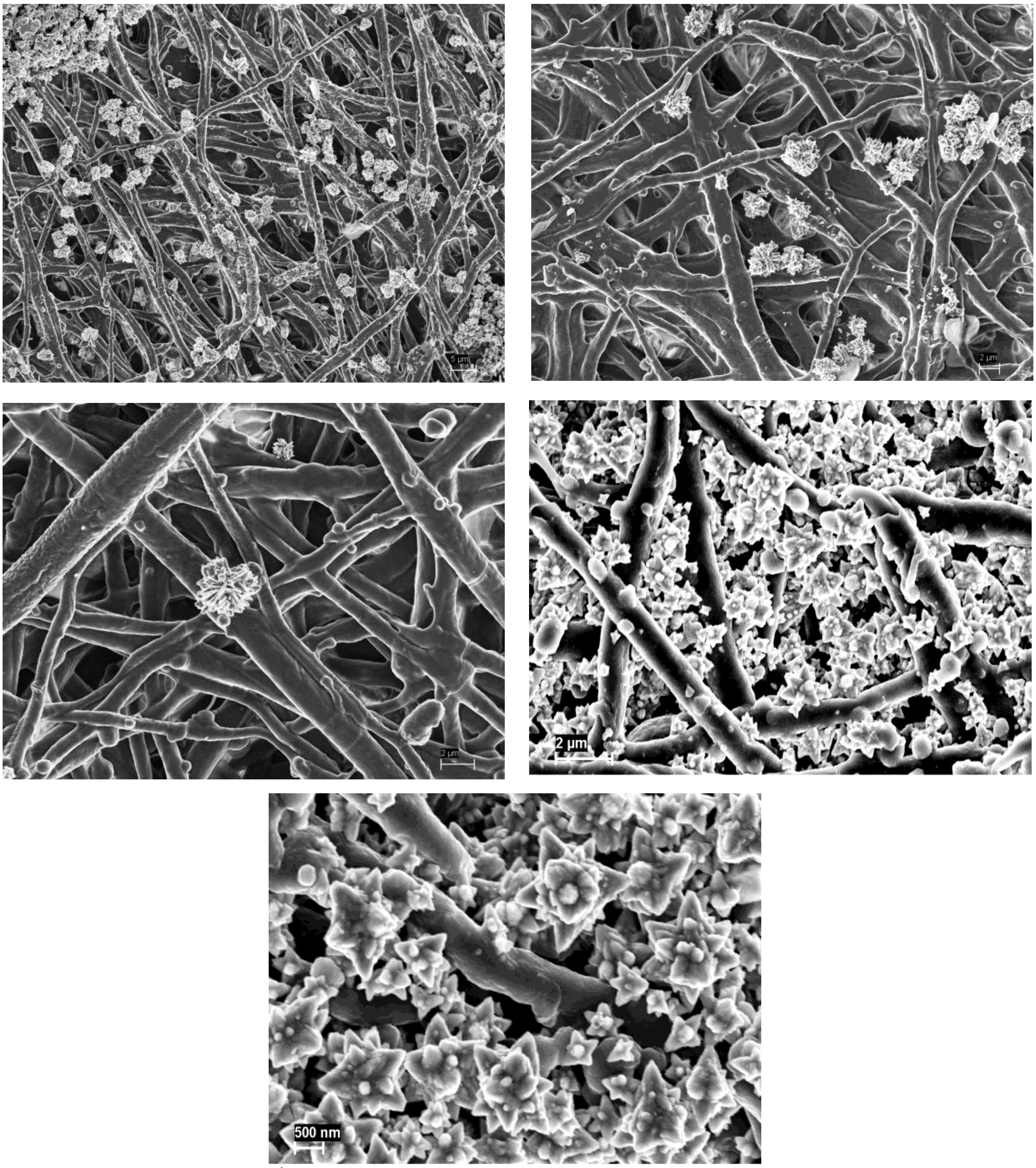

Fig. 4.18: *FESEM images of **(a-c)** ESM/ZnO synthesized with CTAB at different magnifications, **(d-e)** Zinc oxide nanoflowers synthesized with PEG not anchored on ESM*

The relatively sharp peak at 36.3^{o} corresponds to the [101] plane of ZnO crystals, thus signifying a retarded anisotropic growth of [001] plane which is in agreement with the FESEM analysis. The absence of characteristic sharp peaks of ZnO crystals might be due to the magnitude of the amorphous ESM matrix in comparison to the spatially located ZnO crystals.

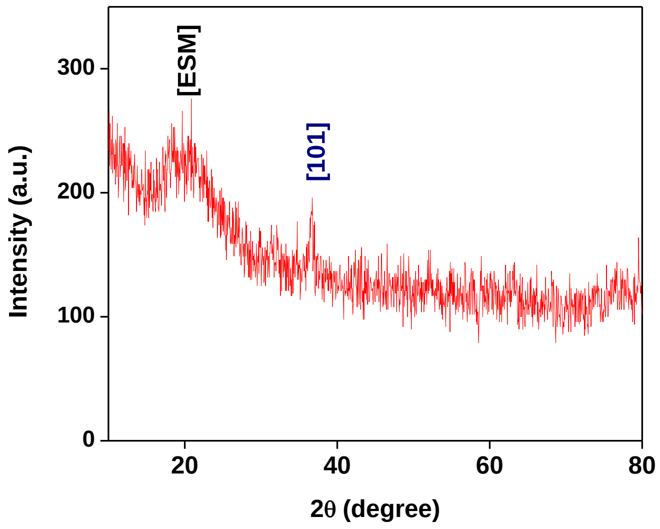

Fig. 4.19. *X-Ray diffraction patterns of room temperature synthesized ESM/ZnO hybrid*

Optical properties of the room temperature synthesized ESM/ZnO hybrid was analysed in the UV-range and shown in **Fig 4.20(a)**. The absorbance band within 300 nm and 327 nm, can be attributed to the aromatic amino acids present in the ESM [65]. A separate absorption band centered at 355 nm could be associated with the intrinsic band-gap absorption of ZnO as a result of the electron transitions from the valence band to the conduction band (O2p → Zn3d) [26]. The absorption peak shows a distinct blue shift of around 30 nm from the bulk ZnO [66], which in turn suggests a broadened band gap of ZnO crystal. The widened band gap, estimated using Plank's equation at 3.49 eV, is deemed favorable for the material to be utilized in applications like gas sensor and thin film transistors.

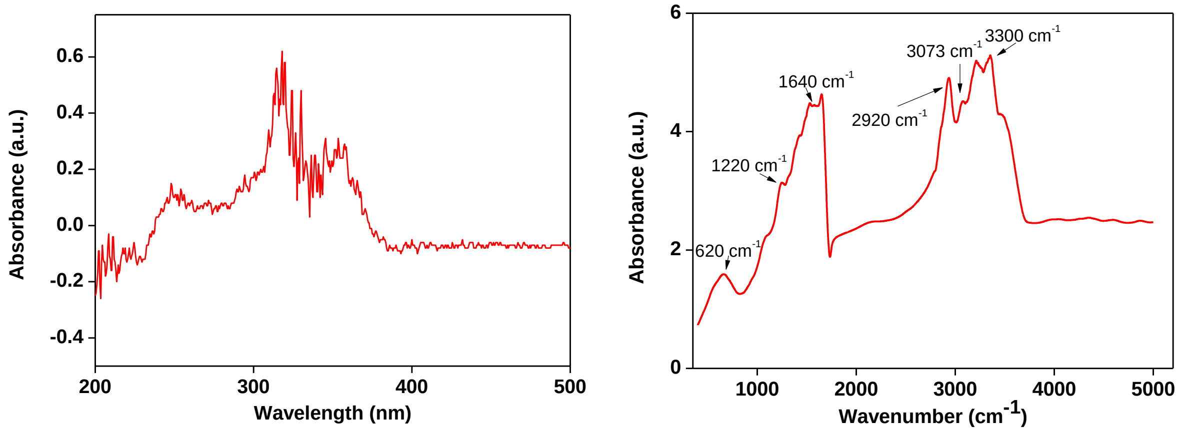

Fig. 4.20(a). *UV-Vis spectrum of the ZnO nanoflowers anchored on the ESM fibers*

Fig. 4.20(b). *FTIR spectrum of the ZnO nanoflowers anchored on the ESM fibers*

The molecular fingerprint of the synthesized composite was obtained by FTIR analysis (**Fig. 4.20(b)**) in the IR range (400-5000 cm^{-1}). Longitudinal vibrations corresponding to Zn-O bond, which are best observed within 400-650 cm^{-1} [26], is found to be centered at 620 cm^{-1} for the synthesized samples. The broad absorption band within 3200-3350 cm^{-1} appears due to stretching vibration of hydroxyl (O-H) bond while the band at 1640 cm^{-1} is associated to the bending vibration of H-O-H bonds present in the physisorbed water on ZnO surface [26].

Fingerprint of the ESM template is also visible in the spectra through an absorption peak at 1220 cm^{-1} which might be attributed to the amide III band relating to CN stretching of the glycoprotein mantle present in the polymer [67]. The peaks at 2920 and 3073 cm^{-1} correspond to the =C-H and =CH_2 asymmetry stretching modes associated with amide B [68] as well as from the remnant CTAB which administered the anchoring of nanoparticles on the egg shell membrane.

Carbon monoxide sensing with ESM/ZnO particles

Sensors were fabricated with the ESM anchored ZnO nanoflowers and deployed for sensing of carbon monoxide. The detection ability for these sensors were slightly superior compared to the prisine ZnO structures as the lower limit of threshold was found to be 30 ppm. The sensing plot when 30 ppm carbon monoxide at 250 °C was dispensed on the sensor surface is provided in **Fig. 4.21**.

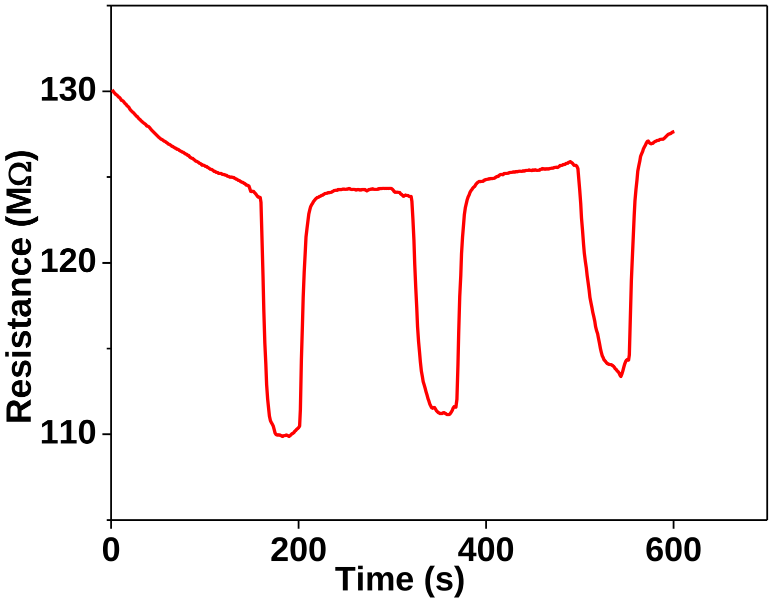

Fig. 4.21. *ESM/ZnO based sensor module showed sensitivity towards 30 ppm CO at 250 °C*

Though the sensors could detect 30 ppm CO, yet the sensitivity for them was much lower comapred to the SnO_2 sensors presented in chapter 3. Moreover, a high base resitance limits the scope of these modules to be interfaced in a standard electronic circuit for transduction. Since the performance of these sensors were found to be much inferior compared to SnO_2 sensors, therefore scope for further investigations with them were discarded.

4.6.2. Layered double hydroxide templated growth of ZnO hollow spheres

Layered Double Hydroxides (LDH) has received lot of attention as a template for synthesis of ceramic and polymers. The characteristic stacked layers of LDH offer interlamellar space where the basic growth units of the target material can be intercalated for incubation. The stacked structures render distinct shapes to the growing composites and can be selectively removed by changing the ambient pH. Layered double hydroxide has been successfully utilised as templates for synthesis of flaky carbon particles [69], controllable size distribution of CdS nanocrystals [70], where the anchored nanoparticles imbibed the templates form.. Zinc oxide has also been synthesized with LDH template as ZnO nanorods of controllable nanoscale diameter and length were grown on HTlc–$ZnAlCO_3$ layers [71]. While LDH has been used as structure guiding templates, its resourcefulness has also been utilised in development of zinc oxide through exfoliation and calcination [72]. The main drawback of functioning with LDH in association with metal oxide semiconductors is their relatively low thermal stability. While most MOS sensors operate at elevated temperature the LDH structures start to lose their integrity beyond 400 ^{o}C [73]. For synthesis executed at room temperature such templates retain their shapes and direct the nucleated particles to follow its form.

The initial concept for choosing LDH as a template was motivated by the possibility of replacement of the intercalated anions within the LDH structure by zincate ions, Thereafter sonication would have dehydrated the intercalated growth units into zinc oxide whose morphology would be governed by the layers of the template. Thus, successful optimization of the protocol would have resulted in ZnO nanosheets with width in the Angstrom order. Such nanosheets with lateral dimensions ranging in nanometers would have large specific surface area in the offering. The concept was mooted by the dimension compatibility of zincate ions estimated by hard sphere models and the intercalated anions.

Synthesis, structural and optical characterisations for the ZnO hollow spheres

For the present study, zinc-aluminium double layered hydroxide (ZnAl:LDH) was used as the template with intercalated nitrates and carbonates anions. The zinc hydroxide sol containing zincate ions was prepared by dissolving zinc nitrate and KOH in 250 ml DI water as elucidated in section 4.3. To the sol, 1 g of the LDH particles were mixed and the mixture was transferred into an autoclave where it was aged at 120 ^{o}C for 24 h. At the end of the stipulated period, the hydrothermally grown crystals of ZnO precipitate were collected and analysed for structural and sensing characterisations.

The structural features of the LDH templated zinc oxide have been presented in the microscopic images of **Fig. 4.22**. The intended zinc oxide nanosheets were not observed but instead hollow ZnO nanospheres were formed.

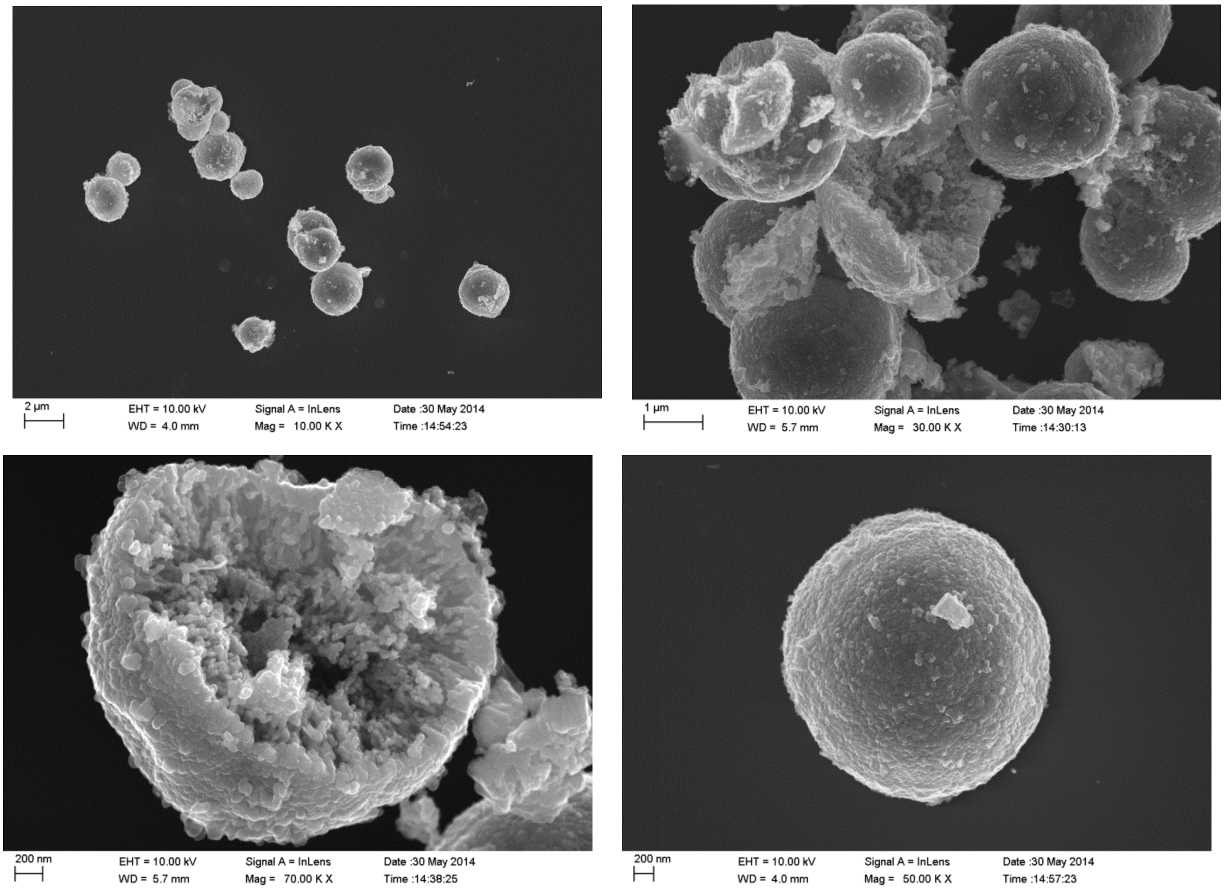

Fig. 4.22. *Different magnification images of LDH templated ZnO hollow nanospheres*

The spheres are uniformly distributed and have a radius of around 1 micrometer. These structures are unique in their form due to their intrinsic hollow nature which is visible whenever a particle is broken. The cavity within each sphere allows the possibility for more target molecules to adsorb and consequently an enhanced response pattern. On closer inspection each sphere is observed to be made of smaller granules of zinc oxide.

The XRD analysis performed on the hollow spheres show simultaneous presence of zinc oxide and α-alumina phases (**Fig. 4.23**). The peaks do not conform to any other phases pertinent to the anions present initially in the interlamellar space. The XRD plot reveals that the peak intensities for the spheres relevant to the [001] plane has a reduced magnitude in comparison to nanorods. This finding can be extrapolated from the isotropic growth resulting in spherical conformation. Lack of characteristic *c*-axis oriented growth translates into a reduced intensity for [002] plane.

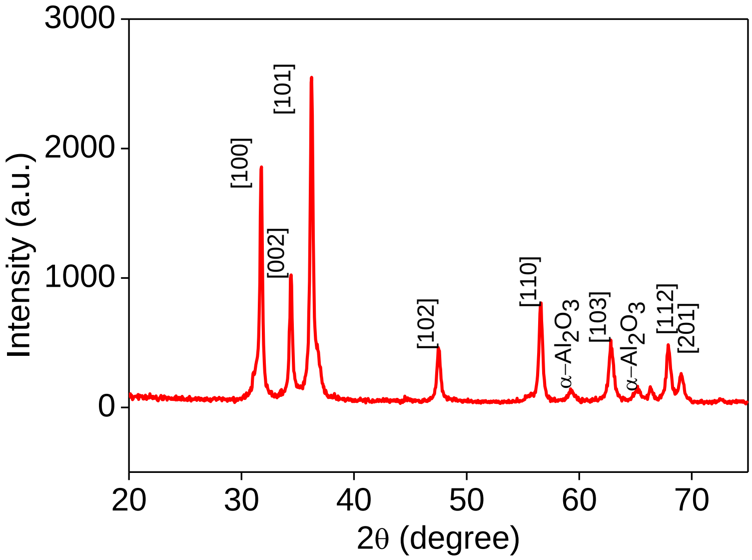

Fig. 4.23. *XRD spectra for zinc oxide hollow spheres*

Additionally, the FTIR spectra for the zinc oxide hollow spheres were recorded to assess the different surface moieties present. The spectra depicted in **Fig 4.24** revealed information which was otherwise inaccessible by other characterization tools.

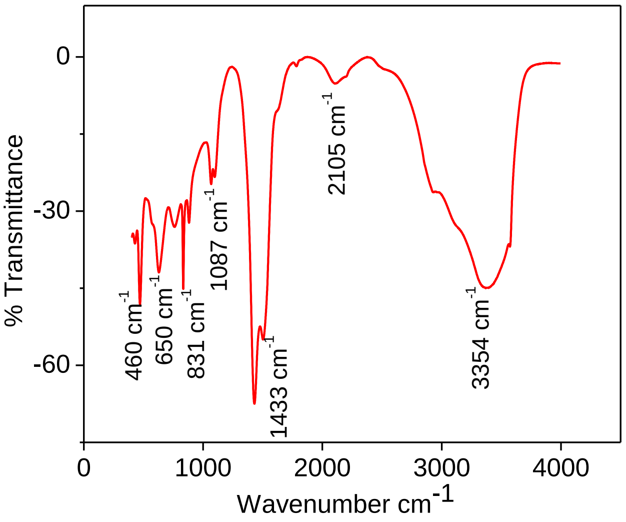

Fig. 4.24. *FTIR spectra of ZnO hollow spheres*

The presence of α-Al_2O_3 phase observed through XRD analysis is corroborated through two distinct peaks at 460 cm^{-1} and 650 cm^{-1} marked for Al-O_6 stretching [74]. The peaks within 450-750 cm^{-1} generally correlate to metallic bonds. The peak corresponding to ZnO vibration mode is generally observed at 450 cm^{-1} [26] and therefore the signature might have possibly merged with the alumina peak of 460 cm^{-1}. The peaks visible at 831 cm^{-1} and 1087 cm^{-1} might be ascribed to the –OH deformation and Zn-OH twisting respectively, while the broad transmittance region within 3000 cm^{-1} and 3350 cm^{-1} is produced through bulk hydroxyl vibrations [26]. The water association band is marked by a peak at 2105 cm^{-1} [75] while the intense peak at 1433 cm^{-1} might be ascribed to the C-H bending from the remnant surfactant.

Carbon monoxide sensing characterization

The sensing plots for the ZnO hollow spheres developed sensors for low ppm carbon monoxide has been presented in **Fig 4.25**. The sensing plot shows improvement in response for 10-30 ppm detection of CO compared to different morphologies of ZnO and the ESM templated ZnO nanoflower sensors. However, the response pattern seems to deteriorate with decrease in carbon monoxide concentration. The repeatability in response is decreased under 30 ppm which is marked by a larger error bar. The sensitivity of the LDH/ZnO hollow spheres when operated at 350 ^{o}C was observed to be around 23% for 30 ppm CO. Thus, despite their unique structures, the zinc oxide based sensors were found to be inferior in terms of performance when compared to their tin dioxide peers.

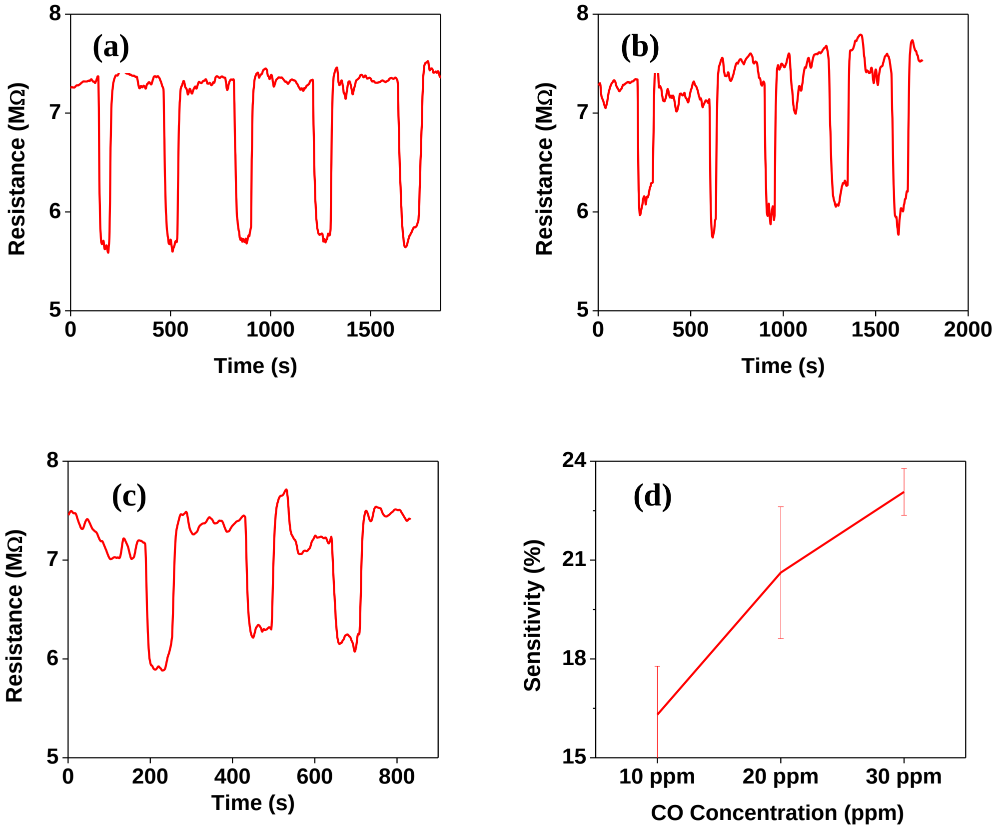

Fig. 4.25. *Dynamic sensor characterisation of ZnO hollow spheres at different concentrations of carbon monoxide at 350 ^{o}C for* ***(a)****30 ppm* ***(b)*** *20 ppm* ***(c)*** *10 ppm and* ***(d)*** *calibration plot*

4.7. Conclusion:

Zinc oxide crystals were engineered to give them different physical forms in order to improve the sensing performance towards carbon monoxide. The concept of manifesting better sensing performance through rendition of different hierarchical structures while simultaneously maintaining the pristine nature of the host lattice seemed intriguing. Two distinct methodologies were adopted for engineering the structural features of ZnO crystals, namely surfactant mediated and templated growth. Strategic optimisation in the growth criteria in presence of different surfactants with varying ionic affiliations resulted in formation of a gamut of superstructures including nanoflowers, sheets, flakes, plates and flowers developed from fusion of nanorods. Unfortunately, the morphologies didn't show noteworthy response towards low ppm of carbon monoxide below its prescribed TLV limits. The sensitivities demonstrated by these structures were considerably inferior when compared to the SnO_2 based sensors. Since dimension for most of the developed structures were in the micrometer range, therefore these materials offered lower specific surface area which may be the reason for such poor performance. Despite these sensors demonstrating inferior response towards carbon monoxide, they produced discerning results when exposed to the volatiles emanated from black tea as shall be elucidated in the chapter 5. The templated synthesis produced a slightly better performance as the ZnO nanoflowers anchored on egg shell membrane showed detection ability towards 30 ppm CO. The sensitivity could be further improved for ZnO hollow spheres produced with LDH as templates. The cavity present within the spheres was expected to offer higher surface coverage and a better response. However, the zinc oxide based sensors were found to fall short in their capacity to detect low ppm carbon monoxide compared to their SnO_2 based counterparts.

References:

[1] W. Park, J.S. Kim, G.C. Yi, M.H. Bae, H.J. Lee, "Fabrication and electrical characteristics of high-performance ZnO nanorod field-effect transistors", Appl. Phys. Lett., 85 (2004) 5052–5054.

[2] C.Y. Jiang, X.W. Sun, G.Q. Lo, D.L. Kwong, J.X. Wang, "Improved dye-sensitized solar cells with a ZnO-nanoflower photoanode", Appl. Phys. Lett., 90 (2007) 263501(1-3).

[3] J. Huang, Y. Wu, C. Gu, M. Zhai, K. Yu, M. Yang, "Large-scale synthesis of flower like ZnO nanostructure by a simple chemical solution route and its gas-sensing property", Sens. Actuators B: Chem., 146 (2010) 206–212.

[4] S. Roy, Z. Gao, "Direct-write fabrication of a nanoscale digital logic element on a single nanowire", Nanotechnology, 21 (2010) 245306(1-5).

[5] C. Mondal, A.K. Sinha, M. Ganguly, J. Pal, S. Dhara, Y. Negishi, T.Pal, "Deposition of zinc oxide nanomaterial on different substrates for useful applications", CrystEngComm, 16 (2014) 4322-4328.

[6] Z.L. Wang, "Zinc oxide nanostructures: growth, properties and applications", J. Phys. Condens. Matter, 16 (2004) R829-R858.

[7] M.R. Alenezi, S.J. Henley, N.G. Emerson, S.R.P. Silva, “From 1D and 2D ZnO nanostructures to 3D hierarchical structures with enhanced gas sensing properties”, Nanoscale, 5 (2014) 235-247.

[8] Y. Tong, Y. Liu, L. Dong, D. Zhao, J. Zhang, Y. Lu, D. Shen, X. Fan, “Growth of ZnO nanostructures with different morphologies by using hydrothermal technique”, J. Phys. Chem. B, 110 (2006) 20263-20267.

[9] G. Shen, Y. Bando, C.J. Lee, “Growth of self-organized hierarchical ZnO nanoarchitectures by a simple In/In_2S_3 controlled thermal evaporation process”, J. Phys. Chem. B, 109 (2005) 10779-10785.

[10] B. Cao, W. Cai, “From ZnO nanorods to nanoplates: chemical bath deposition growth and surface-related emissions”, J. Phys. Chem. C, 112 (2008) 680-685.

[11] T.T. Chen, I.C. Chang, M.C. Tsai, Y.C. Chang, M.H. Yang, P.C. Chen, H.T. Chiu, C. Y. Lee, “Size-controlled wurtzite zinc oxide spheres with the characteristics of visible absorption and Mie scattering”, CrystEngComm, 16 (2014) 3341-3347.

[12] D. Pradhan, K.T. Leung, “Vertical growth of two-dimensional zinc oxide nanostructures on ITO-coated glass: Effects of deposition temperature and deposition time”, J. Phys. Chem. C, 112 (2008) 1357-1364.

[13] T.L. Sounart, J. Liu, J.A. Voigt, M. Huo, E.D. Spoerke, B. McKenzie, “Secondary nucleation and growth of ZnO”, J. Am. Chem. Soc., 129 (2007) 15786-15793.

[14] D.V. Pinjari, A.B. Pandit, “Room temperature synthesis of crystalline CeO_2 nanopowder: Advantage of sonochemical method over conventional method”, Ultrason. Sonochem., 18 (2011) 1118-1123.

[15] A.K. Zak, W.H.A. Majid, H.Z. Wang, R. Yousefi, A.M. Golsheikh, Z.F. Ren, “Sonochemical synthesis of hierarchical ZnO nanostructures”, Ultrason. Sonochem., 20 (2013) 395-400.

[16] P.K. Vabbina, A. Kaushik, N. Pokhrel, S. Bhansali, N. Pala, “Electrochemical cortisol immunosensors based on sonochemically synthesized zinc oxide 1D nanorods and 2D nanoflakes”, Biosens. Bioelectron., 63 (2015) 124-130.

[17] T. Alammar, A. Murding, “Sonochemical synthesis of 0D, 1D, and 2D zinc oxide nanostructures in ionic liquids and their photocatalytic activity”, ChemSusChem, 4 (2011) 1796-1804.

[18] S.H. Jung, E. Oh, K.H. Lee, Y. Yang, C.G. Park, W. Park, S.H. Jeong, “Sonochemical preparation of shape-selective ZnO nanostructures”, Cryst. Growth Des., 8 (2008) 265-269.

[19] S.S. Warule, N.S. Chaudhari, J.D. Ambekar, B.B. Kale, M.A. More, “Hierarchical nanostructured ZnO with nanorods engendered to nanopencils and pin-cushion cactus with its field emission study”, ACS Appl. Mater. Interfaces, 3 (2011) 3454-3462.

[20] F.L. Schein, H.V. Wenckstern, M. Grundmann, “Transparent p-CuI/n-ZnO heterojunction diodes”, Appl. Phys. Lett., 102 (2013) 092109(1-4).

[21] B. Lin, Z. Fu. “Green luminescent center in undoped zinc oxide films deposited on silicon substrates”, Appl. Phys. Lett., 79 (2001) 943-945.

[22] R. Al-Gaashani, S. Radiman, A.R. Daud, N. Tabet, Y. Al-Douri, “XPS and optical studies of different morphologies of ZnO nanostructures prepared by microwave methods”, Ceram. Int., 39 (2013) 2283-2292.

[23] W. Krätschmer, L.D. Lamb, K. Fostiropoulos, D.R. Huffman, “Solid C_{60}: a new form of carbon”, Nature, 347 (1990) 354 – 358.

[24] L. Vayssieres, K. Keis, S.E. Lindquist, A. Hagfeldt, “Purpose-built anisotropic metal oxide material: 3D highly oriented microrod array of ZnO”, J. Phys. Chem. B, 105 (2001) 3350–3352.

[25] K.M. Song, J.M. Kim, J.H. Choi, D.H. Kang, K. Kim, S.M. Hwang, B.K. Kang, D.H. Yoon, “High hole concentration Mg doped a-plane GaN with MgN by metal–organic chemical vapor deposition”, Mater. Lett., 91 (2013) 338–340.

[26] S. Ghosh, D. Majumder, A. Sen. S. Roy, “Facile sonochemical synthesis of zinc oxide nanoflakes at room temperature”, Mater. Lett., 130 (2014) 215-217.

[27] S.H. Zhang, J.O. Lim, J.S. Huh, J.H. Noh, W. Lee, “Two-step fabrication of ZnO nanosheets for high performance VOCs gas sensor”, Curr. Appl. Phys., 13 (2013) S156–S161.

[28] L. Wang, Y. Kang, X. Liu, S. Zhang, W. Huang, S. Wang, “ZnO nanorod gas sensor for ethanol detection”, Sens. Actuators B: Chem., 162 (2012) 237-243.

[29] H. Zhang, D. Yang, Y. Ji, X. Ma, J. Xu, D. Que, “Low temperature synthesis of flower like ZnO nanostructures by cetyltrimethylammonium bromide assisted hydrothermal process”, J. Phys. Chem. B, 108 (2004) 3955–3958.

[30] M.A. Verges, A. Mifsud, C.J. Serna, "Formation of rod-like zinc oxide microcrystals in homogeneous solutions", J. Chem Soc. Faraday. Trans., 86 (1990) 959–963.

[31] S. Cheng, D. Yan, J.T. Chen, R.F. Zhuo, J.J. Feng, H.J. Li, H.T. Feng, P.X. Yan. "Soft-template synthesis and characterization of ZnO_2 and ZnO hollow spheres", J. Phys. Chem. C, 113 (2009) 13630-13635.

[32] R.A. McBride, J.M. Kelly, D.E. McCormack, "Growth of well-defined ZnO microparticles by hydroxide ion hydrolysis of zinc salts", J. Mater. Chem., 13 (2003) 1-7.

[33] M.L. Fuller, "Twinning in zinc oxide", J. Appl. Phys., 15 (1944) 164-170.

[34] D. Krishnan, T. Pradeep, "Precursor-controlled synthesis of hierarchical ZnO nanostructures, using oligoaniline-coated Au nanoparticle seeds", J. Cryst. Growth, 311 (2009) 3889-3897.

[35] S. Ullah, F. Ahmed, A. Badshah, A.A. Altaf, R. Raza, B. Lal, R. Hussain, Solvothermal preparation of ZnO nanorods as anode material for improved cycle life Zn/AgO batteries, PLoS One, 8 (2013) e75999(1-7).

[36] T. Pauporte, D. Lincot, "Electrodeposition of semiconductors for optoelectronic devices: results on zinc oxide", Electrochim. Acta, 45 (2000) 3345-3353.

[37] H. Sun, M. Luo, W. Weng, K. Cheng, P. Du, G. Shen, G. Han, "Room-temperature preparation of ZnO nanosheets grown on Si substrates by a seed-layer assisted solution route", Nanotechnology, 19 (2008) 125603(1-5).

[38] Y. Peng, A.W. Xu, B. Deng, M. Antonietti, H. Cölfen, "Polymer-controlled crystallization of zinc oxide hexagonal nanorings and disks", J. Phys. Chem. B, 110 (2006) 2988-2993.

[39] C.Y. Chee, K. Nadarajah, M.K. Siddiqui, Y. Wong, "Optical and structural characterization of solution processed zinc oxide nanorods via hydrothermal method", Ceram. Int., 40 (2014) 9997-10004.

[40] D.A. Reddy, R. Ma, T.K. Kim, "Efficient photocatalytic degradation of methylene blue by heterostructured ZnO–RGO/RuO_2 nanocomposite under the simulated sunlight irradiation", Ceram. Int., 41 (2015) 6999-7009.

[41] M.J. Height, S.E. Pratsinis, O. Mekasuwandumrong, P. Praserthdam, “Ag-ZnO catalysts for UV-photodegradation of methylene blue”, Appl. Catal. B: Environ., 63 (2006) 305-312.

[42] C. Schmerbauch, J. Gonzalez-Julian, R. Roder, C. Ronning, O. Guillon, “Flash sintering of nanocrystalline zinc oxide and its influence on Microstructure and Defect Formation”, J. Am. Ceram. Soc., 97 (2014) 1728-1735.

[43] A. Önsten, D. Stoltz, P. Palmgren, S. Yu, M. Göthelid, U.O. Karlsson, “Water adsorption on ZnO(0001): transition from triangular surface structures to a disordered hydroxyl terminated phase”, J. Phys. Chem. C, 114 (2010) 11157-11161.

[44] J.S. Loring, E. S. Ilton, J. Chen, C. J. Thompson, P. F. Martin, P. Benezeth, K. M. Rosso, A. R. Felmy, H. T. Schaef, “In situ study of CO_2 and H_2O partitioning between Na− montmorillonite and variably wet supercritical carbon dioxide”, Langmuir, 30 (2014) 6120-6128.

[45] Z. Li, Y. Xiong, Y. Xie, “Selected-control synthesis of ZnO nanowires and nanorods via a PEG-assisted route”, Inorg. Chem., 42 (2003) 8105–8109.

[46] X. Zhou, S. Chen, D. Zhang, X. Guo, W. Ding, Y. Chen, “Microsphere organization of nanorods directed by PEG linear polymer”, Langmuir, 22 (2006) 1383–1387.

[47] H. Zhang, J. Feng, J. Wang, M. Zhang, “Preparation of ZnO nanorods through wet chemical method”, Mater. Lett., 61 (2007) 5202-5205.

[48] P. Li, Y. Wei, H. Liu, X.K. Wang, “Growth of well-defined ZnO microparticles with additives from aqueous solution”, J. Solid State Chem., 178 (2005) 855–860.

[49] H. Li, Q. Zhou, Y. Gao, X. Gui, L. Yang, M. Du, E. Shi, J. Shi, A. Cao, Y. Fang, “Templated synthesis of TiO_2 nanotube macrostructures and their photocatalytic properties”, Nano Res., 8 (2015) 900-906.

[50] B. Wu, L. Wang, H. Wu, K. Kan, G. Zhang, Y. Xie, Y. Tian, L. Li, K. Shi, “Templated synthesis of 3D hierarchical porous Co_3O_4 materials and their NH_3 sensor at room temperature”, Microporous Mesoporous Mater., 225 (2016) 154-163.

[51] P. Atanasova, D. Rothenstein, J.J. Schneider, R.C. Hoffmann, S. Dilfer, S. Eiben, C. Wege, H. Jeske, J. Bill, “Virus-templated synthesis of ZnO nanostructures and formation of field-effect transistors”, Adv. Mater., 23 (2011) 4918–4922.

[52] O. Zuas, A. Kristiani, A. Haryono, “Synthesis of the nano structured zinc oxide using the soft template of cylea barbata miers extract and its promising property for dye adsorbent”, J. Adv. Mater. Process., 3 (2015) 39-50.

[53] N. Jain, A. Bhargava, J.C. Tarafdar, S.K. Singh, J. Panwar, “A biomimetic approach towards synthesis of zinc oxide nanoparticles”, Appl. Microbiol. Biot., 97 (2013) 859-869.

[54] M. Zimbone, P. Musumeci, A. Contino, G. Maccarrone, L. Calcagno, “DNA-triggered asymmetric ZnO nanoparticles”, Colloids Surf. A: Physicochem. Eng. Asp., 489 (2016) 336-342.

[55] M. Chitra, K. Uthayarani, N. Rajasekaran, N. Neelakandeswari, E.K. Girija, D.P. Padiyan, “Rice husk templated mesoporous ZnO nanostructures for ethanol sensing at room temperature”, Chin. Phys. Lett., 7 (2015) 078101(1-4).

[56] W. Zhang, D. Zhang, T. Fan, J. Ding, Q. Guo, H. Ogawa, “Morphosynthesis of hierarchical ZnO replica using butterfly wing scales as templates”, Microporous Mesoporous Mater., 92 (2006) 227-233.

[57] M. Shoeb, B.R. Singh, J.A. Khan, B.N. Singh, H.B. Singh, A.H. Naqvi, “ROS-dependent anticandidal activity of zinc oxide nanoparticles synthesized by using egg albumen as a biotemplate”, Adv. Nat. Sci.: Nanosci. Nanotechnol., 4 (2013) 035015(1-11).

[58] W. Bai, Z. Zhang, W. Tian, X. He, Y. Ma, Y. Zhao, Z. Chai, “Toxicity of zinc oxide nanoparticles to zebrafish embryo: a physicochemical study of toxicity mechanism”, J. Nanoparticle Res., 12 (2009) 1645-1654.

[59] S.M. Lee, G. Grass, G.M. Kim, C. Dresbach, L. Zhang, U. Gösele, M. Knez, “Low-temperature ZnO atomic layer deposition on biotemplates: flexible photocatalytic ZnO structures from eggshell membranes”, Phys. Chem. Chem. Phys., 11 (2009) 3608-3614.

[60] Q. Dong, H. Su, J. Xu, D. Zhang, R. Wang, “Synthesis of biomorphic ZnO interwoven microfibers using eggshell membrane as the biotemplate”, Mater. Lett., 61 (2007) 2714-2717.

[61] J. Xu, H. Su, J. Han, Y. Chen, W. Song, Y. Gu, W.J. Moon, D. Zhang, “In situ deposition of flower-like ZnO on silk fibroin fibers”, Appl. Phys. A, 108 (2012) 235-238.

[62] M.L. Chen, C.B. Gu, T. Yang, Y. Sun, J.H.Wang, “A green sorbent of esterified egg shell membrane for highly selective uptake of arsenate and speciation of inorganic arsenic”, Talanta, 116 (2013) 688-694.

[63] J. Li, F.L. Kwong, J. Zhu, D.H.L. Ng, “Synthesis of biomorphic ZnO nanostructures by using the cetyltrimethylammonium bromide modified silk templates”, J. Am. Ceram. Soc., 93 (2010) 3726-3731.

[64] H. Su, J. Han, N. Wang, Q. Dong, D. Zhang, C. Zhang, “In situ synthesis of lead sulfide nanoclusters on eggshell membrane fibers by an ambient bio-inspired technique”, Smart Mater. Struct., 17 (2008) 015045(1-5).

[65] L. Yao, W. Zhou, T. Wang, M. Liu, C. Yu, “Quantification of egg yolk contamination in egg white using UV/Vis spectroscopy: Prediction model development and analysis”, Food Control, 43 (2014) 88-97.

[66] P. Kumbhakar, D. Singh, C.S. Tiwary, A.K. Mitra, “Chemical synthesis and visible photoluminescence emission from monodispersed ZnO nanoparticles”, Chalcogenide Lett. 5 (2008) 387-394.

[67] Y.H. Zhao, Y.J. Chi, “Characterization of collagen from eggshell membrane”, Biotechnology, 8 (2009) 254-258.

[68] M.K. Rath, B.H. Choi, M.J. Ji, K.T. Lee, “Eggshell-membrane-templated synthesis of hierarchically-ordered NiO-$Ce_{0.8}Gd_{0.2}O_{1.9}$ composite powders and their electrochemical performances as SOFC anodes”, Ceram. Int., 40 (2014) 3295-3304.

[69] A. Pacula, R. Mokya, “Layered double hydroxides as templates for nanocasting porous N-doped graphitic carbons via chemical vapour deposition”, Microporous and Mesoporous Mater., 106 (2007) 147–154.

[70] X. Xu, F. Zhang, S. Xu, J. He, L. Wang, D.G. Evans, X. Duan, “Template synthesis of nanoparticle arrays of CdS in transparent layered double hydroxide films”, Chem. Commun., 48 (2009) 7533-7535.

[71] Y.W. Koh, K.P. Loh, “Hexagonally packed zinc oxide nanorod bundles on hydrotalcite sheets”, J. Mater. Chem., 15 (2005) 2508-2514.

[72] A.A.A. Ahmed, Z.A. Talib, M.Z. bin-Hussein, A. Zakaria, “Improvement of the crystallinity and photocatalytic property of zinc oxide as calcination product of Zn–Al layered double hydroxide”, J. Alloys Compd., 539 (2012) 154-160.

[73] W. Yang, Y. Kim, P.K.T. Liu, M. Sahimi, T.T. Tsotsis, “A study by in situ techniques of the thermal evolution of the structure of a Mg–Al–CO_3 layered double hydroxide”, Chem. Eng. Sci., 57 (2002) 2945-2953.

[74] J. Litvinov, Y.J. Wang, J. George, P. Chinwangso, S. Brankovic, R.C. Willson, D. Litvinov, “Development of pinhole-free amorphous aluminum oxide protective layers for biomedical device applications”, Surf. Coat Technol., 224 (2013) 101–108.

[75] F. Librizzi, E. Vitrano, L. Cordone, “Dehydration and crystallization of trehalose and sucrose glasses containing carbonmonoxy-myoglobin”, Biophys. J., 76 (1999) 2727-2734.

Chapter 5

Detection of principal VOCs in black tea aroma – role of different additives on sensing behaviour of SnO_2 and ZnO

This chapter describes the fabrication of sensor modules for detection of key aroma volatiles emanated from black tea. As highlighted in the introductory chapter, an instrumental alternative for the conventional organoleptic evaluations employed in the industries, shall be extremely beneficial in quality monitoring of the tea grades. The current versions of electronic nose prototypes which are deployed as electronic means for quality monitoring of black tea rely on commercial non-specific sensors for the detection purpose. The mode of detection which relies on the cross-sensitivities of the commercial modules diminish the reliability of the prototypes. Since the aroma is generated through synergistic contributions from a group of odour active volatiles, the VOCs with significant influence on the formation of the aroma were identified and sensors targeted towards these volatiles were developed within the scope of this chapter. It further describes the developed sensors' performance towards the identified volatiles and towards actual emanated aroma from different grades of black tea.

List of Sections

Contents of this chapter are partially based on the specification of the following patent and publication

[1] A. Sen, S. Mandal, M. Narjinary, S. Ghosh, "Sensor compositions for detection of linalool, geraniol, methyl salicylate and trans-2-hexenal with an intention to classify black tea aroma", Patent Filing No. 0537/DEL/2015.

[2] D. Dutta, S. Ghosh, M. Narjianary, N. Bhattacharyya, R. Bandyopadhyay, "Tin oxide based gas sensor array in electronic nose to monitor aroma of black tea", Sensor Letters vol. 14 (2016) pp. 396-401.

5.1. Introduction

The necessity for developing sensors dedicated towards specific detection of volatile organic compounds (VOC) present within black tea aroma was mooted from the significance of quality evaluation of black tea aroma grades and its associated economic impact on the industries. Since conventional quality monitoring techniques are predominantly organoleptic in their origin, they are inherently prone to human cognition related errors. These errors can originate from inexplicable mood swings, health conditions of the taster, unaccountable weather changes, or a combination of these parameters making them extremely difficult to factorize. Moreover, the aroma for a particular grade is built from synergy of a group of odour active volatiles whose subtle variation in the parts per million (ppm) levels alters the overall profile. The human perception of olfaction, on the other hand, is a subjective mode which can discern the presence of an odour active molecule but cannot precisely quantify the concentration. The limitation of human nose in quantifying the signatorial volatiles, in coalition with the aforementioned plausible error paths make the whole organoleptic exertion of tea quality determination unscientific which lack proper authentications.

A quantitative mode of quality estimation should therefore counter these limitations by targeting to specifically detect the volatiles at their precise concentration levels. The electronic nose is the closest prototype developed for the purpose which operates on a philosophy of detecting the variation in the overall synergy of these compounds. Though having performed well in certain areas, the electronic prototypes developed thus far rely heavily on the cross-interference of commercial sensors towards the aroma volatiles. An account of all electronic nose prototypes developed was presented through survey of literatures in chapter 1. These sensor modules were developed for entirely different applications and their commissioning in the electronic nose array compromises the integrity of the device. This necessitates the development of indigenous sensor modules specifically tuned to comprehend the subtle variations in the odour active volatile concentrations. For this the entire process was initiated through identification of the pertinent volatile compounds which govern the aroma profile of the black tea.

5.2. Major volatile organic compounds in black tea

The perception of aroma for the tasters depends upon the combinatorial effect of certain odor-active constituents in black tea. This acuity is generated through binding of the volatiles with the chemoreceptors present in human nose, which generates an impulse beyond the orthonasal threshold. The Flavour Dilution value (FD) of individual volatile, determined as the ratio of the compound's concentration in the initial extract to its odour threshold, is considered as a quantitative measure of the volatile's contribution in formation of the aroma. Aroma Extract Dilution Analysis (AEDA) is an established technique of separating the odour active volatiles contributing to the formation of black tea aroma from the non-active odourless volatiles. This technique was particularly helpful in identifying linalool, with a high FD value, to have a major impact in aroma development [1]. The finding was later corroborated by Schuh and Schieberle, whose significant contribution in understanding the formation of black tea aroma projected linalool as an easily detectable volatile with high FD value following their experiment of serial dilutions of an extract prepared from infused Darjeeling black tea [2]. The investigation also elucidated linalool to be an easily sentient volatile with the highest Odour Activity Values (OAV: ratio of concentration to odour threshold in water) of 145 among odour active compounds. The recombination experiment showed profile of citrus-aroma model (aroma quality of linalool is citrus like) in closely resembles the actual infusion. Thus linalool is found to be a major contributor to the overall aroma and quantitative detection of the same can be helpful for the tea tasters in their exertion in quality monitoring. Apart from linalool, geraniol with a relatively high odour activity value of 45, trans-2-hexenal and methyl salicylate [3] have been deemed as the major contributors in ultimate formation of the aroma [2, 4-5] among the 600 odd constituent volatiles. A high Flavour Dilution index and an OAV of 38 makes methyl salicylate a key candidate in formation of the aroma profile [6]. In contrast, (*E*)-2-hexenal has a low odour activity index of around 10. However, aldehydes of six to ten carbon chain lengths are major contributors in formation of grassy/green smell of tea [6]. Likewise, the volatile demonstrated a positive correlation between its concentration and the overall quality determined for seven grades of Turkish black tea [7]. Gohain *et al*. reported that Darjeeling teas are the highest grown teas in the world and preferred for its flavor, aroma and quality. Upon qualitatively analyzing Darjeeling tea linalool and geraniol were deduced to be important for the typical characteristic flavor of tea produced in this region. They have mentioned variation in linalool, geraniol, trans-2-hexenal at different tea samples. Geraniol for example emanates a woody smell at 10 ppm [8]. Even, it is reported that the percentage production of linalool in all the tea samples is maximum followed by geraniol [9]. Though the tea aroma constitutes of significantly larger amount of volatiles, yet constructive reviews of literatures suggested that variation of these four volatiles drastically modulates the aroma signature. Thus if these volatiles could be monitored, the signature of detection pattern can lead to a precise quality estimation of black tea and subsequent classification among tea grades.

The structure of the chosen volatiles has been depicted in **Fig. 5.1** which illustrates that each of the volatile has a functional group attached to the carbon chain.

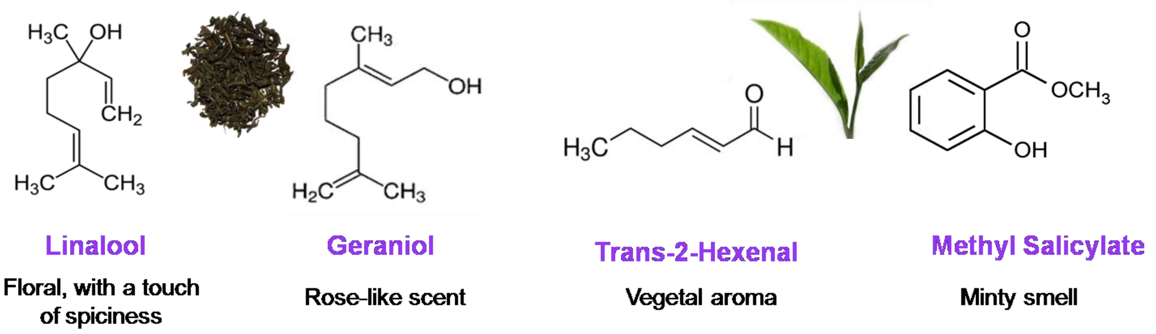

Fig. 5.1. *Molecular structures of the key aroma volatiles*

It is evident from the molecular structure that three of the chosen volatiles consist a hydroxyl group which provides them their characteristic smell while the fourth VOC contains an aldehyde moiety.

Despite the significance of these volatiles in formation of the aroma not only in tea but in many other agro products, there has been limited research in fabrication of sensors for them. Therefore, efforts were made to develop sensors that can specifically detect these volatiles at ppm levels and are capable to sense the variation in their concentrations with adequate resolution. Since the principal reaction mechanism for semiconducting sensors is oxidation of the dispensed analyte by the chemisorbed oxygen on the surface, therefore the targeted VOCs are expected to follow the same trend. Strategic electronic tuning of the host lattice by preferred catalysts for the oxidation process is therefore expected to promote the sensing phenomenon. The oxidative products for the volatiles along with the range of catalysts that promote the oxidation process have been presented in **Table 5.1**. The choice of the additive to be incorporated in SnO_2 or ZnO lattice has thus been governed by their influence in catalytic oxidation of the target volatile. In fact, as shall be elucidated in the subsequent sections, proper choice of additives has been instrumental in enhancing the specificity of a sensor module towards an analyte.

Researchers have explored different domains for development of sensors for the aforementioned volatiles. Linalool is perhaps the most important volatile in aroma generation which features in every report in the purview of this domain. There has been a surge in development of QCM based sensors for linalool where different groups have coated the quartz crystals with polyethylene glycol (PEG) [17] and polyurethane [18] for the purpose. Other groups have resorted to unorthodox techniques like interpretation of the observed cataluminescence generated by oxidation of terpenoids on Dy_2O_3 containing γ-Al_2O_3 sensing

Table 5.1. *Catalysts used in oxidation of the key volatiles identified in tea aroma*

Sr. No.	Ref.	Volatile Organic Compound	Catalyst	Remarks
1	[10]	Linalool	Ag-complex	Catalyzed linalool to form epoxide or their rearrangement products depending on the conditions
2	[11]	Linalool	Pd(II)/Cu(II) complex	High yield of derivatives under benign conditions projects palladium as an efficient catalyst in oxidation of the volatile
3	[12]	Linalool and geraniol	Nickel oxide	Primary alcohol containing moieties like geraniol could be easily oxidized than tertiary -OH group containing linalool
4	[13]	Geraniol	Gold nanoparticles	Gold nanoparticles distributed on various metal oxide semiconductor supports were instrumental in catalytic oxidation of geraniol
5	[14]	Geraniol	Lanthanum	Lanthanum catalyst showed excellent selectivity towrads the citral derivative of geraniol
6	[15]	Methyl Salicylate	Gold nanoparticles	Gold nanoparticle modified electrodes could selectively detect methyl salicylate with high sensitivity, in the presence of interfeing analytes like *cis*-3-hexenol, hexyl acetate and *cis*-hexenyl acetate.
7	[16]	*trans*-2-hexenal	1% Pd/Amberlyst -15	In this reaction 2-ethyhexanal is produced with 70% selectivity

layer for detecting linalool to a lower limit of 0.1 ppm [19]. A recent report investigated the use of slime mould as potential chemical sensor as the inherent oscillation of the mould was observed to change. But close proximity of linalool caused terminal cessation of the organism and hence the distance for linalool from the agar blob was kept larger than those of other chemicals [20]. Researchers have employed molecular imprinted polymer coated on conductive polymer films for detection of both linalool and geraniol [21].

The pertinent compounds have also been detected by MOS sensors which offer a cost effective, rugged yet simpler mode of detection. For example, linalool has been detected by commercial (Figaro Inc.) metal oxide sensors where TGS-832 (CFC sensor) and TGS-823 (Organic Solvent Vapour sensor) showed maximum response [22] towards the volatile. However the sensors have mostly been used in an electronic nose array dedicated to capture the synergy of the volatiles and not the concentration of individual compound within the aroma. Despite the sporadic reports generated from different laboratories, there has been a dearth in research on sensing of these volatiles with MOS type sensors and lack an assertive database.

5.3. Synthesis of tin dioxide and zinc oxide with different additives

In absence of concrete literatures highlighting the efficacy of a particular brand of MOS sensors for detecting the volatiles, two different systems were chosen, namely tin dioxide and zinc oxide based sensors. For the tin dioxide based systems the prime focus was concentrated on loading the base material with additives to improve the specificity towards individual volatile. These additives influenced the sensing parameters and often promoted the oxidation of target analytes. However, the focus for the zinc oxide based sensors veered towards rendering definite morphologies to the base crystals so as to tune their electronic properties in favour of the sensing process. Of the different superstructures synthesized in Chapter 4, the best performing sensors were then loaded with suitable catalysts for enhancing the response. In order to assess the selectivity of the modules towards individual volatiles, initially a common concentration of 20 ppm of individual VOC was exposed to the sensors for screening purpose. Thereafter the sensors with the optimal performance were calibrated and subsequently exposed to different grades of black tea.

SnO_2 based sensors

Tin dioxide based sensors were produced through sonication aided coprecipitation method as elucidated in chapters 2 and 3. Soluble precursor salts of the additives were introduced in the precipitation reaction of stannous chloride by ammonia under sonication by a Sonics, Vibra-Cell, VCF 1500 sonicator probe. The precursors themselves underwent precipitation under the influence of ammonia and subsequent calcination transformed them into their oxide phases.

ZnO based sensors

Different morphologies of zinc oxide were created through protocols provided in chapter 4. However, the inherent anisotropic growth in ZnO crystals enable the morphing of structures at much lower energy and a Hielscher UP200S, 200W, 24kHz sonicator probe suffice the power requirement. The potassium hydroxide present in the medium acts as the precipitating agent for the additive precursor salts. However, precipitation results in formation of hydroxides of the additives which when calcined tend to form the requisite phase of the additives. The high temperature on the other hand adds excess energy to the system which should tend to accelerate the *c*-axis oriented growth. Therefore it is imperative to study the morphological features post calcination to observe the degree of deviation from the original nanostructure. The various additives that have been incorporated into the SnO_2 and ZnO systems are presented in **Fig 5.2**.

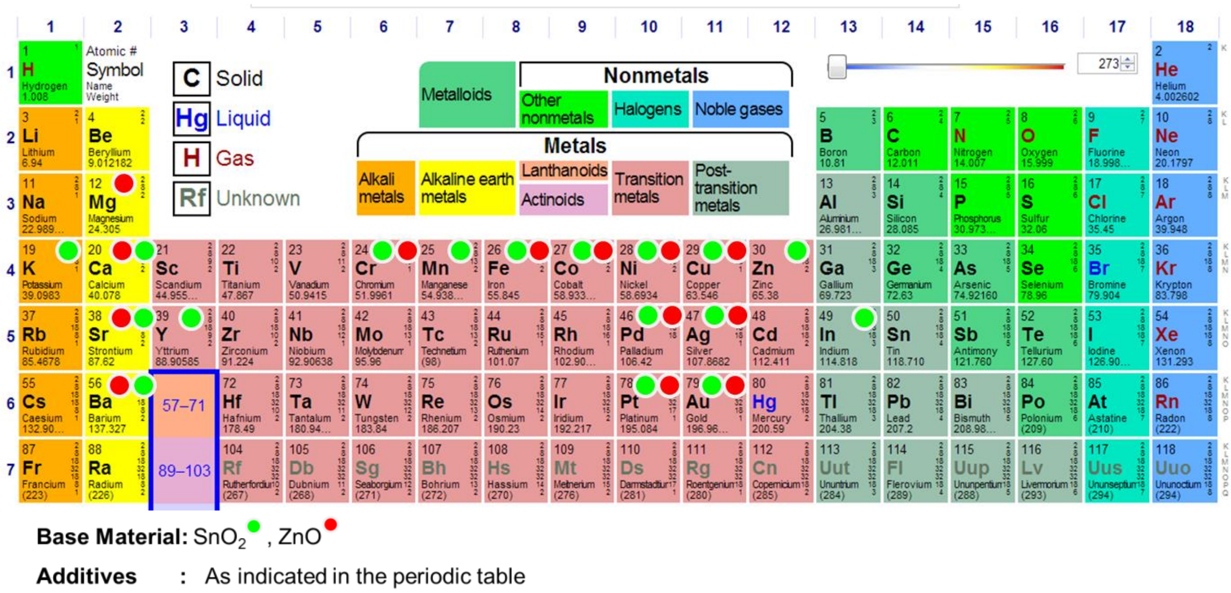

Base Material: SnO_2 ●, ZnO ●

Additives : As indicated in the periodic table

Fig. 5.2*. Material compositions, furnished in the periodic table, which have been synthesized and studied for detection of VOCs present in black tea aroma*

Tin dioxide batch synthesis

A typical synthesis protocol for fabrication of tin dioxide based sensor module has been presented through the following example. In order to prepare a sensor composition having 5 wt% BaO and 95 wt % SnO_2, the following solutions were prepared: a) 3.384 g $SnCl_2.2H_2O$ (Merck, 99 % purity) in 150 mL distilled water, b) 15 mL liquor ammonia with 1:1 dilution with distilled water, c) 0.21 g of anhydrous barium nitrate in 20 mL distilled water in presence of 2 mL concentrated HCl with continuous stirring for 30 min at 100 ºC.

The aqueous solutions of the tin salt, and barium salt were mixed together in a 500 mL beaker and the solution was stirred for 10 min. The solution in the beaker was placed under a high energy sonicator (ultrasonic processor, Sonics, 1500 Watt, model VCF1500) and the probe (diameter ~ 2 cm) dipping length in the solution was ~ 4 cm. During the sonication (sonication time 1 h), ammonia solution was added drop-wise to achieve the desired pH ~ 9 of the solution for complete precipitation. The solution was allowed to cool and at the end of the reaction, a white coloured precipitate was obtained. After completion of sonication, the obtained particles were separated out by centrifuging the solution at 8,000 rpm for 15 min.

The particles were washed several times by centrifuging in distilled water and acetone. Finally, the white precipitate was dried in vacuum oven at 100 ºC for 16 h.

Sensors using the synthesized composition were fabricated by mixing 0.002 g of the synthesized composition with 5 mL of isopropanol to form a slurry, thereafter drop coating about 40 µL of the slurry onto a spinning alumina tube. The sensor substrates were initially prepared by attaching gold electrodes and platinum lead wires at the ends of the alumina tube (4 mm length, 1.5 mm outer diameter and 1 mm diameter) and by heating the system at a temperature of 1000 ^{o}C. Once the compositions were drop coated onto the substrate the entire module was cured at a temperature in the range of 800-850 ^{o}C at a rate of 50 ^{o}C/h. Kanthal wire, which would act as the heating coil, was inserted in the sensor substrate. Finally, the fabricated sensor module was packaged in a standard TO-type (Transistor Outline) head by spot welding.

Zinc oxide batch synthesis

For a typical batch synthesis of zinc oxide nanoflakes, zinc nitrate hexahydrate [$Zn(NO_3)_2$•$6H_2O$], potassium hydroxide (KOH) and cetyltrimethylammonium bromide (CTAB) were procured from Sigma Aldrich and used without further purification. Equal amounts (0.5 g) of $Zn(NO_3)_2$•$6H_2O$ and KOH were dissolved in 250 ml of deionised water, to which CTAB was added in different concentrations (5 – 15 mM) and stirred for 10 min to make a clear solution. The solution was then sonicated using an ultrasonic processor (Hielscher UP200S, 200W, 24kHz) with an intermittent pulse duration of 3 min. Following a sonochemical reaction at room temperature for a definite time (3 – 25 min), a white precipitate was formed, which was then washed with deionised water. The as-synthesized materials were dried at room temperature in vacuum and subsequently analyzed for phase purity and crystallinity by X-Ray diffraction (Bruker D8 Advance, Cu Kα line).

5.5. Sensor characterization for VOCs

5.5.1. Tin dioxide based sensors

The sensitivities of individual sensor module towards uniform concentrations of the VOCs (20 ppm) was recorded and presented in tabulated form. The sensitivities provided a reference point for initial screening of the sensors. The loading levels as well as the operating temperature were varied to enhance the sensing parameters.

Table 5.2. *Sensitivities demonstrated by tin dioxide sensors towards tea aroma volatiles*

Sample	**Working Temperature (^oC)**	**Sensitivity (%)**			
		Linalool	**Geraniol**	**Methyl Salicylate**	**Trans-2-hexenal**
Pure SnO_2	350	69	63	49	52
1% Ag_2O-SnO_2	250	79	63	44	60
	300	72	62	48	66
	350	87	52	68	86
1% Au-SnO_2	250	68	43	33	60
	300	59	55	46	59
	350	81	58	42	82
1% CuO-SnO_2	250	66	61	53	55
	300	64	60	54	59
	350	79	59	59	75
1% Fe_2O_3-SnO_2	250	66	58	47	60
	300	67	54	47	61
	350	84	65	63	77
1% La_2O_3-SnO_2	250	84	76	61	70
	300	84	74	62	71
	350	90	62	64	83
1% Pt-SnO_2	250	68	61	48	68
	300	60	60	59	70
	350	87	63	70	84
1% Pd-SnO_2	250	43	37	61	70
	300	83	73	63	71
	350	62	58	50	67
5% CaO-SnO_2	250	72	75	42	62
	350	71	70	32	44
	450	51	49	24	37
5% NiO-SnO_2	350	80	71	49	62
25% In_2O_3-SnO_2	350	79	56	34	66

5% BaO-SnO_2	250	66	62	26	51
	350	45	41	20	38
	450	23	23	7	19
5% SrO-SnO_2	250	68	59	23	50
	350	61	58	26	41
	450	21	24	9	21
5% Cr_2O_3-SnO_2	350	26	26	15	17
	400	52	55	31	37
1% CaO-SnO_2	350	90	75	48	58
10% CaO-SnO_2	350	82	60	45	35
5% ZnO-SnO_2	350	90	81	64	64

The prime parameter governing the choice of a particular sensor to advance post screening stage was its demonstrated sensitivity. A high sensitivity value towards 20 ppm concentration inevitably suggests that the lower detection limit for the sensor would be below that level. This implication provides higher opportunity towards using the sensor in the electronic nose prototype. Upon close analysis of the sensors performance, five particular modules of SnO_2 based sensors were observed to perform superior than others. The five sensors chosen were:

1. 1 wt% Ag_2O-SnO_2
2. 1 wt% Au-SnO_2
3. 5 wt% BaO-SnO_2
4. 5 wt% SrO-SnO_2
5. 3 wt% La_2O_3-SnO_2

The possible reasons for the modules mentioned above demonstrating superior performance than others have been listed below:

1 wt% Ag_2O-SnO_2 - electronic sensitization of SnO_2 surface occurs due to formation of Ag+/Ag_0 redox pairs through oxidation of metallic silver on the surface. This in turn results in an electron-deficient highly resistive space-charge layer due to the p-n heterojunctions formed by the redox pair on the surface. In presence of a target analyte containing a reducing functional group, silver oxide gets reduced to its metallic form, thus producing a considerable amount of signal through infusion of electrons and reduction of the space-charge layer.

1 wt% Au-SnO_2 – Role of gold nanoparticles in enhancing the sensitivity towards tea volatiles is explained by the catalytic model where gold has been reported to promote the oxidation of alcohol functional groups.

5 wt% BaO-SnO_2 – Surprisingly, the larger Ba loaded SnO_2 particles were found to be effective in detecting VOCs. This might be explained by barium's tendency to catalyse –OH oxidation.

5 wt% SrO-SnO_2 – Strontium also has catalytic tendency towards alcohol oxidation and therefore produce higher sensitivities towards the key volatiles with hydroxyl functional groups.

3 wt% La_2O_3-SnO_2 – Lanthanum oxide and tin dioxide have contrasting Isoelectric point (iep). While La_2O_3 is basic with an iep_{La2O3} ~10–12, SnO_2 is predominantly acidic with an iep range within 4-7. This type of acid/base composite with enhanced catalytic features promotes the dehydrogenation of ethanol.

These sensors were then further exposed towards aroma emanated from different grades of black tea. The tea samples with allotted taster scores were provided by CDAC, Kolkata. For the purpose, three different grades of orthodox black tea and two grades of CTC tea, were assessed by tea tasters who allotted specific scores for them. The headspace generated from these grades was dispensed on the sensor modules for characterisation. The grades of black tea used for the analysis has been summarised in **Table 5.3**.

***Table 5.3**: Details of the black tea grades used for dynamic characterisation of the sensors*

Tea Sample Code	Origin & Type	Taster Score
Grade A	Orthodox	6
Grade B	Orthodox	5
Grade C	Orthodox	4
Grade A_c	CTC grade	5
Grade B_c	CTC grade	3

It is an established fact that orthodox tea emanate better aroma compared to CTC grade tea due to the loss of volatiles from membrane ruptures in the later. The scores allotted by the tasters are influenced by the above fact and a similar score for two different classifications of black tea often doesn't infer similar aroma quotient. The performance of the five sensors and the pristine SnO_2 sensor have been provided through **Fig. 5.3-5.8**.

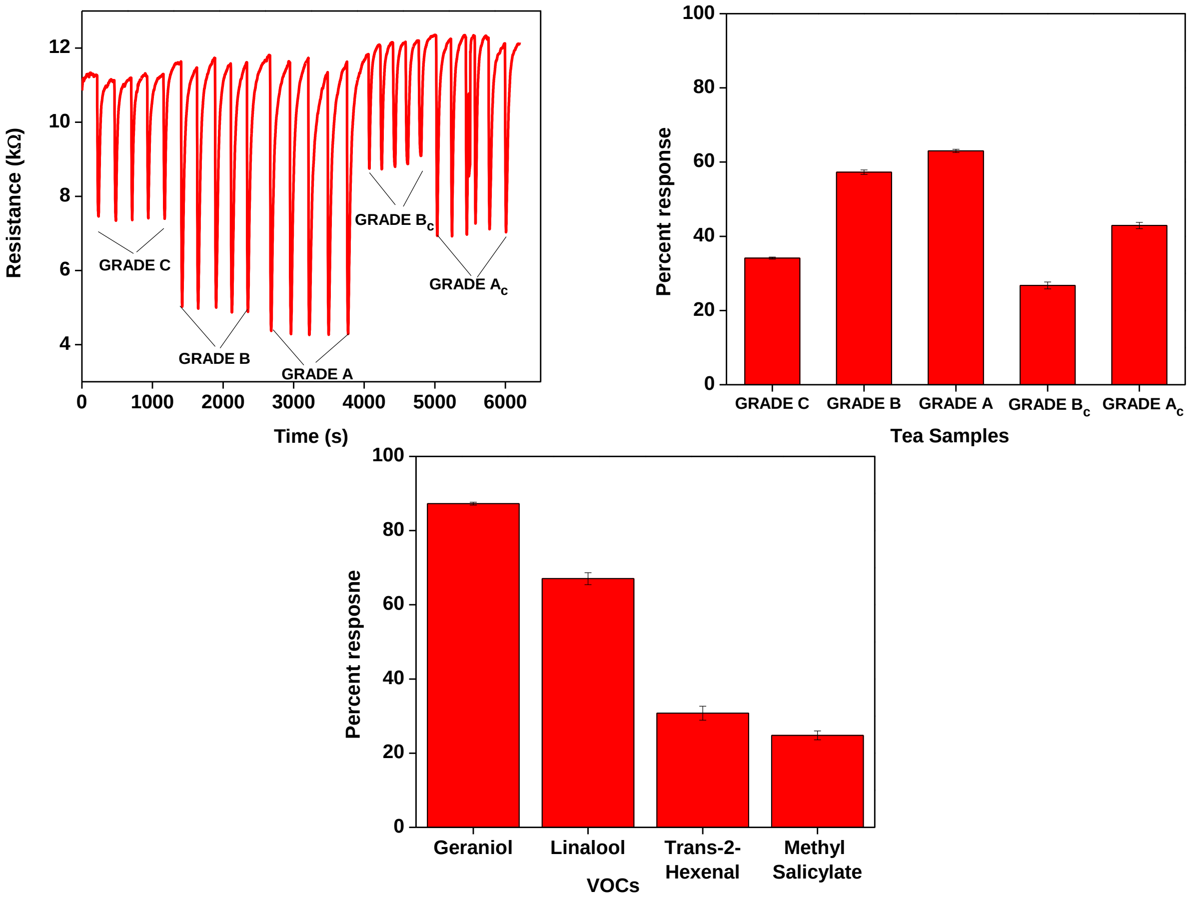

Fig 5.3. *Dynamic sensor response of 1 wt% Ag_2O-SnO_2 towards VOCs and grades of black tea*

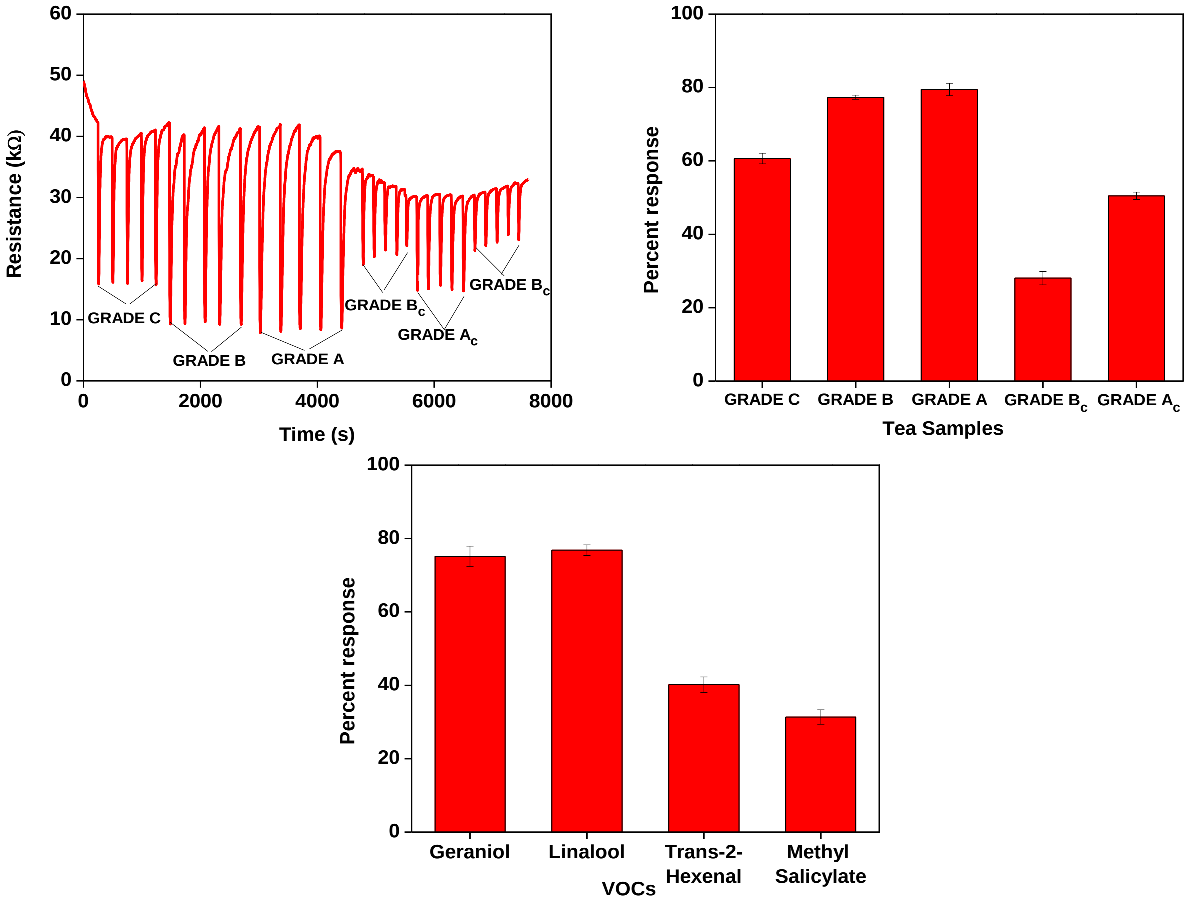

Fig 5.4. *Dynamic sensor response of 1 wt% Au-SnO_2 towards VOCs and grades of black tea*

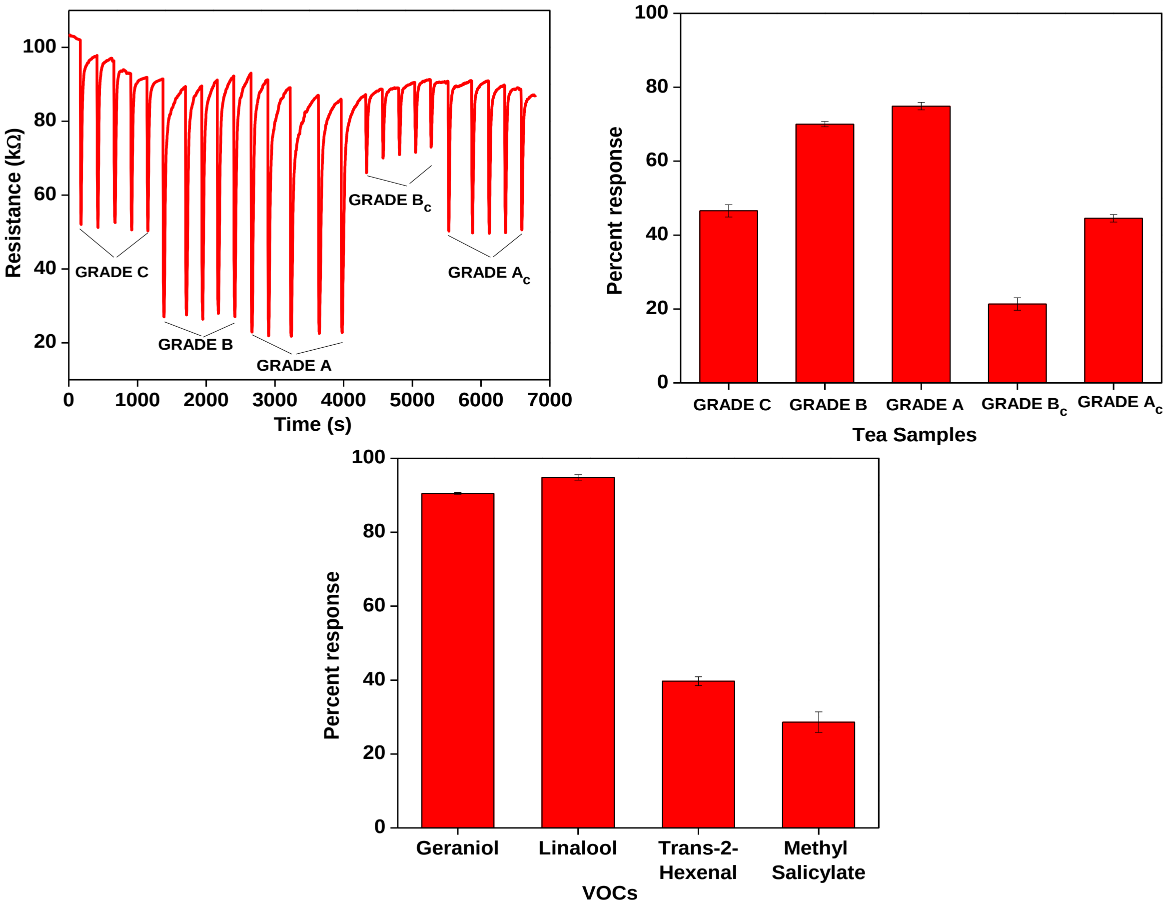

Fig 5.5. *Dynamic sensor response of 5 wt% BaO-SnO_2 towards VOCs and grades of black tea*

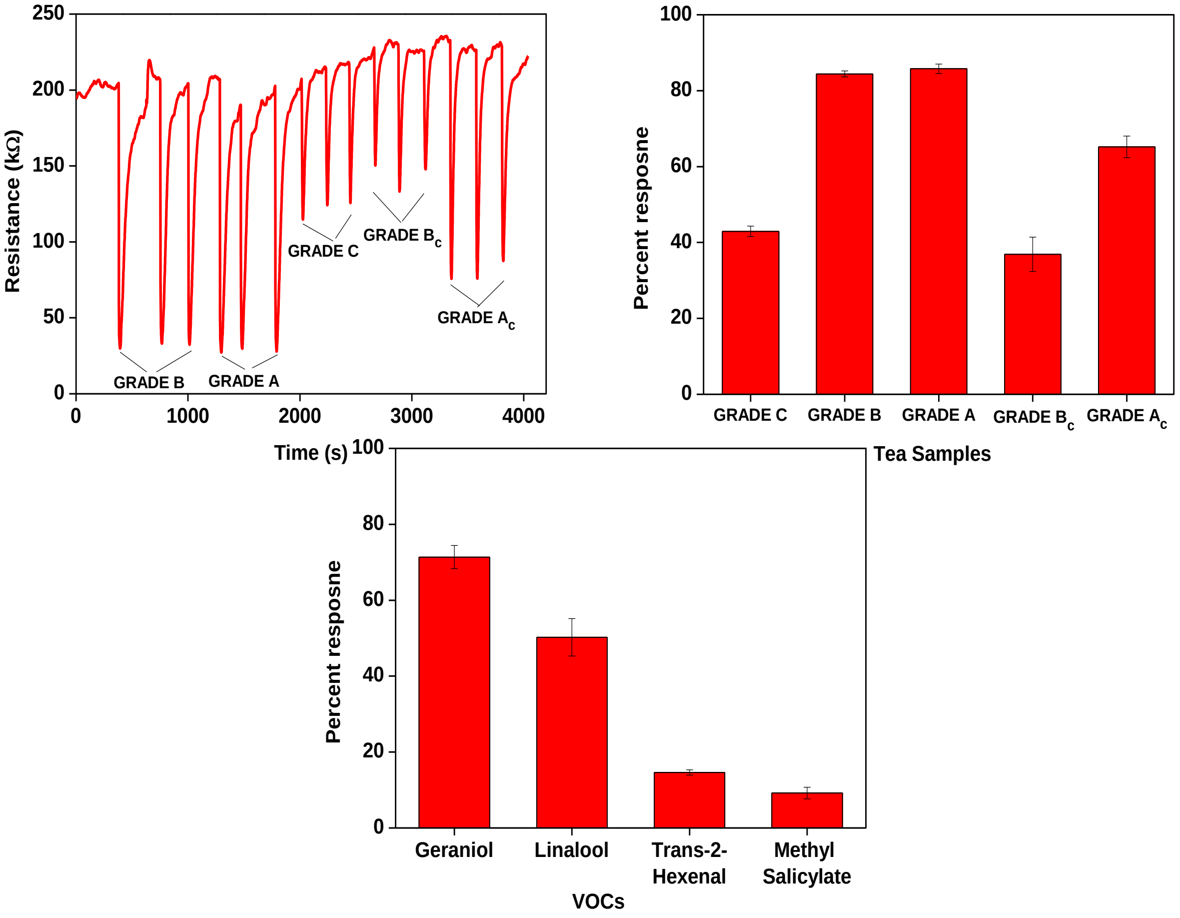

Fig 5.6. *Dynamic sensor response of 5 wt% SrO-SnO_2 towards VOCs and grades of black tea*

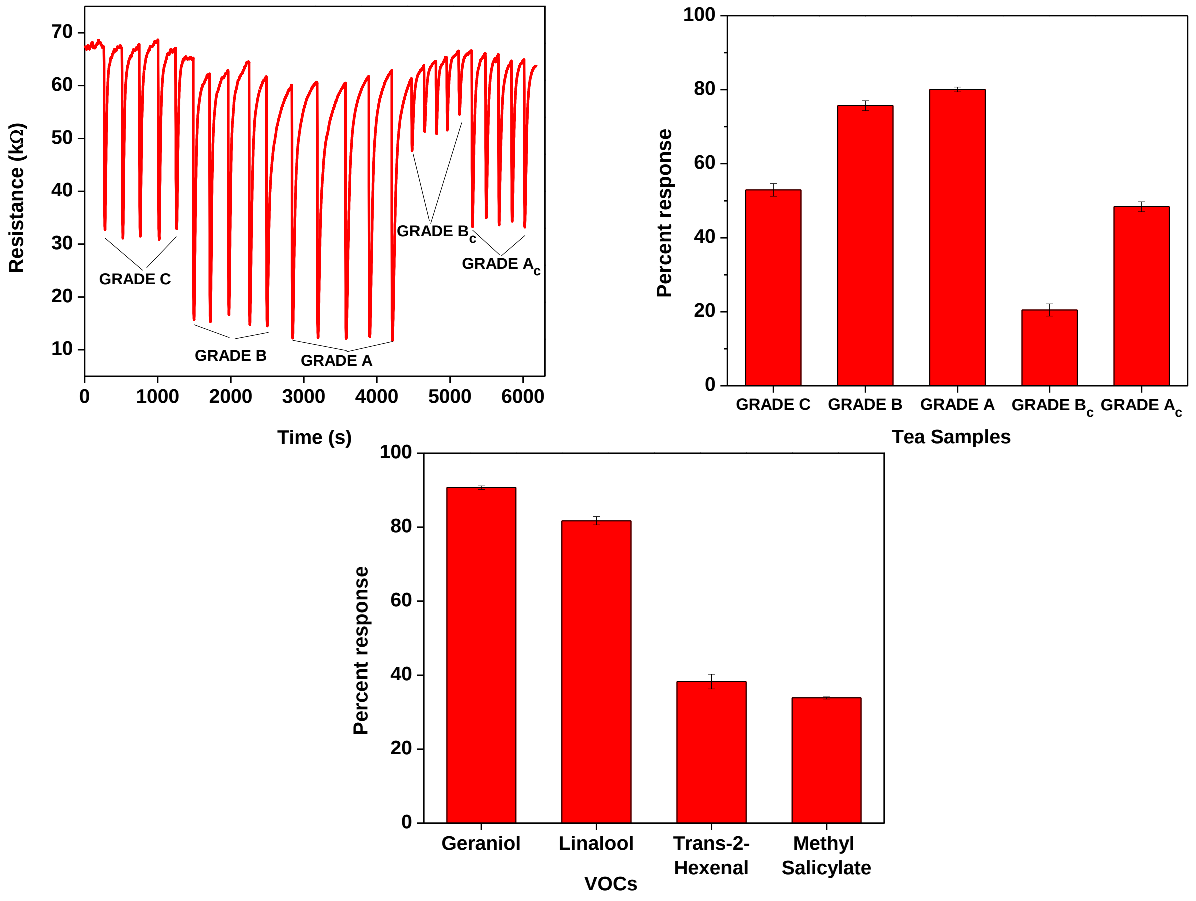

Fig 5.7. *Dynamic sensor response of 3 wt% La_2O_3-SnO_2 towards VOCs and grades of black tea*

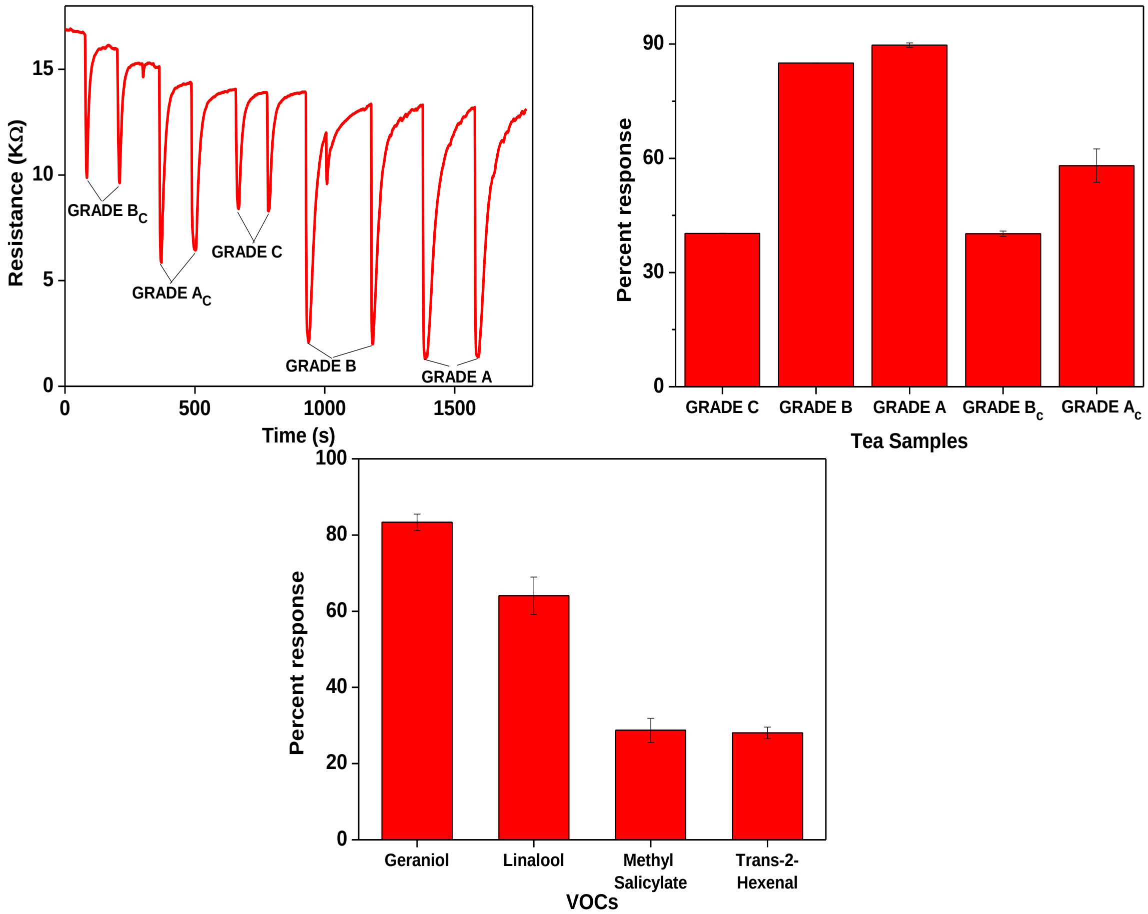

Fig 5.8. *Dynamic sensor response of pristine SnO_2 towards VOCs and grades of black tea*

As can be observed from the figures, the error bars for the engineered materials are significantly less compared to the pristine form of SnO_2. After confirming the efficacy of the developed sensor modules in their ability of detecting the targeted VOCs, the concentration calibration plot was recorded by measuring the sensors response in different concentration of VOCs. Specifically, linalool and geraniol were chosen for the calibration purpose which has been presented in **Fig. 5.9(a)-(b)**. The ratio of impedance in the ambient air and upon exposed to VOCs has been considered as the parameter which highlights the sensitivity.

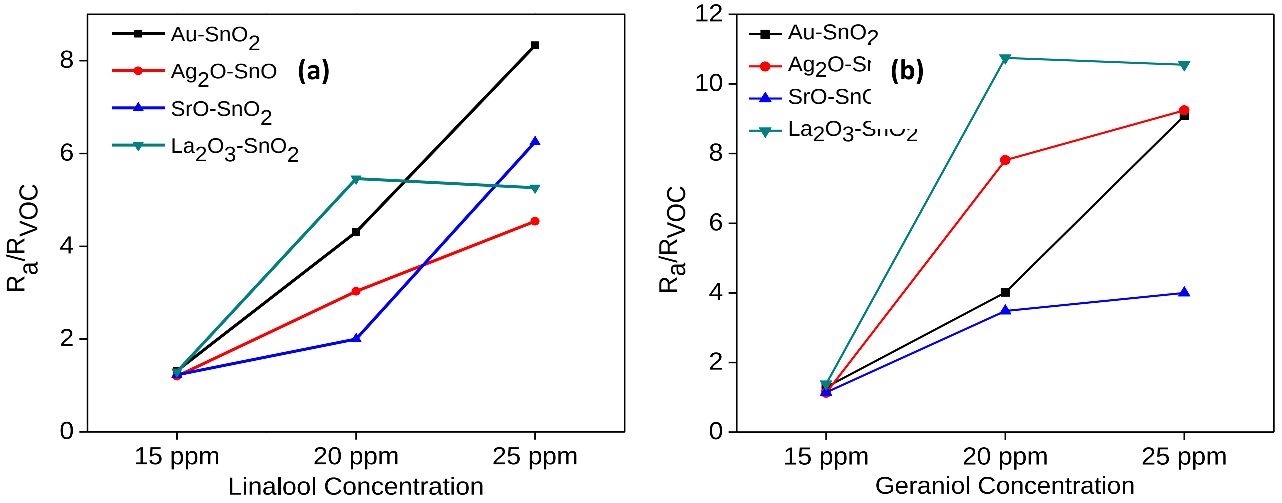

Fig 5.9. *Calibration plot for the developed sensor modules for* ***(a)*** *linalool and* ***(b)*** *geraniol*

The salient observations from the calibration plot has been summarised below

- $Au\text{-}SnO_2$ shows the maximum linearity as well as sensitivity towards linalool. This is expected as gold support have been reported to catalyze the oxidation of the VOCs
- $La_2O_3\text{-}SnO_2$ sensor shows saturation beyond a certain ppm level for both the VOCs
- Silver loaded modules simultaneously show considerable linearity towards the VOCs

The partial selectivity demonstrated by individual sensor module is represented as the ratio of responses among different volatiles and has been tabulated in **Table 5.4**. A higher value would indicate that the sensor is specific towards an individual volatile compared to the other analytes. The table indicates that strontium and barium loaded sensors have higher specificity towards the volatiles compared to other sensors. This observation further corroborates their possible utilization in the electronic nose array for tea aroma detection.

Table 5.4. Partial selectivity of individual sensor towards the targeted VOCs

Sensor Composition	R_{Lin}/R_{Ger}	R_{Lin}/R_{Met}	R_{Lin}/R_{T2H}	R_{Ger}/R_{Met}	R_{Ger}/R_{T2H}	R_{T2H}/R_{Met}
5 wt% BaO-SnO_2	0.71	3.79	2.90	5.32	4.07	1.31
5 wt% SrO-SnO_2	0.70	5.46	3.44	7.75	4.89	1.59
1 wt% Ag_2O-SnO_2	0.77	2.70	2.17	3.52	2.83	1.24
1 wt% Au-SnO_2	1.02	2.45	1.91	2.39	1.87	1.28
3 wt% La_2O_3-SnO_2	0.89	2.40	2.13	2.67	2.37	1.13

5.5.2. Zinc oxide based sensors

The different engineered nanostructures of zinc oxide created in chaper 4 were utilised for sensing VOCs. The different structures were ineffective in detecting carbon monoxide as was elucidated in chapter 4 which subsequently necessitated the templated growth of nanostructures. However, the structures could effectively detect various volatiles measured. The summary of the responses as a measure of percentage change in impedance for the different nanostructures towards different volatiles has been summarised in **Table 5.5**. To adjudge the effect of morphology exclusively all the responses were measured on a single operating temperature of 300 ^{o}C and 30 ppm concentration for individual volatile. A concentration of 20 ppm produced insignificant response for some of the structures therefore the concentration was ramped by 10 ppm. The percent response has been calculated based on the deviation in sensors impedance from its original base value in the ambient air upon exposure to the target analyte.

Table 5.5. Performance of different ZnO morphologies in detection of VOCs

Sensor Morphology	Linalool	Geraniol	Methyl Salicylate	Trans-2-hexenal
ZnO Nanoflakes (CTAB mediated)	55.93	43.72	19.14	21.38
ZnO nanoflowers (PEG mediated)	20.68	31.18	-	20.75
ZnO bulk (No surfactant)	48.37	21.44	-	-

The information extracted from the Table highlights the superior efficacy of ZnO nanoflakes produced after 15 minutes of CTAB mediated sonication compared rest of the nanostructures and the optimised structure was utilised for future sensing purposes. The specific surface area estimated through BET analysis was found to be 17.864 m²/g which is comparable to the surface area observed for the optimized calcium loaded tin dioxide sensors deployed for sensing carbon monoxide as shown in chapter 3.

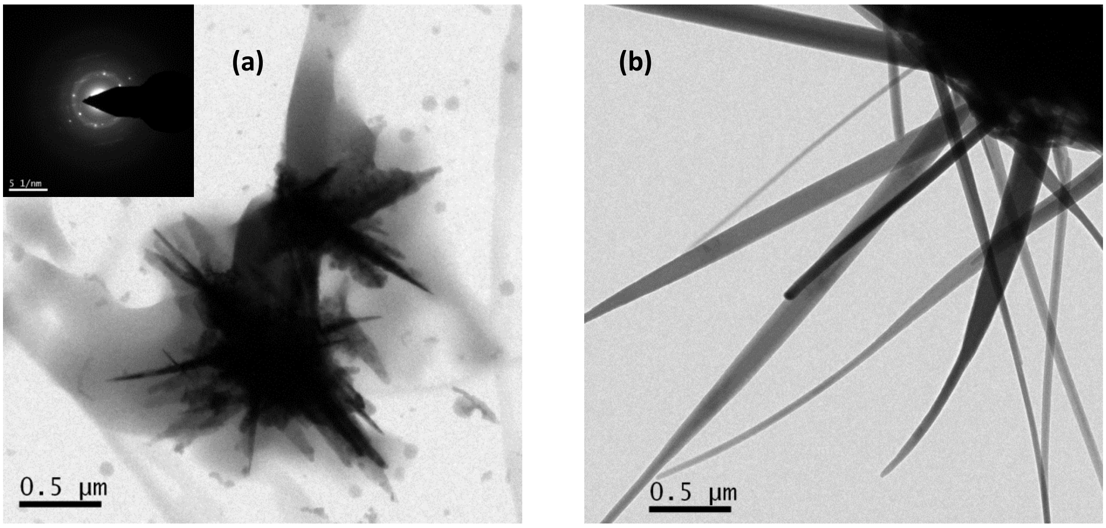

Fig. 5.10. TEM analysis for the zinc oxide nanoflakes showing ***(a)*** *flakes and* ***(b)*** *needle like morphology for individual flake*

Additionally, TEM analysis on the ZnO nanoflakes was performed to further investigate its intriguing structural attributes. The TEM images for the nanoflakes (**Fig. 5.10**) exhibit unique needle like portrusions which might be attributed to the difference in viewing angles for the FESEM and TEM analysis. When the flakes are mounted perpendicular to the grid, they would project needle like shapes. The SAED pattern shown in the inset of **Fig. 5.10 (a)** shows that the crystals are indeed nanorange through the formation of halos.

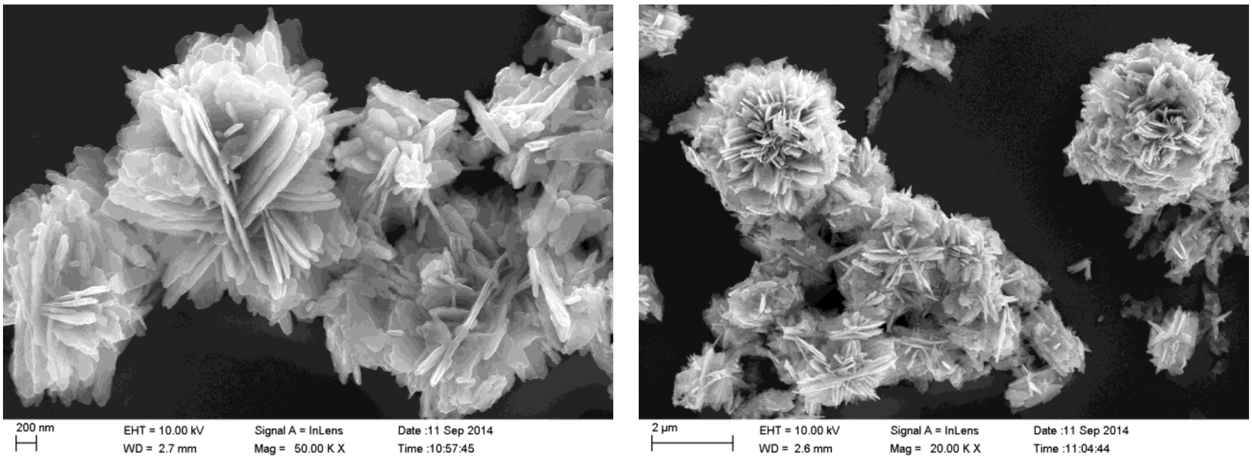

Fig. 5.11. *FESEM images of ZnO nanoflakes showing retainment of morphology even after calcination for 1 h at 400* ^{o}C

However, it is simultaneously imperative that the room temperature synthesized nanoflakes retain its morphology at the operating temperature. Thus the pristine nanoflakes were calcined at 400 °C for 1 h and the final product was analysed through FESEM studies. The microscopic images provided in **Fig 5.11** shows that the nanoflakes indeed retain their inherent structures even after calcining. Since the current morphology was chosen as sensor material among the different nanostructures, this experiment wasn't performed on other structures.

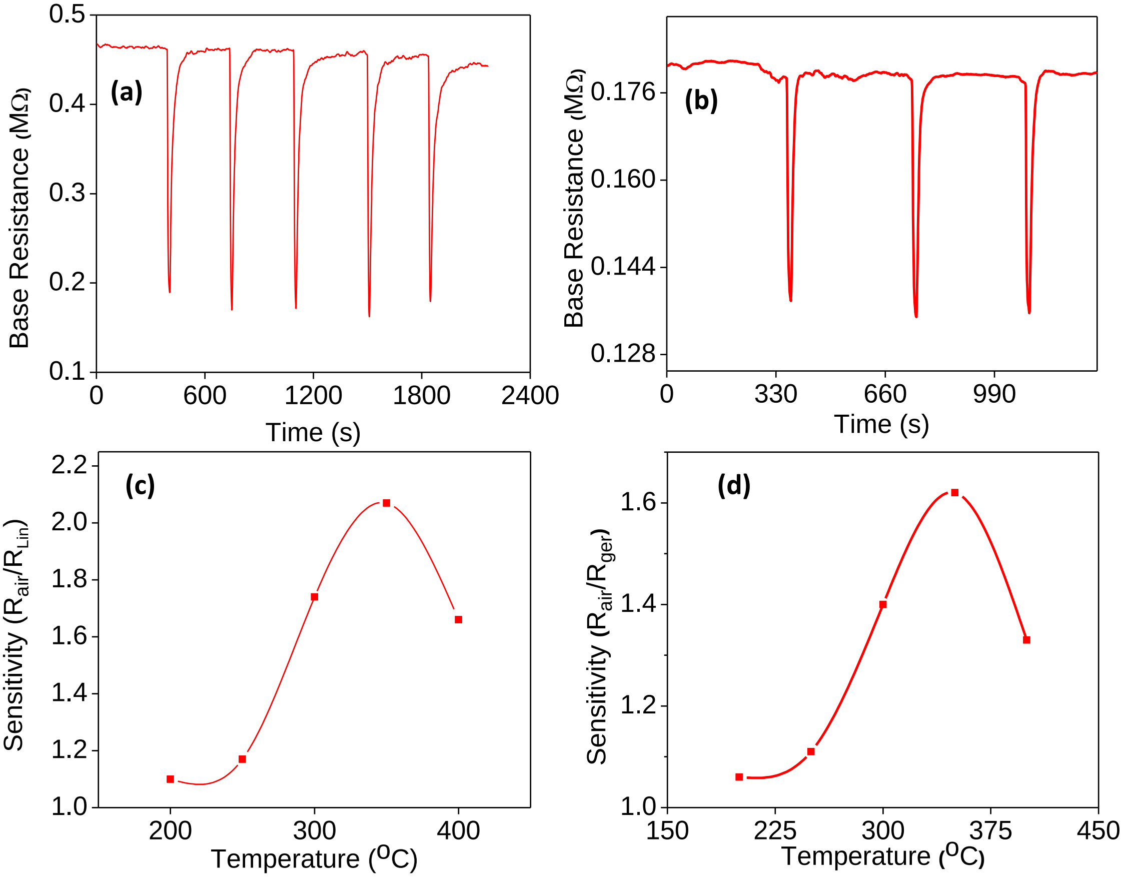

Fig. 5.12. *Dynamic sensing characterisation of zinc oxide nanoflakes sensors upon exposure to* ***(a)*** *20 ppm linalool at 350 °C and* ***(b)*** *20 ppm geraniol at 400 °C. The optimal temperature for operation is found to be 350 °C for* ***(c)*** *linalool and* ***(d)*** *geraniol*

The dynamic characterization for sensor fabricated with the nanoflakes is shown in **Fig. 5.12** which highlights the stability of this sensor over repeated exposure to 20 ppm of linalool and geraniol. Furthermore, the operating temperature of 350 °C was observed to be ideal for sensing applications.

Gold nanoparticle decorated Zinc oxide nanoflakes

Apart from tuning the morphology, surface sensitisation of ZnO particles by implantation of noble metal nanoparticles on their surface is also a prevalent technique applied for enhancing the response of the sensors. In this context, the work of Joshi *et.al.* may be referred where gold nanoparticles were decorated on ZnO nanowires and the amalgamated material was implemented for room temperature detection of CO at relatively higher concentration levels (100-1000 ppm) [23]. A detailed interpretation of the sensing mechanism of gold decorated ZnO nanoparticles towards CO and NO_2 analytes has been provided by Rai *et al.* [24]. In the present study, the as synthesised nanoflakes were then *in situ* decorated with Au nanoparticles with help of low power ultrasonication. The surface decorated nanostructures were then investigated for their response towards low concentration of linalool and geraniol. The synthesis of ZnO nanoflakes were carried out with the aid of sonication at room temperature in the presence of surfactants as elucidated in chapter 4. In order to decorate with gold nanoparticles the as synthesized ZnO nanoflakes (0.3 g) were dispersed in ethanol. To this mixture chloroauric acid ($HAuCL_4$) was added exclusively and sonicated. The reaction temperature for the entire process remained within 27 ^{o}C rendering the whole method to be occurring at room temperature. The sonication was carried out at 200 W for 1 h before the decorated nanoflakes were collected dried and analysed for structural modifications. The electron microscopy studies examining the morphology were carried out on Carl Zeiss-Supra 35VP FESEM system. The microscopic images for the Au-nanoparticles decorated ZnO nanoflakes are presented in **Fig. 5.13** which clearly shows presence of gold specks on the surface of the ZnO crystals. The sporadically distributed gold nanoparticles can be structurally compared to water droplets on the petals of a flower and are expected to catalyse the oxidation of the linalool and geraniol [13].

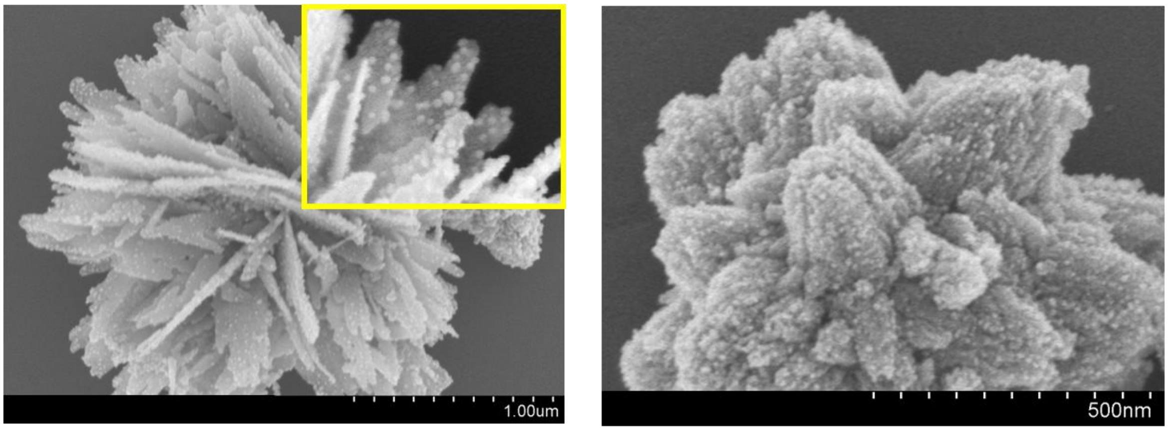

Fig. 5.13. *FESEM images of gold nanoparticles decorated ZnO crystals confirming the presence of the Au-specks on the ZnO surface*

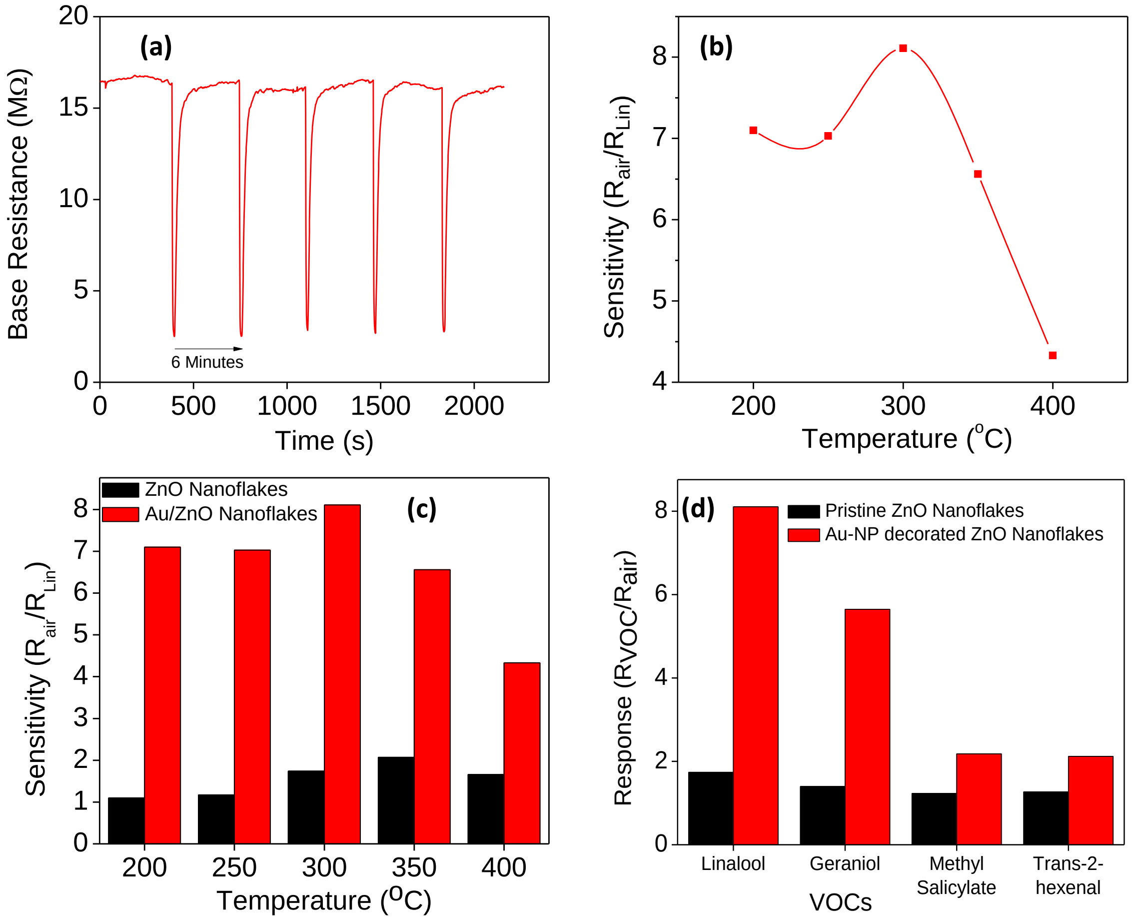

Fig. 5.14. *Dynamic sensing characterisation of zinc oxide nanoflakes sensors upon exposure to **(a)** 20 ppm linalool at 350 ^{o}C. **(b)** The optimal temperature for operation is around 300 ^{o}C. **(b)** Comparison of sensitivities between gold nanoparticles decorated ZnO flakes and pristine ZnO flakes for **(c)** different temperatures and **(d)** different volatiles*

The sensor characterization of gold decorated zinc oxide nanoflakes indeed highlights marked enhancement in response towards linalool and geraniol as shown in **Fig. 5.14**. Yet another improvement in the demonstrated sensor features is the optimised temperature for operation which could be decreased to 300 ^{o}C compared to the pristine ZnO flakes which could ideally be operated at 350 ^{o}C. A comparative plot of sensitivities shown by the gold nanoparticles decorated ZnO nanoflakes against its pristine counterpart shows multifold increase in the response towards same concentration of linalool. The sheer increase in response made the gold decorated ZnO nanoflakes a candidate to reckon for the electronic nose array.

The increased responses towards the aroma volatiles through introduction of gold nanoparticles in the ZnO matrix, motivated in exploring other additives. The list of catalysts introduced into the zinc oxide matrix was presented in **Fig. 5.2**. The response for the sensors towards 20 ppm of target analytes measured at 300 ^{o}C has been summarised in **Table 5.6**.

Table 5.6. *Sensitivities demonstrated by zinc oxide sensors towards tea aroma volatiles*

Samples	**Working Temperature (°C)**	**Sensitivity (%)**			
		Linalool	**Geraniol**	**Methyl Salicylate**	**Trans-2-hexenal**
1% CuO-ZnO	300	28	31	21	26
	350	41	45	28	37
	400	34	38	19	25
5% NiO-ZnO	250	40	37	24	41
	300	57	57	39	53
	350	55	57	39	47
	400	50	46	31	37
5% SrO-ZnO +	250	19	16	17	17
	300	32	40	18	38
	350	45	44	25	42
	400	46	49	31	42
5% BaO-ZnO	250	19	Beyond measurable range.		
	300	30	36	23	32
	350	39	43	28	32
	400	35	38	25	24
5% CoO-ZnO	250	41	35	24	29
	300	49	60	34	50
	350	68	72	54	57
	400	64	67	51	51
5% CaO-ZnO	350	68	34	27	23
5% Cr_2O_3-ZnO	350	48	46	31	36
1% Pd-ZnO	250	32	32	30	38
	300	45	43	41	46
	350	61	60	47	44
	400	60	59	53	52
5% Fe_2O_3- ZnO	350	13	12	5	5

The high base resistance in the megohm range posed a hindrance in incorporation of the modules in the array. Apart from the gold decorated zinc oxide nanoflowers, none of the ZnO based sensors appreciable response. Even the Au-decorated ZnO sensors were limited in their applicability by high baseline impedance although the response for the module towards the VOCs was considerably higher. Therefore, these sensors were eventually discarded in the build up of the array.

5.6. Conclusion

The chapter elucidated development of sensor modules for incorporation within an electronic nose dedicated towards quality monitoring of black tea. The concept of fabricating specific sensors for tea volatiles was mooted from the fact that India is one of the prime producer and consumer of the beverage in the world. Despite the magnitude of the revenue associated with the tea industries, quality estimation of the beverage largely remained a human exertion. A few prototypes that came up used commercial sensors specifically developed for air contaminants and/or toxic gases which relied on the cross sensitivities of the volatiles for calibration. The key volatiles influencing the overall aroma through their synergy were identified based on their odour thresholds. Sensors based on tin dioxide and zinc oxide systems were developed with loaded catalysts that would selectively promote the oxidation of these volatiles on sensor surface. In the zinc oxide system, the nanoflake morphology was observed to be demonstrating better sensing features. The particular nanoflake like structure was then decorated with gold nanoparticles which enhanced the sensitivity by multifold. However, the high base resistance of the zinc oxide based systems proved ominous for their assimilation in the electronic nose array. The high sensitivity and partial selectivity demonstrated by the tin dioxide and zinc oxide based sensors assert their profile as potential replacements for the commercial sensors being utilised in the electronic nose array.

References:

[1] H. Guth, W. Grosch, “Identification of potent odourants in static headspace samples of green and black tea powders on the basis of aroma extract dilution analysis (AEDA)”, Flavour Fragr. J., 8 (1993) 173–178.

[2] C. Schuh, P. Schieberle, “Characterization of the key aroma compounds in the beverage prepared from Darjeeling black tea: quantitative differences between tea leaves and infusion”, J. Agric. Food Chem., 54 (3) (2006) 916–924.

[3] J.H. Moon, N. Watanabe, Y. Ijima, A. Yagi, K. Sakata, “*cis*- and *trans*-linalool 3,7-oxides and methyl salicylate glycosides and (Z)-3-hexenyl β-D-glucopyranoside as aroma precursors from tea leaves for oolong tea”, Biosci. Biotech. Biochem., 60 (1996) 1815-1819.

[4] P. Sharma, A. Ghosh, B. Tudu, L.P. Bhuyan, P. Tamuly, N. Bhattacharyya, R. Bandyopadhyay, U. Das, “A quartz crystal microbalance sensor for detection of geraniol in black tea”, IEEE Sens. J., 15 (2015) 1178-1185.

[5] C.T. Ho, X. Zheng, S. Li, “Tea aroma formation”, Food Sci. Hum. Wellness, 4 (2015) 9-27.

[6] J.C. Zhu, F. Chen, L.Y. Wang, Y.W. Niu, D. Yu, C. Shu, H.X. Chen, H.L. Wang, Z.B. Xiao, “Comparison of aroma-active volatiles in oolong tea infusions using GC–olfactometry, GC–FPD, and GC–MS”, J. Agric. Food Chem., 63 (2015) 7499–7510.

[7] O.G. Vitzthum, P. Werkhoff, P. Hubert, “New volatile constituents of black tea aroma”, J. Agric. Food Chem., 23 (1975) 999–1003.

[8] S.D. Silva, C.B. Moreira, M.A. Esquibel, R.A.D.S.S. Gil, C.A.D.S. Riehl, A. Sato, “Changes in the essential oil composition of *Melissa officinalis* in response to elicitors methyl jasmonate and methyl salicylate”, Agropecu. Téc., 35 (2014) 191-202.

[9] B. Gohain, S. Borchetia, P. Bhorali, N. Agarwal, L.P. Bhuyan, A. Rahman, K. Sakata, M. Mizutani, B. Shimizu, G. Gurusubramaniam, R. Ravindranath, M.C. Kalita, M. Hazarika, S. Das, “Understanding Darjeeling tea flavour on a molecular basis”, Plant Mol. Biol., 78 (2012) 577-597.

[10] H. Rudler, B. Denise, J.R. Gregorio, “X-Ray crystal structure of (tetraphenylimidodiphosphinato)silver(I): an unexpected tetranuclear complex with two modes of coordination of silver”, Chem. Comm., 23 (1997) 2299-2300.

[11] M.G. Speziali, P.A. Robles-Dutenhefner, E.V. Gusevskaya, “Palladium-catalyzed oxidation of monoterpenes: novel aerobic Pd(II)/Cu(II)-catalyzed oxidation of linalool under chloride-free nonacidic conditions”, Organometallics, 26 (2007) 4003–4009.

[12] A. Cantalapiedra, M.J. Gismera, M.P. da Silva, J.R. Procopio, T. Sevilla, “Evaluation of different electrochemical transducers based on polystyrene sulfonate – carbon composites with nickel catalyst for rapid detection of fragrance allergens”, Electroanalysis, 25 (2013) 243 – 251.

[13] D.I. Enache, D.W. Knight, G.J. Hutchings, "Solvent-free oxidation of primary alcohols to aldehydes using supported gold catalysts", Catal. Lett., 103 (2005) 43-52.

[14] N. Marin-Astorga, J.J. Martinez, G. Borda, J. Cubillos, D.N. Suarez, H. Rojas, "Control of the chemoselectivity in the oxidation of geraniol over lanthanum, titanium and niobium catalysts supported on mesoporous silica MCM-41", Top. Catal. 55 (2012) 620-624.

[15] Y. Umasankar, R.P. Ramasamy, "Highly sensitive electrochemical detection of methyl salicylate using electroactive gold nanoparticles", Analyst, 138 (2013) 6623–6631.

[16] T. Seki, J.D. Grunwaldt, N. van Vegten, A. Baiker, "Palladium supported on an acidic resin: a unique bifunctional catalyst for the continuous catalytic hydrogenation of organic compounds in supercritical carbon dioxide", Adv. Synth. Catal., 350 (2008) 691–705.

[17] P. Sharma, A. Ghosh, B. Tudu, L.P. Bhuyan, P. Tamuly, N.Bhattacharyya, R. Bandyopadhyay, A. Chatterjee, "Detection of linalool in black tea using a quartz crystal microbalance sensor", Sens. Actuators B: Chem., 190 (2014) 318-325.

[18] P.A. Lieberzeit, A. Rehman, N. Iqbal, B. Najafi, F.L. Dickert, "QCM sensor array for monitoring terpene emissions from odoriferous plants", Monatsh. Chem., 140 (2009) 947-952.

[19] T. Okabayashi, T. Toda, I. Yamamoto, K. Utsunomiya, N. Yamashita, M. Nakagawa, "Temperature-programmed chemiluminescence measurements for discrimination and determination of fragrance", Sens. Actuators B: Chem., 74 (2001) 152-156.

[20] J.G.H. Whiting, B.P.J.D.L. Costello, A. Adamatzky, "Towards slime mould chemical sensor: mapping chemical inputs onto electrical potential dynamics of *Physarum Polycephalum*", Sens. Actuators B: Chem., 191 (2014) 844-853.

[21] S.P. Lee, "Terpene sensor array with bridge-type resistors by CMOS technology", Mater. Sci. Eng., 87 (2015) 012065(1-5).

[22] N. Bhattacharyya, S. Seth, B. Tudu, P. Tamuly, A. Jana, D. Ghosh, R. Bandyopadhyay, M. Bhuyan, S. Sabhapandit, "Detection of optimum fermentation time for black tea manufacturing using electronic nose", Sens. Actuators B: Chem., 122 (2007) 627-634.

[23] R.K. Joshi, Q. Hu, F. Alvi, N. Joshi, A. Kumar, “Au decorated zinc oxide nanowires for CO sensing”, J. Phys. Chem. C, 113 (2009) 16199–16202.

[24] P. Rai, Y.S. Kim, H.M. Song, M.K. Song, Y.T. Yu, “The role of gold catalyst on the sensing behavior of ZnO nanorods for CO and NO_2 gases”, Sens. Actuators B: Chem., 165 (2012) 133-142.

Chapter 6

Conclusion and Future Scope

This chapter presents a succinct summary of the research findings. It presents some important recommendations for the developed methodology towards various applications while elucidating merits cum limits of the proposed technique. The future directions of research are discussed along with some concluding comments emphasizing the importance and implications of the reported research.

List of Sections

6.1. Summary of findings

The focus of the thesis was concentrated primarily on development of gas sensor modules for instances where the limitations associated with the human olfaction system might potentially have significant adverse effects. Specifically, two instances had been chosen where the utility of sensor modules were determined to be of utmost importance. The aroma quality of black tea is determined by the multidimensional contribution from innumerable volatile organic compounds. Since aroma is a manifestation of olfactory perception in humans, the volatiles with high odour thresholds tend to influence the overall aroma with a greater magnitude. The variation in concentrations of these volatiles emanated within the aroma discerns the overall quality among various tea grades. Presently, the aroma quality determination in tea industries is primarily a human exertion where the oranoleptic perceptions of dedicated experts are utilized. However, the accuracy and reproducibility of human olfaction cannot be relied upon considering the sensory limitation of the biological system. Since the overall aroma depends largely upon the subtle variations in concentration of key volatile organic compounds (VOC), therefore, a segment of the thesis was dedicated towards developing sensor modules for specific detection of these volatile compounds. The sensors, thus fabricated had the opportunity of being incorporated within an electronic nose developed for quality determination of black tea. The electronic nose prototype offers a number of advantages over the conventional technique implemented in the industries presently:

1. Instrumental technique promises to mitigate the errors associated with human organoleptic evaluations and produce a more reliable information about the biochemical features of the tea grades.
2. Depending on the geospatial location and the biochemical parameters of the tea grade the electronic nose can be tuned by incorporating specific sensors calibrated for volatiles particular for that variety of black tea. This allows the flexibility and versatility of the prototype while retaining the inherent simplicity.
3. Earlier versions of the electronic nose utilized commercial sensors developed for detection of air contaminants and toxic gases. The prototype depended upon the cross-sensitivity of the commercial sensors towards the overall aroma. Therefore, calibrated sensors specifically developed for volatiles constituting the aroma provide more opportunity in development of the final prototype.

The other segment of the thesis is also associated with development of sensor modules for the toxic carbon monoxide (CO) gas. The odourless and colourless nature of the fatal gas makes it imperceptible to human olfaction system which cannot deduce its possible presence in the vicinity. Continuos inhalation of the CO molecules results in prolonged adverse effects on the human metabolism and can potentially lead to mortality. While there are no account of commercially available sensors for tea aroma volatiles, modules for carbon monoxide detection are easily accessible and are commercially available. However, these sensors use expensive noble metals as catalysts which adds to the overall production cost. Additionally, these sensors have relatively larger acclimatization period and longer response and recovery period. Moreover, though the commercial sensors cater to the Threshold Limit Value (TLV) prescribed by OSHA of 35 ppm, most of them fall short to the new TLV guidelines provided by other world health regulatory bodies like EPA and WHO of 9 ppm. Thus this thesis tried to develop sensor modules with cost effective catalysts which could detect down to 1 ppm of carbon monoxide reliably.

The problem statement of the current dissertation was framed in the introductory chapter and was divided in two distinct portions:

(a) “The development of sensor modules for selective detection of major volatile organic compounds like linalool, geraniol, methyl salicylate and trans-2-hexenal in tea aroma”

and

(b) “The development of MOS based sensor modules for selective and fast detection of carbon monoxide below their statutory limits with cost effective catalysts”.

The thesis comprise of four technical chapters in addition to the introductory chapter which framed the problem statement. The technical chapters were categorically divided to elucidate the salient findings in our objectives to develop sensor modules for carbon monoxide and tea aroma volatiles.

Chapter 2 describes the different techniques adopted for production of tin dioxide which is incidentally the one of the materials chosen for fabricating sensor modules. The chapter highlights the precipitation technique as an effective modality for producing tin dioxide. Detailed study correlating the phase and electronic evolution of tin dioxide has been performed which revealed the calcination temperature as well as the kinetics to be determining parameter. In a novel synthesis method, pristine tin dioxide as well as tin monoxide could be produced through simple ageing of the interim precipitate acquired after precipitation of the precursor salt with an alkali. The method, although effective in minimizing the thermal budget, was slow for practical purposes. This instigated the advent of sonochemical aided precipitation method for synthesis which rapidly produced relatively smaller crystals compared to the simple precipitation technique. Knowledge about the promoting effect of an increasing cationic ratio within the system through evaporation of water, gathered from the room temperature production method, prompted to introduce manganese as supplements into the system. In an unique observation, variation in the additive concentrations brought about discerning effect in the phase evolution of tin dioxide as tin dioxide and tin monoxide could be produced by simply altering the manganese levels. However, in purview of the mandates for the current dissertation, sonication aided precipitation synthesis was opted as ideal because of its ability to produce crystals with high specific surface area at a rapid rate.

Chapter 3 describes the development of low concentration carbon monoxide sensors with group II elements loaded tin dioxide crystals. The results indicate that the fabricated sensors performed at par or even superior to commercially available modules. The detection limit for the calcium loaded SnO_2 sensor was observed to be as low as 1 ppm with a linear calibration plot. The exciting performance of these cost-effective sensor modules could be attributed to their relatively larger specific surface area. This in turn was a consequence of the grain growth inhibitory effects demonstrated by the oxides of the group II elements utilized as additives.

Chapter 4 describes the synthesis protocol adopted for production of different morphologies of zinc oxide nanostructures. The different structures were expected to show optimized sensor response. However, most of the structures demonstrated minimal response towards carbon monoxide. An alternate approach with templated synthesis of zinc oxide structures was adopted which showed relatively better sensing of the toxic gas. Despite the improvement in overall sensing for the templated zinc oxide crystals, the carbon monoxide detection ability for ZnO nanocrystals were found wanting in comparison to their SnO_2 counterparts.

Chapter 5 describes the engineering of ZnO and SnO_2 crystals for fabricating sensor modules capable of detecting VOCs emanated within black tea aroma. The developed modules could selectively detect the major volatiles and were calibrated for their possible inclusion in the electronic nose array.

The limitations of the engineered nanomaterials developed during this dissertation can be summarised as:

(a) Susceptibility towards moisture: It is an established fact that humidity affects the performance of the MOS sensors adversely.

(b) Absence of benchmarks: This limitation is pertinent for the sensors developed for the electronic nose prototype. The very domain of research lacks a prominent knowledge base and therefore the performance of the sensors could not be compared against an existing benchmark. This creates a hindrance in acceptance of the sensor modules in the electronic nose prototype.

(c) Higher power requirement: The Taguchi type indigenous sensors draw about 1 W power for operating at 350 ^{o}C. In comparison to the monolithic planar sensors with microhotplates which draw power in the microwatt range, the designed modules have a higher power budget.

6.2. Conclusion

The current dissertation focussed on development of engineered nanomaterials as sensing composites for detection of toxic carbon monoxide and volatiles emanated from black tea aroma. The work reported indicates a significant research potential in this field while uncovering the areas where researchers may contribute for improvement. A persistent research towards the aroma based quality estimation of tea is not only very important for enrichment of scientific knowledge base but shall have a profound impact towards the improvement in tea manufacturing practices and may be gainfully implemented in the production line in the tea industries.

The present research embodies two important applications of indigenous gas sensors where they have been implemented for detecting the presence of toxic gases and quality monitoring of an agro product as two separate objectives. The fabricated gas sensors can be recommended for the following applications:

1. Assessment of black tea quality in terms of aroma content to present an accurate and reliable idea about the finished tea samples by incorporating the developed sensors in an electronic nose prototype.
2. Detection of toxic carbon monoxide below its statutory limits in the ambience by interfacing the calibrated sensor modules with a standard data acquisition circuitry.

6.3. Future scope of research

Every directed research program opens up new frontiers for further exploration where invested efforts are expected to yield rich dividends. The current dissertation has been aligned with the mandates framed according to the identified problems, and stated in the introductory chapter. However, vested efforts have brought forward certain areas which demands further exploration and might result in incremental expansion of the existing knowledge base.

1. The aroma content of black tea is constituted by numerous odour active volatiles, off which four major VOCs with high odour threshold were chosen as key components. Accordingly sensors were designed for specific detection of these volatiles. These sensors were made partially selective to these major volatiles through introduction of definite additives and/or rendition of morphologies. However, the perchance of other constituent volatiles influencing the response for these sensors cannot be undermined. Further research should strive towards increasing the selectivity of these sensors towards the selected volatiles with high odour activity values.
2. Different systems other than the SnO_2 and ZnO might be explored for better performance of the sensors. For example TiO_2 or CeO_2 systems might be beneficial for sensing of the toxic gas. Superstructures of ZnO embedded on low-D carbon materials like graphene sheets is another promising material for CO detection.
3. For the current dissertation, Taguchi type hollow cylinders of alumina were used as sensor substrates and standard TSO heads as sensor packages. This modality, though accepted globally, is limited in its application owing to a relatively large power budget. In comparison planar substrates with patterned electrodes require much less power to operate. The electrodes might be designed on the planar silicon wafers through photolithography technique while the deposition of the sensing materials might be made through standard RF-sputtering of CVD methods. An attached coplanar microhotplate shall provide the required operating temperature for the sensing.
4. The sensor array designed for the electronic nose comprise of discrete modules assembled together. This allows the flexibility of interfacing optimized units at ones discretion. But it simultaneously increases the overall power requirement for the prototype. Instead a monolithic approach where sensors are embedded in a single substrate might be suitable in minimizing the power requirements. Appropriate circuitry for acquiring multiplexed data from the monolithic sensor might prove beneficial where real time monitoring is not of primary essence.
5. The electronic nose prototype is currently deployed in user industries where they are commissioned inside the factories. This implies that the electronic nose can only operate after the cultivars bring the tea leaves to the factories. Thus, constant real time monitoring where the electronic nose might transmit information right from the tea gardens upon deployment is not yet possible. However, the scientists have taken special interest in this

domain of research where they have coupled Wireless Sensor Network (WSN) with the electronic nose prototype and are transmitting data directly from the agro-field. A standard Zigbee 802.15.4 transmission protocol is normally utilized for the data transfer, though concepts like cloud computing and GSM based data transfer are categorically being developed. Such mode of data transfer implies that the information can be directly accessed from a cell phone via a dedicated application software.

6. The developed materials have proved their efficacy in detecting the presence of the toxic fumes. Under normal scenario, the sensor shall be interfaced with a data acquisition system and commissioned inside a confined area. This limits the spatial reach of the modules which can then detect carbon monoxide only in its vicinity. However, the scope for such sensor materials drastically improves if they can be interfaced with flexible and wearable data acquisition systems. Such models will ensure that the ambience of an individual shall be monitored constantly thus avoiding any adverse repercussions.
7. Apart from the technological perspective, future investigations might explore the exact phenomenon occurring at the sensor surface when the tea aroma volatiles are dispensed. Oxidation mechanism for carbon monoxide on the metal oxide semiconductor surface has been extensively studied. However, there is a serious lack of knowledge about the nature of the reactions undergone by the complex volatiles like linalool and geraniol on the sensor surface. This might be studied by collecting the desorbed vapours and performing a GC-MS analysis on them.